Chromatographic and Adsorptive Behavior of Bivalent Bispecific Antibodies

A dissertation presented to the faculty of the
School of Engineering and Applied Science
University of Virginia

In partial fulfillment of the requirements for the degree of
Doctor of Philosophy in Chemical Engineering

by

Lucas K. Kimerer

May 2021

APPROVAL SHEET

This Dissertation
is submitted in partial fulfillment of the requirements
for the degree of
Doctor of Philosophy

Author Signature: 

This Dissertation has been read and approved by the examining committee:

Advisor: Giorgio Carta

Committee Member: Geoffrey Geise

Committee Member: Roseanne Ford

Committee Member: Chris Highley

Committee Member: Andreas Gahlmann

Accepted for the School of Engineering and Applied Science:

Craig H. Benson, School of Engineering and Applied Science

May 2021

Abstract

Bivalent bispecific antibodies are structurally comprised of an entire framework immunoglobulin G (IgG) genetically fused to two single chain variable fragments (scFv) via flexible peptide linkers. The flexibility of the linkers allows three extreme configurations where each scFv can be collapsed and interact with the framework IgG, or extended and able to interact with a surface or binding epitope with greater affinity. Slow interconversion between these configurations is found to cause multiple peak elution and complex adsorption kinetics on chromatography media. Surface catalyzed conformational changes greatly decrease separation efficiency and complicate the design of separations. The overall goal of this work is to fundamentally understand the conformational changes of BiSAbs and their major effects on column behavior and adsorption kinetics for cation exchange (CEX) and hydrophobic interaction (HIC) chromatography media.

This work first characterizes the reversible, multiple peak phenomena observed for linear gradient elution. Pure BiSAb samples elute three peaks at room temperature and low residence time (~2 min). All three peaks are monomer-sized, measured by dynamic light scattering. When the residence time is elongated to ~40 min or temperature is elevated to ~55 °C, a single peak elutes with average retention. When the protein is held bound on the resin, the relative size of the strongest binding peak increases. BiSAb fragments with a single linked scFv follow the same trends as the intact molecules, but with reversible two peak elution. BiSAb fragments or the framework IgG, containing zero linked scFvs, elute a single peak regardless of operating conditions. The BiSAb multiple peak elution behavior is qualitatively consistent regardless of: scFv attachment location to the framework IgG, resin structure (pellicular or porous), pH of the mobile phase, and resin functional ligand (weak CEX, strong CEX, or HIC). These effects are

therefore driven by the molecular properties of the BiSAbs, rather than resin specific factors. Adsorption kinetics of these complex proteins was studied by viewing transient intraparticle bound profiles using confocal microscopy. The BiSAb intraparticle profiles showed smooth characteristics caused by the slow exchange from the weaker binding, collapsed configuration to the stronger binding, extended configurations. Phenomenological models were developed at the column scale, to predict the multiple peak elution behavior, and at the particle scale, to predict the complex adsorption kinetics.

Finally, the separation between the intact BiSAb molecule and two associated fragments was studied on CEX resins. Both fragments were found to have one scFv missing and elute prior to the intact protein. The fragment with intermediate binding strength contained one additional amino acid, a C-terminal lysine. Linear gradient elution measured fairly small differences in binding strength between the protein species. However, at high load, high selectivity was observed and the intact molecule was found to displace the fragments with relatively fast kinetics.

Acknowledgements

I am extremely grateful for all the mentors and friends who supported and had an impact on me throughout my time at UVa. My accomplishments and career interests are shaped by the individuals I strive to model myself after.

To my advisor, Giorgio Carta, thank you for your guidance throughout graduate school and encouragement to take risks in lab and look at problems from unique viewpoints. One of the biggest lessons I will take away from our discussions is that when we start with measuring the fundamentals and understand how experiments should behave, it allows you to notice very interesting phenomena. I really appreciate how connected our group was with the rest of the field. Through short course, conferences, and visiting students it was great to be able to connect with and make friends internationally throughout the field. I will always remember our trip to Milan.

To my collaborators, Alan Hunter, Tim Pabst, Ben Niu, and the team at AstraZeneca, thank you for great discussions and support for this project. Your contributions and insight have made this project successful.

To my committee, Prof. Geoffrey Geise, Prof. Andreas Gahlmann, Prof. Roseanne Ford, and Prof. Chris Highley, and to the rest of the chemical engineering department faculty, thank you for your valuable discussions and teachings.

To my fellow labmates, Joey, Preston, Arch, Jason, Yiran, Andreas, Jing, Xue, Christiane, Calef, and Patricía, thank you for making lab a fun and supportive environment. Research inherently has many setbacks and struggles. I learned the most during the countless hours we spent in lab together troubleshooting each other's experiments and workshopping ideas.

To my class, I feel very lucky to have been with such a fun group. I will cherish all the memories we've made in Charlottesville and miss our BBQ's in the backyard and trips to the breweries and vineyards.

To Wai Keen Chung, thank you for inspiring my interests in the field and being a great mentor ever since we met. I really appreciate your advice and support.

To my family, our frequent phone calls and trips have kept us very close throughout this time. Your guidance has made me the person I am today.

Finally, to my fiancé, Makenzie, your love and encouragement through each step has meant everything to me. While we will definitely miss Charlottesville, I am very excited for the next steps in our lives together.

Lucas Kimerer May, 2021 Charlottesville, VA

Table of Contents

List of Figures

List of Tables

List of Symbols

Symbols

A	Equilibrium binding constant
C	Solution phase protein concentration (mg/ml)
C_{Na^+}	Sodium concentration in solution
$C_{Na^+}^{f}$	Sodium concentration at end of linear gradient
$C_{Na^+}^{o}$	Sodium concentration at start of linear gradient
$C_{Na^+}^{R}$	Sodium concentration at peak maximum of gradient
CV	Column volume
CV_G	Length of gradient in column volumes
D_e	Effective diffusivity (cm^2/s)
D_o	Free solution diffusivity (cm^2/s)

d_p Resin particle diameter (μm)

h Reduced plate height $h = HETP/d_p$

$K_{a,i}$ Henry's constant, isotherm slope at low load conditions

k_b Boltzmann constant

K_L Langmuir equilibrium constant (ml/mg)

$\overline{k_i}$ Interconversion adsorbed phase kinetic rate constant

$\overline{K_i}$ Interconversion adsorbed phase equilibrium constant

k_i Interconversion solution phase kinetic rate constant

K_i Interconversion solution phase equilibrium constant

k' Protein retention factor

q_o Ionic capacity of resin (mM)

r_h Hydrodynamic radius (nm)

$\boldsymbol{r_1}$ Net rate of formation in solution phase

$\overline{\boldsymbol{r_1}}$ Net rate of formation in adsorbed phase

r_p Resin particle radius (μm)

q Adsorbed phase protein concentration (mg/ml)

$\hat{q}_i$ Total solute concentration in the particle $\hat{q}_i = q_i + \varepsilon_p C_i$

q_m Maximum adsorption capacity (mg/ml)

t Time

v Mobile phase interstitial velocity

ν Reduced velocity $\nu' = \nu d_p / D_0$

x Column axial coordinate

z Effective binding charge

Greek Symbols

α	Temperature dependent interconversion rate factor
ε	Extraparticle (or external) void fraction
ε_p	Intraparticle (or internal) void fraction
λ_{max}	Fluorescence maximum emission wavelength (nm)
λ_i	Solvophobic model equilibrium parameter
γ'	Normalized gradient slope
ϕ	Phase ratio of column, $\phi = (1-\varepsilon)/\varepsilon$
μ	Solution viscosity
ρ_s	Normalized front position of protein in the particle, $\rho_s = r_s/r_p$
σ	Protein shielding factor in steric mass action model
τ_p	Tortuosity factor
ψ_p	Hindrance factor

1 Introduction and Objectives

1.1 Introduction

1.1.1 Bispecific Antibodies as Therapeutic Proteins

Recombinant DNA technology is based on the insertion of genes that code for a desired protein into a host cell. The inserted genes propogate with the cells in a bioreactor and direct the manufacture of the protein of interest. Once expressed, the cell culture broth is purified using a series of chromatography and filtration steps to separate host cell contaminants from the desired protein. This technology has profoundly impacted the pharmaceutical industry and provided methods of production for a wide range of biotherapeutics. Proteins used as therapeutics can be broadly characterized in three groups: those expressed as replicates of protein that a patient is deficient in, such as insulin or human growth factor [1]; native proteins whose primary structure has been partially altered to direct its inherent function towards a therapeutic target, such as monoclonal antibodies (mAbs) which bind with high specificity to a targeted epitope and thereby neutralize that target [2][3]; or novel protein structures that are expressed to provide new mechanisms of action not found in nature, such as bispecific antibodies or antibody drug conjugates [4][5].

Bispecific antibodies are engineered for the ability to bind simultaneously two unique targets with a single molecule. Simultaneous binding of two targets allows unique mechanisms of action not possible with combinations of monoclonal antibodies, such as T cell localization or clotting factor replacement [6][7][8]. As a result, increased therapeutic efficacy has been observed for bispecific antibodies over combinations of monoclonal antibodies for a variety of indications including cancer and infectious diseases [9][10]. Interest in bispecific antibodies as therapeutics is increasing. For example, there were 10 clinical trials for bispecific formats in 2010 and 56 clinical trials in 2018 [4]. Currently there are two USFDA approved bispecific antibodies [4]. Structurally,

many bispecific formats have been developed. The formats range in size from fused antibody fragments (25-50 kDa), to bispecific immunoglobulin G (IgG) which pair heavy and light chains from separate parental antibodies (150 kDa), to appended IgGs which fuse additional domains or full antibodies to termini of the full framework IgG (>150 kDa) [4][11].

This work focuses on one particular appended IgG bispecific class, bivalent bispecific antibodies (BiSAbs). These proteins are comprised of an entire IgG genetically fused to two single chain variable fragments (scFv) via flexible polypeptide linkers. The molecules of this work have linkers made of glycine and serine in series $(G_4S)_2$ [12]. The scFvs each are ~25 kDa in molecular weight bringing the total BiSAb molecular weight to ~200 kDa. The flexibility of the linkers allows the scFvs to be attached to different locations along the framework IgG while still ensuring proper folding [10]. The attachment location varies the interparatopic distance between binding domains. Depending on therapeutic use, having the binding domains in close proximity to one another or on opposite ends of the framework IgG could be desired [10].

A series of homologous BiSAbs which contain the same primary sequence of amino acids, but vary by scFv attachment location are the subject of this work. BiSA, BiSB, and BiSC have scFvs attached to the N-terminus of the heavy chain, C-terminus of the heavy chain, and between the CH2 and CH3 domains in the fragment crystallizable (Fc) region, respectively. Pictographs of the three BiSAb structures are shown in Figure 1.1. The Fab domains are colored in blue, Fc domains in green, scFvs in orange, and the complementarity determining regions (CDR), which bind to the targeted epitopes, are shown in red. The linkers also confer a high degree of quaternary structure flexibility. The protein structures are shown with scFvs in an outstretched conformation, but many other conformations are possible with different extents of association between the scFvs and framework IgG.

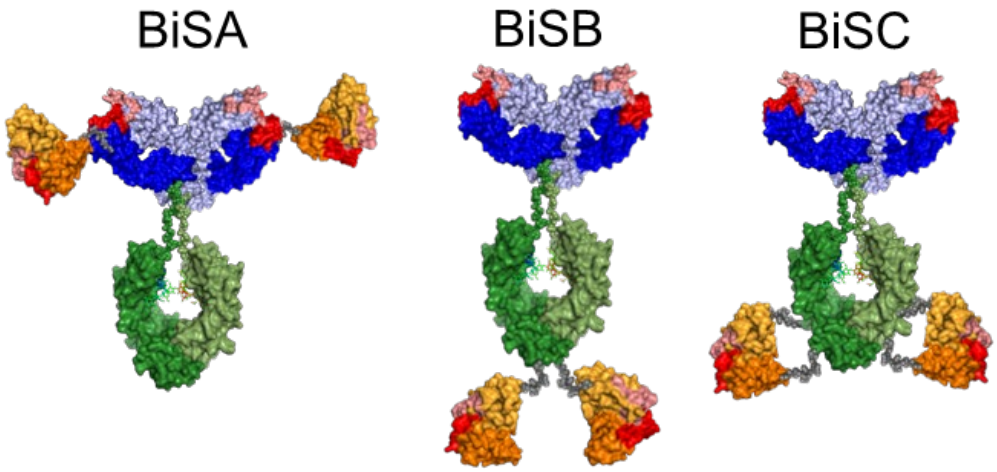

Figure 1.1. BiSAb protein structures used in this work. Molecules vary by attachment location of scFv domains, shown in yellow and orange, alone. Complementarity determining regions are shown in red. Fab domains are shown in blue. The Fc domains and hinge are shown in green.

As a result of their structural complexity, the expression of recombinant heterologous proteins is very frequently accompanied by a vast array of protein variants that originate from transcription, translation, and post translational modification steps. In the context of producing biopharmaceuticals, many of these variants, including certain charge variants, are mute and do not affect stability or efficacy [13]. However, other variants, such as misfolded proteins, fragments, and aggregates, can have greatly reduced potency, cause an undesirable immunogenic response, or even destabilize the product. In these cases, removal of these variants becomes paramount [14][15]. Because of their chemical and structural similarity to the desired product, removal of these variants will often have to rely on highly selective chromatographic methods. Large, multidomain proteins can exhibit complex interactions with surfaces as each domain has its own distribution of surface exposed charged and hydrophobic patches increasing the difficulty of separations. The focus of this work is to understand the complex behavior observed for bivalent bispecific antibodies on chromatography columns used in the downstream purification or analytical characterization of these molecules.

1.1.2 Downstream Purification

The downstream purification of BiSAbs generally follows the so-called platform process for monoclonal antibodies [16]. The process begins with affinity capture using protein A chromatography which binds with high selectivity the Fc domain of the framework IgG. A series of filtration and polishing chromatography steps are then performed to further remove host cell proteins, nucleotides, and product related variants [17][18]. Product related variants are especially prevalent with these non-native, engineered proteins. Andrade et al. [19] reported aggregate content for similar BiSAb formats of ~15-30% from the bioreactor. Hall et al. [17] identified a structural variant caused by a misformed disulfide bond between the two linked scFvs that made

up ~12% of the monomer. Chapter 6 of this work explores fragments of BiSB with one missing scFv that made up ~26% of the sample [20]. Separation strategies for removing these variants include cation exchange chromatography (CEX), hydrophobic interaction chromatography (HIC), and ceramic hydroxyapatite chromatography [19][18][21][22]. An understanding of BiSAb adsorption on these chromatography modes is therefore desired. This work focuses on BiSAb behavior for cation exchange and hydrophobic interaction chromatography.

Although the binding mechanisms are very different between CEX and HIC, both provide separation based on differences in binding strength between proteins for the resin surface. Binding strength is modulated by changing the mobile phase composition. In CEX, protein adsorption is driven by electrostatic interactions between the protein's surface exposed charged residues and the resin's charged ligands. These interactions are promoted at low salt conditions and elution is obtained by increasing the concentration of a chaotropic salt [18][23][24]. In HIC, adsorption occurs at high kosmotropic salt conditions driven by a combination of salting out entropic forces and hydrophobic interactions between the protein's surface exposed nonpolar residues and the resin's mildly hydrophobic ligands [21][18][25]. The high kosmotropic salt conditions stabilize the protein to allow reversible interactions. Elution is thus, obtained by reducing the kosmotropic salt concentration. In both CEX and HIC, the strength of binding can be thought of as being dependent on the footprint of the protein on the surface. For example, both HIC and CEX are found to be effective for the separation of monomer and aggregate species, with aggregates generally binding more strongly than monomeric forms [26][27][28][29][30]. Besides the size of the binding footprint, interactions between specific areas of the protein surface and the chromatographic surface are likely to play an important role as they determine the preferred binding orientation. Hubbuch and co-workers [31][32][33], for example, have demonstrated that even a small protein

like lysozyme (~15 kDa molecular mass) can interact with chromatographic surfaces in orientation-specific ways dependent on factors such as load, pH, and resin structure. More recently, Robinson et al. [34] have shown that for larger and more complex proteins like antibodies, different protein domains interact differently with chromatographic ligands each contributing to the overall binding strength and selectivity. Small structural or conformational changes in the protein or changes in the mobile phase significantly alters binding strength which allows these nonaffinity chromatographic surfaces to have high separation efficiency between closely related molecules.

Whether motivated by the incentive of market exclusivity through patent protection awarded to the first therapeutic approved for a specific indication, or in response to a global pandemic such as COVID-19, speed in development is of great importance. Rational design of these process steps can reduce development time of determining operating parameters that are robust and provide purity that satisfies USFDA requirements. A common approach in modeling chromatography steps is to employ an isotherm model to describe effects of protein concentration and mobile phase composition on adsorption equilibrium and to use a rate model to describe kinetics [21]. Conformational changes of the protein while adsorbed to the chromatographic surface can disrupt this approach in several ways. It can alter the structural integrity of the protein, cause the protein in different binding orientations to elute at multiple salt concentrations, or cause competition between binding configurations during transient adsorption. These phenomena obviously complicate the isotherm and kinetic model and impact recovery and separation efficiency. We seek to understand conformational changes of BiSAb proteins and develop models to predict these effects to aid in rational design of chromatography steps.

1.1.3 Surface Catalyzed Conformational Changes

Both cation exchange and hydrophobic interaction chromatography are generally regarded as non-denaturing separation techniques. However, recent work from several authors has shown that conformational changes occur on both CEX and HIC media more commonly than previously thought. From a macroscopic viewpoint, such conformational changes are typically manifested as multiple peak elution behavior where loading a pure protein to a column results in complex elution patterns. Gillespie et al. [35], for example, showed that loading a highly pure aglycosyalated antibody on a cation exchange column and eluting it with a salt gradient resulted in two elution peaks – one comprised almost exclusively of the monomeric form of the antibody and one comprised of a mixture of monomer and aggregated species formed within the column. Qualitatively similar multiple peak elution behaviors were observed by other authors for various proteins on both cation and anion exchangers [36][37][38][39][40] and HIC resins [41][42][43][44][45][46]. The molecular basis for these behaviors is typically assumed to be the existence of kinetically limited conformational changes catalyzed by the adsorbent surface. Guo et al. [37], for example, using hydrogen-deuterium exchange mass spectrometry (HXMS), showed that the solvent exposure of a monoclonal antibody bound to a CEX resin, increased over time while holding the protein on the surface creating an increased percentage of a destabilized intermediate which aggregated upon elution resulting in two peak elution patterns. The combination of these behaviors including both reversible conformational changes and irreversible on-column aggregation has also been observed leading to three peak elution [47]. For HIC, propensity of unfolding increases with increasing hydrophobicity of the resin's ligands [42][43][46].

Mechanisms other than secondary structure unfolding have also been shown to result in multiple peak elution for different proteins. Kunitani et al. [48], for example, found that the trimeric protein tumor necrosis factor (TNF) dissociated when bound on the HIC resin TSK Phenyl 5-PW resulting in multiple eluted peaks. Nunes and Dias-Cabral [49] observed a two-peak elution behavior for the peptide angiotensin I, on the resin Butyl-Sepharose which was attributed to reversible a cis-trans proline isomerization. Luo et al. [40] also observed a two peak elution behavior for a monoclonal antibody and attributed this behavior to the kinetically limited, reversible protonation of a histidine residue, resulting in more strongly and more weakly bound forms.

In practice, it is plausible that a distribution of binding states or binding orientations exists for most proteins with the most favorable binding configuration being the most probable to be found on the chromatographic surface. This behavior is likely to be exacerbated in the case of multi-domain proteins when the different domains possess diverse characteristics in terms of electrostatics and hydrophobicity. Whether multiple binding states cause multiple peak elution depends on the relative time scales of column time and transition rates between binding configurations. If transition rates are much faster than column time, which is the typical case, a single peak elutes with retention corresponding to the strongest binding configuration. If transition rates are slower than column time, multiple peaks elute with retention corresponding to binding strength of each of the major configurations. In the same manner, for intraparticle adsorption kinetics, if transitions between binding configurations are on the order of diffusion time and they differ in binding strength, competition between configurations could cause complex intraparticle uptake profiles.

In the case of bivalent bispecific antibodies, the multi-domain structure and conformational flexibility caused reversible three peak elution at the column level and complex patterns of bound protein within the particles during transient adsorption. The elution behavior did not follow

mechanisms previously reported. In-line dynamic light scattering measured all three reversible peaks to have the same, monomer-sized hydrodynamic radius showing that secondary structure unfolding leading to aggregation is not the cause of the multiple peak behavior. The elution patterns were not affected by pH over the range 5-8.5, showing that slow titration of charged amino acids is also not the mechanism. The BiSAb biophysical mechanism is driven by the flexible peptide linkers which allow each scFv to be present in two extreme conformations: collapsed with the scFv able to interact with the framework IgG, or outstretched, with the scFv is able to bind to the surface with greater affinity. The three peaks therefore correspond to the following three BiSAb configurations: both scFvs collapsed, one scFv collapsed and one outstretched, or both scFvs outstretched. The competing domain-domain and domain-surface interactions slowed transition rates between binding configurations.

Parameters that affect the relative time scales of transitions between molecular configurations and column time for elution behavior will be seen to have the greatest effects. While holding other parameters constant, varying residence time, temperature, or hold time significantly altered elution profiles. At short residence times and room temperature, three reversible peaks elute with high resolution. Elongating residence time or increasing temperature gradually altered profiles decreasing the resolution between peaks. Eventually, at ~40 min residence time or ~55 °C, a single, merged peak eluted. Increasing hold time enriched the relative size of the third, strongest binding peak at the cost of the weaker binding peaks. Intramolecular crosslinking, which freezes the protein in its conformation, eliminated the multiple peak behavior. The observed BiSAb behavior is qualitatively consistent for different BiSAbs in this class, and occurs regardless of: the scFv attachment location to framework IgG, the chromatographic surface (pellicular or porous resins), and the resin's ligand (weak CEX, strong CEX, or HIC). Thus, these effects appear to be

fundamentally driven by the intrinsic molecular properties of the BiSAbs, rather than by factors specific to the resin.

During high load adsorption, BiSAb molecules showed complex intraparticle uptake profiles not expected for conditions with a favorable isotherm and pore diffusion control. Adsorbed concentrations were maximum at the particle radius followed by a smooth decrease towards the center of the bead until a sharp drop to the protein free core. Once the protein front reached the center of the particle, a slow filling of the center of the particle occurred until equilibrium is reached. Analogous to the elution behavior, parameters that alter the relative time scales of mass transfer and interconversion kinetics greatly affected the intraparticle uptake profiles. Increasing temperature led to faster equilibration due to increased interconversion, and intramolecular crosslinking eliminated the smooth characteristics of the uptake profiles. This work seeks to characterize consequences of BiSAb conformational flexibility on chromatographic elution and adsorptive behavior.

1.2 Research Scope and Objectives

The primary purpose of this dissertation is to understand the chromatographic and adsorptive behavior of bivalent bispecific antibodies, which exhibit configurational interconversion. Multiple peak elution greatly decreases separation efficiency and confuses analysis by appearing as multiple species. Fundamentally understanding the complex elution phenomena will assist process development scientists to identify instances of configurational interconversion and utilize key parameters to alter the profiles for use in analysis or preparative separations. Mechanistic models that are informed with the conformational changes on the column can be used for rational process design to optimize difficult separations.

The specific objectives of this dissertation are to:

1. Characterize multiple peak elution behavior of BiSAbs on cation exchange columns: (a) identify the key parameters which affect the profiles such as the scFv attachment location, residence time, hold time, temperature, and mobile phase composition, and (b) develop a phenomenological model and compare predictions to experimental behavior.
2. Understand the biophysical mechanism causing multiple peak elution using intramolecular crosslinking, homology modeling, and tryptophan autofluorescence, and enzyme proteolysis to determine domain contributions to binding.
3. Evaluate the effects of configurational interconversion on high load adsorption kinetics within macroporous cation exchange resins and develop a model to assist in understanding the complex behavior.
4. Compare multiple peak elution phenomena on hydrophobic interaction columns with that studied on cation exchange columns and develop a phenomenological model capable of predicting behavior.
5. Characterize chromatographic and multicomponent adsorptive behavior of two BiSAb fragments and the intact BiSAb protein: (a) identify their molecular structure via mass spectrometry, (b) compare BiSAb fragment's linear elution behavior with the intact molecules, and (c) study the high load separation of fragments and intact BiSAb molecules on macroporous cation exchange resins with the aim of modeling the three-component binding behavior.

1.3 References

[1] J.E. Bailey, D.F. Ollis, Biochemical Engineering Fundamentals, 2nd ed., McGraw Hill, 1986.

[2] J.K.H. Liu, The history of monoclonal antibody development-Progress, remaining challenges and future innovations, Ann. Med. Surg. 3 (2014) 113–116.

[3] A.L. Grilo, A. Mantalaris, The Increasingly Human and Profitable Monoclonal Antibody Market, Trends Biotechnol. 37 (2019) 9–16.

[4] A.F. Labrijn, M.L. Janmaat, J.M. Reichert, P.W.H.I. Parren, Bispecific antibodies: a mechanistic review of the pipeline, Nat. Rev. Drug Discov. 18 (2019) 585–608. doi:10.1038/s41573-019-0028-1.

[5] A. Beck, L. Goetsch, C. Dumontet, N. Corvaïa, Strategies and challenges for the next generation of antibody–drug conjugates, Nat. Rev. Drug Discov. 16 (2017) 315–337. doi:10.1038/nrd.2016.268.

[6] K. Garber, Bispecific antibodies rise again, Nat. Rev. Drug Discov. 13 (2014) 799–801.

[7] J. Oldenburg, J.N. Mahlangu, B. Kim, C. Schmitt, M.U. Callaghan, G. Young, E. Santagostino, R. Kruse-Jarres, C. Negrier, C. Kessler, N. Valente, E. Asikanius, G.G. Levy, J. Windyga, M. Shima, Emicizumab Prophylaxis in Hemophilia A with Inhibitors, N. Engl. J. Med. 377 (2017) 809–818.

[8] A. Mullard, Bispecific antibody pipeline moves beyond oncology, Nat. Rev. Drug Discov. 16 (2017) 666–668.

[9] S.E. Sedykh, V. V Prinz, V. V Buneva, G.A. Nevinsky, Bispecific antibodies: design, therapy, perspectives, Drug Des. Devel. Ther. 12 (2018) 195–208.

[10] A. Digiandomenico, A.E. Keller, C. Gao, G.J. Rainey, P. Warrener, M.M. Camara, J. Bonnell, R. Fleming, B. Bezabeh, N. Dimasi, B.R. Sellman, J. Hilliard, C.M. Guenther, V. Datta, W. Zhao, C. Gao, X.-Q. Yu, J.A. Suzich, C.K. Stover, A multifunctional bispecific antibody protects against Pseudomonas aeruginosa, Sci. Transl. Med. 6 (2014) 1–12.

[11] C. Spiess, Q. Zhai, P.J. Carter, Alternative molecular formats and therapeutic applications for bispecific antibodies, Mol. Immunol. 67 (2015) 95–106.

[12] J.M. Coloma, S.L. Morrison, Design and production of novel tetravalent bispecific antibodies, Nat. Biotechnol. 15 (1997) 159–163.

[13] L.A. Khawli, S. Goswami, R. Hutchinson, Z.W. Kwong, J. Yang, X. Wang, Z. Yao, A. Sreedhara, T. Cano, D. Tesar, I. Nijem, D.E. Allison, P.Y. Wong, Y. Kao, C. Quan, A. Joshi, R.J. Harris, P. Motchnik, Charge variants in IgG1 isolation, characterization, in vitro binding properties and pharmacokinetics in rats, MAbs. 2 (2010) 613–624. doi:10.4161/mabs.2.6.13333.

[14] W.K. Chung, B. Russell, Y. Yang, M. Handlogten, S. Hudak, M. Cao, J. Wang, D. Robbins, S. Ahuja, M. Zhu, Effects of antibody disulfide bond reduction on purification process performance and final drug substance stability, Biotechnol. Bioeng. 114 (2017)

1264–1274. doi:10.1002/bit.26265.

[15] A.S. Rosenberg, Effects of protein aggregates: an immunologic perspective., AAPS J. 8 (2006) E501–E507.

[16] C. Scanlan, R. Waghmare, E. Gousseinov, A. Becerra-Artega, Challenges and strategies for the downstream procesing of bispecific antibodies (bsAbs), Adc Rev. (2016) 1–7.

[17] T. Hall, J.J. Wilson, T.J. Brownlee, J.R. Swartling, S.E. Langan, P.K. Lambooy, Alkaline cation-exchange chromatography for the reduction of aggregate and a mis-formed disulfide variant in a bispecific antibody purification process, J. Chromatogr. B. 975 (2015) 1–8.

[18] P. Gagnon, Purification Tools for Monoclonal Antibodies, Validated Biosystems, Tuscon, Arizona, USA, 1996.

[19] C. Andrade, L. Arnold, D. Motabar, M. Aspelund, A. Tang, A. Hunter, W.K. Chung, An Integrated Approach to Aggregate Control for Therapeutic Bispecific Antibodies Using an Improved Three Column Mab Platform-Like Purification Process, Biotechnol. Prog. 35 (2019) 1–13.

[20] L.K. Kimerer, B. Niu, W. Zhai, T.M. Pabst, A.K. Hunter, G. Carta, Chromatographic and Adsorptive Behavior of a Bivalent Bispecific Antibody and its Associated Fragments, J. Chromatogr. A. (2021).

[21] G. Carta, A. Jungbauer, Protein Chromatography, 2nd ed., Wiley-VCH, Weinheim, Germany, 2020.

[22] Y. Wang, G. Carta, Competitive binding of monoclonal antibody monomer-dimer mixtures on ceramic hydroxyapatite, J. Chromatogr. A. 1587 (2019) 136–145. doi:10.1016/j.chroma.2018.12.023.

[23] W. Kopaciewicz, M.A. Rounds, J. Fausnaugh, F.E. Regnier, Retention model for high-performance ion-exchange chromatography, J. Chromatogr. 266 (1983) 3–21.

[24] F.E. Regnier, The Role of Protein Structure in Chromatographic Behavior, Science (80-.). 238 (1987) 319–323.

[25] B.H.J. Hofstee, Hydrophobic adsorption chromatography of proteins. Methods of protein separation, Springer, New York, 1976.

[26] J.F. Kramarczyk, B.D. Kelley, J.L. Coffman, High-Throughput Screening of Chromatographic Separations: II. Hydrophobic Interaction, Biotechnol. Bioeng. 100 (2008) 707–720.

[27] J.X. Zhou, S. Dermawan, F. Solamo, G. Flynn, R. Stenson, T. Tressel, S. Guhan, pH-conductivity hybrid gradient cation-exchange chromatography for process-scale monoclonal antibody purification, J. Chromatogr. A. 1175 (2007) 69–80.

[28] J.T. McCue, P. Engel, A. Ng, R. Macniven, J. Thommes, Modeling of protein monomer / aggregate purification and separation using hydrophobic interaction chromatography, Biopr. Biosyst. Eng. 31 (2008) 261–275.

[29] J. Chen, J. Tetrault, A. Ley, Comparison of standard and new generation hydrophobic interaction chromatography resins in the monoclonal antibody purification process, J. Chromatogr. A. 1177 (2008) 272–281.

[30] J.M. Reck, T.M. Pabst, A.K. Hunter, X. Wang, G. Carta, Adsorption equilibrium and kinetics of monomer-dimer monoclonal antibody mixtures on a cation exchange resin, J. Chromatogr. A. 1402 (2015) 46–59.

[31] F. Dismer, J. Hubbuch, A novel approach to characterize the binding orientation of lysozyme on ion-exchange resins, J. Chromatogr. A. 1149 (2007) 312–320.

[32] F. Dismer, M. Petzold, J. Hubbuch, Effects of ionic strength and mobile phase pH on the binding orientation of lysozyme on different ion-exchange adsorbents, J. Chromatogr. A. 1194 (2008) 11–21.

[33] J. Kittelmann, K.M.H. Lang, M. Ottens, J. Hubbuch, An orientation sensitive approach in biomolecule interaction quantitative structure – activity relationship modeling and its application in ion-exchange chromatography, J. Chromatogr. A. 1482 (2017) 48–56.

[34] J. Robinson, D. Roush, S. Cramer, Domain contributions to antibody retention in multimodal chromatography systems, J. Chromatogr. A. 1563 (2018) 89–98.

[35] R. Gillespie, T. Nguyen, S. Macneil, L. Jones, S. Crampton, S. Vunnum, Cation exchange surface-mediated denaturation of an aglycosylated immunoglobulin (IgG1), J. Chromatogr. A. 1251 (2012) 101–110.

[36] J. Guo, S. Zhang, G. Carta, Unfolding and aggregation of a glycosylated monoclonal antibody on a cation exchange column. Part I. Chromatographic elution and batch adsorption behavior, J. Chromatogr. A. 1356 (2014) 117–128.

[37] J. Guo, G. Carta, Unfolding and aggregation of a glycosylated monoclonal antibody on a cation exchange column. Part II. Protein structure effects by hydrogen deuterium exchange mass spectrometry, J. Chromatogr. A. 1356 (2014) 129–137.

[38] J. Guo, G. Carta, Unfolding and aggregation of monoclonal antibodies on cation exchange columns: Effects of resin type , load buffer, and protein stability, J. Chromatogr. A. 1388 (2015) 184–194.

[39] H. Luo, N. Macapagal, K. Newell, A. Man, A. Parupudi, Y. Li, Y. Li, Effects of salt-induced reversible self-association on the elution behavior of a monoclonal antibody in cation exchange chromatography, J. Chromatogr. A. 1362 (2014) 186–193.

[40] H. Luo, M. Cao, K. Newell, C. Afdahl, J. Wang, W.K. Wang, Y. Li, Double-peak elution profile of a monoclonal antibody in cation exchange chromatography is caused by histidine-protonation-based charge variants, J. Chromatogr. A. 1424 (2015) 92–101.

[41] S. Wu, K. Benedek, B.L. Karger, Thermal behavior of proteins in high performance hydrophobic interaction chromatography, J. Chromatogr. 359 (1986) 3–17.

[42] E. Haimer, A. Tscheliessnig, R. Hahn, A. Jungbauer, Hydrophobic interaction chromatography of proteins IV Kinetics of protein spreading, J. Chromatogr. A. 1139 (2007) 84–94.

[43] A. Jungbauer, C. Machold, R. Hahn, Hydrophobic interaction chromatography of proteins: III. Unfolding of proteins upon adsorption, J. Chromatogr. A. 1079 (2005) 221–228. doi:10.1016/j.chroma.2005.04.002.

[44] Principles of hydrophobic interaction chromatography, Tosoh Biosci. (n.d.). https://www.separations.eu.tosohbioscience.com/solutions/process-media-products/by-mode/hic (accessed September 8, 2019).

[45] J.L. Fogle, J.P.O. Connell, E.J. Fernandez, Loading, stationary phase, and salt effects during hydrophobic interaction chromatography : a-Lactalbumin is stabilized at high loadings, J. Chromatogr. A. 1121 (2006) 209–218.

[46] B. Beyer, A. Jungbauer, Conformational changes of antibodies upon adsorption onto hydrophobic interaction chromatography surfaces, J. Chromatogr. A. 1552 (2018) 60–66.

[47] J. Guo, A.D. Creasy, G. Barker, G. Carta, Surface induced three-peak elution behavior of a monoclonal antibody during cation exchange chromatography, J. Chromatogr. A. 1474 (2016) 85–94.

[48] M.G. Kunitani, R.L. Cunico, Reversible subunit dissociation of tumor necrosis factor during hydrophobic interaction chromatography, J. Chromatogr. 443 (1988) 205–220.

[49] C.A. Nunes, A.C.M. Dias-Cabral, Angiotensin I retention behavior on Butyl-Sepharose under linear loading chromatographic conditions, J. Chromatogr. A. 1216 (2009) 2332–2338. doi:10.1016/j.chroma.2009.01.006.

2 Chromatographic Behavior on Cation Exchange Columns

2.1 Introduction

The chromatographic behavior of bivalent bispecific antibodies at low load, linear isotherm conditions is explored. At low load there is relatively high resin surface area compared to the amount of applied protein. Therefore, there is almost no competition between proteins for binding sites and protein-surface interactions dominate measured behavior. Complex, multiple-peak elution profiles are observed for the bivalent bispecific antibody samples. First, this chapter focuses on experimentally characterizing the behavior and understanding the effects of BiSAb format, residence time, temperature, and hold time. Second, a phenomenological column model is developed to test our understanding of the system. This work was published in the Journal of Chromatography A as ref. [1].

2.2 Materials and Methods

2.2.1 Materials

Bivalent bispecific antibodies and the corresponding framework monoclonal antibody samples were provided by AstraZeneca (Gaithersburg, MD, USA). The proteins were expressed in CHO cells and purified by Protein A, ion exchange, and hydroxyapatite chromatography. The three BiSAb molecules are sequence homologs and vary exclusively by scFv attachment location. All protein samples were stored at -80 °C until use. Samples were thawed and buffer exchanged using a HiPrep 26/10 desalting column (Cytiva, Marlborough, MA, USA) prior to use. BiSAb samples dialyzed into 100 mM Na_2PO_4, 300 mM NaCl, at pH 6.8 were analyzed by size exclusion chromatography with a TSKGel SW 3000XL column (Tosoh Biosciences, Kyoto, Japan) at 1.0 ml/min. Shown in Figure 2.1, the three BiSAb samples were found to consist of almost exclusively

monomer-sized protein based on SEC analysis with a hydrodynamic radius of 6.3±0.2 nm, based on DLS measurements with an in-line detector as described below. Each BiSAb sample was also found to be quite pure with respect to the presence of pI variants with a pI of 9.2±0.1 based on isoelectric focusing using an Isogel agarose IEF plate pH 7-11 from Lonza (Rockland, ME, USA) on a Multiphor II unit (Cytiva). IEF was run according to the plate manufacturer instructions. IEF standards were obtained from Bio-Rad Laboratories (Hercules, CA, USA) and used to determine the approximate pI of each BiSAb molecule.

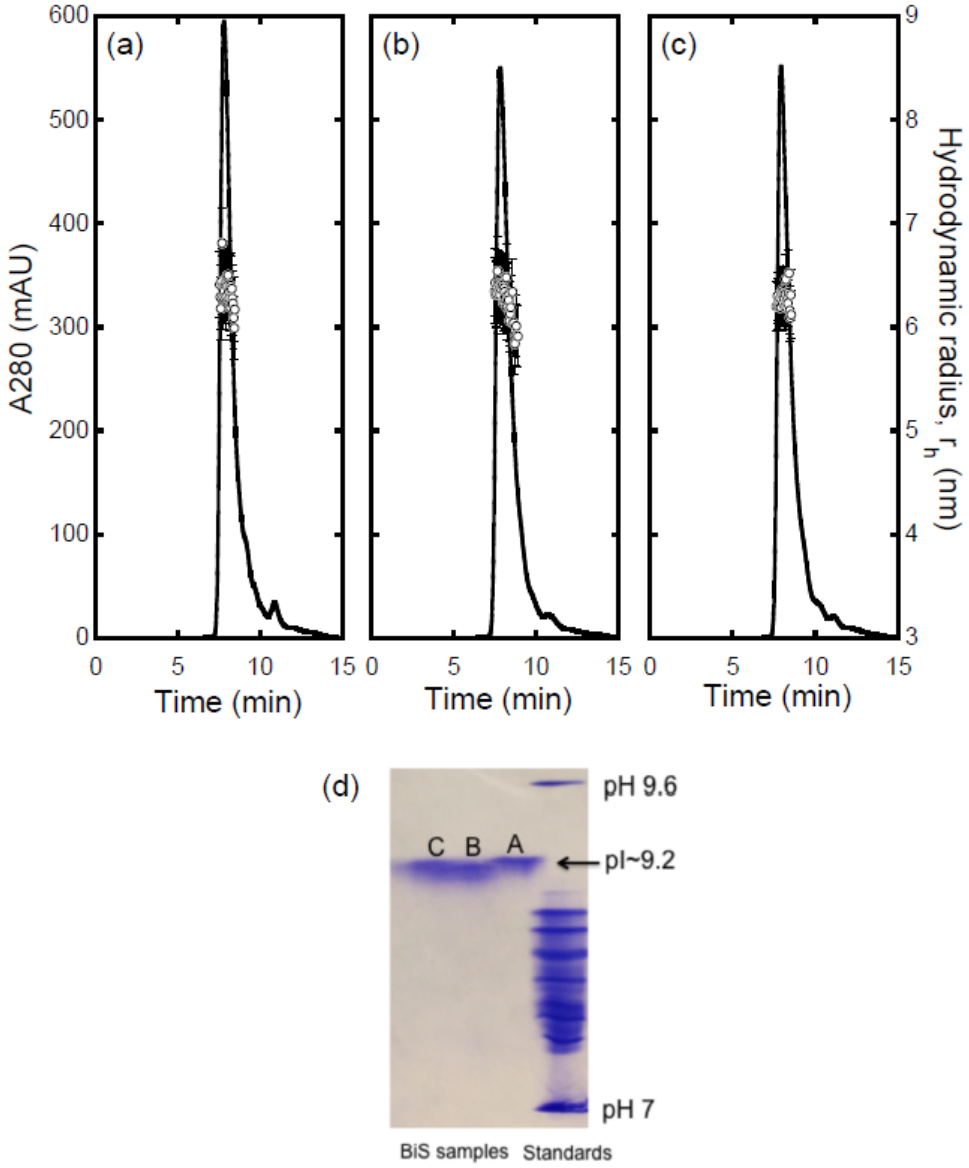

Figure 2.1. Size exclusion chromatography on TSKGel SW 3000XL with inline dynamic light scattering of BiSA (a), BiSB (b), and BiSC (c). Isoelectric focusing of BiSAb samples on Isogel agarose plate pH 7-11 (d).

Cation exchange chromatography resins used in this work are ProPac WCX 10 and Source 15S. ProPac is a pellicular weak cation exchanger based on a 10 µm non porous, ethylvinylbenzene-divinylbenzene crosslinked polymer matrix modified with carboxylic acid groups. Source 15S is a strong cation exchanger based on a porous 15 µm monosized, rigid polystyrene-divinyl benzene polymer matrix modified with sulphonate groups. A ProPac WCX 10 column 0.4 cm diameter and 10 cm long was purchased from Dionex Corporation (Sunnyvale, CA). Source 15S was purchased from Cytiva (Marlborough, MA, USA) and flow packed according to the resin manufacturer instructions in 0.5-cm diameter Tricorn columns, also from Cytiva, with bed heights between 2.3 and 10 cm. Salts for buffer preparation were purchased from ThermoFisher Scientific (Waltham, MA, USA) and MilliporeSigma (St. Louis, MO, USA).

2.2.2 Methods

Chromatographic experiments were performed using an ÄKTA Pure 25 (Cytiva) except for SEC-DLS analyses and temperature studies which were conducted with a Waters e-2695 HPLC (Milford, MA, USA) equipped with a UV detector and a Wyatt miniDAWN DLS detector (Santa Barbara, CA, USA). Source 15S was flow-packed according to the manufacturer instructions. Packing quality was assessed by the HETP and asymmetry factor of a pulse injection of salt. Asymmetry factor values of the columns utilized in this work were 1.1 ± 0.2 and plate counts were 3250 ± 500 plates/m.

Linear gradient elution (LGE) experiments were conducted by first equilibrating the column with load buffer followed by injection of the sample and elution with a salt gradient to a final NaCl concentration that varied dependent on pH. The buffers used were 10 mM Na_2PO_4 with 0-125 mM NaCl gradients at pH 7.0 and 20 mM $NaCH_3COO$ with 0-500 mM NaCl at pH 5.0. Three different Source 15S columns were used. Two with 9.4 and 10 cm bed lengths were used for most of the

LGE experiments. A third with a 2.3 cm bed height was used for temperature studies and to study the effects of hold time. Operating the shorter column at high flow rates allowed elution to be completed in under 10 min minimizing back exchange to the state favored in solution.

The extraparticle porosity of these Source columns, ε =0.4±0.01, was determined by measuring the pressure drop across the column while varying flow rate and using the Carman-Kozeny equation as described in ref. [2]. The intraparticle porosity, ε_p = 0.80±0.01, was determined based on the retention of a NaCl pulse injection.

The hydrodynamic radius of the eluate from the Source columns, rh, was measured using the Waters e-2695 HPLC with a miniDawn TREOS detector (Wyatt Technologies, Santa Barbara, CA, USA) connected to a NanoStar dynamic light scattering (DLS) unit through a fiber optic link.

2.3 Results and Discussion

2.3.1 Chromatographic Behavior

Figure 2.2 shows the chromatographic behavior of the three BiSAb molecules on the 9.4-cm long Source column using, in each case, a 20 column volumes (CV) NaCl gradient at room temperature and pH 7 at a flow rate of 2.5 ml/min, which corresponds to a residence time of 0.74 min. As seen in this figure, despite the apparent size and pI homogeneity of the three samples, each resulted in multiple peak elution. Three major peaks are evident for each of the BiSAb molecules while BiSB also exhibits two additional, minor early eluting peaks. We found that these two minor peaks were fragments that could be separated without affecting the behavior of the three major peaks (further discussion of their separation in Chapter 6). The remaining three peaks behaved similarly to the three peaks exhibited by BiSA and BiSC but eluted at higher conductivities.

Figure 2.3 shows the elution of BiSA from the 2.3-cm long Source column for the conditions of Fig. 2.2 but with flow rate of 1.0 ml/min, corresponding to a residence time of 0.44 min, using both UV280 and DLS detection. As seen in this figure, the hydrodynamic radius of the three major peaks observed for this molecule remains relative constant in the range 6.1±0.3 nm, consistent with the SEC-DLS analysis of the raw BiSAb samples. The results indicate that the multiple peak elution behavior is not related to on-column aggregate formation as has been observed for mAbs [3].

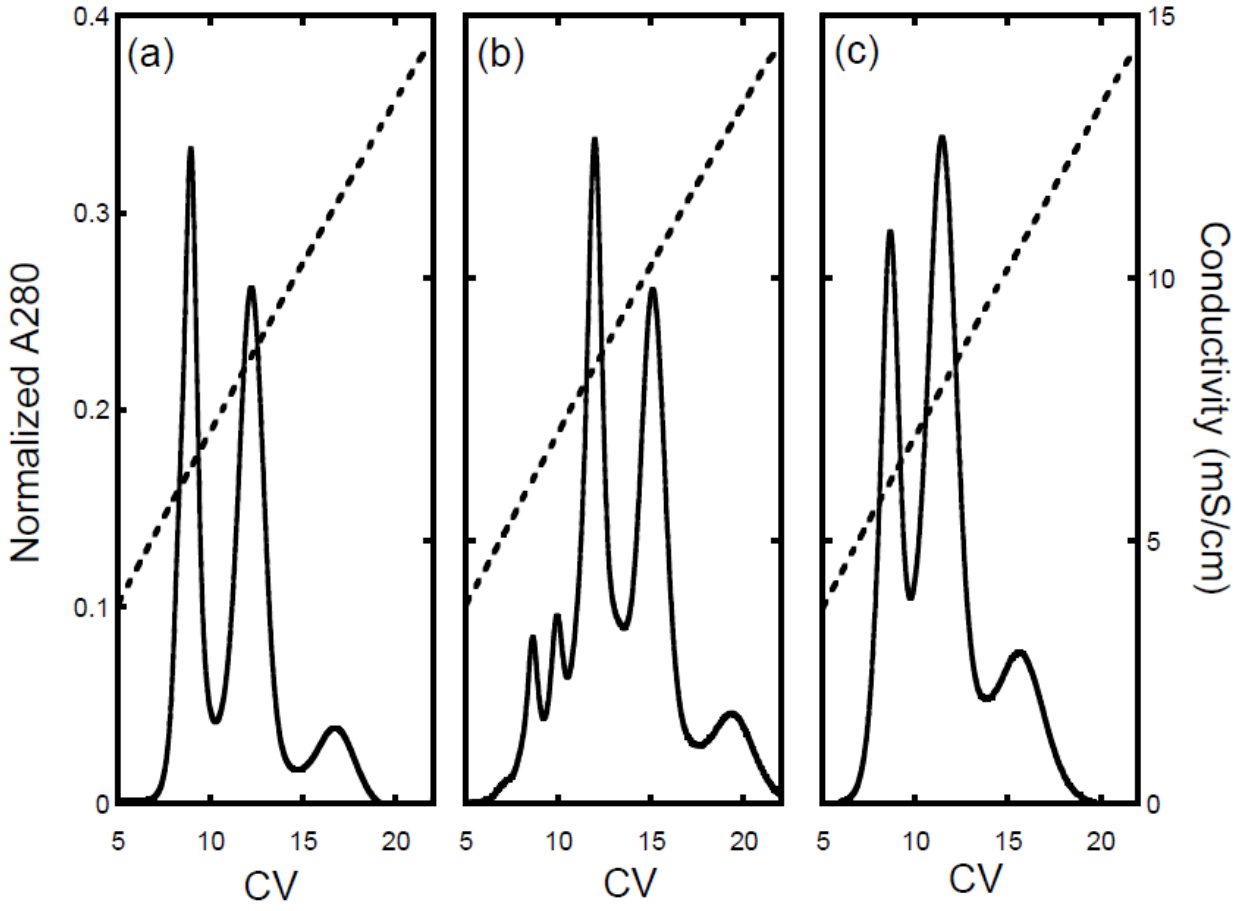

Figure 2.2. Elution behavior of BiSA (a), BiSB (b), and BiSC (c) on a 9.4-cm long Source 15S column with a 0-125 mM NaCl gradient over 20 CV at pH 7 and room temperature with a flow rate of 2.5 ml/min (0.74 min residence time). The mass of protein injected was 0.3±0.1 mg/ml CV. The A280 absorbance is normalized to obtain the same peak area in order to account for slight differences in the amount of protein injected.

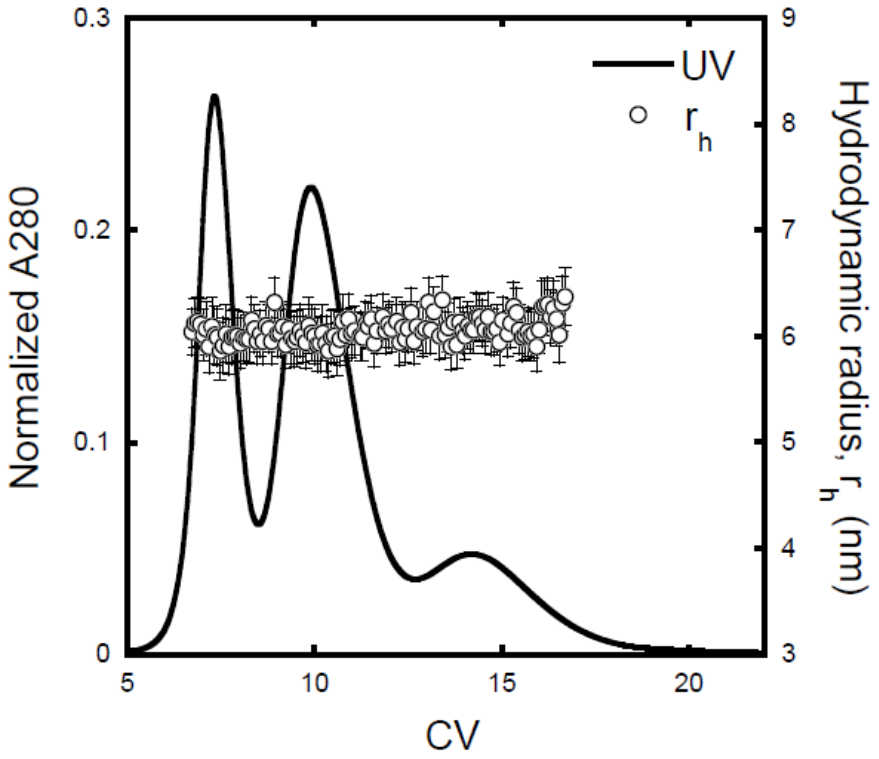

Figure 2.3. Elution behavior of BiSA on a 2.3-cm long Source 15S column with UV and in-line DLS detection. Error bars on the r_h data correspond to regression error of the autocorrelation function. Elution was with a 0-125 mM NaCl gradient over 20 CV at pH 7 and room temperature with a flow rate of 1.0 ml/min (0.44 min residence time). The mass of protein injected was 5.0 mg/ml CV. The A280 absorbance is normalized to UV total peak area.

Figure 2.4 shows the results of re-injecting fractions corresponding to the three major peaks obtained for BiSA on the 10 cm Source column. Three fractions, F1, F2, and F3, were first collected from the column operated at a flow rate of 1 ml/min (residence time of 2.0 min), diluted three-fold with the load buffer (10 mM Na_2PO_4 at pH 7), injected into either the same Source column or the ProPac column, and then eluted in both cases with a 0-125 mM NaCl gradient at a 2.0 min residence time for the Source column and at 2.5 min residence time for the ProPac column. As seen in Fig. 2.4b, re-injecting each of the three fractions results in the same three-peak elution pattern seen for the original Source column injection suggesting that the behavior is reversible. Minor differences in retention do exist, but can likely be ascribed to moderate changes in the load conductivity resulting from dilution of the sample prior to reinjection. Interestingly, as seen in Fig. 2.4c, injecting the diluted fractions from the Source column into the ProPac column also resulted in a three-peak elution behavior, quite comparable to that obtained by directly injecting the original BiSA sample into the ProPac column. Source and ProPac widely differ in characteristics as Source is a strong cation exchanger based on a porous particle, and ProPac is a weak cation exchanger based on a pellicular particle.

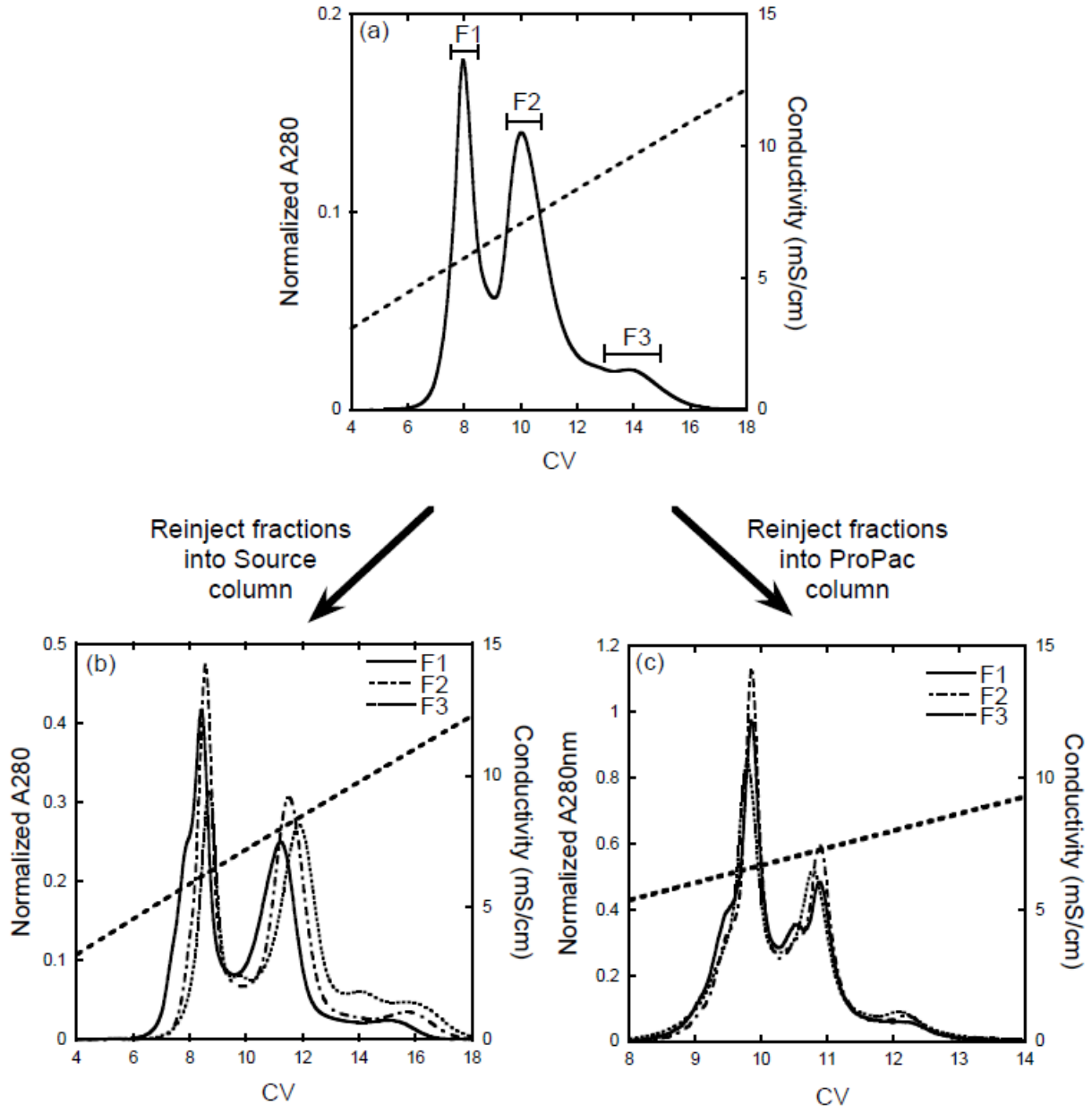

Figure 2.4. Collection of fractions of BiSA eluted from a 10-cm long Source 15S column (a) and reinjection of each fraction after three-fold dilution with the load buffer into the same Source 15S column (b) and into a ProPac WCX-10 column (c). Conditions were pH 7 and room temperature for all three cases. Protein loads were 5.5 mg/ml for (a) and 0.55, 0.71, and 0.12 mg/ml for F1, F2, and F3 injections respectively for both (b) and (c). The A280 absorbance is normalized to obtain the same peak area.

Figure 2.5 shows the effects of flow rate and, hence, residence time on the multiple peak elution behavior of BiSA on the 9.4-cm long Source column at pH 7 with a 0-125 mM NaCl gradient over 20 CV at flow rates of 2.5, 1.0, 0.5, 0.25, 0.10, 0.05, and 0.01 ml/min. The corresponding residence times are 0.74, 1.9, 3.7, 7.4, 18.5, 37, and 185 min. The data are shown as a function of time, on a logarithmic scale in the top panel and as a function of CV in the bottom panel. As seen in this figure, reducing the flow rate and, thus, increasing the residence time results in varying elution patterns with a gradual progression from three major peaks at 2.5 ml/min, to two-peaks at 0.25 ml/min, to a single peak with a shoulder at 0.1 ml/min, and to a single, nearly symmetrical peak at 0.01 ml/min. In terms of conductivities at elution, the highest flow rate of 2.5 ml/min results in three peaks with peak maxima at approximately 6.7, 8.9, and 11.8 mS/cm, while the lowest flow rate of 0.01 ml/min results in a single peak with peak maximum at approximately 7.5 mS/cm, intermediate between the first and second peaks obtained at 2.5 ml/min. These results suggest that the multiple peak elution behavior observed for BiSA is associated with reversible molecular changes that occur within the column over time scales that are comparable to the time scale of elution. At high flow rates, the time available is apparently insufficient for such changes to occur during elution resulting in three distinct peaks. Conversely, at the lowest flow rate, the time available is sufficient for these changes to occur during elution resulting in a single peak with multiple molecular forms eluting in equilibrium with each other. The apparent increased resolution between the eluted peaks at higher flow rate is thus likely a result of the interplay of chromatographic separation and a kinetically-limited interconversion of molecular forms that have different retentivities.

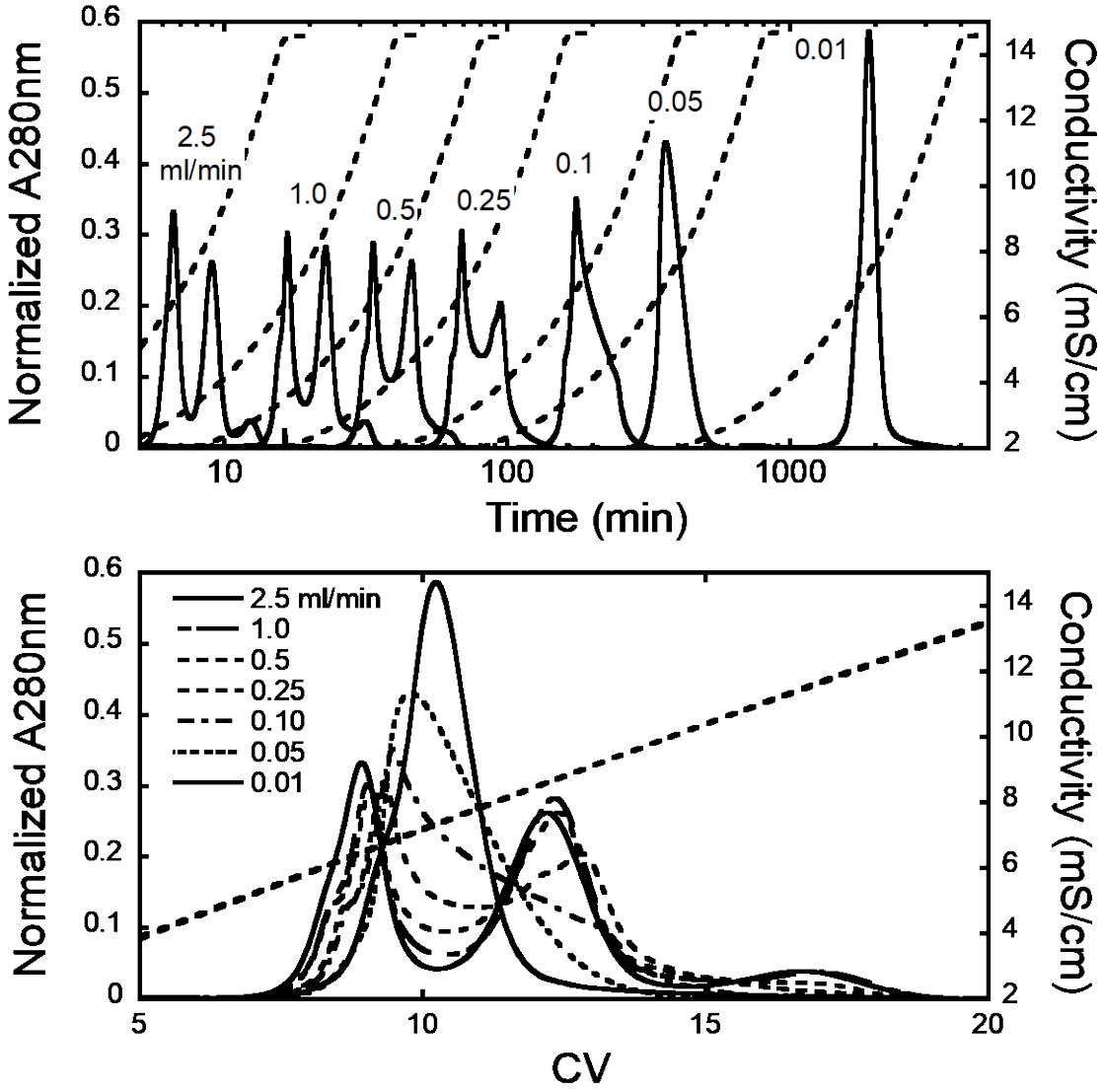

Figure 2.5. Effect of flow rate on the elution behavior of BiSA on a 9.4-cm long Source 15S column with a 0-125 mM NaCl gradient over 20 CV at pH 7 and room temperature. Residence times corresponding to the flow rates indicated for each run were 0.74, 1.9, 3.7, 7.4, 18.5, 37, and 185 min. The mass of protein injected was 0.22±0.1 mg/ml. The same data are shown in both panels, as a function of time on a log scale in the top panel and as a function of CV in the bottom panel. The A280 absorbance is normalized to obtain the same peak area in order to account for slight differences in the amount of protein injected.

Further insight can be obtained by exploring the effects of the BiSAb type, of the mobile phase pH, of the operating temperature, and of hold times on the resin. Figure 2.6 shows the effects of flow rate on the elution of BiSB and BiSC on the 9.4-cm Source column for conditions otherwise identical to those of Fig. 2.5. As seen in Fig. 2.6b, the elution behavior of BiSC is perfectly analogous to that of BiSA; i.e. three major peaks are eluted at 2.5 ml/min, which merge into a single nearly symmetrical peak when the elution flow rate is reduced to 0.05 ml/min. Conductivities at elution of the three resolved peaks and of the single merged peak are also comparable to those of the corresponding BiSA peaks. As seen in Fig. 2.6a, BiSB exhibits 5 elution peaks at 2.5 ml/min (cf. Fig. 2.2). The three more retained peaks behave analogously to the elution peaks of BiSA and BiSC, albeit eluting at higher conductivities, gradually merging into a single peak at low flow rates. The two early eluting peaks of BiSB persist, however, as the flow rate is reduced actually resulting in slightly better resolution at lower flow rates (the log-scale obscures somewhat this observation) behaving in a manner consistent with that of independent molecular species. These results indicate that the multiple peak elution behavior is qualitatively independent of the particular type of BiSAb molecule in this homologous series, regardless of the position of the scFv domain along the framework IgG structure.

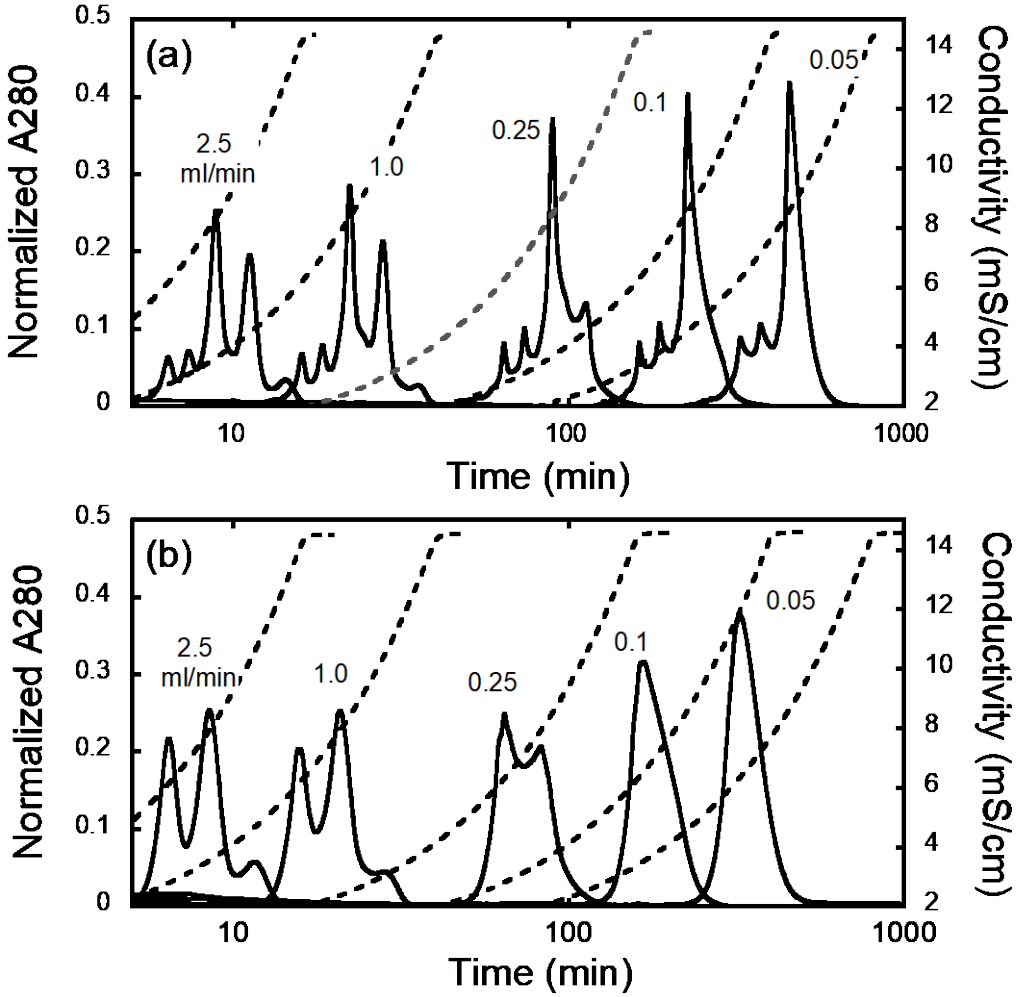

Figure 2.6. Effect of flow rate on the elution behavior of BiSB (a) and BiSC (b) on a 9.4-cm long Source 15S column with a 0-125 mM NaCl gradient over 20 CV at pH 7 and room temperature. Residence times corresponding to the flow rates indicated for each run were 0.74, 1.9, 7.4, 18.5, and 37 min. The mass of protein injected was 0.23±0.01 mg/ml for BiSB and 0.11±0.05 mg/ml for BiSC. The data are shown as a function of time on a log scale. The A280 absorbance is normalized to obtain the same peak area in order to account for slight differences in the amount of protein injected.

Figure 2.7 shows the effect of operating at pH 5 on the BiSA elution behavior on the 9.4-cm long Source column. The buffer in this case is 20 mM $NaCH_3COO$ adjusted to pH 5 with acetic acid and the gradient is from 0 to 500 mM NaCl over 20 CV. Comparing the pH 5 result to the pH 7 result in Fig. 2.5, it is evident that the BiSA elution behavior is qualitatively the same. The main difference is that elution occurs at higher conductivities, which is expected since the protein positive charge is expected to increase as the solution pH is decreased further below the protein pI. For these, conditions, stronger binding to the Source resin is expected, requiring a higher NaCl concentration at elution. It should be noted, that the time scales over which elution occurs in the pH 7 experiments (Fig. 2.5) and in the pH 5 experiment (Fig. 2.7) are comparable at each corresponding flow rate. This occurs because the higher final NaCl concentration used balances the stronger protein-resin interaction expected at pH 5. For these conditions, the elution behavior is comparable at the two pH values with the elution pattern transitioning from three distinct peaks at the higher flow rate to a single merged peak at the lower flow rate. This result is significant in mechanistic terms. For example, Luo et al. [4] have determined that the reversible, multiple peak elution behavior of a mAb on a cation exchange resin was associated with the kinetically limited protonation/deprotonation of a specific histidine residue. The fact that the multiple peak elution behavior observed in our case is the same at pH 5 and 7, which bracket the pKa of histidine, indicates that histidine protonation/deprotonation is likely not the root cause of the elution behavior observed for the BiSAb molecules considered in this work. Although not shown for brevity, the three-peak elution behavior also persisted at pH 8.5.

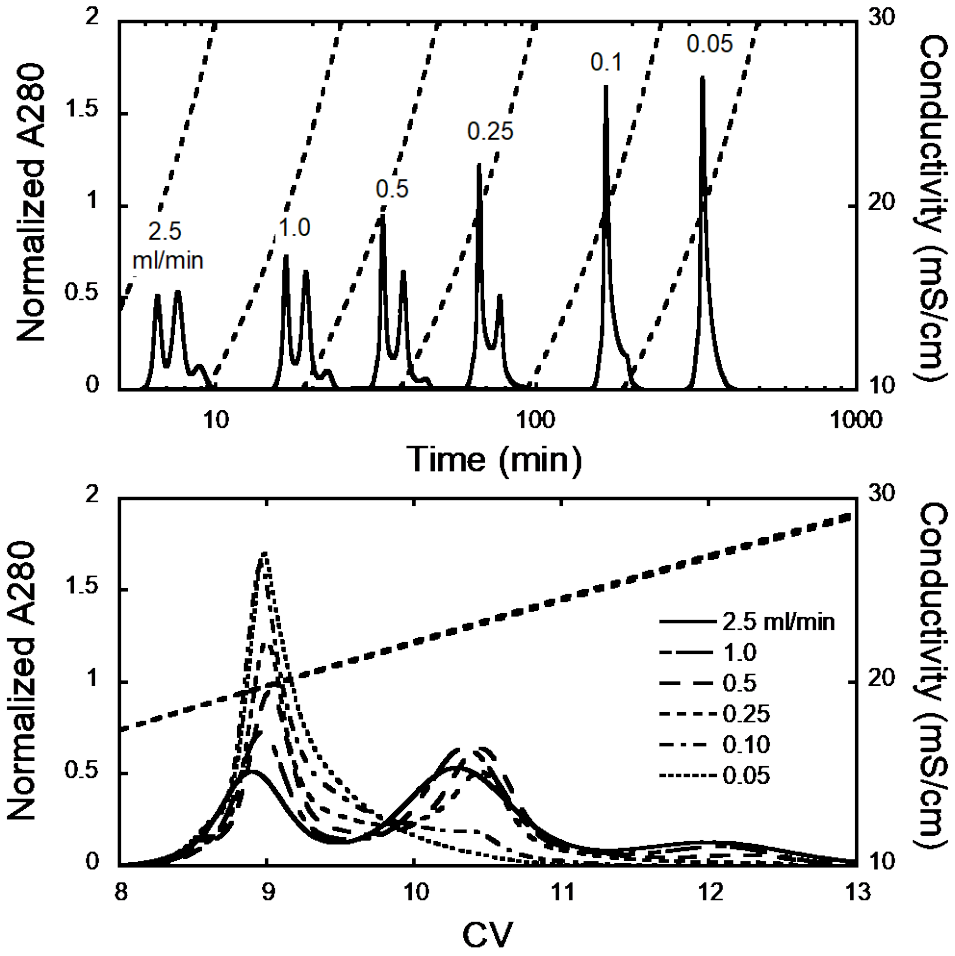

Figure 2.7. Effect of flow rate on the elution behavior of BiSA on a 9.4-cm long Source 15S column with a 0-500 mM NaCl gradient over 20 CV at pH 5 and room temperature. Residence times corresponding to the flow rates indicated for each run were 0.74, 1.9, 3.7, 7.4, 18.5, and 37 min. The mass of protein injected was 0.14±0.02 mg/ml. The same data are shown in both panels, as a function of time on a log scale in the top panel and as a function of CV in the bottom panel. The A280 absorbance is normalized to obtain the same peak area in order to account for slight differences in the amount of protein injected.

Figure 2.8 shows the effect of temperature on the BiSA elution behavior on the 2.3-cm Source column at pH 7. A 0-125 mM NaCl gradient over 20 CV and a flow rate of 1.0 ml/min were used for these runs. As seen from this figure, operating the column at temperatures increasing from the room temperature value of 21 °C to 35, 45, and 55 °C resulted in a gradually shifting elution behavior from three distinct peaks at room temperature to two peaks at 45 °C, to nearly a single peak with a slight shoulder at 55 °C. This behavior is qualitatively consistent with a rate of on-column interconversion among multiple molecular forms that increases as the temperature is increased. The rate of such interconversion is likely to increase at higher temperatures resulting in a merged peak at near equilibrium conditions for the same conditions were multiple peaks are observed at room temperature. It should be noted, however, that the merged peak elutes somewhat earlier at 55 °C compared to the room temperature case indicating that the effect of temperature is more complex, also affecting binding strength and, thus, retention to some extent.

Interestingly the trends of the elution patterns observed in this work for BiSA as a function of temperature are similar to the trends observed for the chromatographic elution of carbohydrates on calcium-form cation exchange columns as reported by Carta et al. [5] and, more recently, by Ortner et al. [6]. Although, molecules, resins, interaction mode, and operating mode (isocratic vs. gradient) were completely different in these studies compared to the present work, the similarity in chromatographic behavior suggests a common reason, which is the on-column reversible interconversion of molecular forms. In both cases, increasing temperature appears to speed up the respective interconversion rates causing the elution pattern to evolve from multiple peaks to a single equilibrium peak when the interconversion rates become faster than the rate of chromatographic elution.

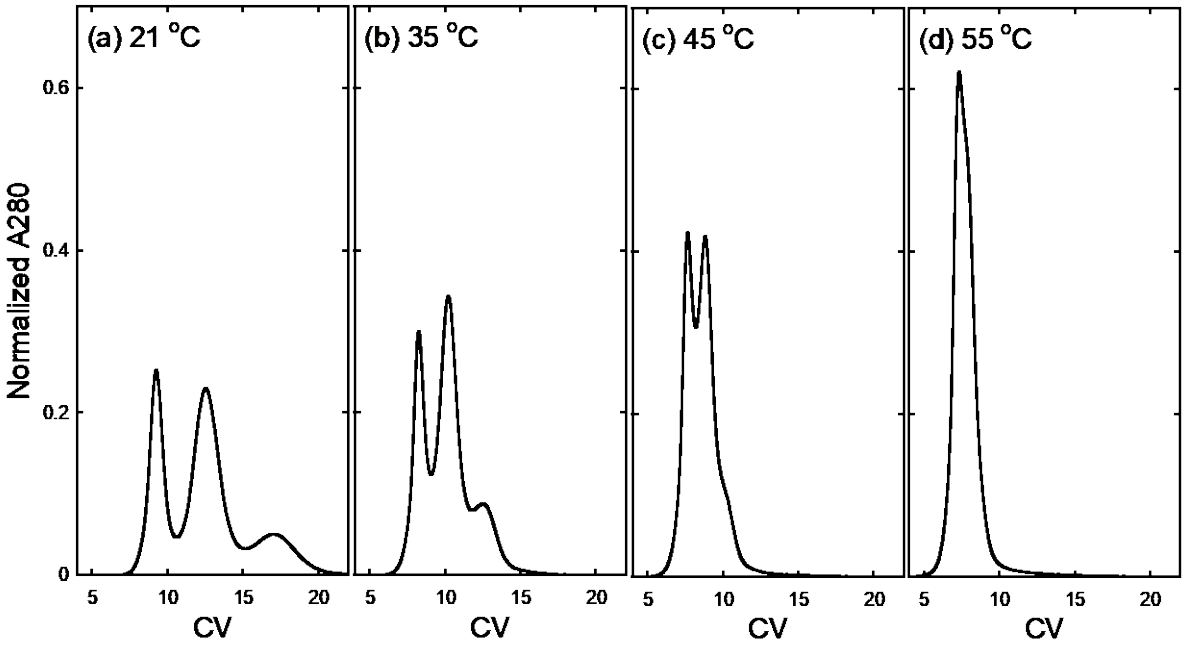

Figure 2.8. Effect of temperature on the elution behavior of BiSA on a 2.3-cm long Source 15S column with a 0-125 mM NaCl gradient over 20 CV at pH 7 with a flow rate of 1.0 ml/min corresponding to a residence time of 0.44 min. The mass of protein injected was 2.0±0.25 mg/ml. The A280 absorbance is normalized to obtain the same peak area in order to account for slight differences in the amount of protein injected.

The last experimental conditions investigated in this work were designed to test the effects of holding the protein bound to the stationary phase prior to elution. The experiments were done with BiSA using the 2.3-cm Source column at room temperature and pH 7 with a 0-125 mM NaCl gradient over 20 CV. Figure 2.9a shows the result of the first of these two experiments. In this case, a virgin BiSA sample was first loaded and immediately eluted at 2.0 ml/min (corresponding to a 0.22 min residence time) giving rise to three peaks (dashed line in Fig. 2.9a). In the second case, the BiSA sample was loaded but then held bound on the stationary phase for 60 min with the load buffer flowing at 0.44 ml/min, prior to elution with a 0-125 mM NaCl gradient over 20 CV at 2.0 ml/min. As seen in Fig. 2.9a (solid line), the peaks eluted after holding the protein on the resin for 60 min contains a much larger percentage of the late eluting peak. The first peak is almost completely gone, the second peak is slightly increased, and the third peak is more than doubled compared to the case where the protein is loaded and immediately eluted. The areas of the each peak were determined by fitting the overall profile to three combined exponentially modified Gaussian (EMG) curves [7]. Since the residence time was extremely short during elution (0.22 min) in these runs, little interconversion was possible. As a result, the areas of the eluted peaks provide an estimate of the extent of interconversion that occurred while bound on the chromatographic surface. Figure 2.9b shows the proportion of the three peak areas for different hold times up to 90 min. It is evident that immediately upon binding the protein is distributed among the different forms in approximately the 0.324:0.461:0.210 proportion. Holding the protein in the bound state prior to elution gradually shifts this distribution further toward the more retained form. At about 60 min or longer, an equilibrium is apparently reached with the three peaks in the 0.094:0.377:0.538 proportion.

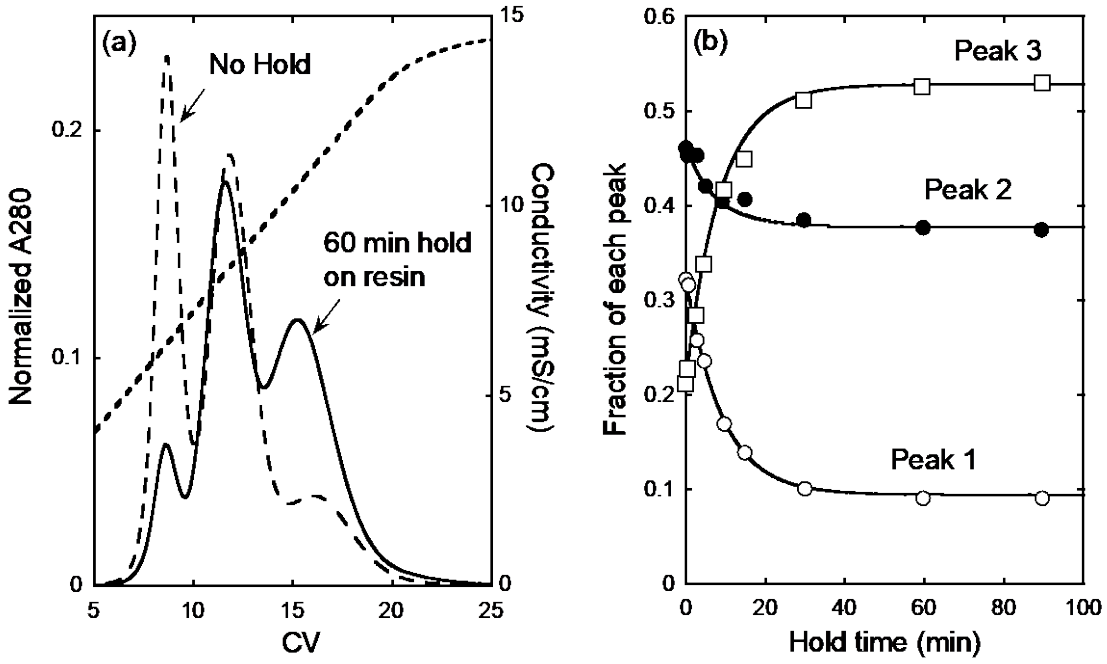

Figure 2.9. Comparison of BiSA elution profiles from a 2.3 cm Source 15S column eluted immediately with a salt gradient and after a 60 min hold in the load buffer (a) and effect of hold time on the fraction of each eluted peak (b). The gradient was 0-125 mM NaCl over 20 CV at pH 7 and room temperature. The elution flow rate was 2.0 ml/min, corresponding to a 0.22 min residence time. The mass of protein injected was 1.6±0.6 mg/ml. The A280 absorbance is normalized to obtain the same peak area in order to account for slight differences in the amount of protein injected. The solid lines in (b) are calculated from the model described in 2.3.2.

2.3.2 Modeling

A phenomenological model was developed to describe the multiple peak elution behavior of the BiSAb molecules considered in this work. The goal is primarily to test consistency with the hypothesis that the observed multiple peak elution behavior results from molecular interconversions occurring reversibly within the column. Phenomenological models of this type have been presented by others previously including the model of Voitl et al. [8] to describe multiple binding conformations of HSA on CEX resins, the model of Muca et al. [9] to describe on-column unfolding, and the model of Guo et al. [10] to describe multiple peak elution of a mAb on a CEX column.

We focus on modeling the behavior of BiSA on Source, which we have characterized more extensively. Although the basic structure of our model is similar to previous work, ours considers three different molecular forms of the protein, P_1, P_2, and P_3 that interact differently with the stationary phase while interconverting into each other during binding, hold, and elution steps. In the ensuing development P_1 denotes the form that interacts most weakly with the resin, P_2 the form with intermediate interaction strength, and P_3 the form that interacts most strongly. The model and associated rate and equilibrium constants were derived as follows. The model has four key components that are needed to represent the complex elution behavior observed for BiSA. The first component describes retention of the three forms on the chromatographic surface. We assume that this conform to the stoichiometric displacement model [11][12]. Accordingly, for the dilute conditions used in this work, the bound concentration of each form, q_i, is related to its concentration in solution, C_i, by the equation:

$$q_i = \frac{A_i}{\left(C_{Na^+}\right)^{z_i}} C_i = K_{a,i} C_i \tag{2.1}$$

where z_i is the effective binding charge of each form and A_i is an equilibrium constant. $K_{a,i} = A_i / \left(C_{Na^+}\right)^{z_i}$ is the so-called Henry's constant of distribution coefficient. Without interconversion, the A_i and z_i parameters can be obtained conveniently from LGE by determining the Na^+ concentration at which the peak elutes from the column, $C^R_{Na^+,i}$, as a function of the gradient slope according to the so-called Yamamoto method [12] [13] [14]. Accordingly, we have:

$$\log\left(\gamma'\right) = -\log\left[A_i\left(z_i+1\right)\right] + \left(z_i+1\right)\log\left(C^R_{Na^+}\right) \tag{2.2}$$

where $\gamma' = \left(1-\varepsilon\right)\left(C^f_{Na^+} - C^0_{Na^+}\right)/CV_G$ is a normalized gradient slope and CV_G is the duration of the gradient in column volumes. $C^0_{Na^+}$ and $C^f_{Na^+}$ are the initial and final Na^+ concentrations in the gradient. Based on eq. 2.2, a plot of the log γ' vs log $C^R_{Na^+,i}$ should be linear with slope equal to z_i+1. Even if interconversion occurs, however, the same relationship is expected to hold provided that the residence time is sufficiently short to allow the three forms to elute as distinct peaks. Experimental data were obtained for the 10 cm Source column at a flow rate of 1 ml/min, corresponding to a 2 min residence time, with 10, 15, 20, 25, and 40 CV gradients. Figure 2.10 shows the results plotted according to eq. 2.2. As seen in this figure, the plot is highly linear for all three forms. Parameter values obtained by regressing these data are summarized in Table 2.1.

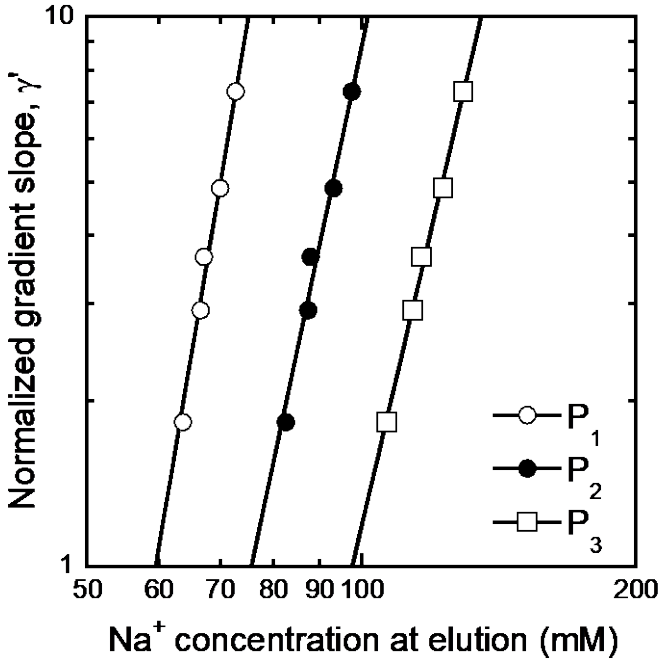

Figure 2.10. Plot of the normalized gradient slope vs the Na+ concentration at which each peak elutes for BiSA on a 9.4 cm Source 15S column at room temperature and pH 7. Gradients were 0-125 mM NaCl over 10, 15, 20, 25, and 40 CV at a flow rate of 1 ml/min. The lines are regressed to the data according to eq. 2.2. Regressed parameters A_i and z_i are given in Table 2.1.

Table 2.1. Parameter values estimated to describe the elution behavior of BiSA on Source 15S at pH 7 and room temperature.

Parameter	P_1	P_2	P_3
z	8.83	6.81	6.07
A (mM)^z	2.84×10^{16}	6.12×10^{13}	1.66×10^{13}
k_1 (s^{-1})	0.0064		
k_2 (s^{-1})	0.0008		
$\bar{k}_1$ (s^{-1})	0.002		
$\bar{k}_2$ (s^{-1})	0.002		
K_1	0.16		
K_2	0.01		
$\bar{K}_1$	4.0		
$\bar{K}_2$	1.4		

The second component of the model describes the evolution of the different forms during the initial binding and any subsequent hold step. Both of these steps occur at low Na^+ for conditions where protein binding is very strong and practically irreversible. As seen in Fig. 2.9, protein loading followed by immediate elution with a gradient (i.e. zero hold time) results in three distinct peaks. As discussed earlier, since the residence time was very short (0.22 min) there was insufficient time for significant interconversion during elution. Thus, the areas of the eluted peaks are proportional to the initial distribution of bound protein forms. Assuming that no desorption occurs after loading because of the favorable binding conditions and that conversion of one form to another follows first order consecutive kinetics, the following equations are used to describe the evolution of the different forms during the hold step:

$$\frac{\partial q_1}{\partial t} = -\bar{k}_1\left(q_1 - \frac{q_2}{\bar{K}_1}\right) \tag{2.3a}$$

$$\frac{\partial q_2}{\partial t} = \bar{k}_1\left(q_1 - \frac{q_2}{\bar{K}_1}\right) - \bar{k}_2\left(q_2 - \frac{q_3}{\bar{K}_2}\right) \tag{2.3b}$$

$$\frac{\partial q_3}{\partial t} = \bar{k}_2\left(q_2 - \frac{q_3}{\bar{K}_2}\right) \tag{2.3c}$$

where $\bar{k}_i$ and $\bar{K}_i$ are, respectively, rate and equilibrium constants for the interconversion of the three molecular forms on the chromatographic surface. These constants were fitted to the experimental data in Fig. 2.9b and are summarized in Table 2.1. As seen in Fig. 2.9b, these equations provide an excellent description of the data. The values of the equilibrium constants $\bar{K}_1$ = 4.0 and $\bar{K}_2 = 1.4$ indicate that equilibrium on the chromatographic surface favors form 3.

The third model component describes interconversion in the solution during the elution process. We first determine the equilibrium constants K_1 and K_2 for the interconversion of forms 1 and 2

and of forms 2 and 3 by considering the single peak position observed at the longest residence time corresponding to 0.01 ml/min (cf. Fig. 2.5). In this case, there is enough time to approximate local equilibrium conditions so that a single peak is observed. Under these conditions, the $C^R_{Na^+}$ of the equilibrium peak is a weighted average of the values at which the individual forms would elute in the absence of interconversion. Extending the analyses of Klinkenberg [15] and Carta et al. [5] to the case of gradient elution as shown in Appendix of ref [1], yields the following result:

$$\gamma' = \int_{C^0_{Na^+}}^{C^R_{Na^+}} \frac{1 + K_1 + K_1 K_2}{K_{a,1} + K_{a,2} K_1 + K_{a,3} K_1 K_2} dC_{Na+} \tag{2.4}$$

For a 20 CV gradient, under the experimental conditions of Fig. 2.5, the three peaks observed at high flow rates eluted at 6.74, 8.96, and 11.8 mS/cm (corresponding to Na^+ concentrations of 68.1, 89.8, and 118 mM, respectively). On the other hand, the single peak obtained at the lowest flow rate eluted at 7.50 mS/cm (corresponding to 81.3 mM Na^+). Integrating eq. 2.4 with the A_i and z_i values in Table 1 yields $K_1 = 0.16$ and $K_2 = 0.05$. These values indicate that equilibrium in solution largely favors form 1, with the three forms becoming distributed in the ratios 0.856:0.137:0.0068 for forms 1, 2, and 3, respectively.

The final component of the model describes mass transfer between the solution and the chromatographic surface. We assume that protein transport is diffusion-controlled and describe the rate according to the so-called linear driving force (LDF) approximation. Without interconversion, the rate can be expressed as [16]:

$$\frac{\partial \hat{q}_i}{\partial t} = \frac{15 D_{e,i}}{r_p^2} \left(C_i - C_i^* \right) \tag{2.5}$$

where $\hat{q}_i = q_i + \varepsilon_p C_i$ is the total solute concentration in the particle, including both protein held in the pores and bound protein, $D_{e,i}$ is the effective diffusivity, r_p, is the resin particle radius, C_i the solute concentration in solution, and C_i^* the solution concentration at equilibrium with $\hat{q}_i$. We determined $D_{e,i}$ from the column response to pulse injections of BiSA to the Source column for non-binding conditions (1000 mM NaCl) at different flow rates. The pulse response was analyzed by the moment method to generate a plot of reduced plate height ($h = HETP/d_p$) vs. reduced velocity $\nu' = \nu d_p / D_0$ where d_p is the resin particle diameter, ν is the mobile phase interstitial velocity, and D_0 is the BiSA diffusivity in free solution. As seen in Figure 2.11, the h vs. ν' data follow the linear relationship expected from the generalized van Deemter equation whose slope c, was used to calculate D_e according to the relationship [17]:

$$D_e = \frac{1}{30}\frac{\varepsilon}{1-\varepsilon}\left(\frac{k'}{1+k}\right)^2 \frac{D_0}{k'} \tag{2.6}$$

where k' is the protein retention factor. The resulting value of $D_e = 4.0 \times 10^{-8}$ cm^2/s is comparable to values reported for antibody diffusion in analogous porous resins without grafted polymers [18][19][20].

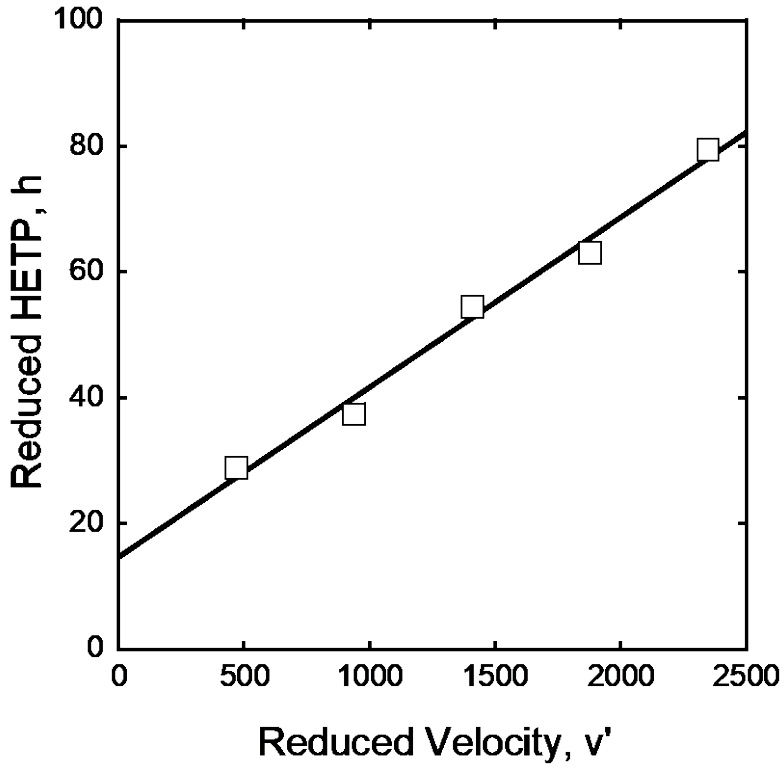

Figure 2.11. Van Deemter plot for BiSA from pulse injections under nonbinding conditions on a 10 cm long Source 15S column. Mobile phase: 10 mM Na_2PO_4, 1000 mM NaCl, pH 7.0. Pulse injection load was 0.11±0.004 mg/ml. Linearity shows dominance of mass transfer as dispersion mechanism in the experimental range of reduced velocities.

Combining the four model components described above, the interconversion scheme shown in Fig. 2.12 is obtained. In this figure, overbars indicate quantities on the chromatographic surface, solid arrows represent interconversions between one form and the other, and dashed lines represent transport to the surface from solution and vice-versa. During the initial loading, P_1 (along with smaller amounts of P_2) is strongly bound and upon binding is instantly converted to initial ratios favoring P_2. Further conversion toward P_3, which is favored at equilibrium on the chromatographic surface, is kinetically limited as shown in Fig. 2.9b and occurs slowly during the hold step over a 1-2 hour period. When the salt gradient is started at the end of the hold period, interconversion on the surface continues slowly until binding becomes sufficiently weak that desorption begins to occur. At this point, interconversion in solution becomes dominant with the desorbed P_3 and P_2 gradually converting back to P_1, which is favored in solution. The degree of conversion depends on the time available during the gradient elution process, which, in turn, determines whether three peaks (at low residence times), two peaks (at intermediate residence times) or just one equilibrium peak (at long residence times) is observed.

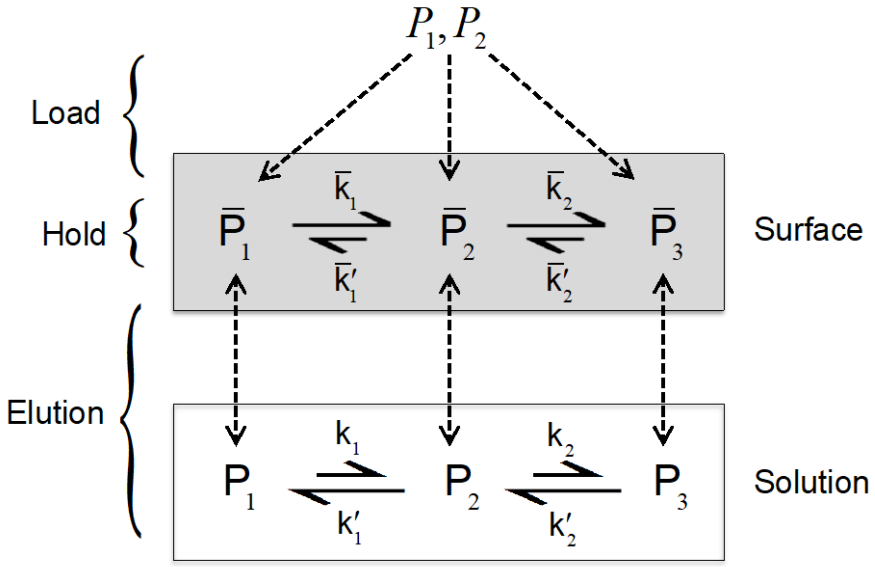

Figure 2.12. Conceptual model illustrating the interconversion of molecular forms during the load, hold, and elution process for BiSA on a Source 15S column. Dashed lines show mass transfer between solution and resin phase. Solid arrows show interconversion of the three molecular forms P_1, P_2, and P_3. Overbars indicate quantities pertaining to the chromatographic surface.

The mathematical description of this conceptual model is given by the following equations derived form the resin and solution phase material balances:

$$\frac{\partial \hat{q}_1}{\partial t} = \frac{15 D_{e,1}}{r_p^2}\left(C_1 - C_1^*\right) - \bar{k}_1\left(q_1 - \frac{q_2}{\bar{K}_1}\right) \tag{2.7a}$$

$$\frac{\partial \hat{q}_2}{\partial t} = \frac{15 D_{e,2}}{r_p^2}\left(C_2 - C_2^*\right) + \bar{k}_1\left(q_1 - \frac{q_2}{\bar{K}_1}\right) - \bar{k}_2\left(q_2 - \frac{q_3}{\bar{K}_2}\right) \tag{2.7b}$$

$$\frac{\partial \hat{q}_3}{\partial t} = \frac{15 D_{e,3}}{r_p^2}\left(C_3 - C_3^*\right) + \bar{k}_2\left(q_2 - \frac{q_3}{\bar{K}_2}\right) \tag{2.7c}$$

$$\varepsilon\frac{\partial C_1}{\partial t} = -\varepsilon v\frac{\partial C_1}{\partial x} - (1-\varepsilon)\frac{15 D_e}{r_p^2}\left(C_1 - C_1^*\right) - \varepsilon k_1\left(C_1 - \frac{C_2}{K_1}\right) \tag{2.8a}$$

$$\varepsilon\frac{\partial C_2}{\partial t} = -\varepsilon v\frac{\partial C_2}{\partial x} - (1-\varepsilon)\frac{15 D_e}{r_p^2}\left(C_2 - C_2^*\right) + \varepsilon k_1\left(C_1 - \frac{C_2}{K_1}\right) - \varepsilon k_2\left(C_2 - \frac{C_3}{K_2}\right) \tag{2.8b}$$

$$\varepsilon\frac{\partial C_3}{\partial t} = -\varepsilon v\frac{\partial C_3}{\partial x} - (1-\varepsilon)\frac{15 D_{e,3}}{r_p^2}\left(C_3 - C_3^*\right) + \varepsilon k_2\left(C_2 - \frac{C_3}{K_2}\right) \tag{2.8c}$$

where x is the column axial coordinate. The only parameters left to determine in these equations are the rate constants for the interconversion in solution, k_1 and k_2. These two parameters were thus estimated by matching the numerical solution of the above equations to the experimental results varying the elution flow rate. The equations were solved numerically by discretizing the axial derivatives in eqs. 7a-c using backwards-finite differences and solving the resulting set of ordinary differential equations together with eqs. 2.8a-c using MATLAB's multistep, variable order solver, ode15s. As is well known [21][22], backwards discretization introduces numerical dispersion. Thus, the number of axial discretization points was used to simulate axial dispersion (which is not explicitly included in eqs. 2.8a-c) by setting it equal to the number of theoretical

plates determined from a salt pulse injection for the actual experimental column. This number was equal to 250 for the 9.4 cm Source column used in this work. The Na^+ in the column during the gradient elution process was calculated assuming ideal conditions since rigorous calculations considering axial dispersion and mass transfer effects resulted in predicted profiles that were practically indistinguishable from the ideal model results (e.g. see ref. [23]).

Figure 2.13 compares experimental and numerically calculated elution profiles for the conditions of Fig. 2.4 using k_1= 0.0064 s^{-1} and k_2=0.0008 s^{-1}, determined by trial and error, with the remaining parameters as previously estimated and summarized in Table 2.1. For simplicity we show only three cases but the trends as a function of flow rate, gradient slope, and hold time were equally well predicted. As seen in this figure the model correctly predicts the trend of a single near equilibrium peak at low flow rates (Fig. 2.13a) becoming three distinct peaks at a high flow rate (Fig. 2.13b) and the trend of a higher percentage of the late eluting peak with a longer hold time prior to elution (Fig. 2.13c). Experimental and predicted peak positions along the gradient and peak widths are also reasonably well predicted indicating that the model captures the essential traits of the process.

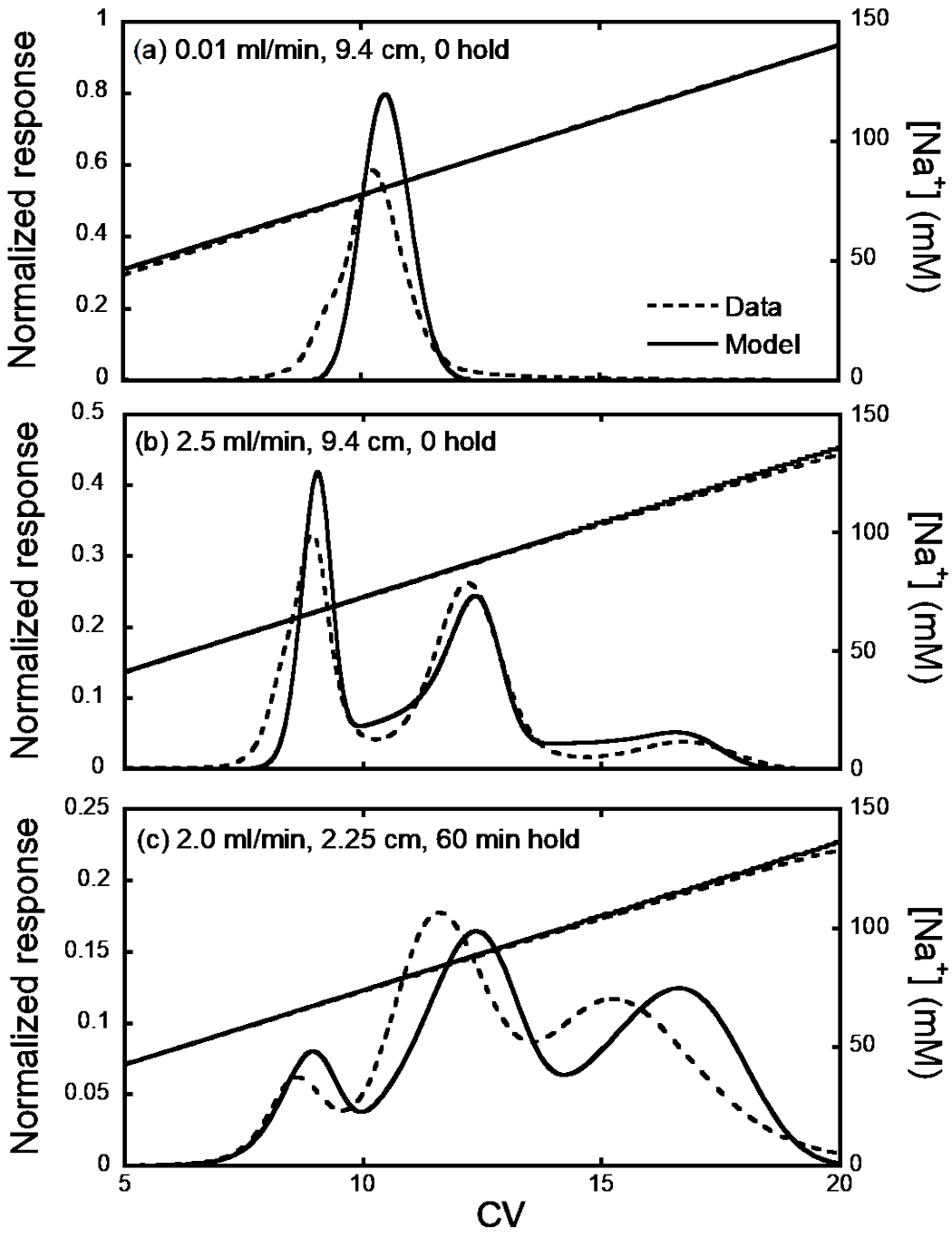

Figure 2.13. Comparison of experimental and predicted elution profiles for BiSA on a 9.4 Source 15S column (a) and (b) for the conditions of Fig. 6 with no hold and on a 2.3 cm Source 15S column for the conditions of Fig. 2.9 with a 60 min hold (c). Elution flow rates were 0.01 ml/min (a), 2.5 ml/min (b), and 2.0 ml/min (c). The UV 280 signal of the experimental profiles are normalized to obtain the same peak area as the model.

2.4 References

[1] L.K. Kimerer, T.M. Pabst, A.K. Hunter, G. Carta, Chromatographic behavior of bivalent bispecific antibodies on cation exchange columns. I. Experimental observations and phenomenological model, J. Chromatogr. A. 1601 (2019) 121–132.

[2] G. Carta, A. Jungbauer, Protein Chromatography, 2nd ed., Wiley-VCH, Weinheim, Germany, 2020.

[3] R. Gillespie, T. Nguyen, S. Macneil, L. Jones, S. Crampton, S. Vunnum, Cation exchange surface-mediated denaturation of an aglycosylated immunoglobulin (IgG1), J. Chromatogr. A. 1251 (2012) 101–110.

[4] H. Luo, M. Cao, K. Newell, C. Afdahl, J. Wang, W.K. Wang, Y. Li, Double-peak elution profile of a monoclonal antibody in cation exchange chromatography is caused by histidine-protonation-based charge variants, J. Chromatogr. A. 1424 (2015) 92–101.

[5] G. Carta, A.J. Mahajan, L.M. Cohen, Chromatography of reversibly reacting mixtures: mutarotation effects in sugar separations, Chem. Eng. Sci. 47 (1992) 1645–1657.

[6] F. Ortner, H. Wiemeyer, M. Mazzotti, Interconversion of carbohydrate stereoisomers on polystyrene-divinylbenzene resins, Chem. Eng. Sci. 1517 (2017) 1645–1657.

[7] Y. Kalambet, Y. Kozmin, K. Mikhailova, I. Nagaev, P. Tikhonov, Reconstruction of chromatographic peaks using the exponentially modified Gaussian function, J. Chemom. 25 (2011) 352–356.

[8] A. Voitl, A. Butté, M. Morbidelli, Behavior of human serum albumin on strong cation exchange resins: II. Model analysis, J. Chromatogr. A. 1217 (2010) 5492–5500.

[9] R. Muca, W. Marek, W. Pi, D. Antos, Influence of the sample-solvent on protein retention, mass transfer and unfolding kinetics in hydrophobic interaction chromatography, J. Chromatogr. A. 1217 (2010) 2812–2820.

[10] J. Guo, A.D. Creasy, G. Barker, G. Carta, Surface induced three-peak elution behavior of a monoclonal antibody during cation exchange chromatography, J. Chromatogr. A. 1474 (2016) 85–94.

[11] W. Kopaciewicz, M.A. Rounds, J. Fausnaugh, F.E. Regnier, Retention model for high-performance ion-exchange chromatography, J. Chromatogr. 266 (1983) 3–21.

[12] S. Yamamoto, K. Nakanishi, R. Matsuno, Ion-Exchange Chromatography of Proteins, Marcel-Dekker, New York, 1988.

[13] S. Yamamoto, K. Nakanishi, R. Matsuno, T. Kamikubo, Ion Exchange Chromatography of Proteins-Prediction of Elution Curves and Operating Conditions. I. Theoretical Considerations, Biotechnol. Bioeng. XXV (1983) 1465–1483.

[14] S. Yamamoto, K. Nakanishi, R. Matsuno, T. Kamikubo, Ion Exchange Chromatography of Proteins-Prediction of Elution Curves and Operating Conditions. II. Experimental Verification, Biotechnol. Bioeng. XXV (1983) 1373–1391.

[15] A. Klinkenberg, Chromatography of substances undergoing reactions slow reversible chemical, Chem. Eng. Sci. 15 (1961) 255–259.

[16] M.D. LeVan, G. Carta, J.A. Ritter, K.S. Walton, Section 16 Adsorption and Ion Exchange, in: D.W. Green, M.Z. Southward (Eds.), Perry's Chem. Eng. Handb., 9th ed., McGraw Hill, 2018.

[17] G. Carta, A.R. Ubiera, T.M. Pabst, Protein Mass Transfer Kinetics in Ion Exchange Media : Measurements and Interpretations, Chem. Eng. Technol. Rev. 28 (2005) 1252–1264.

[18] Y. Tao, G. Carta, G. Ferreira, D. Robbins, Adsorption of deamidated antibody variants on macroporous and dextran-grafted cation exchangers : II . Adsorption kinetics, J. Chromatogr. A. 1218 (2011) 1530–1537. doi:10.1016/j.chroma.2011.01.050.

[19] E.X.P. Almodovar, Y. Tao, G. Carta, Protein adsorption and transport in cation exchangers with a rigid backbone matrix with and without polymeric surface extenders, Biotechnol. Prog. 27 (2011) 1264–1272. doi:10.1002/btpr.643.

[20] J.M. Reck, T.M. Pabst, A.K. Hunter, X. Wang, G. Carta, Adsorption equilibrium and kinetics of monomer-dimer monoclonal antibody mixtures on a cation exchange resin, J. Chromatogr. A. 1402 (2015) 46–59.

[21] Z. Ma, G. Guiochon, Application of orthogonal collocation on finite elements in the simulation of non-linear chromatography, Comput. Chem. Eng. 15 (1991) 415–426.

[22] M. Czok, G. Guiochon, The physical sense of simulation models of liquid chromatography: propogation through a grid or solution of the mass balance equation, Anal. Chem. 62 (1990) 189–200.

[23] A. Creasy, J. Lomino, G. Carta, Gradient elution behavior of proteins in hydrophobic interaction chromatography with a U-shaped retention factor curve under overloaded conditions, J. Chromatogr. A. 1578 (2018) 28–34.

3 Biophysical Basis

3.1 Introduction

Complex chromatographic behavior was observed for bivalent bispecific antibodies during linear gradient elution. A pure protein feed eluted three peaks at low residence time and room temperature and a single, merged peak when residence time was elongated or temperature was elevated. The mechanism was found not to be due to mechanisms previously reported such as secondary structure unfolding leading to aggregation or slow titration of histidine residues as the three peaks were measured with dynamic light scattering to be of consistent monomer size and the behavior was qualitatively unchanged regardless of pH. The biophysical basis of the multiple peaks for BiSAbs is probed through chemical crosslinking, enzyme proteolysis to determine domain contributions, tryptophan autofluorescence, resin and buffer screening, and homology modeling. Results reveal a mechanism where each linked scFv can adopt one of two extreme configurations: collapsed and the scFv is interacting with the framework mAb which is favored in solution, or outstretched and the scFv can more strongly bind to the resin surface. Examples of the three resulting BiSAb configurations are shown for BiSA in Figure 3.1. This work was published in the Journal of Chromatography A as ref. [1].

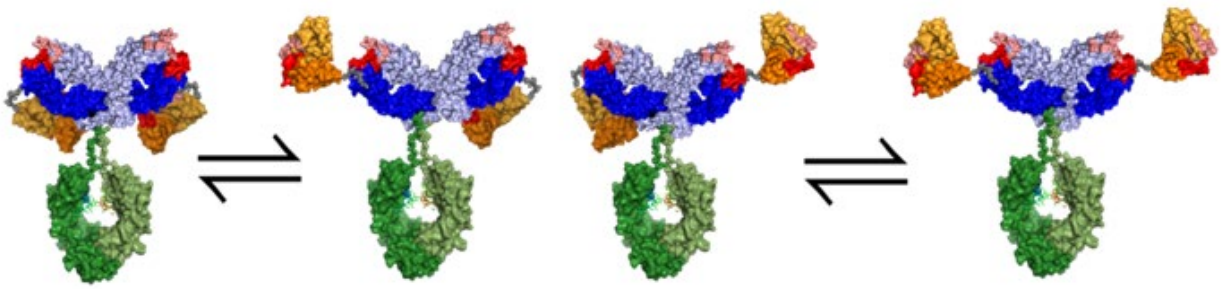

Figure 3.1. Examples of possible configurations for BiSA. Subunit images are from ref. [2], were rendered in PyMOL (Delano Scientific), and assembled in PowerPoint.

3.2 Materials and Methods

3.2.1 Experimental Methods

Cation exchange chromatography resins used in this work are ProPac WCX 10, Source 15S, and SP Sepharose HP. The Source columns are the same as those packed in section 2.2.2. SP Sepharose HP (Cytiva) is a strong cation exchanger based on a porous 30 μm agarose particle. SP Sepharose HP was purchased as a slurry and packed into 0.5-cm diameter columns to a final height of 10.3 cm.

Chromatographic experiments were performed following method in 2.2.2 using an ÄKTA Pure 25 (Cytiva) except for the UPLC-SEC and in-line fluorescence measurements which were performed on an Acquity UPLC H-Class system from Waters (Milford, MA, USA). Autofluorescence of tryptophan residues was measured using a fluorescence detector plumbed to the outlet of the column. The excitation wavelength was set to 295 nm and emission spectrum was monitored over the range 310-400 nm [3][4]. The fluorescence intensity was normalized by the UV280 signal in order to allow a quantitative comparison of the spectra of the different peaks.

The crosslinking method used in this work follows the protocol described by Bankston and Carta [5] to crosslink recombinant apo-lipoprotein with dimethyl suberimidate (DMS) and is based on the original development of Davies and Stark [6]. The approach favors intramolecular crosslinking and does not promote the formation of aggregates [6]. For this purpose, a solution containing 1.0 mg/ml (5 μM) BiSA and of 1.4 mg/ml (5 mM) DMS in 20 mM triethanolamine at pH 8.0 was prepared and allowed to incubate for 2 hr at room temperature under mild agitation. After 2 hr, Tris was added to a final concentration of 50 mM in order to quench the crosslinking reaction. The reaction pool was then buffer exchanged to 10 mM Na_2PO_4 at pH 7.0 to remove the quenched DMS using a HiPrep 26/10 desalting column. The crosslinked protein was characterized by SDS-

PAGE. The effect of cross-linking on the elution behavior was assessed by conducting linear gradient elution experiments on a Source 15S column in comparison with the behavior of the unmodified protein.

BiSA and BiSB were clipped using FabRICATOR and FabALACTICA immunoglobulin-degrading proteases from Genovis AB (Cambridge, MA, USA) to study effects of the scFvs attached to either the Fab or Fc region of the framework IgG and to determine the domain contributions to binding on the resin. Both enzymes have high specificity and efficacy for specific sequences of IgG1 and cleave at different locations [7][8]. FabRICATOR cleaves below the IgG hinge region while FabALACTICA cleaves above the hinge. The expected product fragments are shown in Table 3.1 along with theoretical molecular masses calculated according to the known sequence and the expected cleavage locations. In the case of BiSA, FabRICATOR is expected to yield $(Fab\text{-}scFv)_2$ along with full Fc and, potentially, Fc/2 fragments, while FabALACTICA is expected to yield monomeric Fab-scFv and Fc intact fragments. In the case of BiSB, FabRICATOR is expected to yield $(Fab)_2$ along with full Fc-$(scFv)_2$ and Fc/2-scFv fragments while FabALACTICA is expected to yield Fab and Fc-$(scFv)_2$ fragments. For both BiSAb molecules, whether full Fc or Fc/2 fragments depends on the degree of association of the heavy chains. In our experience, even with elimination of the hinge region, full Fc fragments are predominantly generated.

While BiSA was used without further purification, BiSB was further purified prior to enzymatic digestion to remove early eluting impurities using a Source 15S column with a 40 CV NaCl gradient. The samples were dialyzed into 100 mM Na_2PO_4, pH 7.0 at a concentration of 2 mg/mL. Protein samples were mixed in a vial with either enzyme at a ratio of one unit enzyme per µg BiSAb and incubated overnight in a water bath at 37 °C. Reaction products were analyzed by

UPLC SEC and non-reduced SDS-PAGE. SEC was done with a Waters UPLC BEH SEC 200 Å using an Acquity H-Class UPLC system (Waters, Milford, MA, USA) with a 100 mM Na_2PO_4, 300 mM NaCl, pH 7.0 buffer at 0.3 mL/min. SDS-PAGE was done on NuPage 4-12% Bis-Tris SDS-PAGE gels (ThermoFisher, Fair Lawn, NJ, USA) with NuPage LDS sample buffer and MES running buffer using an Invitrogen Mini Gel Tank (ThermoFisher). The protein samples were added to sample buffer and denatured by heating at 100 °C for 10 minutes. One lane with intact monomer was run under reduced conditions, using dithiothreitol (DTT) as a reducing agent added to a final concentration of 50 mM prior to heating. Kaleidoscope Precision Protein Standards from BioRad (Hercules, CA, USA) were used. The gels were run at 150 V for 1 hour followed by staining with EZBlue Gel Staining Reagent (MilliporeSigma, St. Louis, MO, USA) and imaged with an Odyssey CLX gel scanner (LI-COR, Lincoln, NE, USA).

Fc-domain containing fragments from enzyme cleavage were separated from other fragments by Protein A chromatography using a 0.5 diameter, 5 cm long MabSelect SuRe (GE Healthcare) column. The nonbinding fragments which included Fab, $(Fab)_2$, Fab-scFv, $(Fab\text{-}scFv)_2$, and the added enzymes were collected in the flow through. Fragments containing the Fc-domain were eluted with a 20 CV linear pH gradient from pH 7.0 to 3.0 using a buffer system designed according to [9] utilizing mixtures of acetate, 2-(N-mopholino)ethanesulfonate (MES), and phosphate. Once isolated, intact fragments were diluted three-fold with 10 mM Na_2PO_4, pH 7.0 and injected onto ProPac WCX-10. A 20 CV linear gradient was then performed from 0-125 mM NaCl to determine the domain contributions to the cation exchange elution profile.

3.2.2 Computational Homology Modeling

Molecular properties of the Fab and Fc domains of the framework IgG and of the scFv domain in the BiSAb molecules considered in this work were generated by homology modeling. The Fab

region was modeled based on the actual sequence of the BiSAb molecules using the PIGSPro server which is optimized to predict immunoglobulin variable domains based on the canonical structure method [10]. The Fc domain was modeled with the SWISS-MODEL server according to refs. [10][11][12] using 1HZH in the SWISS PdB database as a template. Finally, the scFv domain was modeled instead using the I-TASSER server according to refs. [13][14][15]. Sequence identities were nearly 100% and 76%, respectively. Molecular structures were rendered in PyMol, which was also used to calculate the protein contact potential based on vacuum electrostatics. Surface hydrophobicity was visualized by coloring the residues according to ref. [16]. The scFv linker was not included explicitly in these models but the respective N- and C-terminus attachment points were removed from charge calculations by converting them to the corresponding acetyl and methyl forms.

3.3 Results and Discussion

Figure 3.2 shows the chromatographic behavior of the framework mAb and of BiSA on the ProPac and Source columns at low and high flow rates. As seen in Figs. 3.2a and b, the mAb exhibits the chromatographic behavior normally observed for typical proteins in gradient elution chromatography. In this case, the ProPac column exhibits similar peak broadening at high or low flow rate as a result of the pellicular structure of this resin and the corresponding absence of intraparticle mass transfer limitations. On the other hand, the Source column shows a sharper peak at the lower flow rate and a broader peak at the higher flow rate as a result of the porous structure of this resin and the associated mass transfer effects. In contrast to the mAb, as seen in Figs. 3.2c and d, BiSA exhibits multiple peaks at the highest flow rate for each resin and a single peak at the lowest flow rate. While the conductivities at elution and the peak widths are different for the two resins, it is evident that the behaviors are qualitatively the same for both suggesting that the underlying molecular mechanisms that are responsible for this unusual behavior are similar for the two resins despite the different ligands, resin structure, and bead size. As shown in Figure 2.4, collecting fractions of any of the three peaks obtained at high flow rate and re-injecting them for the same conditions resulted in the same three peaks for both resins suggesting that the underlying mechanisms are reversible. Finally, comparing the mAb and BiSA behaviors, it is evident that the mAb is retained much less strongly compared to BiSA eluting at substantially lower conductivities for both resins. As shown in Figure 2.6, BiSB and BiSC behaved in a manner qualitatively similar to BiSA with multiple peak elution at high flow rates, merging into a single peak at low flow rates.

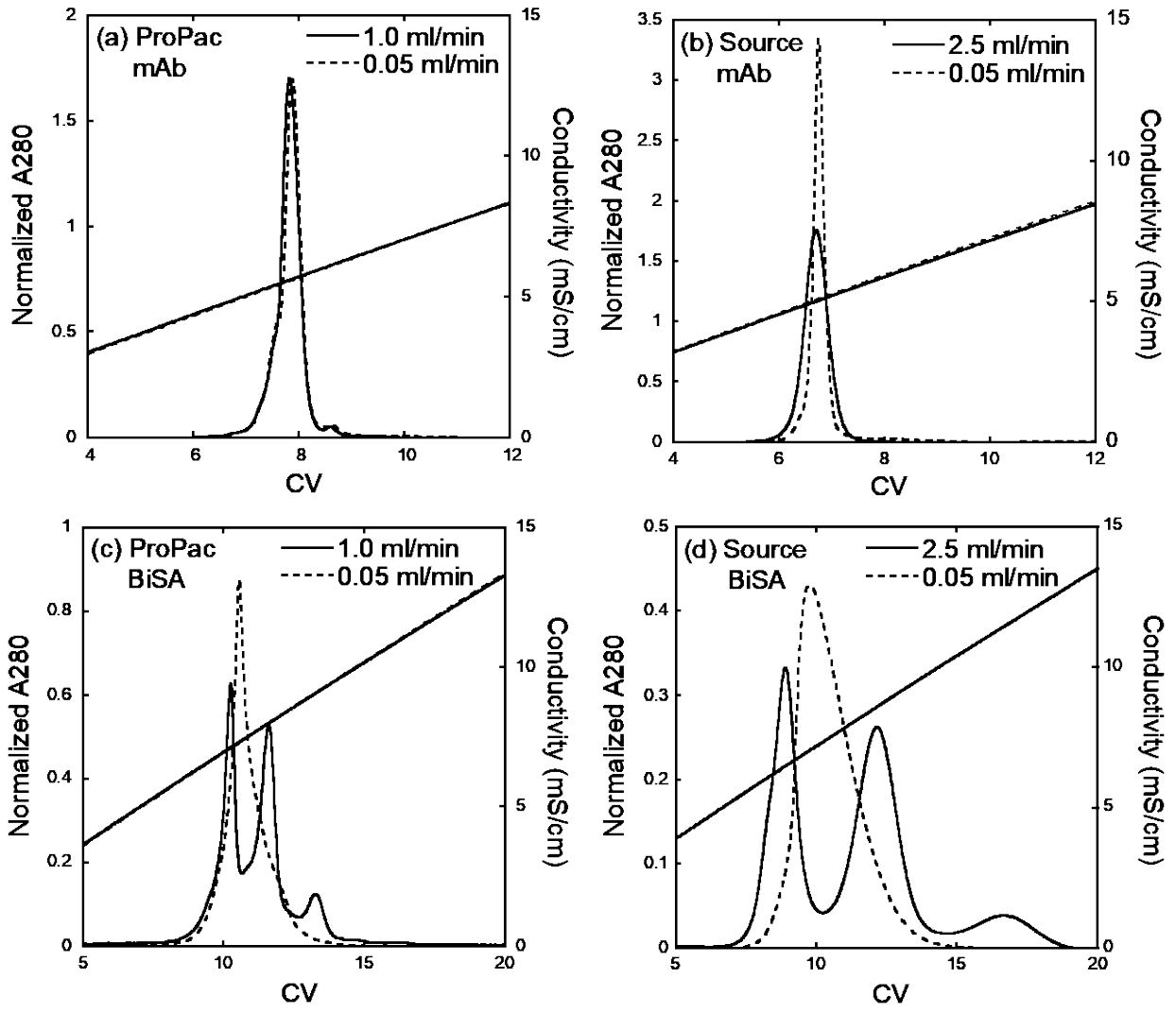

Figure 3.2. Comparison of the gradient elution behavior of a mAb with the same sequence as the framework IgG in BiSA (a,b) and that of BiSA (c,d) on ProPac WCX-10 (a,c) and Source 15S (b,d) columns with a 0-125 mM NaCl 20 CV in 10 mM Na_2PO_4 at pH 7.0 at high and low flow rates. Flow rates of 1.0 and 0.05 ml/min correspond to residence times of 1.25 and 25.12 min for the ProPac column, while flow rates of 2.5 and 0.05 ml/min correspond to residence times of 0.74 and 37 min for the Source column. The mass of protein injected was 0.15±0.03 mg/ml for ProPac and 0.20±0.3 mg/ml for Source. The A280 absorbance is normalized to obtain the same peak area in order to account for slight differences in the amount of protein injected.

Figure 3.3 compares the chromatographic behavior of the unmodified BiSA (a) with that of the crosslinked BiSA sample (b) on the Source column at a flow rate of 1.0 ml/min for otherwise identical conditions. As seen from this figure, the chromatographic behavior is dramatically different in the two cases. While three distinct peaks are eluted for the unmodified BiSA, a single broader peak emerges for the crosslinked BiSA sample eluting at a conductivity intermediate between the elution conductivities of the three peaks obtained with the unmodified protein. In order to understand why the crosslinked peak is broader, fractions of the eluted peaks were collected as shown in Fig. 3.3b and re-chromatographed in the same column for identical conditions. As seen in Fig. 3.3c, each fraction emerges as a single peak at conductivities that increase in the order in which the fractions were collected. We conclude that crosslinking stabilized the protein multidomain structure, reducing conformational flexibility, but also generating multiple crosslinked forms that were retained differently on the Source 15S column. This result was confirmed by conducting SDS-PAGE analysis under reducing conditions for the unmodified and crosslinked protein. As shown in Figure 3.4, multiple bands with molecular mass between 75 and 200 kDa were obtained indicating the presence of multiple species resulting from crosslinks between the various domains in the BiSA molecule. The main conclusion is that impeding conformational flexibility removes the multiple peak elution behavior observed for the unmodified BiSA.

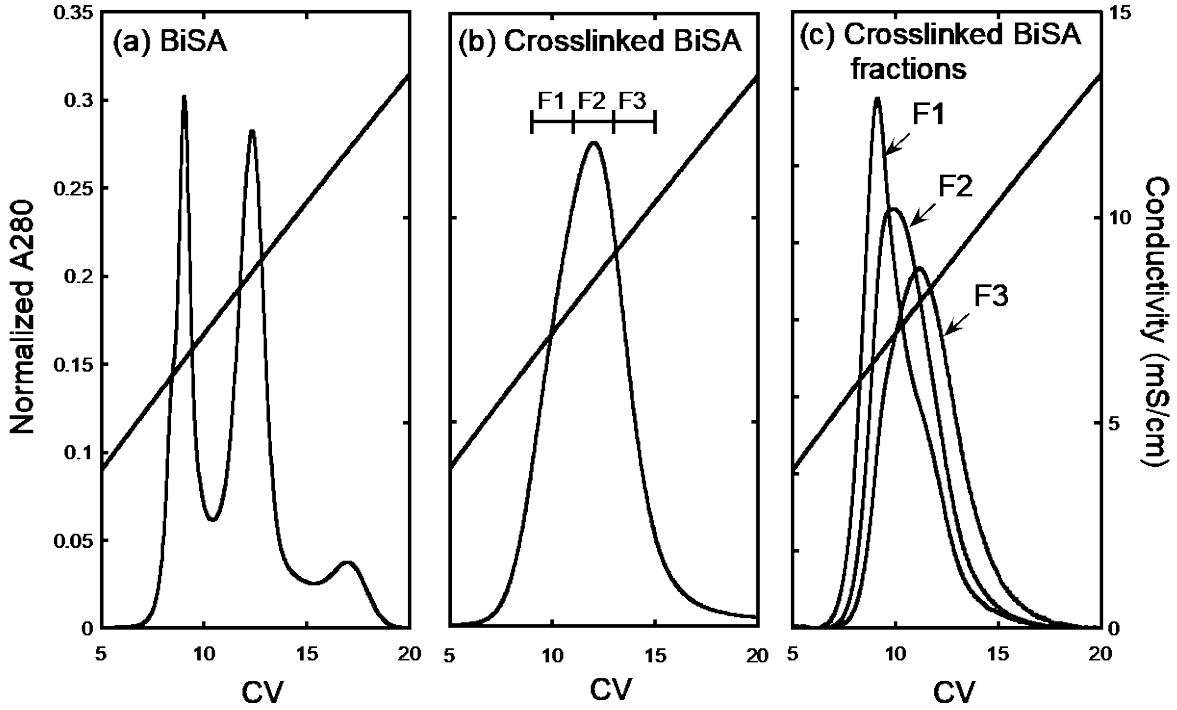

Figure 3.3. Comparison of the gradient elution behavior of BiSA (a) and crosslinked BiSA (b,c) on the Source 15S column with a 0-125 mM NaCl 20 CV in 10 mM Na_2PO_4 at pH 7.0 at 1.0 ml/min corresponding to 1.85 min residence time. Protein mass load was 0.22 mg/ml in (a), 3.4 mg/ml in (b), and 0.085±0.04 in (c). The A280 absorbance is normalized to obtain the same peak area in order to account for slight differences in the amount of protein injected.

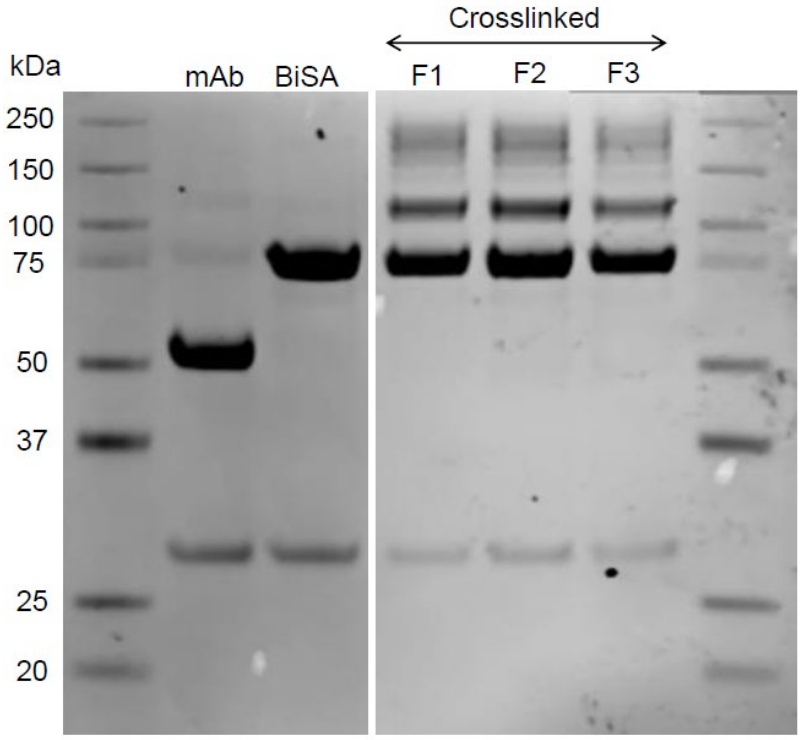

Figure 3.4. Reduced, denatured SDS-PAGE of a mAb, BiSA, and crosslinked fractions shown in Fig. 3.3b. Protein samples were mixed with NuPage LDS sample buffer and Dithiothreitol with a final concentration of 50 mM. Mixture was heated at 100 °C for 10 minutes before loaded onto gel. Kaleidagraph Precision Protein Standards from BioRad were used. A NuPage 4-12% Bis-Tris SDS-PAGE gel was run using MES running buffer on an Invitrogen Mini Gel Tank for 1 hr. The gel was stained with EZBlue and imaged with an Odyssey CLX gel scanner. Middle lanes of the actual gel were removed for clarity as indicated by the gap.

FabRICATOR and FabALACTICA were used for separate digestions of BiSA and BiSB. As noted above, the first of these enzymes is designed to selectively cleave IgG below the hinge, while the second is designed to selectively cleave above the hinge. Figure 3.5a shows the SEC analyses of the digestion products compared to the intact BiSAb molecules. Table 3.1 compares the molecular masses for the expected digestion products with those estimated based on SEC. The latter were calculated according to the calibration curve shown in Fig. 3.5c, which was constructed using standard proteins. As shown in Table 3.1, for BiSA, FabRICATOR is expected to produce a (Fab-scFv)$_2$ fragment and Fc/2 fragments while FabALACTICA is expected to produce Fab-scFv fragments and a Fc fragment including a portion of the hinge region. For BiSB, on the other hand, FabRICATOR is expected to produce a (Fab)$_2$ fragment and a Fc-(scFv)$_2$ with no hinge while FabALACTICA is expected to produce and Fab fragments along with a Fc-(scFv)$_2$ fragment including a hinge region.

As seen in Fig. 3.5 and in Table 3.1, the experimental results are in line with the theoretical expectations confirming that the desired fragments were obtained. No Fc/2 fragment was obtained with FabRICATOR suggesting that despite the clip below the hinge region, the full Fc domain remains intact for both BiSA and BiSB. These results were further confirmed by SDS-PAGE as shown in Figure 3.6.

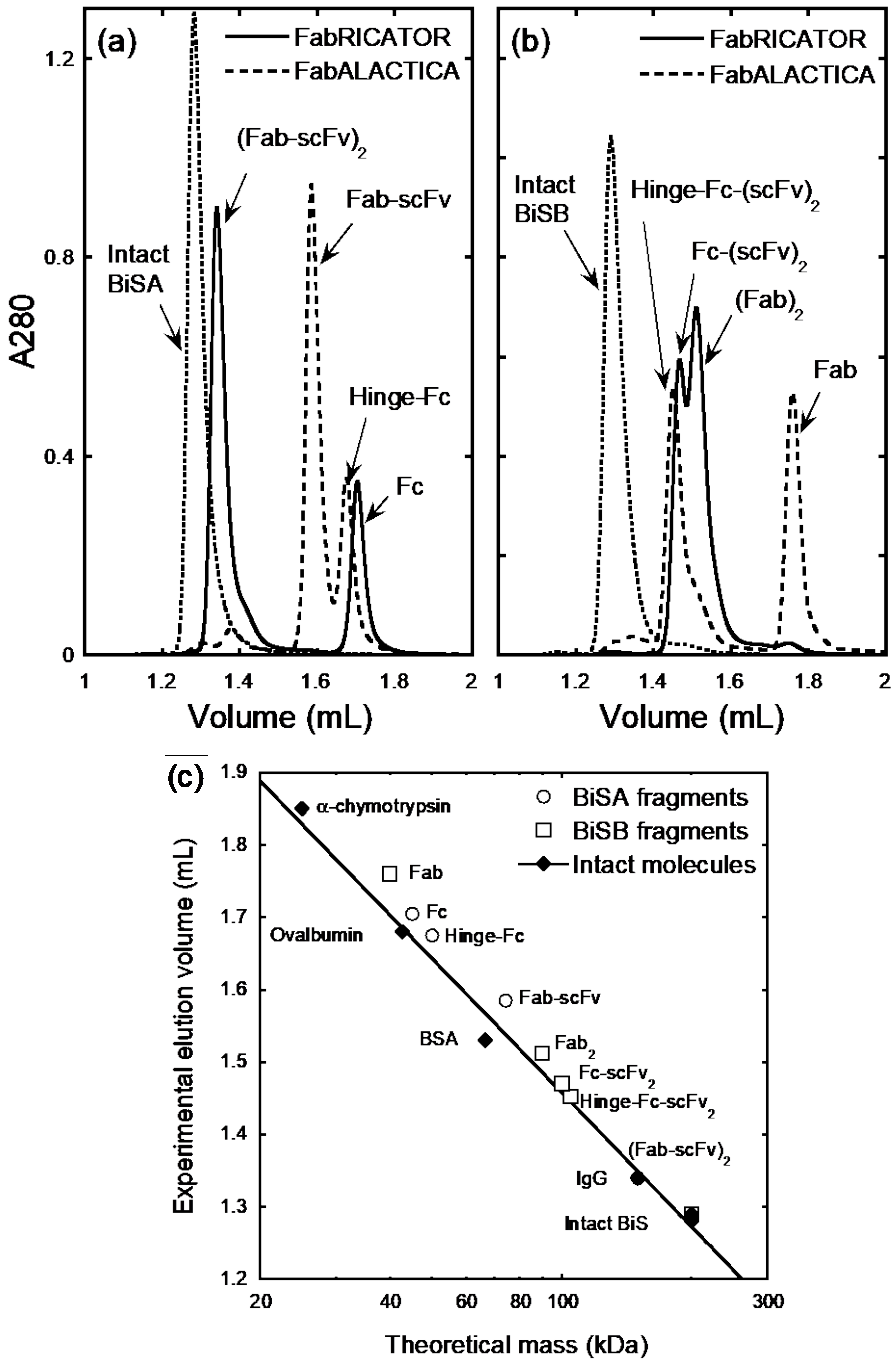

Figure 3.5. UPLC SEC analysis of BiSA (a) and BiSB (b) digestion products obtained with FabRICATOR and FabALACTICA enzymes compared to the chromatograms of the intact molecules. SEC calibration curve based on retention of model proteins (c). Chromatograms were obtained with a Waters Acquity BEH 200Å UPLC-SEC column at 0.3 mL/min flow rate with 300 mM NaCl in 100 mM Na_2PO_4 at pH 7.0. Mass load for each injection was 0.04 ±0.02 mg.

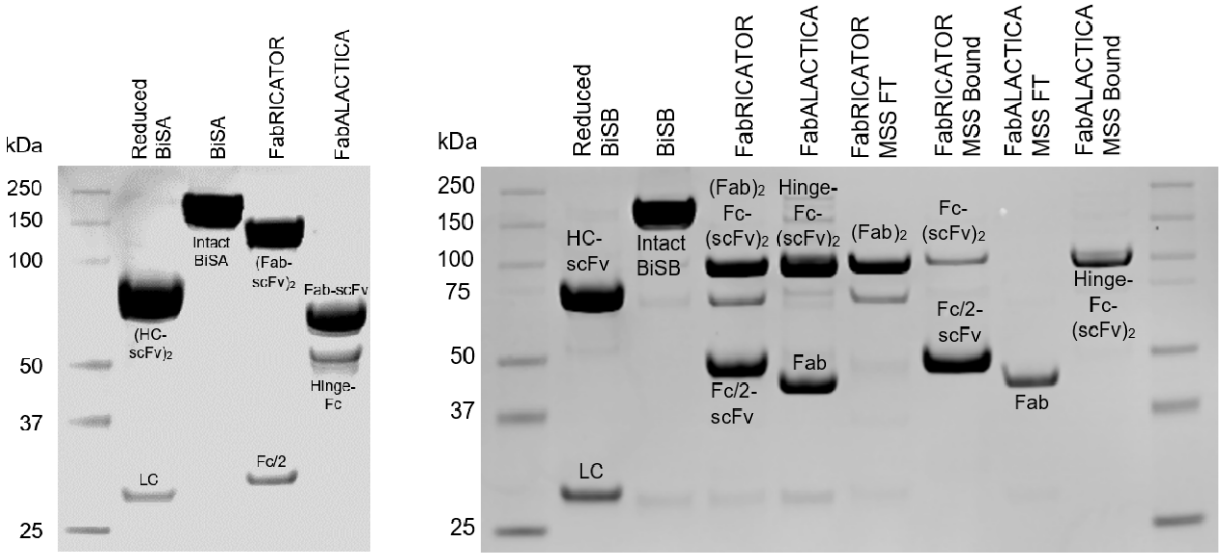

Figure 3.6. Denatured SDS-PAGE of BiSA (left panel) and BiSB (right panel) with their respective enzyme-clipped species. Lane 1 of both panels show reduced BiSA or BiSB for this sample Dithiothreitol was added to 50 mM prior to heating. For all samples, NuPage LDS sample buffer was added to protein samples and heated at 100 °C for 10 min before loading onto gel. Due to the similar molecular weight for multiple fragments of cleaved BiSB, Protein A MabSelect SuRe (MSS) bound, Fc-containing, and flow through (FT) fractions are also run on the gel in panel (b). Kaleidagraph Precision Protein Standards from BioRad were used. A NuPage 4-12% Bis-Tris SDS-PAGE gel was run using MES running buffer on an Invitrogen Mini Gel Tank for 1 hr. The gels were stained with EZBlue and imaged with an Odyssey CLX gel scanner. Note that unlike SEC that was run under non-denaturing conditions, denatured FabRICATOR-cleaved Fc fragments without hinge region separated to run as monomeric Fc/2.

Table 3.1. Comparison of theoretical and experimental molecular mass determined by SEC for fragments obtained by digestion of BiSA and BiSB with FabRICATOR and FabALACTICA enzymes based on UPLC SEC analysis.

BiSA Species				BiSB Species			
		Theor. Mass (kDa)	Exp. Mass (kDa)			Theor. Mass (kDa)	Exp. Mass (kDa)
Intact BiSA	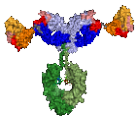	200	180	Intact BiSB		200	170
FabRICATOR – Cleaves below hinge							
$(Fab\text{-}scFv)_2$		~150	144	$(Fab)_2$		~90	78
Fc		~45	39	$Fc\text{-}(scFv)_2$		~95	90
Fc/2		25	NA	Fc/2-scFv		~50	NA
FabALACTICA – Cleaves above hinge							
Fab-scFv		~70	60	Fab		~45	32
Hinge-Fc	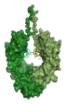	~50	43	Hinge-Fc-$(scFv)_2$		~100	96

Following isolation of the fragments by Protein A chromatography, their chromatographic behavior was studied on the ProPac column. Results are shown in Figs. 3.7 and 3.8, for BiSA and BiSB, respectively, at high and low flow rates. Table 3.2 summarizes the conductivities at elution for each of the peaks observed. In the case of BiSA (Fig. 3.7), both intact BiSA and the (Fab-scFv)$_2$ domain yielded three peaks at high flow rate suggesting that in both cases the molecules exists in three different configurations. On the other hand, the Fab-scFv fragment yielded only two peaks at high flow rate indicating that only two configurations are possible. In all three cases, the multiple peaks merge into one at low flow rate. Overall, this behavior confirms the hypothesis that the multiple peak elution behavior is associated with the flexibility of the scFv linker which allow the reversible interconversion of protein configurations with either outstretched or collapsed scFv domains that interact differently with the chromatographic surface. If two scFv domains are present, three peaks are obtained since three major isoforms are possible. On other hand, if only one scFv domain is present, two peaks are obtained since only two major configurations are possible. A final observation is that, as seen in Table 3.2, retention of the intact BiSA and retention of the (Fab-scFv)$_2$ fragment are very similar (conductivities at elution of 7.1, 8.0, and 9.1 mS/cm for the three intact BiSA peaks vs. and conductivities at elution of 6.8, 7.5, and 8.5 mS/cm for the three (Fab-scFv)$_2$ fragment peaks) indicating that the Fc domain plays only a small role in the protein-surface interaction. On the other hand, retention of the Fab-scFv fragment is weaker with conductivities at elution of 5.0 and 6.3 mS/cm for peaks 1 and 2, respectively. This result is also expected since because of the higher mass and charge of the (Fab-scFv)$_2$ compared to the Fab-scFv fragment.

In the case of BiSB (Fig. 3.8), both the intact protein and the two scFv-containing fragments yielded three peaks at high flow rate, which merge into a single peak at low flow rate. All three

species contain two flexibly linked scFv domains and can, thus, exist in three major interconverting configurations with scFv domains extended and collapsed according. A significant difference compared to BiSA is that, as seen in Table 3.2, retention is similar for the intact BiSB and for the two scFv containing fragments (conductivities at elution all within about 1 mS/cm) indicating that, in this case, the Fab domain plays only a modest role on the protein-surface interaction. Whether the hinge region is included or not also seems to have a small effect on the interaction strength, likely because of the small size of the region.

Finally, it should be noted that the Fc fragments of BiSA or the Fab fragments of BiSB, neither of which is connected to a scFv, showed very weak retention, eluting at conductivities below 5.5 mS/cm as single peaks.

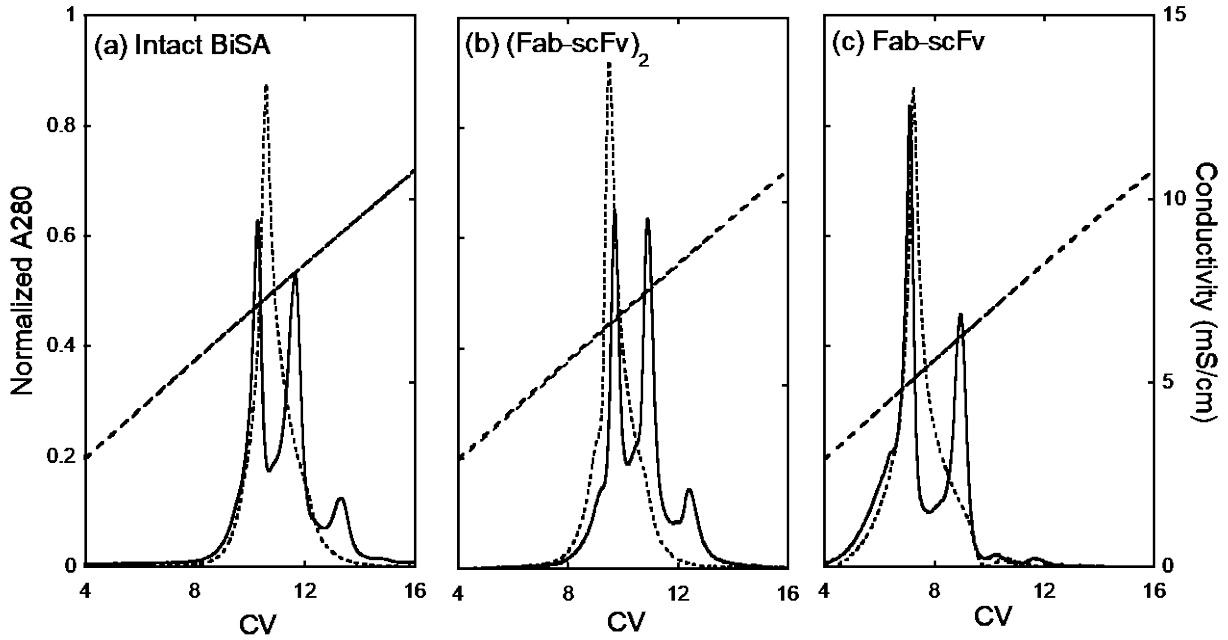

Figure 3.7. Comparison of the gradient elution behavior of intact BiSA (a) with that of BiSA fragments obtained by digestion with FabRICATOR (b) and FabALACTICA (c) enzymes on ProPac WCX-10 with a 0-125 mM NaCl 20 CV in 10 mM Na_2PO_4 at pH 7.0 at flow rates of 1.0 ml/min (solid lines) and 0.05 ml/min (dashed lines) correspond to residence times of 1.25 and 25.1 min, respectively. The mass of protein injected was 0.055±0.005 mg/ml for enzyme clipped species and 0.12±0.03 mg/ml for intact BiSA. The A280 absorbance is normalized to obtain the same peak area in order to account for slight differences in the amount of protein injected. Note that three peaks are eluted at high flow rates in (a) and (b) while only two peaks are eluted at high flow rate in (c). A single merged peak is eluted at low flow rate in all three cases.

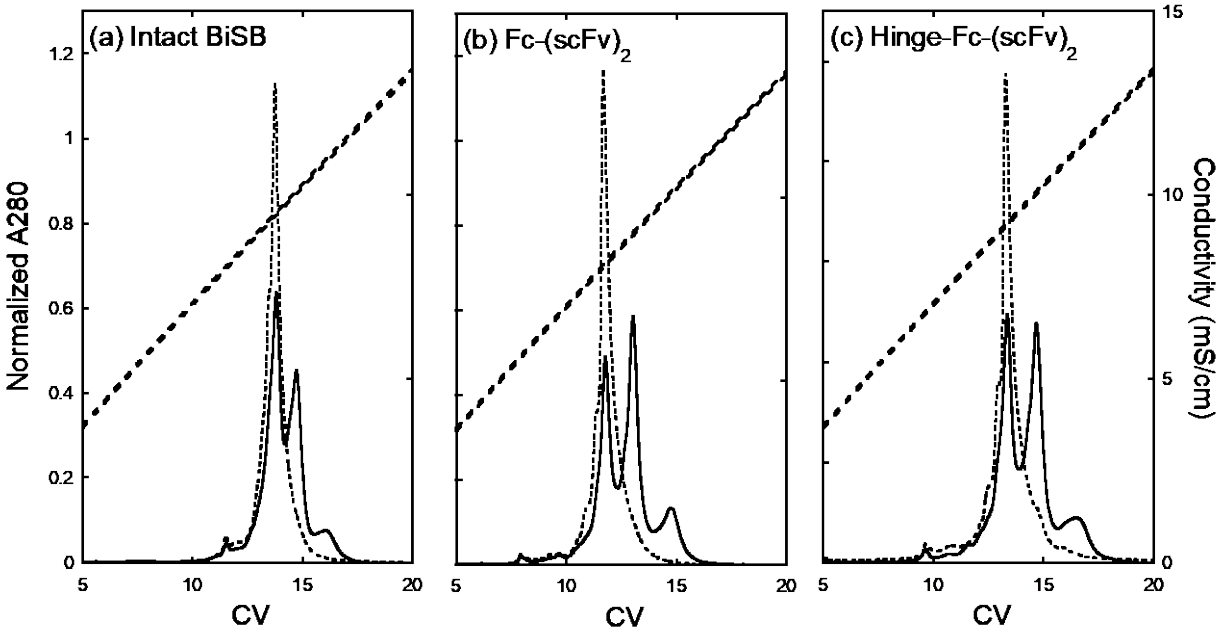

Figure 3.8. Comparison of the gradient elution behavior of intact BiSB (a) with that of BiSB fragments obtained by digestion with FabRICATOR (b) and FabALACTICA (c) enzymes on ProPac WCX-10 with a 0-125 mM NaCl 20 CV in 10 mM Na_2PO_4 at pH 7.0 at flow rates of 1.0 ml/min (solid lines) and 0.05 ml/min (dashed lines) correspond to residence times of 1.25 and 25.1 min, respectively. The mass of protein injected was 0.075±0.01 mg/ml for enzyme clipped species and 0.12±0.03 mg/ml for intact BiSB. The A280 absorbance is normalized to obtain the same peak area in order to account for slight differences in the amount of protein injected. Note that in all three cases, three peaks are eluted at high flow rates in and a single merged peak is eluted at low flow rate.

Table 3.2. Conductivities at elution in mS/cm for each of the scFv-containing fragments of BiSA and BiSB during gradient elution on the ProPac column with a 20 CV, 0-125 mM NaCl gradient.

	High flow rate (1.0/ml/min)			Low flow rate (0.05 ml/min)
	Peak 1	Peak 2	Peak 3	Merged peak
BiSA species				
Intact	7.1	8.0	9.1	7.3
$(Fab\text{-}scFv)_2$	6.8	7.6	8.6	6.6
Fab-scFv	5.0	6.2	-	5.1
BiSB species				
Intact	9.5	10.0	11.0	9.5
$Fc\text{-}(scFv)_2$	8.2	9.0	10.1	8.2
$Hinge\text{-}Fc\text{-}(scFv)_2$	9.2	10.0	11.0	9.2

In order to gain insight about the possible roles of electrostatics and hydrophobicity on inter-domain and protein-surface interactions, we studied the effects of mobile phase composition and chromatographic surface properties on the elution behavior of BiSA. With the goal of understanding the relationship between protein surface properties and chromatographic behavior, we also carried out a homology modeling to study as described in Section 3.2.2. We limited this modeling to the Fab and Fc regions of the framework IgG and to the scFv domains. In BiSA, the scFv domains are linked to the N-terminus of the heavy chains in the Fab region. In BiSB, the scFv domains are linked to the C-terminus of the heavy chain in the Fc region. The net charge at pH 7 was also calculated for each of the relevant domains based on the sequence. For BiSA, the net charge at this pH is -1 for each Fab region of the framework IgG, +6 for the full Fc region, and +6 for each scFv domain. BiSB has a homologous sequence compared to BiSA therefore the differences in charge are only due to the scFvs linked to the C-termini. Thus, the Fc region of BiSB loses both heavy chain C-termini charge and becomes +8 while each Fab arm gains an N-terminus causing this domain to be net neutral, and each scFv becomes +4. The overall net charge of both BiSAb molecules is +16.

Figure 3.9 and 3.10 show different views (rotated 90^{o} apart from each other as indicated by the arrows) of the secondary structure, of the electrostatic potential, and of the residues hydrophobicity for the Fab region and the scFv, respectively. As seen in these images, in both cases the charge residues are generally heterogeneously distributed. However, a patch of strong positive potential is clearly evident on the face of the scFv domain opposite to where it is linked to the Fab domain (see middle row image in view B in Fig. 3.10). It is likely that this part of the scFv domain interacts most strongly with the negatively charged chromatographic surface. The distribution of hydrophobic residues on the surface of each domain also shows patches of hydrophobicity on the

surfaces of both the Fab and the scFv domain and it is likely that these regions are responsible for both inter-domain hydrophobic interactions and for interactions between the protein and the chromatographic surface.

The distribution of tryptophan residues is of particular interest not only because of its high hydrophobicity, but also because of its fluorescence properties that depend on solvent exposure. Although both the Fab and the scFv contain tryptophan residues (5 in the Fab and 7 in the scFv), as seen in Figs. 3.9 and 3.10, only one of these Fab tryptophan residues appears to be surface exposed (see view B in Fig. 3.9), while 4 of these residues appear to have significant surface exposure in the scFv domain. Notably, two of these residues are close to the most positively charged patch on the scFv surface (see views A and B of Fig. 3.10), while the other two are close to a negatively charged region of the scFv domain. This region is, of course, fairly hydrophobic and may be able to interact strongly with the Fab, particularly the side shown in view B of Fig. 3.10, which appears to have the most hydrophobic character.

Figure 3.11 shows the Fc domain properties. A patch of positive charge capable of interacting strongly with the negatively charged chromatographic surface appears on the bottom side (view C, also visible on and side views A and B) along with a mostly uncharged hydrophobic region shown on the side view (view B). For BiSA, these regions are unlikely to interact with the scFv domains. On the other hand, hydrophobic interactions with the hydrophobic areas of the scFv domains are also obviously possible in BiSB since in the case, these domains are linked at the C-termini of the heavy chains, shown in cyan in Fig. 3.11. Interestingly, no surface exposed tryptophan residues appear in the Fc region. Overall, we conclude that surface molecular properties derived from these images support the idea that the interaction of both BiSA and BiSB with the chromatographic surface depends on a balance of electrostatic and hydrophobic interactions with

the chromatographic surface and of hydrophobic interactions between the Fab and scFv domains. In the case of BiSA, protein-resin interactions are likely to be dominated by the Fab-scFv region, while for BiSB, protein-resin interactions are likely dominated by the Fc-scFv region. For BiSB, electrostatic interactions with the resin surface are stronger likely because the positive charge associated with the scFv domain is supplemented by the positive charge associated with the tip of the Fc-region. Both of these observations are supported by the experimental behaviors of the respective BiSAb fragments.

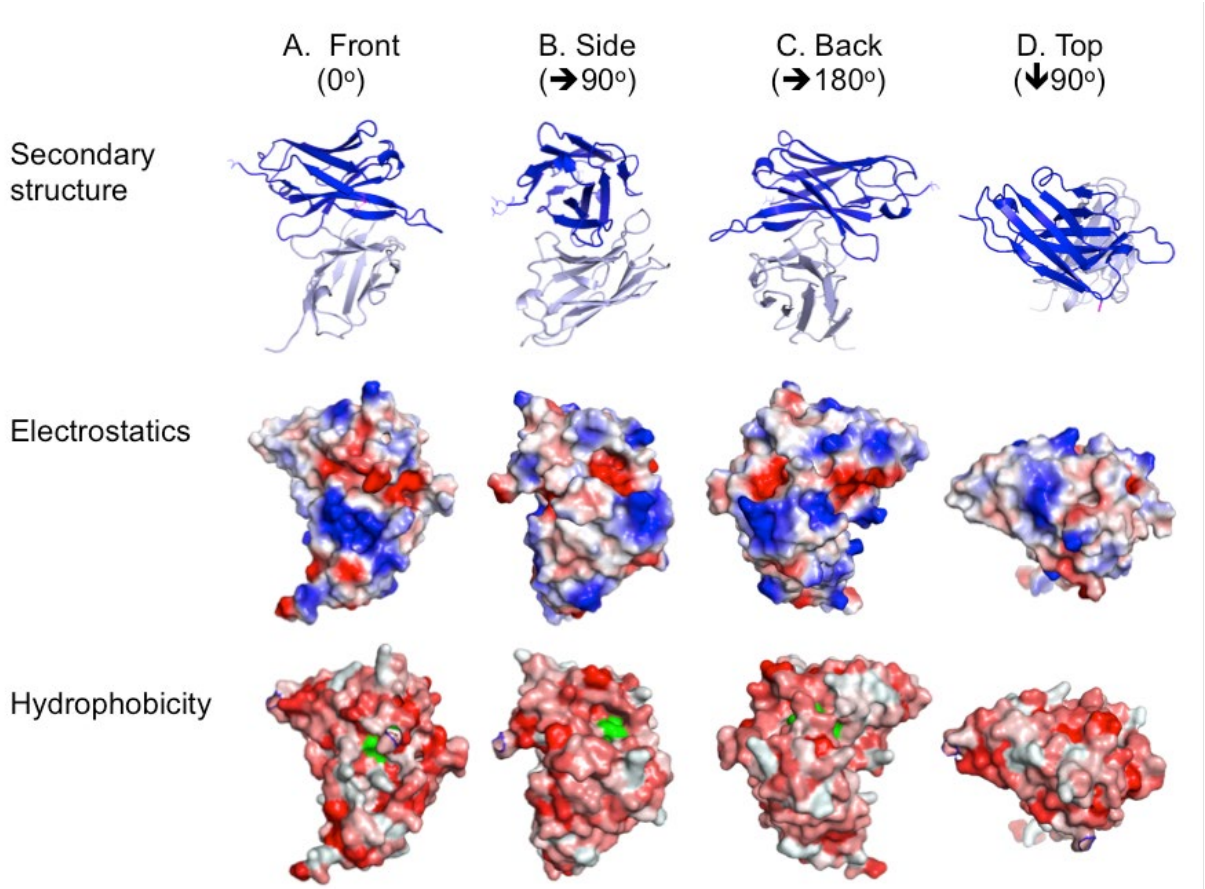

Figure 3.9. 3-D views of the Fab region of the framework IgG in BiSA and BiSB generated by homology modeling and rendered in PyMol. Top row: heavy chain in blue, light chain in light blue. Middle row: surface electrostatic potential showing positive areas in blue and negative areas in red. Bottom row is colored according to ref. [16], where darker red depicts residues with greater hydrophobicity. Tryptophan residues in green. N-terminus of heavy chain in magenta.

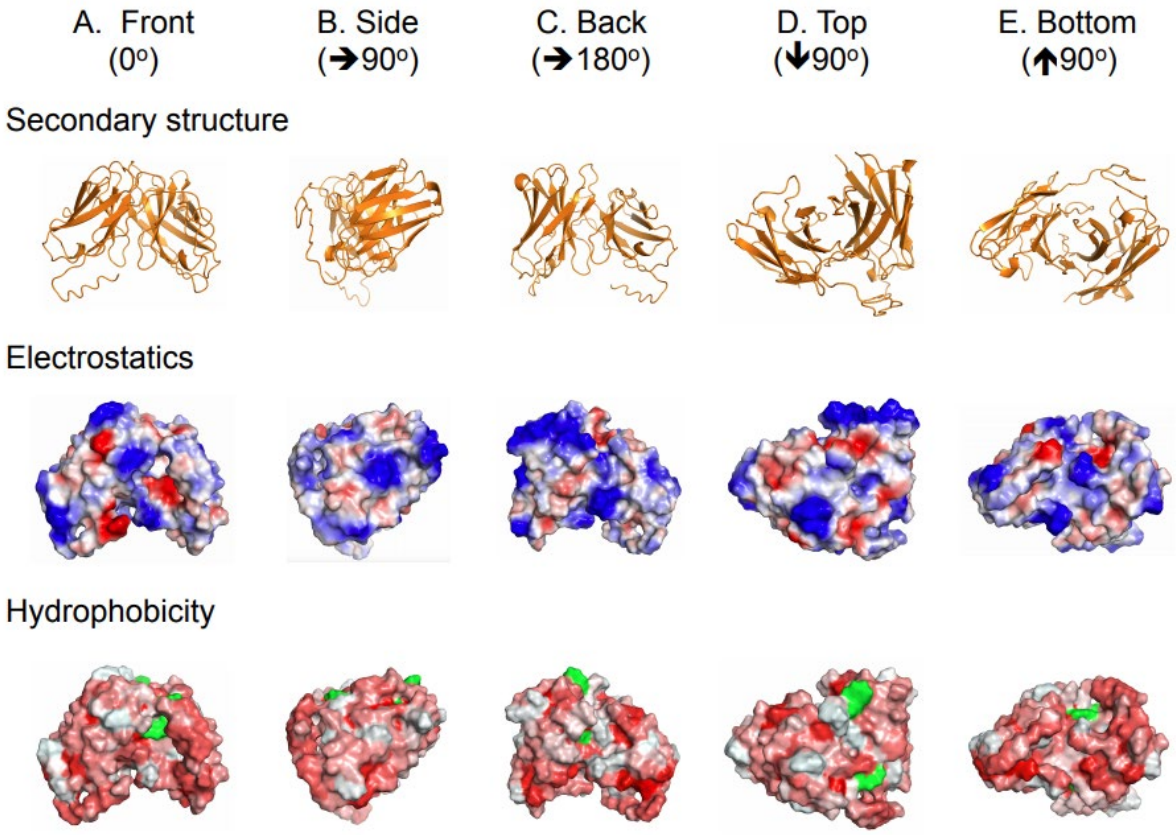

Figure 3.10. 3-D views of the scFv domain generated by homology modeling and rendered in PyMol. Top row: secondary structure shown in orange. Middle row: surface electrostatic potential showing positive areas in blue and negative areas in red. Bottom row is colored according to ref. [16], where darker red depicts residues with greater hydrophobicity. Tryptophan residues in green. C-terminus in cyan. The unstructured, flexible linker is seen in the bottom right of the molecule in front view, panel A.

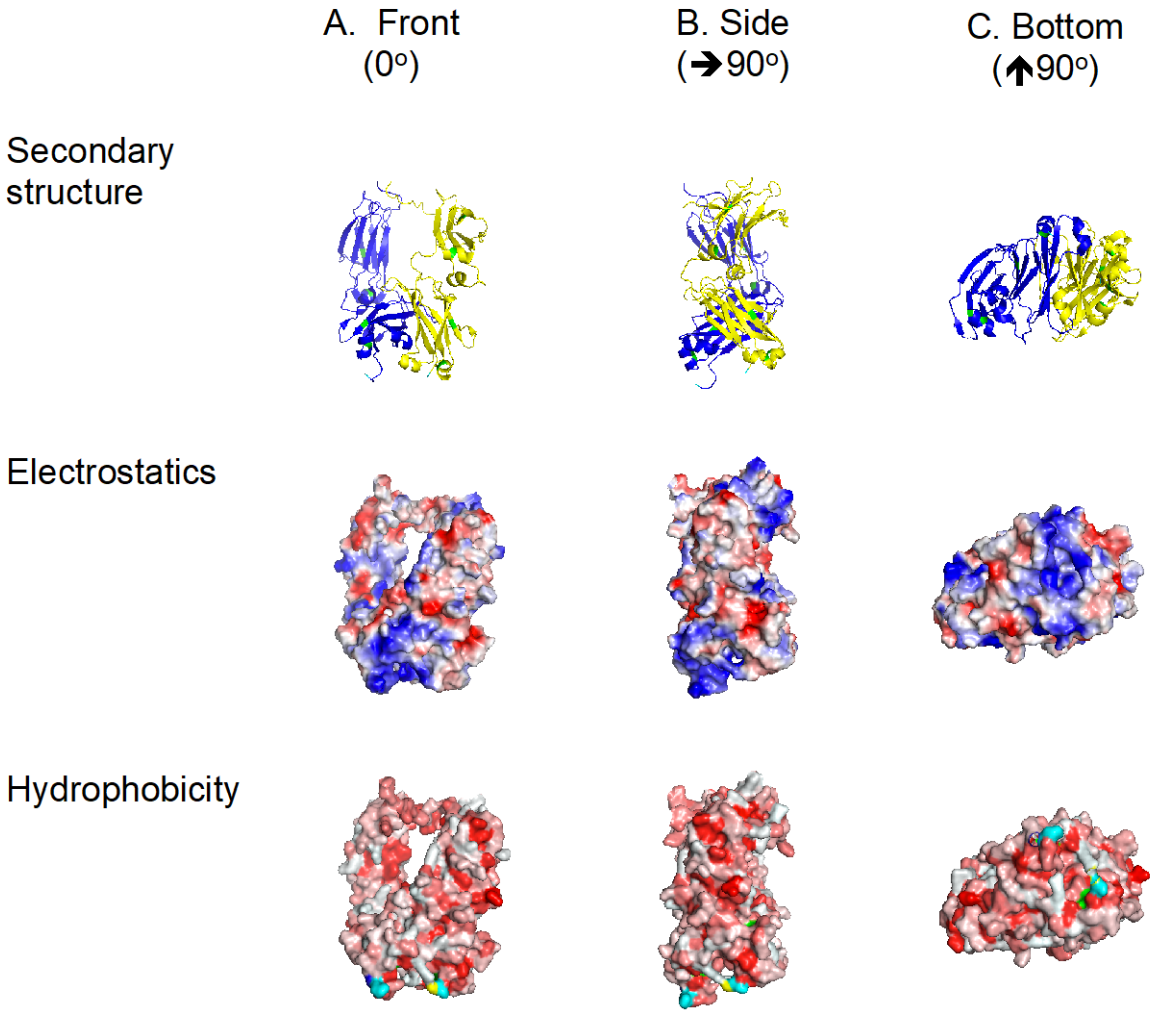

Figure 3.11. 3-D views of the Fc region of the framework IgG in BiSA and BiSB generated by homology modeling and rendered in PyMol. Top row: heavy chains in blue and yellow. Middle row: surface electrostatic potential showing positive areas in blue and negative areas in red. Bottom row is colored according to ref. [16], where darker red depicts residues with greater hydrophobicity. Tryptophan residues in green. C-termini of the heavy chain in cyan.

Unfortunately, it is not possible to test the observations above based on homology modeling directly through exactly independent chromatographic measurements since varying one chromatographic condition (i.e. the mobile phase composition) can simultaneously affect both inter-domain and protein-surface interactions. Nevertheless, such measurement can still provide further insight. First is the effect of Na+ concentration during the load step, which is expected to weaken the electrostatic interaction between protein and resin surface. Figure 3.12 compares the BiSA elution profiles obtained with and without the addition of 15 mM NaCl to the load buffer (bringing the total Na+ concentration to 35 mM) with the Source column. As seen in this figure, the main effect of the higher Na+ concentration is to reduce the magnitude of the more retained peaks observed at the high flow rate while leaving the conductivity at elution virtually unchanged. This result suggests that stronger electrostatic interactions during the initial binding to the resin favor the formation of species associated with the late eluting peaks. At the low flow rate of 0.1 ml/min, the elution profiles are nearly identical for both Na+ concentrations showing a merged peak eluting at comparable conductivities, indicating similar rates of interconversion between species exist in both cases.

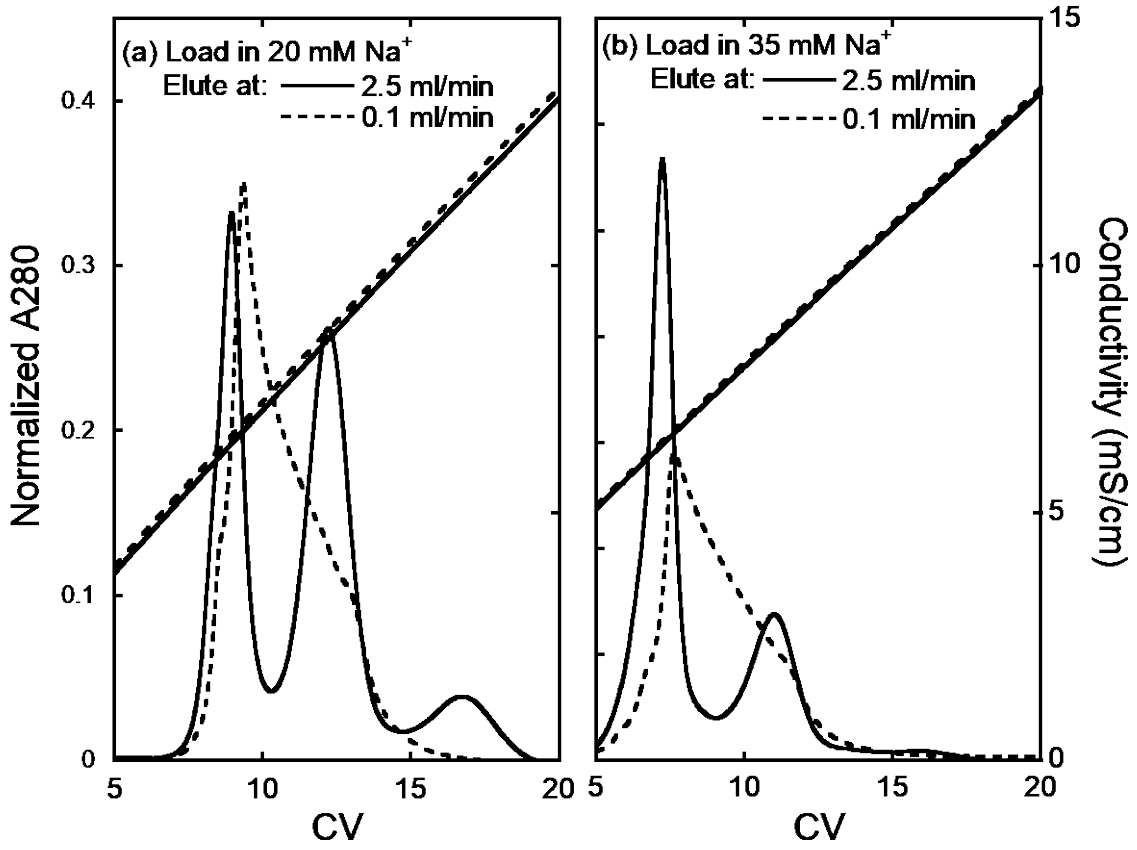

Figure 3.12. Effect sodium ion concentration in the load buffer on the elution behavior of BiSA on the Source column. (a) Load 10 mM Na_2HPO_4 at pH 7 and elute with a 0-125 mM NaCl gradient in 20 CV. (b) Load in 10 mM Na_2HPO_4 at pH 7 with 15 mM NaCl and elute with a 15-125 mM NaCl in 20 CV. Flow rate of 2.5 and 0.1 ml/min correspond to 0.75 and 18.7 min residence times. Protein mass load was 0.22±0.1 mg/ml in (a) and 0.11±0.01 mg/ml in (b). The A280 absorbance is normalized to obtain the same peak area in order to account for differences in the amount of protein injected.

Second is the effect of the resin backbone hydrophobicity. Figure 3.13 compares the results obtained for BiSA using the SP Sepharose HP column with those obtained with the ProPac and Source columns for otherwise identical conditions. Although the three resins have different ligands (sulphopropyl, carboxylate, and methyl sulphonate, in Sepharose, ProPac, and Source, respectively), all three are negatively charged at pH 7 and are likely to exhibit comparable electrostatic interactions with the charged residues on the protein surface. On the other hand, while both ProPac and Source are based on hydrophobic polystyrene backbones, SP Sepharose HP is based on a very hydrophilic agarose backbone. Thus, substituting the Sepharose resin for either ProPac or Source is likely to influence mainly the protein-surface hydrophobic interactions. As seen in Fig. 3.13, the main effect of this substitution is to eliminate the multiple peak elution behavior, yielding a single peak eluting at a conductivity comparable to that observed for the earliest elution peak seen with the Source or ProPac columns. The hydrophobic backbone of Source and ProPac likely assists in stabilizing the out-stretched configurations corresponding to peaks 2 and 3.

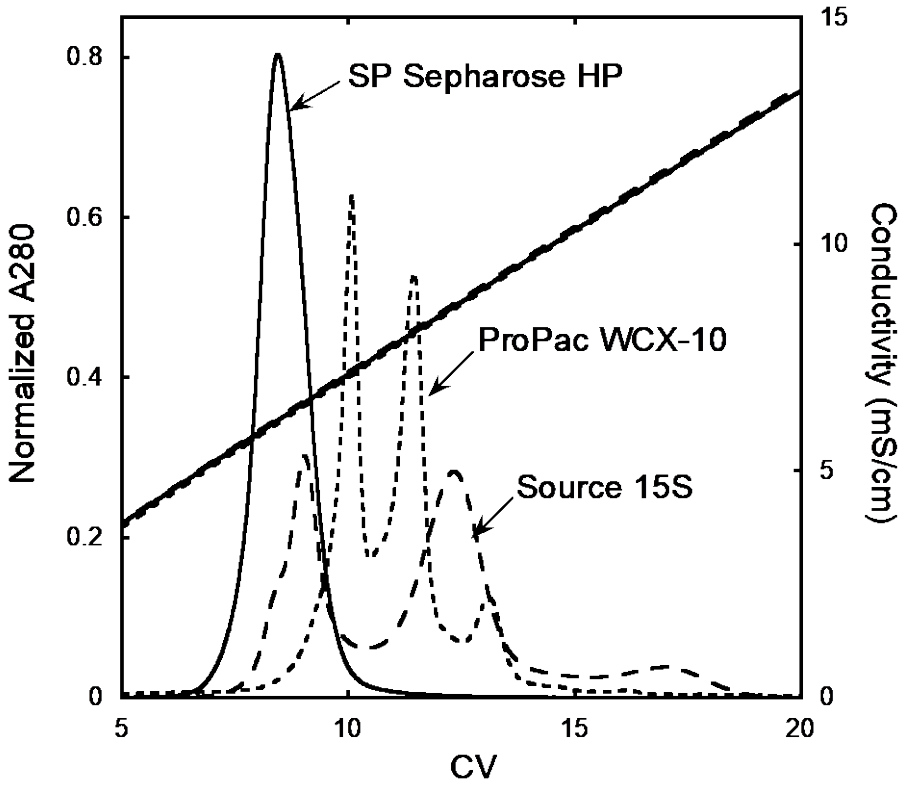

Figure 3.13. Elution behavior of BiSA on SP Sepharose HP, ProPac, and Source columns, loading in a 10 mM Na_2PO_4, pH 7.0 buffer and eluting with 0-125 mM NaCl gradient over 20 CV with a flow rate of 1.0 ml/min. The mass of protein injected was 0.22 mg/ml for SP Sepharose HP, 0.12 mg/ml for ProPac, and 0.22 mg/ml for Source. The A280 absorbance is normalized to obtain the same peak area in order to account for slight differences in the amount of protein injected.

The final result is obtained by measuring the tryptophan autofluorescence in-line for the eluted peaks. As shown, for example, in refs. [4], tryptophan autofluorescence in proteins depends in a complex way on folding as a result of varying degree of fluorescence quenching by adjacent amino acid residues and exposure to water. Since as shown in Fig. 3.10, the scFv domain contains several surface exposed tryptophan residues whose fluorescence spectra may be influenced by interactions with the framework Fab for BiSA or framework Fc region for BiSB, the autofluorescence spectra provides information on the configuration of the scFv domains relative to the framework IgG during elution. Figure 3.14 shows the results for BiSA on the ProPac column. As seen in this figure, the fluorescence spectra magnitude, normalized by concentration using the UV280 signal, increases with peak number. The ratio of fluorescence to UV280 normalized to peak 1 is overlayed on the chromatogram in open circles in Fig. 3.14b. A red shift in the emission wavelength peak maximum is observed from peak 1, to peak 2, and to peak 3, which indicates increasing solvent exposure from the early to the late eluting peaks. The red shift from peak 1 emission wavelength maxima is plotted as closed circles overlaying the chromatogram in Fig. 3.14b. Since the surface tryptophan residues in BiSA are primarily associated with the scFv domain (see Fig. 3.9-3.11), this result suggests that collapsed scFvs interacting with the framework mAb decreases solvent exposure and correspond to peak 1 while a single or pair of out-stretched scFvs correspond to peak 2 and 3 respectively.

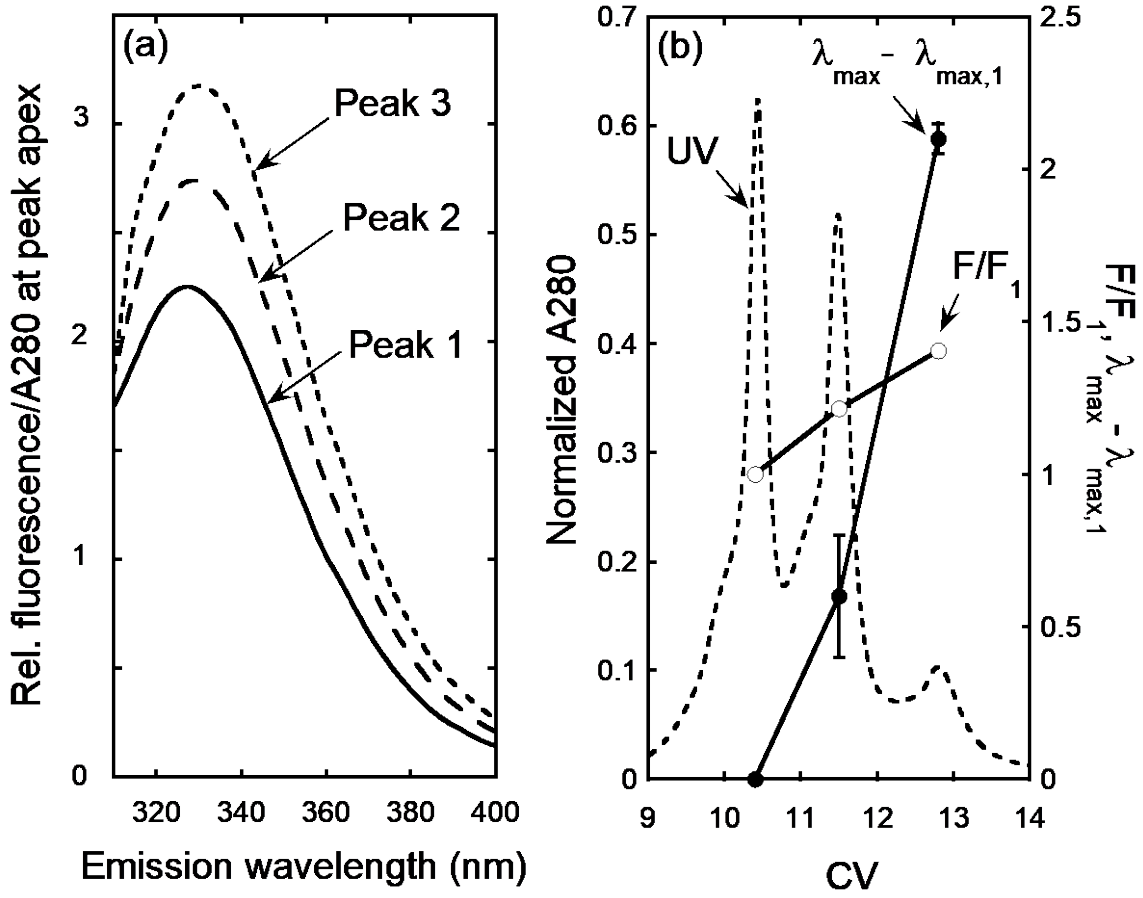

Figure 3.14. Tryptophan autofluorescence measurements with excitation at 295 nm and emission collection at 310-400 nm for BiSA on the ProPac column showing (a) the emission spectra at the peak apex normalized by the corresponding A280 and (b) the maximum fluorescence intensity normalized by F/A280 for peak 1and the wavelength shift of the emission maximum relative to peak 1 overlaid to the UV-based chromatogram. Load was in 10 mM Na_2PO_4, pH 7.0, and elution with a 0-125 mM NaCl gradient over 20 CVs at 1.0 ml/min (1.25 min residence time). The protein mass load was 0.04 mg/ml.

3.4 References

[1] L.K. Kimerer, T.M. Pabst, A.K. Hunter, G. Carta, Chromatographic behavior of bivalent bispecific antibodies on cation exchange columns. II. Biomolecular perspectives, J. Chromatogr. A. 1601 (2019) 133–144.

[2] A. Digiandomenico, A.E. Keller, C. Gao, G.J. Rainey, P. Warrener, M.M. Camara, J. Bonnell, R. Fleming, B. Bezabeh, N. Dimasi, B.R. Sellman, J. Hilliard, C.M. Guenther, V. Datta, W. Zhao, C. Gao, X.-Q. Yu, J.A. Suzich, C.K. Stover, A multifunctional bispecific antibody protects against Pseudomonas aeruginosa, Sci. Transl. Med. 6 (2014) 1–12.

[3] R. Loewenthal, J. Sancho, A.R. Fersht, Fluorescence Spectrum of Barnase: Contributions of Three Tryptophan Residues and a Histidine-Related pH Dependence, Biochemistry. 30 (1991) 6775–6779.

[4] M. Weichel, S. Bassarab, P. Garidel, Probing Thermal Stability of MAbs By Intrinsic Tryptophan Fluorescence, Bioprocess Int. (2008) 42–52.

[5] T.E. Bankston, G. Carta, Apolipoprotein A-IMilano anion exchange chromatography: Self association and adsorption equilibrium, Biotechnol. J. 5 (2010) 1028–1039.

[6] G.E. Davies, G.R. Stark, Use of Dimethyl Suberimidate, a Cross-Linking Reagent, in Studying the Subunit Structure of Oligomeric Proteins, Proc. Natl. Acad. Sci. 66 (1970) 651–656.

[7] Y. An, Y. Zhang, H.M. Mueller, M. Shameem, X. Chen, A new tool for monoclonal antibody analysis Application of IdeS proteolysis in IgG domain-specific characterization, MAbs. (2014).

[8] C. Spoerry, P. Hessle, M.J. Lewis, L. Paton, J.M. Woof, U. Von Pawel-Rammingen, Novel IgG-degrading enzymes of the IgdE protease family link substrate specificity to host tropism of streptococcus species, PLoS One. 11 (2016) 1–20.

[9] A. Creasy, G. Barker, G. Carta, Systematic interpolation method predicts protein chromatographic elution with salt gradients, pH gradients and combined salt/pH gradients, Biotechnol. J. 12 (2017).

[10] P. Marcatili, A. Rosi, A. Tramontano, PIGS: automatic prediction of antibody structures, Bioinformatics. 24 (2008) 1953–1954.

[11] N. Guex, M.C. Peitsch, T. Schwede, Celebrating 30 years Automated comparative protein structure modeling with SWISS-MODEL and Swiss- PdbViewer: A historical perspective, Electrophoresis. 30 (2009) 162–173.

[12] P. Benkert, M. Biasini, T. Schwede, Toward the estimation of the absolute quality of individual protein structure models, Bioinformatics. 27 (2011) 343–350.

[13] Y. Zhang, I-TASSER server for protein 3D prediction, BMC Bioinformatics. 9 (2008).

[14] A. Roy, A. Kucukural, Y. Zhang, I-TASSER: a unified platform for automated protein structure and function prediction, Nat. Protoc. 5 (2010) 725–738.

[15] J. Yang, R. Yan, A. Roy, D. Xu, J. Poisson, Y. Zhang, The I-TASSER Suite: protein structure and function prediction, Nat. Methods. 12 (2015) 7–8.

[16] D. Eisenberg, E. Schwarz, M. Komaromy, R. Wall, Analysis of membrane and surface protein sequences with the hydrophobic moment plot, J. Mol. Biol. 179 (1984) 125–142.

4 Adsorption Kinetics

4.1 Introduction

This chapter studies the adsorption kinetics into cation exchange media for the series of bivalent bispecific antibodies (BiSAb), which have high quaternary structure flexibility allowing three binding configurations that interconvert and differ in binding strength. A monoclonal antibody (mAb) studied in refs. [1][2][3] which has a similarly favorable isotherm and similar molecular weight is also studied as the reference case. For the mAb, adsorption kinetics is controlled by pore diffusion and conforms to the classical shrinking core model. While the mAb adsorption rate increases with temperature, the ratio of effective and pore diffusivity, D_e/D_0, remains constant and has a value of 0.20. As a result of the configurational flexibility, adsorption of the BiSAbs show complex patterns of total bound protein within the particles. These BiSAb adsorption patterns are studied by varying buffer ionic strength, pH, temperature, and intramolecularly crosslinking the protein. Sharper intraparticle profiles are observed for conditions where the binding strength is greater (lower buffer concentration and/or pH) or when the protein is chemically crosslinked to restrict configurational flexibility. Temperature affects the BiSAb pore diffusivity as well as the interconversion kinetics. While the effects of temperature on BiSAb transport are also described by a constant $D_e/D_0 = 0.15$, the temperature also affects the rate of interconversion between binding forms leading to faster equilibration at higher temperatures. A phenomenological model is then developed informed by the mechanism of pore diffusion and adsorption with the kinetically limited interconversion between binding forms. The model is shown to be capable of predicting the experimental trends. This work was published as ref. [4].

4.2 Materials and Methods

The BiSAb and framework IgG samples are the same as those used throughout this work. The reference monoclonal antibody (mAb) is well studied and is the same as the molecule as that used in refs. [1][2][3][5]. The mAb has molecular weight ~150 kDa and a pI from isoelectric focusing of 8.5 [1]. The corresponding solution diffusivities for the molecules, D_0, at 21°C based on the Stokes-Einstein equation are $(3.6\pm0.2)\times10^{-7}$ cm^2/s for the BiSAb molecules and $(4.0\pm0.2)\times10^{-7}$ cm^2/s for the framework IgG and reference mAb.

The resin used in this work, Nuvia HR-S, was obtained from Bio-Rad Laboratories (Hercules, CA, USA) and is based on macroporous, vinyl-acrylamido copolymer beads functionalized with sulfopropyl groups with a charge density 132 μmol/ml [1]. As reported previously, the resin has a narrow particle size distribution with volume-average diameter of 50 μm, a total intraparticle porosity $\varepsilon_p = 0.78\pm0.01$, and an average pore diameter of approximately 120 nm [3]. Buffers were prepared by dissolving weighed amounts of sodium phosphate or sodium acetate salts in deionized, distilled water followed by drop-wise addition of either phosphoric or acetic acid to obtain the desired pH. Thus, buffer concentrations are reported in terms of the corresponding Na+ concentration. Chemicals used in buffer preparation were purchased from ThermoFisher Scientific (Waltham, MA, USA) and MilliporeSigma (St. Louis, MO, USA). The amine-reactive fluorescent dyes Rhodamine Red-X and Rhodamine Green-X used to label the proteins for CLSM were purchased from ThermoFisher Scientific (Waltham, MA, USA). The chemical crosslinker dimethyl suberimidate was purchased from MilliporeSigma (St. Louis, MO, USA).

Adsorption isotherms were obtained at room temperature (21 °C) from batch measurements where samples of protein solutions, dialyzed into the desired buffer, were equilibrated for 24 h with resin samples in 1.5 ml tubes rotated end-over-end at a few rpm. The resin samples used were pre-

equilibrated with the same buffer and filtered prior to addition to the protein solution to remove excess buffer using Costar Spin-X centrifuge filter tubes (Corning, NY, USA) with a Minispin centrifuge (Eppendorf, Hamburg, Germany) at 5000 RPM for 20 min. After equilibration, protein concentration in the supernatant was measured using a NanoDrop 2000 UV-Vis spectrophotometer (ThermoFisher Scientific) and used to calculate the bound protein concentration by mass balance. Binding capacities were expressed as mg of bound protein per ml of resin bead using the hydrated resin bead density of 1.076 g/ml [3].

The adsorption kinetics was studied by confocal laser scanning microscopy (CLSM) following the methods described in [6][7][1][8]. For this purpose, the protein samples were labeled with either Rhodamine Red-X or Rhodamine Green-X amine-reactive dyes (ThermoFisher Scientific, CITY, STATE, USA) using a 3 mol protein to 1 mol dye ratio for 1 hr in 500 mM $NaHCO_3$ at pH 8.5. Econopac DG-10 (Bio-Rad Laboratories, Hercules, CA, USA) desalting columns were used to remove the unreacted dye. The resulting labeling ratios, determined using the NanoDrop 2000 UV-Vis spectrophotometer, were 23% for BiSA, 21% for BiSB, 15% for BiSC, and 28 % for the reference mAb. For the actual CLSM experiment, each labeled protein stock was diluted with the corresponding unlabeled protein to obtain a final labeling ratio of 1 labeled protein to 160 unmodified protein molecules. Potential effects of labeling on protein binding were checked by comparing the gradient elution behavior of the labeled protein with that of the unmodified protein both on a Nuvia HR-S column on a ProPac WCX-10 column obtained from Dionex Corporation (Sunnyvale, CA, USA). As shown for BiSA in Fig. 4.1, nearly identical elution peaks were obtained for both labeled and non-labeled protein on both columns confirming that labeling did not significantly alter the binding and elution behavior. We also tested the effects of switching the

dyes on the CLSM-based bound protein concentration profiles. As shown for BiSA in Fig. 4.2, essentially identical profiles were obtained regardless of which dye was used.

For the actual CLSM measurements, small resin samples equilibrated in the desired buffer and filtered as described above were added to a tube containing 7 ml of the protein sample and mixed on a rotator at a few rpm for room temperature experiments. For experiments at nonambient conditions, 1.5 ml of protein sample was added to 1.5 ml tubes and mixed in a Multitherm thermostatted shaker (Benchmark Scientific, Sayrevill, NJ, USA) with controlled temperature set at 8, 40, or 55 °C. The amount of resin added (~1 mg) was small enough to ensure that there would be less than a 10% change in protein concentration as a result of adsorption. At periodic times, a small portion of the suspension was pipetted out, rapidly filtered, and resuspended in a 20 mM sodium acetate buffer at pH 5 containing 50% (w/w) sucrose for refractive index matching [9]. Since the binding strength at pH 5 is higher than at the pH used for the measurement, the protein within the particle is essentially immobilized. CLSM imaging was done with a Zeiss LSM 510 microscope (Carl Zeiss MicroImaging, Thornwood, NY, USA) using a 63x oil-immersion objective.

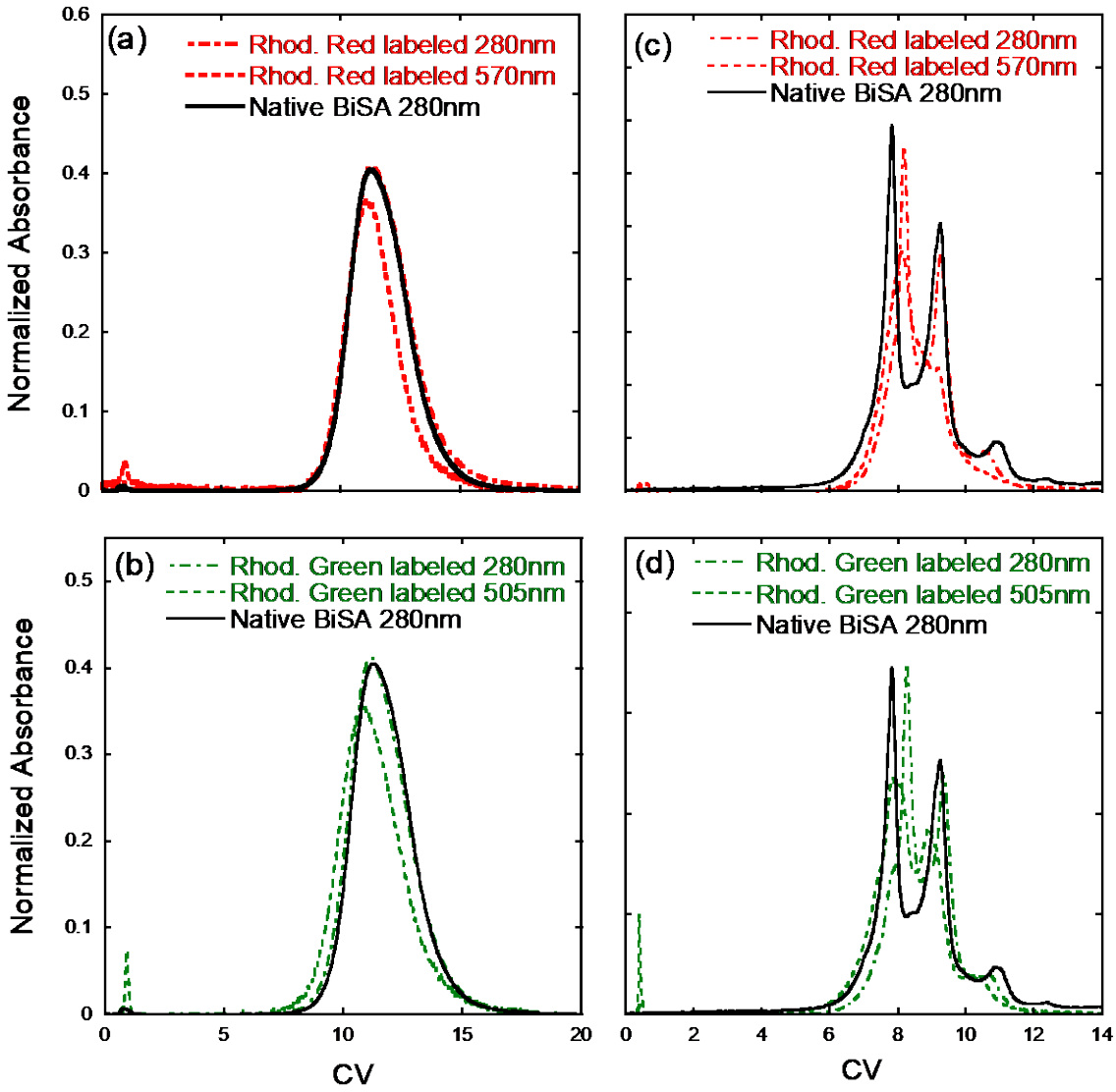

Figure 4.1. Linear gradient elution of native and Rhodamine labeled BiSA with a 20 CV gradient from 0-125 mM NaCl in a 20 mM sodium phosphate buffer at pH 7. (a) and (b) show the results for a 0.5x14.9 cm Nuvia HR-S column at 2.0 ml/min. (c) and (d) show the results for a 0.4x10 cm ProPac WCX-10 column at 0.5 ml/min. Absorbance is normalized based on peak area and measured at 280 nm for total protein and at the absorbance maximum for each label (570 nm for Rhodamine Red-X and 505 nm for Rhodamine Green-X).

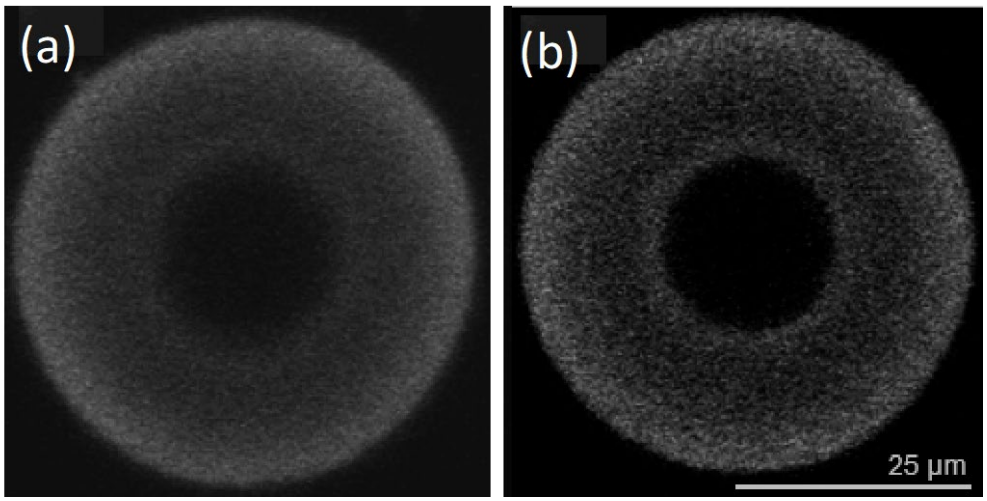

Figure 4.2. CLSM images after adsorption for 10 min of 2 mg/ml of BiSA in a pH 7 buffer containing 20 mM Na+. BiSA is labeled with Rhodamine Red-X in (a) and Rhodamine Green-X in (b). The image brightness was adjusted to compensate for different laser intensities used in the two runs.

Crosslinking with dimethyl suberimidate (DMS) was done as described in section 3.2.1 except with BiSA that had been labeled with Rhodamine Red-X and prepared in the ratio of 1 labeled protein to 160 unmodified proteins.

4.3 Experimental Results

The experimental measurements encompass a range of proteins, buffer concentration and pH, protein concentration, and temperature. In all cases, the buffer concentration is reported in terms of the Na^+ to facilitate comparisons. Unless otherwise indicated, the experimental results are at room temperature, 21±2 ºC. Figure 4.3 shows the adsorption isotherms obtained for the BiSAb molecules, the framework IgG, and the reference mAb in 20 mM sodium phosphate buffer at pH 7 (Fig. 4.3a) and for BiSA in different combinations of buffer concentration and pH (Fig. 4.3b). The Langmuir isotherm model:

$$q = \frac{q_m K_L C}{1 + K_L C} \tag{4.1}$$

was used for an empirical description of the data. In this equation, q is the bound protein concentration, C is the concentration of protein in solution, q_m is the maximum binding capacity, and K_L is the Langmuir equilibrium constant. The regressed parameter values are given in Table 4.1 and calculated lines are shown in Fig. 4.3. These parameters do not account for the existence of multiple binding configurations. Thus, for the BiSAb molecules, they should be regarded as averages. As seen from Fig. 4.3a and from the fitted K_L values, the overall protein binding is very favorable for all these conditions. Binding capacities on a mass basis are somewhat higher for the BiSAbs compared to the framework IgG but lower than the capacity for the reference mAb at this pH. Surface property maps for the BiSAb domains were shown in Fig. 3.9-3.11. The scFv and the C-terminus of the Fc domain were found to have patches of highly positive charge, which interact

strongly with the negatively charged cation exchange surface and results in greater binding strength compared to the framework IgG. The location of the scFvs also appears to affect the binding strength, with BiSA and BiSB exhibiting somewhat higher binding capacity and binding strength (i.e., higher K_L) compared to BiSC. As seen in Fig. 4.3b, the effect of pH and buffer concentration on the BiSA isotherms is consistent with typical cation exchange behavior, with binding becoming stronger at lower pH, where the positive protein charge becomes higher, and at lower buffer concentration, where attractive electrostatic interactions are more favorable.

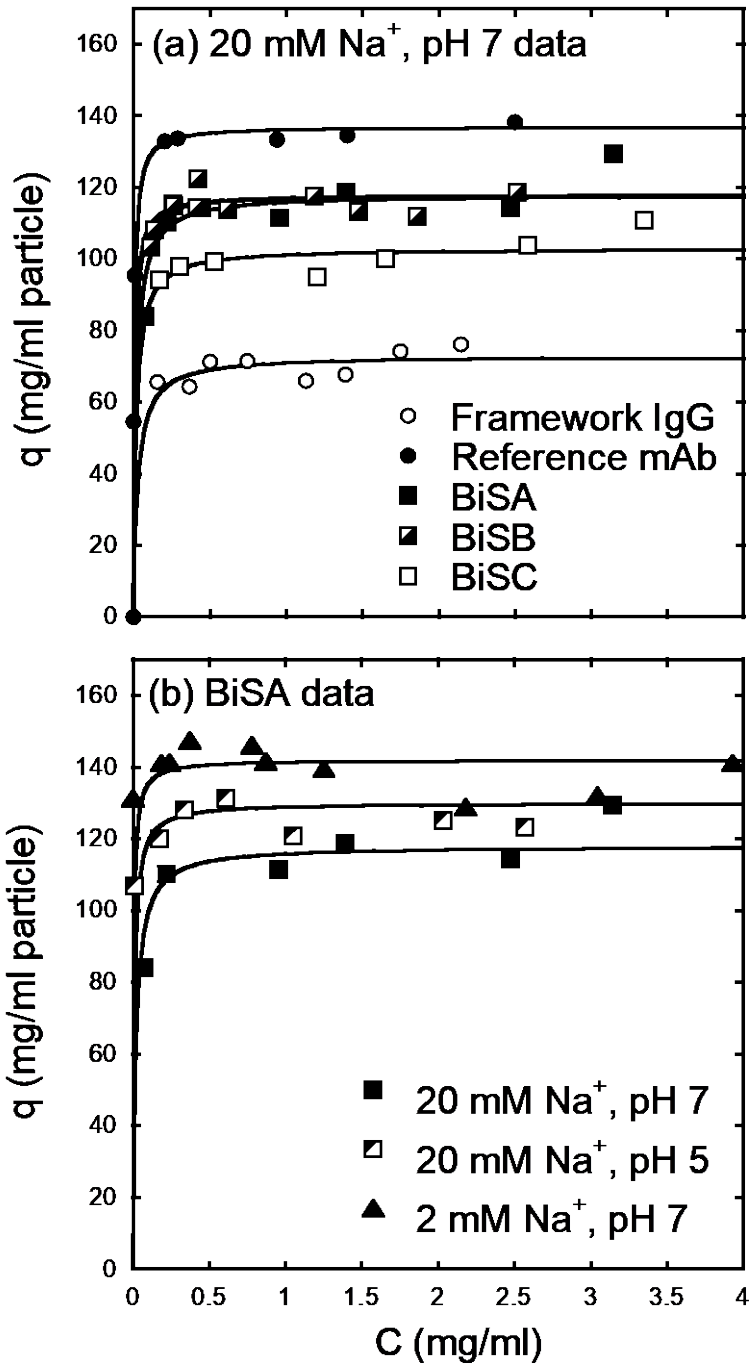

Figure 4.3. Adsorption isotherms determined after 24 h of contact time in (a) pH 7 buffer containing 20 mM Na^+ buffer and (b) pH 7 and pH 5 buffers containing 20 mM Na^+ and a pH 7 buffer containing 2 mM Na^+. The reference mAb data in (a) are from ref. [1].

Table 4.1. Langmuir isotherm model parameters (21 °C).

Protein	Buffer	q_m (mg/ml)	K_L (ml/mg)
Framework IgG	20 mM Na^+, pH 7	73	35
Reference mAb	20 mM Na^+, pH 7	137	145
BiSA	20 mM Na^+, pH 7	118	53
	2 mM Na^+, pH 7	142	200
	20 mM Na^+, pH 5	130	130
BiSB	20 mM Na^+, pH 7	119	130
BiSC	20 mM Na^+, pH 7	103	54

Figure 4.4 shows representative CLSM images for the adsorption of the reference mAb and of the three BiSAb molecules, all in the pH 7 buffer containing 20 mM Na^+. As seen in these images, the reference mAb shows a distinctly sharp adsorption front, consistent with the typical shrinking core behavior expected for pore diffusion with a rectangular isotherm [10][11][12][13]. This front reaches the center of the particle in about 20 min with no further change afterwards, indicating that equilibrium is established. In contrast, each of the BiSAb molecules results in a more complex pattern of bound protein. For short times, there is a smooth transition from a higher bound protein concentration near the edge of the particle to a sharp front toward the center of the particle, where the bound protein concentration drops to zero. The patterns remain smooth even after this front reaches the center of the particles and it is only at 24 h that we see a uniform distribution of bound protein in the resin.

Figure 4.5 compares the CLSM results for the adsorption of BiSA in the pH 7 buffer containing 20 mM Na^+ at protein concentrations of 0.2 and 4 mg/ml. The images included in this figure are shown at times that scale in inverse proportion to the protein concentration; i.e., at 20 and 40 min for the 0.2 mg/ml concentration and at 1 and 2 min for the 4 mg/ml concentration. As seen in this figure, the bound protein profiles are essentially the same at each set of proportionally spaced times. Similar results (not shown for brevity), showing essentially identical profiles at times spaced in inverse proportion to the protein concentration, were obtained when comparing images at 1 and 2 mg/ml BiSA concentrations with those obtained and 0.2 and 4 mg/ml. This result confirms that pore diffusion, whose rate is expected to be directly proportional to the protein concentration in solution, is the dominant transport mechanism.

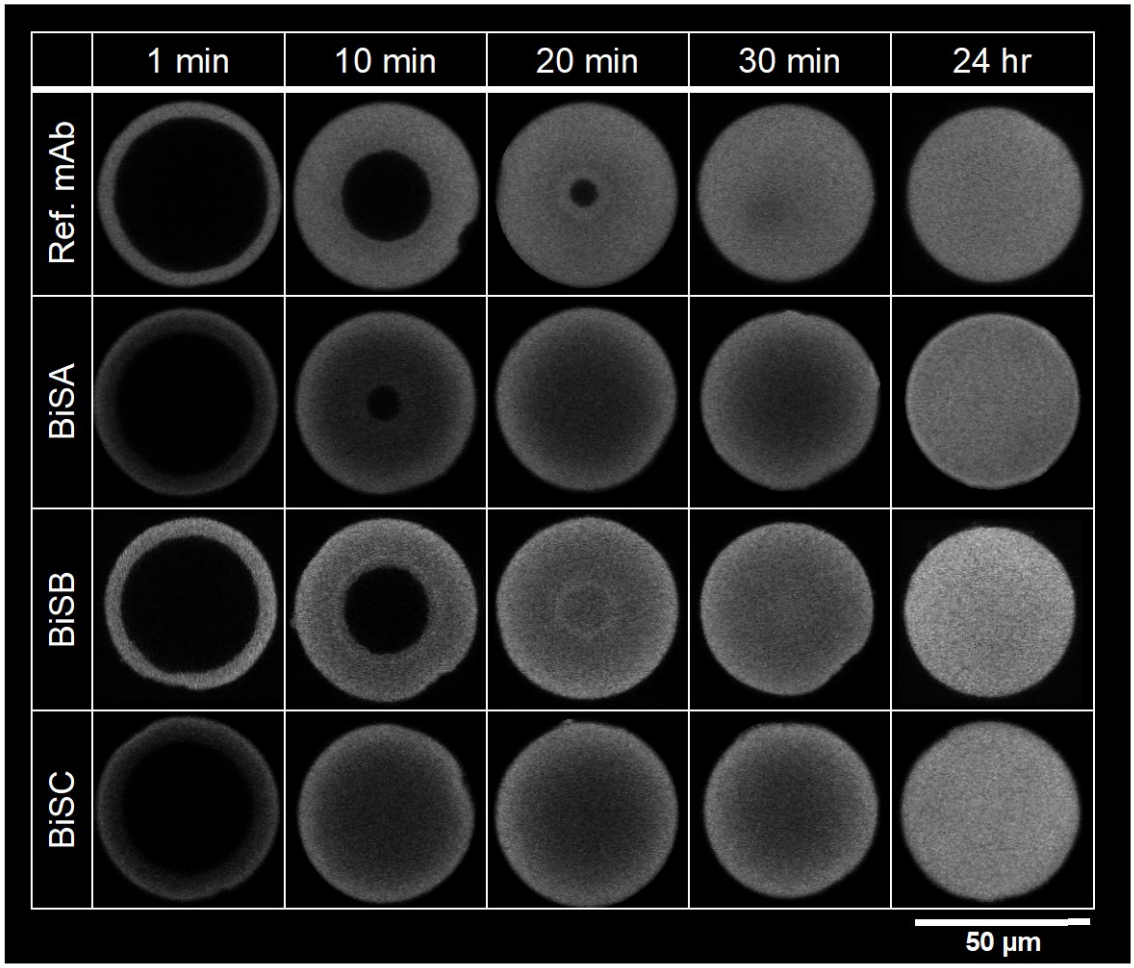

Figure 4.4. CLSM images of the adsorption of the reference mAb (top row), BiSA (second row), BiSB (third row), and BiSC (bottom row) in pH 7 buffers containing 20 mM Na^+. The protein concentration was 2 mg/ml in all four cases.

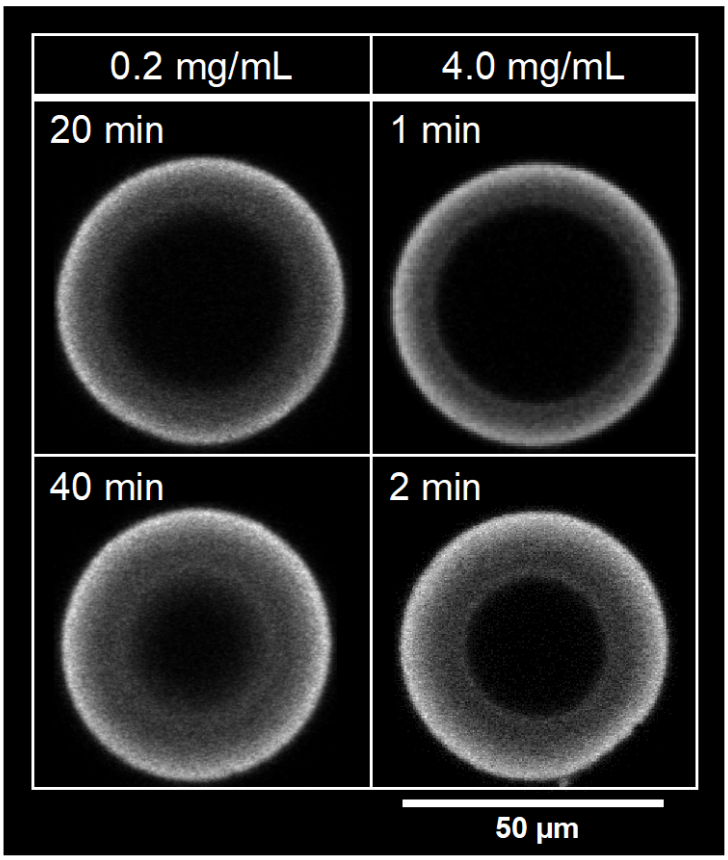

Figure 4.5. CLSM images showing the effect of protein concentration on BiSA adsorption in pH 7 buffers containing 20 mM Na+. The images are shown at times scaled in inverse proportion to the protein concentration (20 and 40 min for the 0.2 mg/ml run and 1 and 2 min for the 4 mg/ml run). The image brightness was adjusted to compensate for different laser intensities used in the two runs.

Figure 4.6 shows the CLSM profiles obtained for the reference mAb and for BiSA at 8 °C (top two rows) and 55 °C (bottom two rows) in the pH 7 buffer containing 20 mM Na^+. As seen in these images, for the reference mAb, the only significant effect of temperature is to speed up the movement of the adsorption front. This behavior is expected for pore diffusion, since a higher temperature results in a higher diffusivity of the protein and, thus, in a faster adsorption kinetics. In contrast, for BiSA, not only are the rates affected by temperature, but also the evolution of the bound protein concentration profiles after the leading front reaches the particle center. For example, as seen in this figure, the BiSA front reached the bead center in a little over 20 min at 8 ºC but in less than 10 min at 55 ºC. However, it took more than 270 min to reach a uniform bound protein profile at 8 ºC but only between 20 min and 60 min to achieve the same uniformity at 55 ºC. This result indicating that not only diffusion is affected, but that other factors influencing the adsorption kinetics, such as the exchange of multiple binding configurations, are also affected. Analogous results, not shown for brevity, intermediate between those shown in Fig. 4.6, were obtained at 21 and 40 ºC.

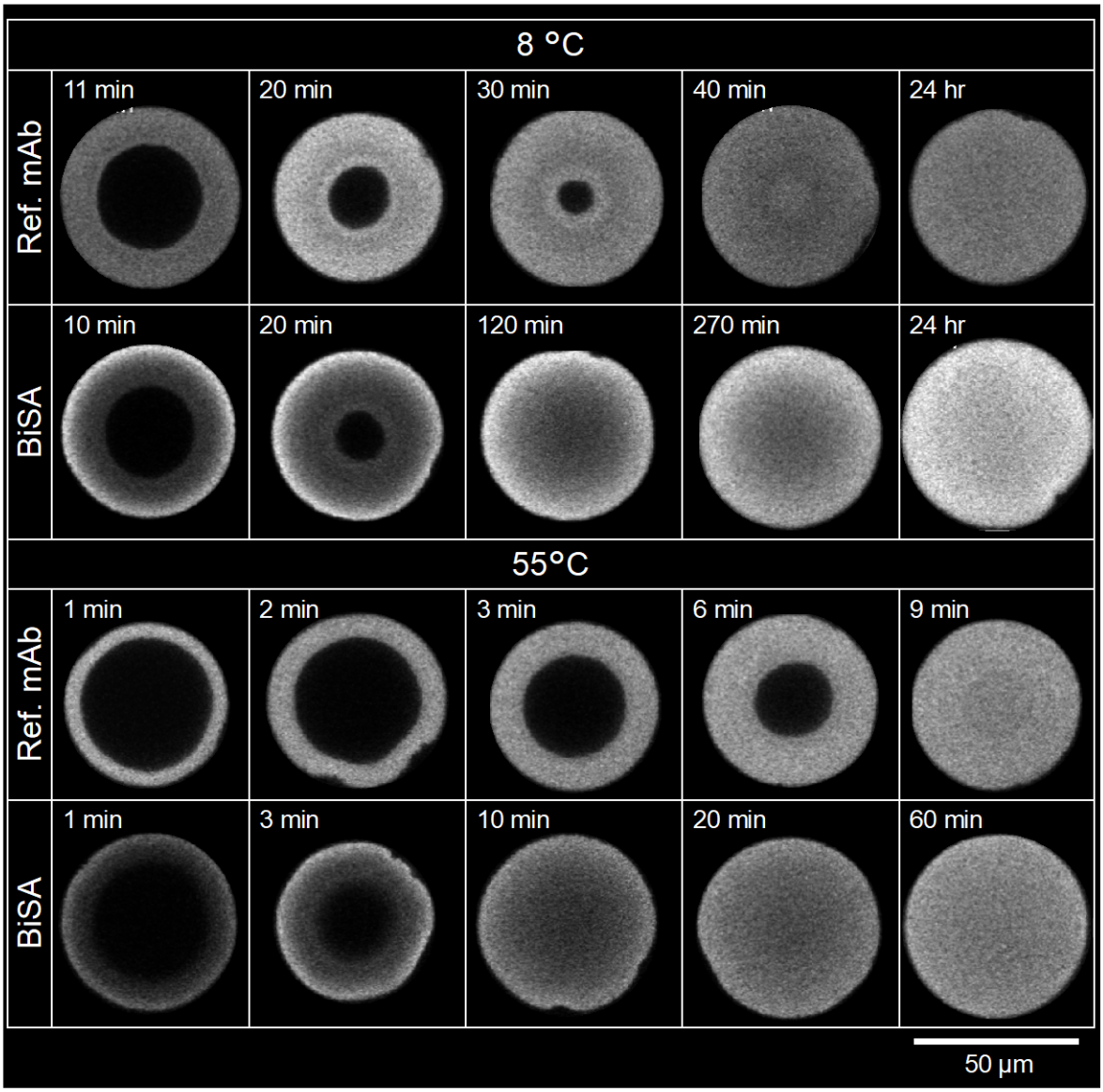

Figure 4.6. CLSM images showing the effect of temperature on the adsorption of reference mAb and of BiSA adsorption in pH 7 buffers containing 20 mM Na^{+}. The protein concentration was 1.0±0.1 mg/ml. Additional experiments conducted at 21 and 40 ºC, but not shown for brevity, yielded results consistent with the trends observed at 8 and 55 ºC.

Figure 4.7 shows the CLSM bound protein profiles for the adsorption of 2 mg/ml BiSA in the pH 7 buffer containing 2 mM Na^+ (top row) and in the pH 5 buffer containing 20 mM Na^+ (middle row). As seen in Fig. 4.3b, both of these buffers lead to stronger binding of BiSA. From Fig. 4.7, it is evident that both of these conditions also lead to sharp adsorption fronts again in apparent agreement with typical shrinking core behavior. Figure 4.7 shows the CLSM images for adsorption of 1 mg/ml crosslinked BiSA in the pH 7 buffer containing 20 mM Na^+ (bottom row), which are the same conditions of the experiments in Fig. 4.4 and 4.5. As seen in Fig. 4.7, crosslinking the protein and, thus, restricting conformational flexibility dramatically alters the pattern of bound protein concentration compared to that seen in Figs. 4.4 and 4.5. Specifically, crosslinking leads to a sharp adsorption front that progresses toward the center of the bead as was observed for the reference mAb. In Fig. 3.3, we showed that the crosslinking restricts configurational flexibility, resulting in one-peak elution behavior for conditions where the unmodified protein resulted in a multiple peak elution behavior. As shown here, the loss of configurational flexibility alters the patterns of bound protein within the particle during transient adsorption.

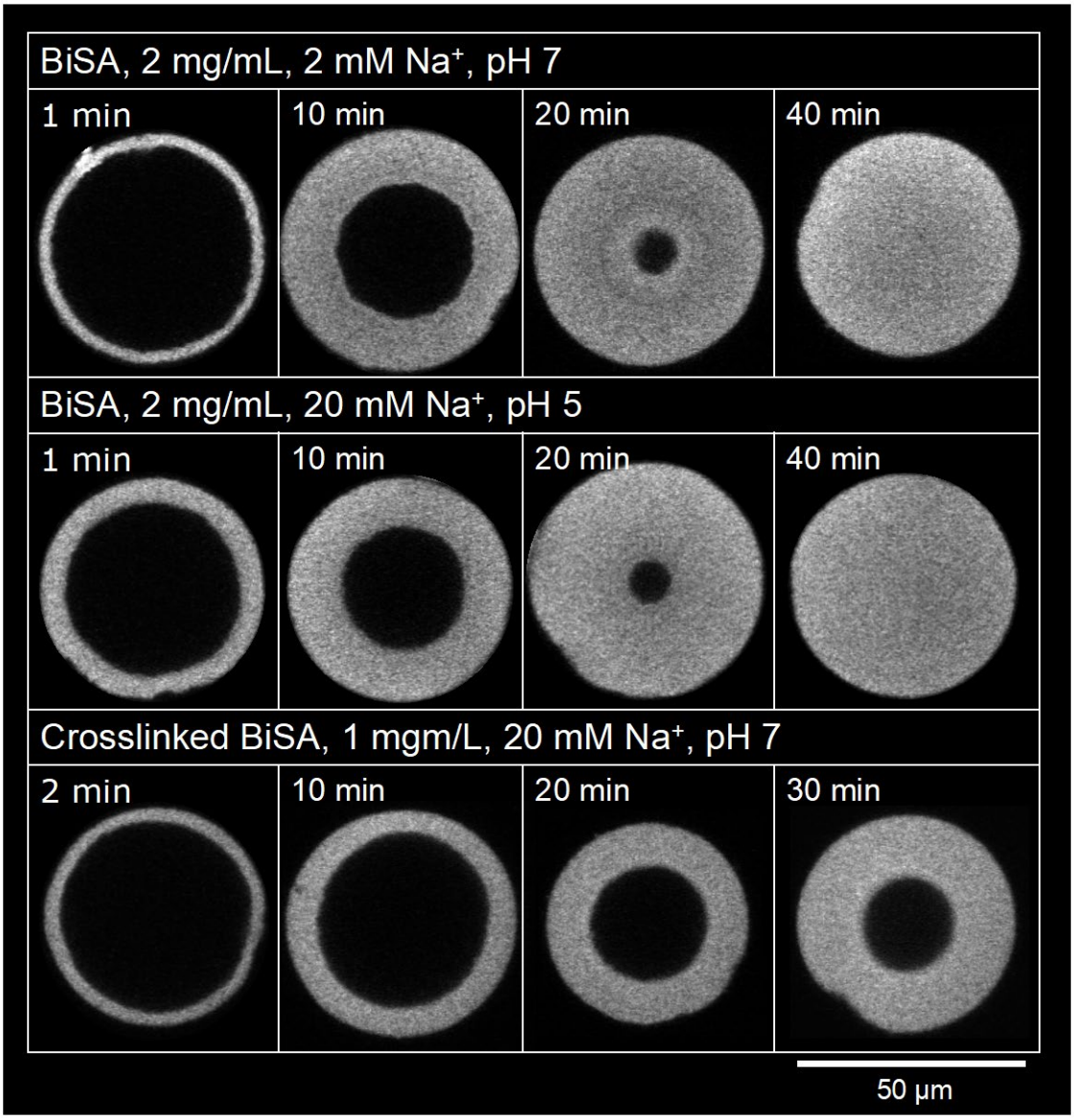

Figure 4.7. CLSM images of the adsorption of 2 mg/ml BiSA in a pH 7 buffer containing 2 mM Na^+ (top row), 2 mg/ml BiSA in a pH 5 buffer containing 20 mM Na^+ (middle row), and 1 mg/m crosslinked BiSA in a pH 7 buffer containing 20 mM Na^+ (bottom row).

4.4 Discussion and Model Development

The experimental results reported in Section 4.3 show that the adsorption kinetics behavior of the BiSAb molecules is different from that of the reference mAb. The latter exhibits sharp fronts that are consistent with a pore diffusion mechanism coupled with a highly favorable isotherm. The former, despite the fact that the isotherms are still highly favorable, exhibit more complex patterns of bound protein comprising a smooth profile leading to a sharp front toward the center of the bead. These patterns are independent of the protein solution concentration, which suggests that pore diffusion is still the dominant transport mechanism. However, these patterns vary both quantitatively and qualitatively with buffer composition and with temperature. Notably, the profiles become sharp, similar to those observed for the reference mAb, in buffers where the binding strength is higher or when the protein is crosslinked. Limited CLSM measurements were also done with the framework IgG (without scFv domains) as shown in Fig. 4.8. While these results are influenced by the presence of a significant charge variant that prevents quantitative analysis, there is clear evidence of a sharp adsorption front. Taken together, these results suggest that the BiSAb binding behaviors are linked to the presence of the scFv domains and to the associated configuration flexibility.

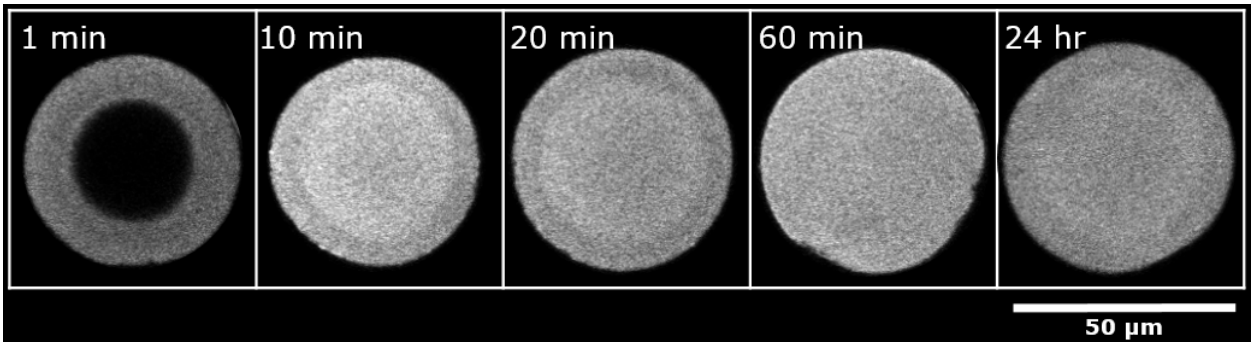

Figure 4.8. CLSM images of the adsorption of 2 mg/ml of the framework IgG in a pH 7 buffer containing 20 mM Na^+. Adsorption results in a sharp front consistent with the shrinking core model. Note that the framework IgG contains a significant charge variant that complicates the pattern of adsorbed protein.

In order to explain the BiSAb results, a model was developed to describe the experimental trends. Because of the complexity of the system and of the inaccessibility of many of the relevant parameters, the goal was not to develop an exact model. Rather, the goal was to determine what aspects of the various molecular interactions need to be included in order to generate simulated results that are in agreement with the experimental trends. The first step in this development was to model the behavior of the reference mAb. Since, as shown in Fig. 4.3a, the mAb isotherm is very favorable for the conditions studied, the position of the adsorption front in the Nuvia HR-S particles is expected to conform to the shrinking core model. Accordingly, the position of the adsorption front is expected to be related to time by the following relationship [12][13]:

$$2\rho_s^3 - 3\rho_s^2 + 1 = \frac{6D_e C_0 t}{q_m r_p^2} \tag{4.2}$$

where $\rho_s = r_s / r_p$ is the dimensionless radial position of the adsorption front defined as the actual radial position of the front, r_s, divided by the radius of the particle, r_p, and D_e is the effective pore diffusivity. The latter is related to the solution diffusivity D_0 by [12]:

$$D_e = \frac{\varepsilon_p \psi_p D_0}{\tau_p} \tag{4.3}$$

where τ_p is the tortuosity factor, which depends on the pore structure, and ψ_p is the hindrance factor, which depends on the ratio of molecule radius and pore radius. Temperature is expected to affect D_0 according to the Stokes-Einstein equation:

$$D_o = \frac{k_b T}{6\pi\mu r_h} \tag{4.4}$$

where k_b is the Boltzmann constant, r_h is the hydrodynamic radius of the protein, T is the absolute temperature, and μ is the solution viscosity. Figure 4.9a shows the position of the

adsorption front for the reference mAb observed at different times and temperatures plotted according to eq. 4.2 along with lines predicted from this equation with the same value of $D_e/D_0 = \varepsilon_p \psi_p / \tau_p = 0.20$ for all conditions. This value is consistent with the value reported previously at 21 ºC in [11] and fall in the range typically observed in macroporous protein chromatography resins. The close agreement between eq. 4.2 with the same $\varepsilon_p \psi_p / \tau_p$ and the data at different temperatures confirms that pore diffusion is dominant. The same model can also be used to describe the behavior of BiSA shown in Fig. 4.9 at pH 5 or at pH 7 in the low Na^+ concentration buffer since, for these conditions, a sharp adsorption front is observed. Figure 4.9b shows the corresponding plot of ρ_s vs $C_0 t / q_m r_p^2$. In this case, both sets of data are fitted by eq. 4.2 with $D_e/D_0 = \varepsilon_p \psi_p / \tau_p = 0.15$. This value is somewhat smaller than that determined for the reference mAb, but this is expected because the larger size of BiSA compared to the reference mAb is likely to cause greater diffusional hindrance and, thus, lead to a lower value of ψ_p.

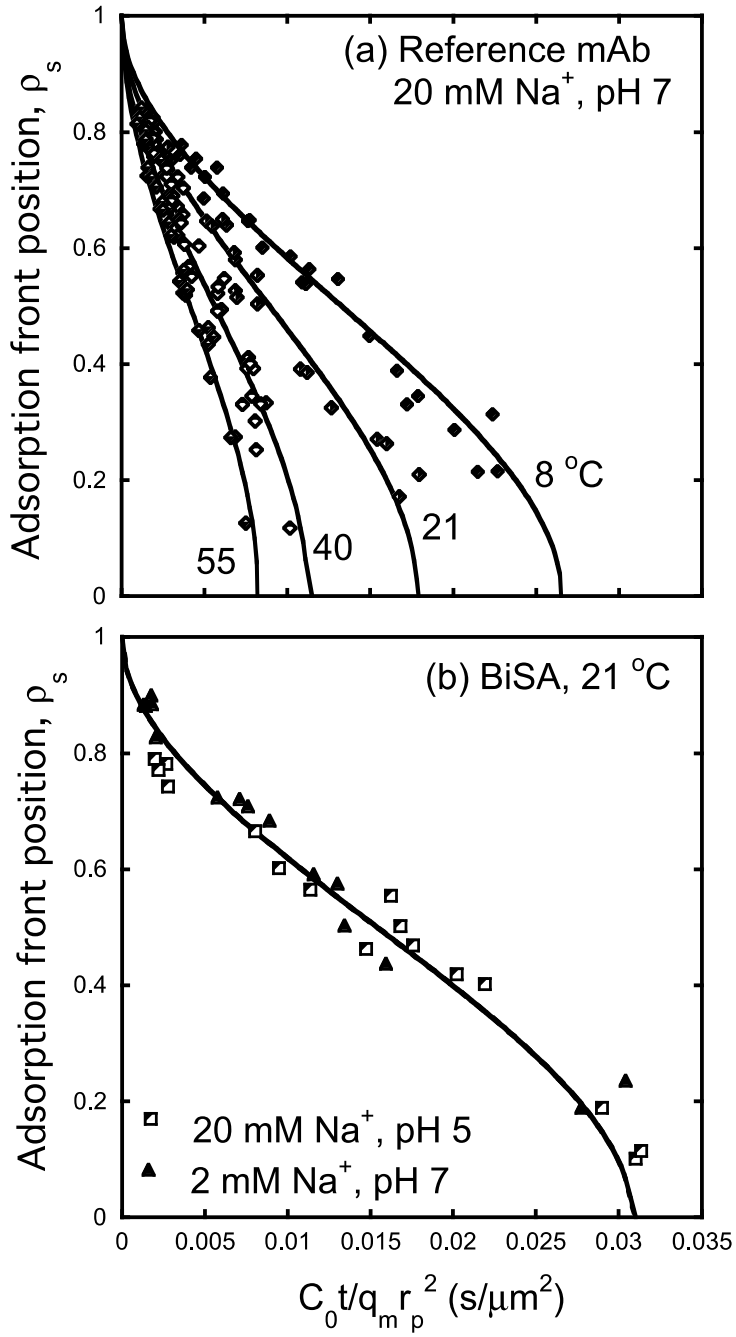

Figure 4.9. Dimensionless position of the adsorption front during adsorption of 1 mg/ml of the reference mAb in a pH 7 buffer containing 20 mM Na^+ at different temperatures (a) and during the adsorption of 2 mg/ml BiSA in a pH 5 and 7 buffers containing 20 mM and 2 mM Na^+, respectively at 21 ºC (b). The lines are based on the shrinking core model, eq. 4.2. The corresponding effective diffusivities are D_e = 0.54x10^{-7}, 0.80x10^{-7}, 1.3x10^{-7}, and 1.7x10^{-7} cm^2/s for the reference mAb at 8, 21, 40, and 55 ºC, respectively, and D_e = 0.54x10^{-7} cm^2/s for BiSA at 21 ºC.

Obviously, the shrinking core model cannot be used to describe the BiSAb adsorption behavior for other conditions where complex patterns of bound protein are observed. In other cases, involving different proteins and resins and, particularly, with polymer-grafted resins, surface or solid diffusion has been shown to describe smooth bound protein concentration profiles [8][14][15][16][17]. However, while this mechanism predicts smooth profiles with a highly favorable isotherm, somewhat like those observed for the BiSAb molecules in this work, it also predicts adsorption patterns that, at the same time, are independent of protein solution concentration. As shown in Fig. 4.5, the opposite is observed in our system with essentially identical profiles obtained not at the same time, but at times that scale in inverse proportion to the protein solution concentration. A more realistic hypothesis is, thus, that the patterns observed in our system result from the different binding configurations of the BiSAb molecules. Since these different configurations interconvert reversibly and, as shown previously, interact differently with the chromatographic surface, this hypothesis leads to an adsorption kinetics that is determined by the interplay of adsorption, diffusion, and interconversion kinetics. Qualitatively, if, in a given buffer, the different binding configurations were to exhibit different adsorption capacity, we would expect the weakest binding form to initially make faster progress into the particle [11]. For longer time, under the same scenario, we would expect this form to be gradually displaced by the stronger binding forms. Accordingly, the pattern of bound protein within the particle would comprise a series of transitions evolving from a pattern where the weakest binding form is dominant throughout the bead, for short times, to one, observed for long times, where the stronger binding forms become predominant. This conceptual model could also explain the effect of the buffer composition on the BiSA adsorption kinetics seen in Fig. 4.7 based on how the Na^+ concentration and pH can be expected to affect binding of each of the different forms. As observed

experimentally in Fig. 4.3b, reducing the Na^+ concentration or reducing the pH leads to greater overall binding strength. We can expect that the adsorption of each of the binding forms individually will be affected in a similar way. In that case, at lower Na^+ or lower pH, the binding capacities of the different forms will approach their maximum value, resulting in overall adsorption patterns conforming to those seen if a single binding form were present.

Finally, this conceptual model could also explain how the adsorption patterns are affected by temperature beyond the expected effect on diffusivity. As shown previously based on our chromatographic elution studies, the rate of interconversion among different binding forms increases with temperature, with one elution peak observed at high temperatures, when the interconversion kinetics is faster. Analogously, the effects of temperature on the interconversion kinetics are likely to affect the adsorption kinetics leading to trends like those seen experimentally in Fig. 4.6.

In order to test whether this conceptual model can explain the experimental trends, the following mathematical formulation was adopted. In this model, we consider three adsorbable configurations P_1, P_2, and P_3, consistent with the model that we have used previously to describe chromatographic elution. Physically, the first of these three forms corresponds to a configuration where the scFv domains are collapsed onto the framework IgG (P_1), the second to a configuration where one scFv is collapsed while the other is extended away from the framework IgG (P_2), and the third to a configuration where both scFv domains are extended away from the framework IgG (P_3). Since, as shown in Fig. 3.10, the scFvs in these molecules are highly positively charged, we expect that configurations where one or both of the scFv domains are extended away from the framework IgG and, thus, toward the chromatographic surface will be more strongly bound.

Next, we describe competitive binding of the three different configurations based on the steric mass action (SMA) model, which gives [18]:

$$q_i = \frac{K_{e,i}\left[q_0 - \sum_{j=1}^{3}\left(z_j + \sigma_j\right)q_j\right]^{z_i}}{\left(C_{Na^+}\right)^{z_i}} c_i \tag{4.5}$$

where $K_{e,i}$ is the equilibrium constant, z_i is the protein binding charge, σ is the shielding or steric hindrance parameter, q_0 is the resin charge density, C_{Na^+} is the Na^+ concentration, and c_i is the concentration of each form in the particle pores. The latter is equal to the bulk concentration C_i at equilibrium. At low protein loads, this equation yields:

$$q_i = \frac{K_{e,i}\left(q_0\right)^{z_i}}{\left(C_{Na^+}\right)^{z_i}} c_i \tag{4.6}$$

which is the same relationship used to describe retention in our previous chromatographic elution studies. We then consider interconversion of the three forms to occur both in solution and on the chromatographic surface according to the following kinetics:

$$\bar{r}_1 = -\bar{k}_1\left(q_1 - \frac{q_2}{\bar{K}_1}\right) \tag{4.7a}$$

$$\bar{r}_2 = \bar{k}_1\left(q_1 - \frac{q_2}{\bar{K}_1}\right) - \bar{k}_2\left(q_2 - \frac{q_3}{\bar{K}_2}\right) \tag{4.7b}$$

$$\bar{r}_3 = \bar{k}_2\left(q_2 - \frac{q_3}{\bar{K}_2}\right) \tag{4.7c}$$

$$r_1 = -k_1\left(c_1 - \frac{c_2}{K_1}\right) \tag{4.8a}$$

$$r_2 = k_1\left(c_1 - \frac{c_2}{K_1}\right) - k_2\left(c_2 - \frac{c_3}{K_2}\right) \tag{4.8b}$$

$$r_3 = k_2\left(c_2 - \frac{c_3}{K_2}\right) \tag{4.8c}$$

In these equations, $\bar{r}_1$, $\bar{r}_2$, and $\bar{r}_3$ are the net rates of formation of the three forms on the chromatographic surface and r_1, r_2, and r_3 are the rates in solution, while $\bar{k}_i$ and $\bar{K}_i$ on the chromatographic surface and k_i and K_i are the corresponding rate and equilibrium constants, respectively. These equations have the same form as those used to model the chromatographic elution behavior of these molecules in prior work. However, while in Section 2.2.3 we used a lumped rate model written in terms of average protein concentrations, in this formulation, eqs. 4.7-4.8 describe local rates expressed as functions of the local adsorbed concentrations, q_i, and pore concentrations, c_i, at each point within the particle. Finally, we assume that intraparticle transport occurs by pore diffusion and that pore and adsorbed protein concentrations are locally in equilibrium with each at each point within the particle. The corresponding conservation equations describing adsorption, diffusion, and interconversion are as follows:

$$\frac{\partial c_i}{\partial t} = \frac{1}{\varepsilon_p}\left[\frac{D_e}{r^2}\frac{\partial}{\partial r}\left(r^2\frac{\partial c_i}{\partial r}\right) - \left(\frac{\partial q_i}{\partial t}\right)_a + r_i\right] \tag{4.9}$$

$$\frac{\partial q_i}{\partial t} = \left(\frac{\partial q_i}{\partial t}\right)_a + \bar{r}_i \tag{4.10}$$

$$\begin{aligned} &t = 0 : c_i = 0, q_i = 0 \\ &r = 0 : \partial c_i / \partial r = 0 \\ &r = r_p : c_i = C_{0,i} \end{aligned} \tag{4.11}$$

The term $\left(\partial q_i/\partial t\right)_a$ in eqs. 4.9 and 4.10 represents the rate of adsorption. For computational expediency, this term was replaced by a linear driving force rate equation (applied locally) with a rate coefficient chosen to be large enough as to approximate local adsorption equilibrium conditions. A numerical solution of these equations was obtained by discretizing the spatial derivatives by finite differences and solving the discretized equations using the variable order differential equation solver ode15s in MATLAB R2020a (The Mathworks, Natick, MA, USA).

Unfortunately, the model contains a large number of parameters, only some of which could be determined independently. As a result, the following additional assumptions were made. To describe adsorption equilibrium according to eq. 4.5, we used the same effective charge z for all three forms. This assumption is supported by the data for BiSB in Chapter 6, which will show that even intact molecule and fragments have similar z-values due to the fairly small area of the protein that interacts with the surface bound ligands compared to the large size of the protein. To determine the average z for BiSA, we used the Yamamoto method [10][19] by measuring the salt concentration at which the protein elutes as a function of the gradient slope. The experimental results and calculation details are shown in the Fig. 4.10. An average value of z = 7.07 was determined.

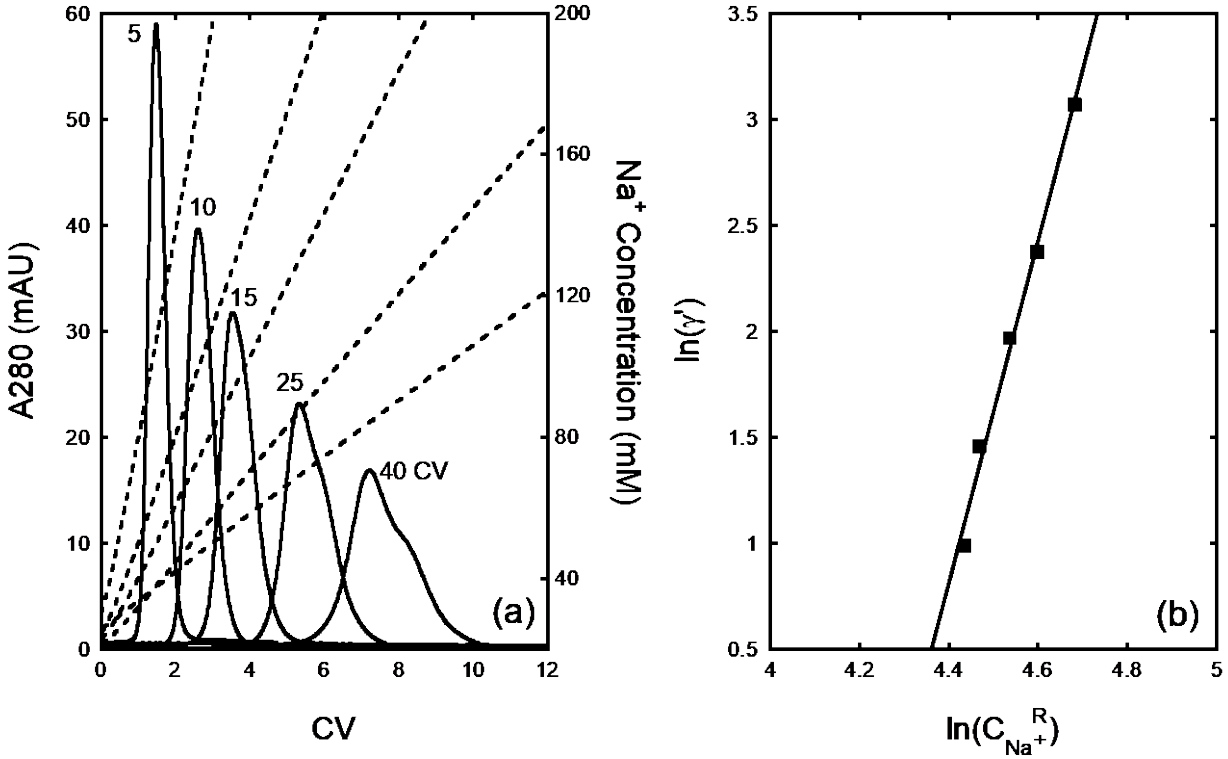

Figure 4.10. (a) Linear gradient elution of BiSA on a 0.5x9.4 cm Nuvia HR-S column at 0.5 ml/min with 0-300 mM NaCl gradients over 5, 10, 15, 25, and 40 CVs in a 20 mM sodium phosphate buffer at pH 7. (b) Plot of the log of normalized gradient slope, γ, in mM vs. the log of the Na^+ concentration at elution in mM. The protein binding charge *z* is calculated from the slope of the regressed line in (b) according to Yamamoto method described in ref. [10].

Next, we determined an average value of the hindrance parameter σ by comparing the adsorption capacities calculated from eq. 4.5 with the experimental isotherms assuming, again, that all three forms will have the same value. A value of $\sigma = 170$ was found. Finally, we determined individual values of the equilibrium constants, $K_{e,i}$, by running model simulations with multiple sets of values and determining which set provides a close match of the experimentally observed intraparticle concentration profiles. For the effective pore diffusivity, the value of $D_e / D_0 = \varepsilon_p \psi_p / \tau_p = 0.15$ was assumed to be the same for all three forms and equal to the value determined based on the shrinking core model from the CLSM data in the strong binding buffers. The remaining parameters are the equilibrium and rate constants in the interconversion kinetics model, eq. 4.7-4.8. As seen in our prior work based on our lumped model description, different values of these parameters can be expected in solution and on the chromatographic surface. For the solution, we used the same values determined in Section 2.3.2. For the chromatographic surface, since we have assumed adsorption equilibrium and have assumed the same values of z and σ for all three forms, the corresponding equilibrium constants, $\bar{K}_1$ and $\bar{K}_2$, are related to the SMA constants $K_{e,1}$, $K_{e,2}$, and $K_{e,3}$ and to the values of K_1 and K_2 by the following equations:

$$\bar{K}_1 = \frac{K_{e,2}}{K_{e,1}} K_1 \tag{12}$$

$$\bar{K}_2 = \frac{K_{e,3}}{K_{e,2}} K_2 \tag{13}$$

Finally, values of the rate constants $\bar{k}_1$ and $\bar{k}_2$ were selected to provide agreement with the experimental trends. Fortunately, based on simulations, these parameters affect the predicted concentration profiles primarily for long times, since they control the interconversion of different

binding forms. In contrast, the SMA parameters $K_{e,i}$ affect the distribution of the different bound forms in the particles primarily for short times. Thus, the SMA and interconversion rate parameters are relatively independent of each other. Table 4.2 provides a summary of all of the parameter values used.

Figure 4.11 shows experimental and predicted BiSA isotherms at pH 7 in buffers containing 20 and 2 mM Na^+ as a function of the total protein concentration in solution. Based on the values of K_1 and K_2, in solution, the proportion of the different forms in solution, $P_1 : P_2 : P_3$, is predicted to be 1.0 : 0.16 : 0.0016. In contrast, on the chromatographic surface, since the $\bar{K}_1$ and $\bar{K}_2$ value are much larger than the corresponding solution values, the proportion $P_1 : P_2 : P_3$ becomes 1 : 32 : 9600. Thus, P_3 is predicted to be largely dominant at equilibrium on the chromatographic surface despite its very low value in solution. Figure 4.11 also shows the adsorption isotherms predicted by the model for each form individually. These lines are calculated for a hypothetical case where the interconversion rate is zero and each form can exist independent of the others. Experimentally, since the interconversion rate is finite, this could only be seen temporarily. As seen in Fig. 4.11, different results are predicted for the high and low Na^+ buffers. For the high Na^+ buffer (Fig. 4.10a), the binding capacities predicted for the three individual forms are different from each other, being lowest for P_1, which is the weakest binding form, and highest for P_3, which is the strongest binding form. The binding capacity of P_2, whose binding strength is intermediate, is, of course, predicted to be intermediate. Conversely, in the low Na^+ buffer, where binding becomes very strong for all three forms, the binding capacities for the individual forms become nearly coincident and almost indistinguishable from the overall binding isotherm.

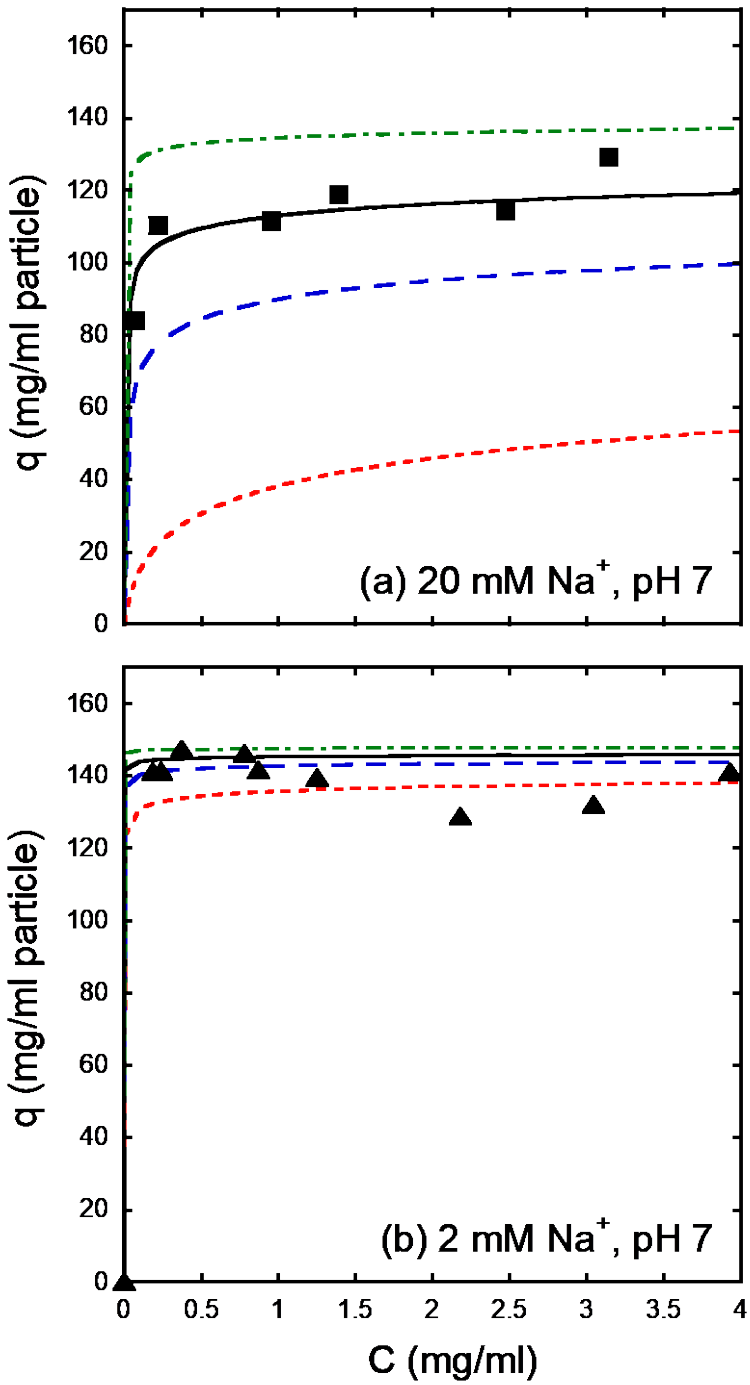

Figure 4.11. Adsorption isotherm for BiSA in a pH 7 buffers containing 20 mM Na^+ (a) and 2 mM Na^+ (b) plotted as a function of total protein concentration. Symbols are experimental values from Fig. 4.3. The lines are calculated from the SMA model, eq. 4.2, with parameters from Table 4.2. The solid line shows the composite isotherm for the three forms combined with a $P_1 : P_2 : P_3$ ratio of 1.0 : 0.16 : 0.016 in solution. The dashed lines show hypothetical one-component SMA isotherms for each individual form neglecting interconversion. - - - - : P_1, – – – :P_2, – - – - : P_3.

Table 4.2. Parameters used to model the BiSA adsorption kinetics at pH 7 and 21 ºC.

	P_1	P_2	P_3
$K_{e,i}$	0.0005	0.1	3000
z_i	7.07	7.07	7.07
σ_i	170	170	170
$\bar{k}_1$ (s^{-1})	0.0007	k_1 (s^{-1})	0.0064
$\bar{k}_2$ (s^{-1})	0.0003	k_2 (s^{-1})	0.0008
$\bar{K}_1$	32	K_1	0.16
$\bar{K}_2$	300	K_2	0.01
q_0 (mM)	132	ε_p $\varepsilon_p \psi_p / \tau_p$	0.5 0.15

Figure 4.12 compares experimental and predicted BiSA intraparticle concentration profiles in the pH 7 buffers containing 20 mM Na^+ and 2 mM Na^+. In each case, the experimental profiles were obtained from the color intensity of the digitized CLSM images, while the predicted profiles were obtained from the model by adding q_1, q_2, and q_3 at each radial position. The same set of parameters has been used for both predictions, with the Na^+ concentration being the only difference. As seen in Fig. 4.12, the shape and evolution of the model-predicted profiles are in substantial agreement with the experimental ones. In the 20 mM Na^+ buffer, where the different forms exhibit substantially different binding strengths, for short times, the predicted results show a smooth profile starting at the bead surface and leading to a plateau with a fairly sharp front to zero toward the center of the bead. For longer times, the front reaches the center of the bead and the profile exhibits a plateau becoming uniform only after very long time. In contrast, in the 2 mM Na^+ buffer, where binding is predicted to be strong for all three forms, the predicted results show just a sharp front. In this case, the total bound protein concentration profile becomes instantly uniform when the front reaches the particle center.

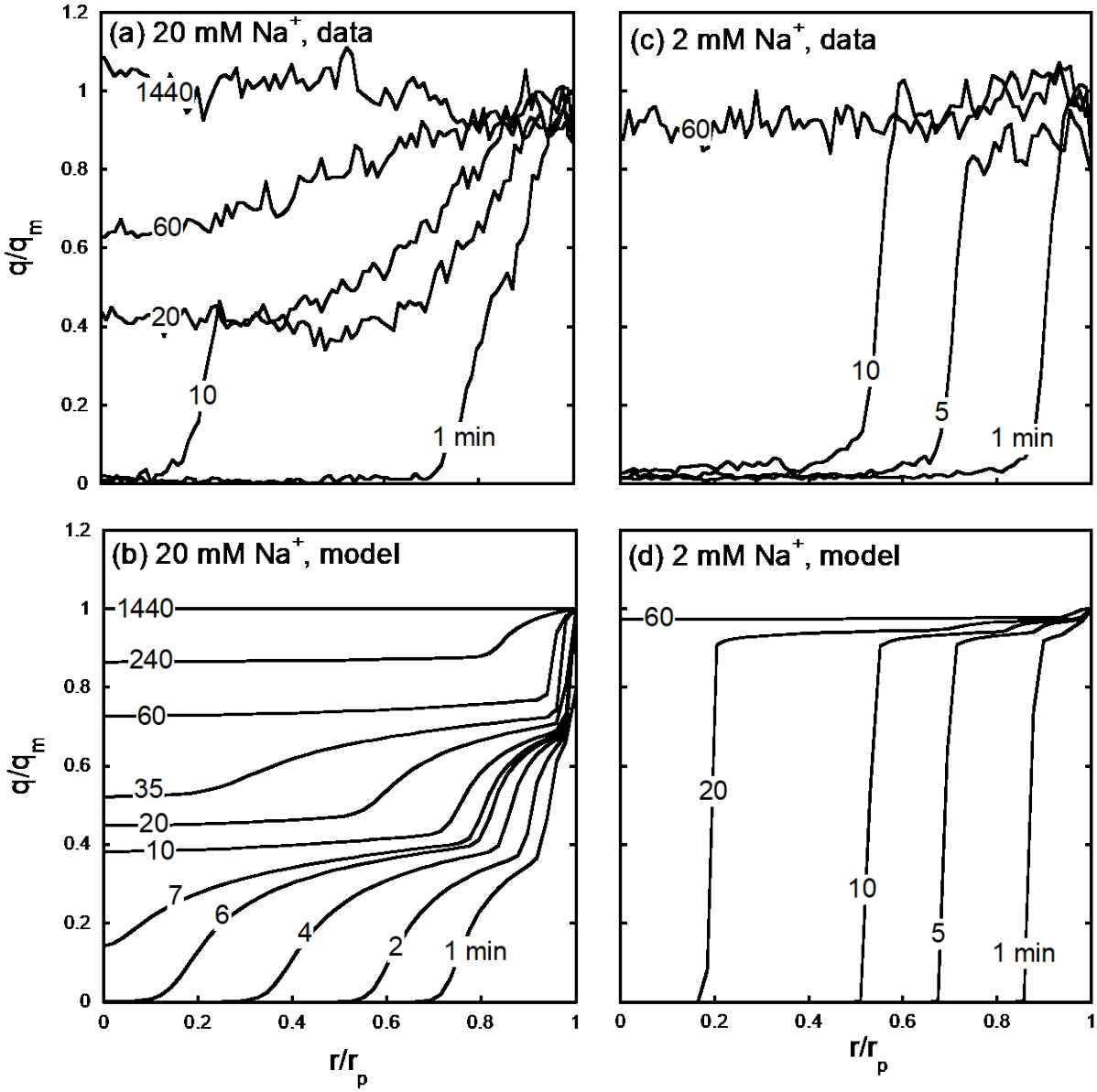

Figure 4.12. Comparison of experimental (a,c) and simulated (b,d) bound protein concentration profiles for the adsorption of 2 mg/ml BiSA in pH 7 buffers containing 20 mM Na^+ (a, b) and 2 mM Na^+ (c, d). Experimental conditions are the same as in Fig. 4.4 for (a) and (b) and in Fig. 4.7 for (c) and (d). Model parameters are from Table 4.2.

Better insight in this behavior can be gained by considering the distribution of the different bound forms in the particle predicted by the model in the two different buffers shown in Fig. 4.13. For both conditions, the model predicts displacement of P_1 by P_2 and displacement of P_2 by P_3. As a result, early on, first P_1 and then P_2 are pushed toward the center of the bead by the stronger binding P_3 form. Later on, after P_1 reaches the center of the bead, P_1 gets replaced by P_2 and then by P_3 as interconversion gradually leads to formation of more and more P_3. For long times, as equilibrium is approached, P_3 becomes largely predominant in both cases despite its much lower concentration in solution, as predicted by eq. 4.5. The difference between the two conditions is mainly that in the higher Na^+ case, the surface does not become saturated with P_1 in the leading front as the individual binding capacity for this form is lower than the maximum (cf. Fig. 4.11). In contrast, in the low Na^+ case, P_1 binding is strong enough for q_1 to closely approach the maximum binding capacity. As a result, for this condition, the overall bound protein profile ($q_1 + q_2 + q_3$) consists of just a single front.

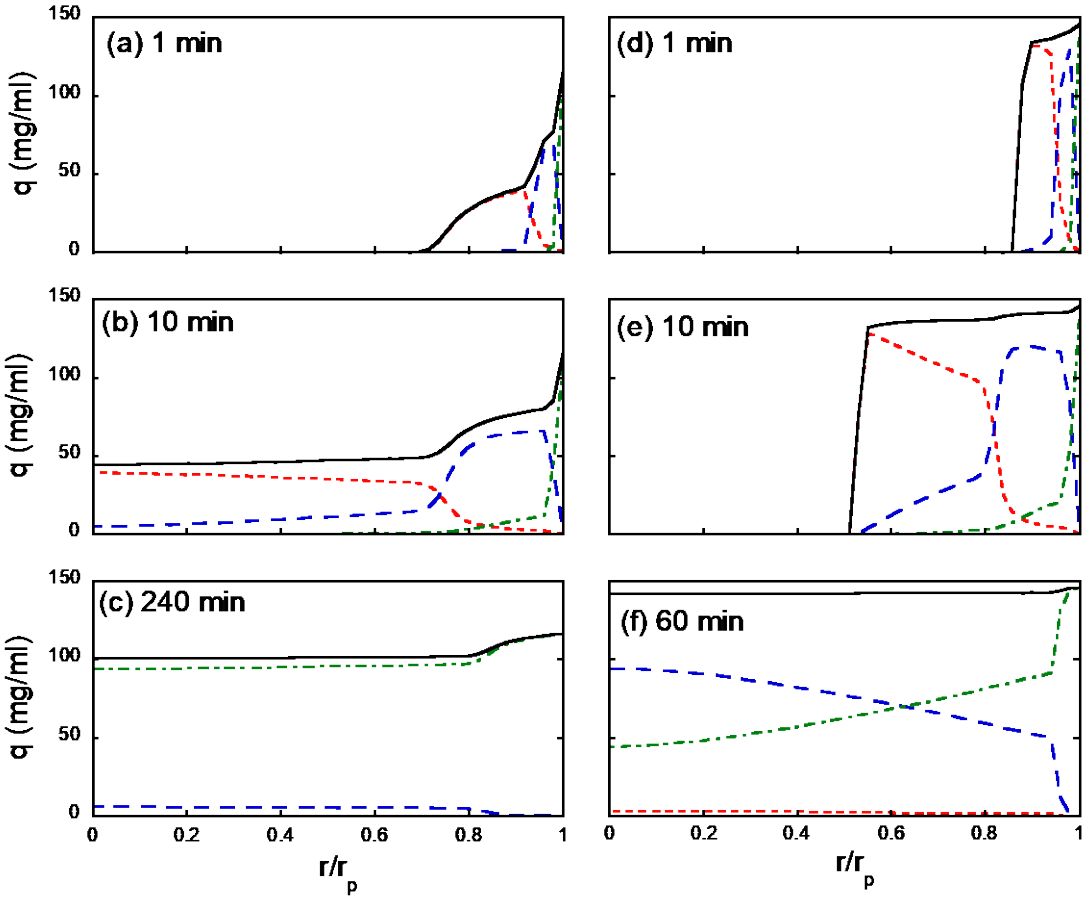

Figure 4.13. Predicted evolution of the bound concentration profiles of each individual form for the adsorption of 2 mg/ml BiSA in pH 7 buffers containing 20 mM Na^+ (a, b, c) and 2 mM Na^+ (d, e, f). Experimental conditions are the same as Fig. 4.11. Model parameters are from Table 4.2.

- - - - : P_1, — — :P_2, — · — · : P_3, —— : $P_1+P_2+P_2$.

It is interesting to see if the same model can also describe the profiles observed at different temperatures shown in Fig. 4.6. Because of the electrostatic nature of the binding mechanism, the adsorption isotherms are unlikely to be strongly affected by temperature. However, significant effects can be expected both on the diffusivities and the rates of interconversion between different forms. As seen in Fig. 4.9a, for the reference mAb, for which interconversion is not a factor, the effect of temperature on the effective pore diffusivity is predicted by eqs. 4.3 and 4.4. Since the transport mechanism is the same as that of the reference mAb, we assumed the same dependence of D_e on temperature for BiSA although with lower value of $D_e / D_0 = \varepsilon_p \psi_p / \tau_p = 0.15$ as found from the analysis of the data in Fig. 4.9b. The rate constants are expected to be affected by temperature to a greater extent than diffusion. In order to account for this effect, for simplicity, we multiplied each rate constant by the same temperature-dependent interconversion rate factor $\alpha(T)$. The values of this factor were determined by running simulations for a range of values and choosing the value that best represent the evolution of the BiSA bound concentration profiles at each temperature. Figure 4.14 compares the experimental profiles obtained for BiSA at 8 and 55 ºC with those predicted with α = 0.1 and 25, respectively, which were found to be optimum at these two temperatures. Similar trends were obtained at 40 ºC with α = 5.0 (data not shown for brevity). As seen Fig. 4.14, while the match of experimental and predicted profiles is not exact, the trends are in close agreement. Consistent with the experimental profiles, the model predicts more fronting profiles at 8 ºC, when the interconversion rates are lower and the different forms tends to behave more as if they were individual species. In contrast, the model predicts smoother profiles at 55 ºC, when interconversion rates are higher and there is greater coupling of the three forms as they diffuse, bind, and interconvert. The differences between the profiles at the two

temperatures are especially evident for long times when the process becomes almost completely dominated by the interconversion of the different forms.

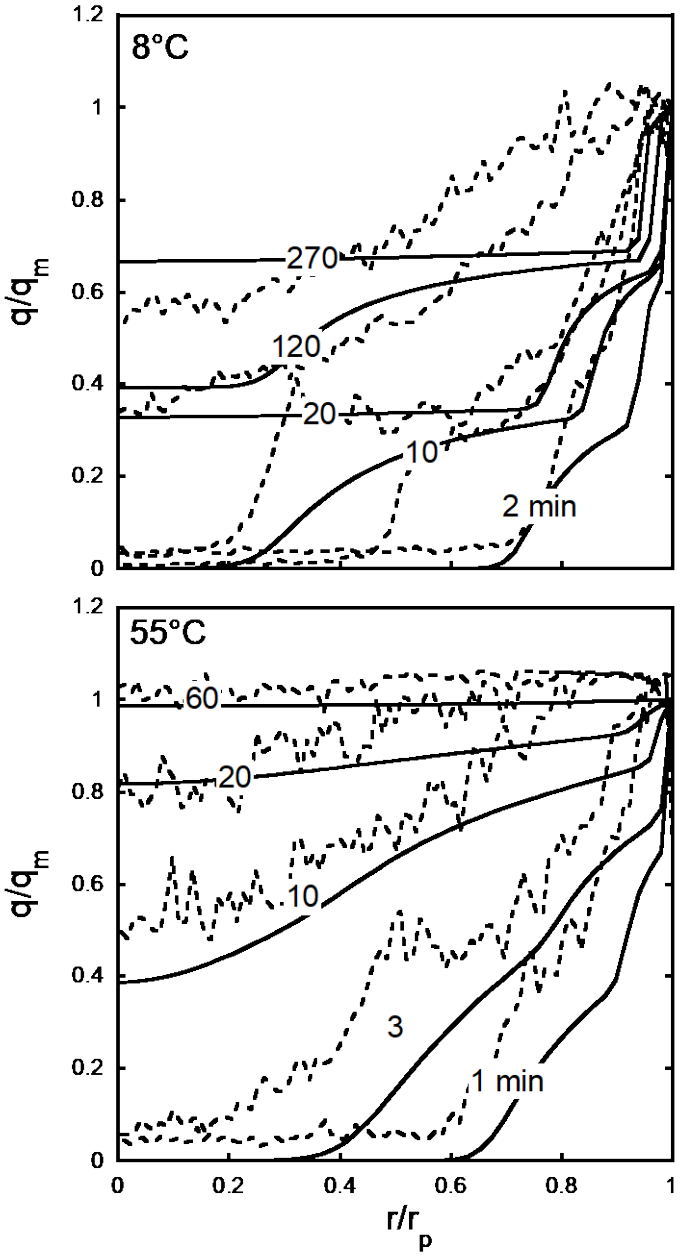

Figure 4.14. Comparison of experimental (dashed lines) and simulated (solid lines) bound protein concentration profiles for the adsorption of 1±0.1 mg/ml BiSA in pH 7 buffers containing 20 mM Na^+ at 8 ºC (a) and 55 ºC (b). Experimental conditions are the same as in Fig. 4.6. Model parameters are from Table 4.2 but with $D_e = 0.36\text{x}10^{-7}$ cm^2/s and $\alpha = 0.1$ in (a) and with $D_e = 1.2\text{x}10^{-7}$ cm^2/s and $\alpha = 25$ in (b). Data at 40 ºC, not shown for brevity, were in similar agreement with the model using $D_e = 0.86\text{x}10^{-7}$ cm^2/s and $\alpha = 5.0$.

Figure 4.15 shows an Arrhenius plot of the corresponding D_e values vs. temperature and gives an apparent activation energy for diffusion of 19 kJ/mol, which is comparable to values reported for other systems (e.g., ref. [20]). An Arrhenius plot of the interconversion rate factor α shown in Fig. 4.15 yields an apparent activation energy of 88 kJ/mol. This value is much lower than the activation energies typically found for the thermal denaturation of proteins, which have been reported to be in the range 150-300 kJ/mol [21][22]. However, this value comparable with the activation energies for protein folding/unfolding in solution [23] and on hydrophobic interaction chromatography surfaces [24], which have been reported to be in the range 50-120 kJ/mol. This result suggests that the underlying interconversion mechanism involves local conformational changes, rather than denaturation with complete loss of protein structure. As shown in our prior work, based on tryptophan autofluorescence measurements, these conformational changes appear to be related to the collapse of the scFv domains on the framework IgG, which leads to weaker binding, and their extension away from the framework IgG, which leads to stronger binding.

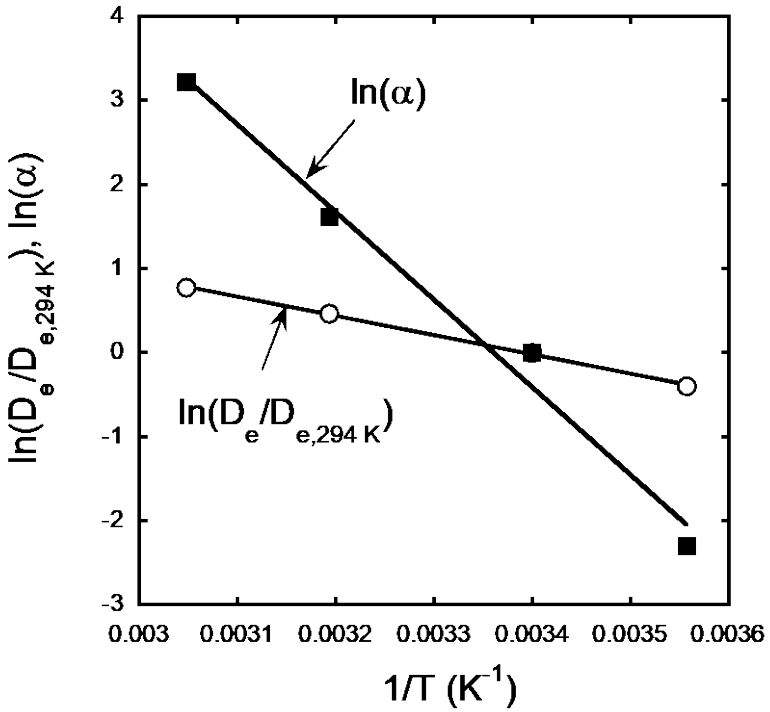

Figure 4.15. Arrhenius plot showing the temperature dependence of De/De predicted by eqs. 3-4 and of the interconversion reaction rate factor α for BiSA at pH 7. The corresponding activation energies based on the regressed lines are 19 kJ/mol for diffusion and 88 kJ/mol for the interconversion rate.

4.5 References

[1] J.M. Reck, T.M. Pabst, A.K. Hunter, X. Wang, G. Carta, Adsorption equilibrium and kinetics of monomer-dimer monoclonal antibody mixtures on a cation exchange resin, J. Chromatogr. A. 1402 (2015) 46–59.

[2] J.M. Reck, T.M. Pabst, A.K. Hunter, G. Carta, Separation of antibody monomer-dimer mixtures by frontal analysis, J. Chromatogr. A. 1500 (2017) 96–104.

[3] A. Creasy, J. Reck, T. Pabst, A. Hunter, G. Barker, G. Carta, Systematic Interpolation Method Predicts Antibody Monomer-Dimer Separation by Gradient Elution Chromatography at High Protein Loads, Biotechnol. J. 14 (2019) 1800132. doi:10.1002/biot.201800132.

[4] L.K. Kimerer, T.M. Pabst, A.K. Hunter, G. Carta, Role of Configurational Flexibility on the Kinetics of Binding of Bivalent Bispecific Antibodies on Porous Cation Exchange Resins, Chem. Eng. Sci. In Review (2021).

[5] Y. Wang, G. Carta, Competitive binding of monoclonal antibody monomer-dimer mixtures on ceramic hydroxyapatite, J. Chromatogr. A. 1587 (2019) 136–145. doi:10.1016/j.chroma.2018.12.023.

[6] Y. Tao, E.X. Perez Almodovar, G. Carta, G. Ferreira, D. Robbins, Adsorption kinetics of deamidated antibody variants on macroporous and dextran-grafted cation exchangers. III. Microscopic studies, J. Chromatogr. A. 1218 (2011) 8027–8035.

[7] Y. Tao, E.X.P. Almodovar, G. Carta, G. Ferreira, D. Robbins, Adsorption kinetics of deamidated antibody variants on macroporous and dextran-grafted cation exchangers. III. Microscopic studies, J. Chromatogr. A. 1218 (2011) 8027–8035.

[8] A. Ljunglöf, R. Hjorth, Confocal microscopy as a tool for studying protein adsorption to chromatographic matrices, J. Chromatogr. A. 743 (1996) 75–83.

[9] U. Tallarek, M. Paces, E. Rapp, Perfusive flow and intraparticle distribution of a neutral analyte in capillary electrochromatography, Electrophoresis. 24 (2003) 4241–4253.

[10] G. Carta, A.R. Ubiera, T.M. Pabst, Protein Mass Transfer Kinetics in Ion Exchange Media : Measurements and Interpretations, Chem. Eng. Technol. Rev. 28 (2005) 1252–1264.

[11] C. Martin, G. Iberer, A. Ubiera, G. Carta, Two-component protein adsorption kinetics in porous ion exchange media, J. Chromatogr. A. 1079 (2005) 105–115. doi:10.1016/j.chroma.2005.03.007.

[12] G. Carta, A. Jungbauer, Protein Chromatography, 2nd ed., Wiley-VCH, Weinheim, Germany, 2020.

[13] D. Ruthven, Principles of Adsorption and Adsorption Processes, 1984.

[14] E.X. Perez-Almodovar, Y. Wu, G. Carta, Multicomponent adsorption of monoclonal antibodies on macroporous and polymer grafted cation exchangers, J. Chromatogr. A. 1264 (2012) 48–56. doi:10.1016/j.chroma.2012.09.064.

[15] E. Schirmer, G. Carta, Protein Adsorption in Charged Agarose Gels Studied by Light Microscopy, AIChE J. 53 (2007).

[16] A.M. Lenhoff, Multiscale Modeling of Protein Uptake Patterns in Chromatographic Particles, Langmuir. 24 (2008) 5991–5995.

[17] B.D. Bowes, A.M. Lenhoff, Protein adsorption and transport in dextran-modified ion-exchange media. III. Effects of resin charge density and dextran content on adsorption and intraparticle uptake, J. Chromatogr. A. 1218 (2011) 7180–7188. doi:10.1016/j.chroma.2011.08.039.Protein.

[18] C.A. Brooks, S.M. Cramer, Steric mass-action ion exchange: Displacement profiles and induced salt gradients, AIChE J. 38 (1992) 1969–1978. doi:10.1002/aic.690381212.

[19] S. Yamamoto, K. Nakanishi, R. Matsuno, Ion-Exchange Chromatography of Proteins, Marcel-Dekker, New York, 1988.

[20] A.C. English, M. Dole, Diffusion of sucrose in supersaturated solutions, J. Am. Chem. Soc. 72 (1950) 3261–3267.

[21] A. Rosenberg, J. Enberg, Studies of hydrogen exchange in proteins. II. The reversible thermal unfolding of chymotrypsinogen A as studied by exchange kinetics, J. Biol. Chem. 244 (1969) 6153–6159.

[22] V.R. Harwalkar, Kinetics of thermal denaturation of B-lactoglobulin, J. Dairy Sci. 63 (1980) 1052–1057.

[23] M.L. Scalley, D. Baker, Protein folding kinetics exhibit and Arrhenius temperature dependence when corrected for the temperature dependence of protein stability, Proc. Natl. Acad. Sci. 94 (1997) 10636–10640.

[24] E. Haimer, A. Tscheliessnig, R. Hahn, A. Jungbauer, Hydrophobic interaction chromatography of proteins IV Kinetics of protein spreading, J. Chromatogr. A. 1139 (2007) 84–94.

5 Chromatographic Behavior on Hydrophobic Interaction Columns

5.1 Introduction

The cation exchange base matrix hydrophobicity was found to play a role in catalyzing the outstretched conformations in Figure 3.12. In order to further elucidate the chromatographic behavior of these complex BiSAb molecules, in this chapter, we have studied their elution behavior in HIC using ammonium sulfate gradients. We hypothesized that reversible, three peak elution may also occur on HIC media, without the contribution of charged ligands on the resin as in CEX. In fact, based on homology modeling of the BiSAb molecules shown in Figures 3.9-3.11, the Fab and Fc regions of the framework IgG were found to have distributed patches of positive and negative charges, while the scFvs were found to have both large positively charged patches as well as a high hydrophobicity including multiple surface-exposed tryptophan residues. We anticipated that the balance of inter-domain and domain-surface interactions could result in complex elution behaviors analogous to those observed in CEX columns. Indeed, complex elution behavior was observed for HIC. To further investigate the system, the effects of resin structure, resin ligand, residence time, reversibility of peaks, hold time, and temperature are studied. A phenomenological column model similar to that of section 2.3.2 is developed to test our understanding of the system and assist in comparing the behavior across chromatography modalities. This work was published in the Journal of Chromatography A as ref. [1].

5.2 Materials and Methods

The HIC resins used in this work were Protein Pak Hi-Res HIC from Waters (Milford, MA, USA), based on 2.5 μm nonporous, polymethacrylate particles with butyl functional groups with low ligand density; Toyopearl PPG600M, a commercial resin from Tosoh Bioscience GmbH (Griesheim, Germany) based on macroporous polymethacrylate particles with polypropylene glycol (PPG) functional groups; and a second PPG-based experimental resin also from Tosoh Bioscience GmbH with backbone structure and hydrophobicity similar to those of Toyopearl PPG600M but smaller particle size. For simplicity, we refer to the two Toyopearl resins as PPG-M and PPG-S. Particle size distribution was measured using a light microscope and are shown in Fig. 5.1. Volume-average particle diameters of 73 and 33 μm were found for PPG-M and PPG-S, respectively. Other HIC resins with higher hydrophobicity than the PPG resins were also considered, including Butyl Sepharose HP, Phenyl Sepharose HP (low sub), and Butyl S Sepharose FF from GE Healthcare. However, protein recovery from these resins was low and in some cases zero indicating that protein unfolding with loss of secondary structure occurs for our BiSAb molecules on these resins. For all the runs for the Protein Pak and PPG columns, full recovery of protein was calculated by integrating UV signal in chromatogram and comparing with offline concentrations measured using the NanoDrop 2000c.

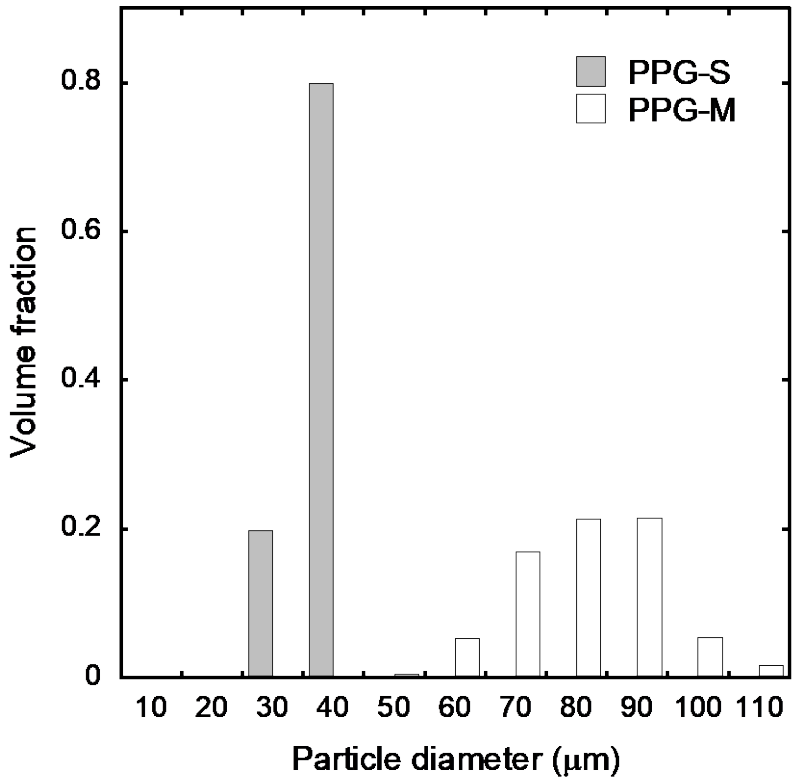

Figure 5.1. Particle size distributions of PPG resin samples used in this work.

Protein Pak Hi-Res HIC was purchased pre-packed as a UPLC column with inner dimensions of 0.45 cm in diameter and 3.5 cm long. The Toyopearl resins were obtained in slurry form and were flow-packed using 20% (v/v) aqueous ethanol as the packing buffer into 0.5 cm diameter Tricorn columns from Cytiva. The packing flow rates were chosen to obtain a desired pressure drop of 0.25 MPa for PPG-S and 0.05 MPa for PPG-M. Two PPG-S columns were packed, one with 5.0 cm bed height and the other with 13.8 cm packed bed height. A third column was packed with PPG-M with 14.6 cm bed height. In each case, the column packing quality was determined by measuring the HETP and the peak asymmetry factor for a salt pulse injection. HETP values were 0.029, 0.039, and 0.049 cm and asymmetry factors were 1.2, 1.2, and 1.0 for the 5.0 cm PPG-S, for the 13.8 cm PPG-S, and for the PPG-M column, respectively. The 13.8 cm PPG-S column was characterized further to determine the extraparticle (or external) porosity, ε, and the intraparticle (or internal) porosity, ε_p, since this column was used to develop a mechanistic model to describe the three-peak elution behavior. ε was determined from pressure-flow curves based on the well-known Carman-Kozeny equation as described in ref. [2]. The corresponding values were $\varepsilon = 0.35$ and $\varepsilon_p = 0.71$.

Linear gradients were operated in the same manner as previously discussed except with a HIC appropriate buffer of 1000-0 mM ammonium sulfate buffered with 50 mM Na_3PO_4, pH 7. Columns were cleaned in place in between runs using a series of washes: distilled-deionized water, 1 M NaOH, distilled-deonized buffer before equilibrating with the high salt load buffer. Protein recovery was calculated by comparing offline measurements of load protein concentration found using a Nanodrop 2000c spectrophotomer (Thermo Fisher Scientific) with the integrated UV trace of the chromatogram. All experiments were done at room temperature (21±2 ^{o}C) unless otherwise indicated.

5.3 Results and Discussion

The elution behaviors of the BiSAb molecules and of the framework mAb were studied for the three different HIC columns over a range of flow rates, temperatures, and hold times. Figure 5.2 shows the elution profiles of the mAb (top row) and of BiSA (bottom row) using, in each case, a 1000-0 mM ammonium sulfate gradient in 20 column volumes (CV) and at two different flow rates: 1 ml/min, shown by the solid lines, and 0.05 ml/min, shown by the dashed lines. The residence times corresponding to these two flow rates are 0.55 and 11.1 min, respectively, for the Protein Pak Hi-Res HIC column, 2.7 and 54 min, respectively, for the PPG-S column, and 2.9 and 57 min, respectively, for the PPG-M column. As seen in this figure, in all three cases the mAb elutes as a single peak (beside a small, late eluting impurity peak resolved by the Protein Pak Hi-Res HIC column) regardless of the flow rate and, thus, residence time used. The peak is unchanged as a function of flow rate for the Protein Pak Hi-Res HIC column, but is broader at the higher flow rate for the PPG-S and even more so for the PPG-M column. This result is expected since Protein Pak Hi-Res HIC resin is comprised of small non-porous beads, which offer little or no mass transfer resistance. On the other hand, PPG-S and PPG-M consist of porous particles. As a result, for these resins the peak broadens at higher flow rates (or, correspondingly, at shorter residence times) because of mass transfer effects. Retention of both the mAb and BiSA is similar for PPG-S and PPG-M, which is expected because these resins are based on the same bead structure and chemistry differing only in particle size. Slight differences in hydrophobicity do exist, however. For example, the mAb elutes at about 620 mM ammonium sulfate for the PPG-S column and at about 640 mM ammonium sulfate for the PPG-M column indicating that PPG-S is slightly more hydrophobic. By comparison, the Protein Pak Hi-Res HIC column is much less hydrophobic than either PPG column with the mAb eluting at about 890 mM ammonium sulfate.

As seen in Fig. 5.2, the elution behavior of BiSA is completely different from that of the mAb. In this case, for all three resins, at 1.0 ml/min, the protein elutes as three peaks. These peaks are nearly completely resolved for the Protein Pak Hi-Res HIC column but are overlapped for both PPG resins but especially for the PPG-M column, which has larger particle size and, hence, increased band broadening due to mass transfer. Comparing the results obtained for the Protein Pak Hi-Res HIC column with those obtained for the PPG columns, it is evident that the first eluting peak is dominant for the former, while, the middle peak appears dominant for the latter.

Remarkably, for all three resins, when the flow rate is reduced to 0.05 ml/min, BiSA elutes as a single merged peak, which is centered near the elution volume of the middle peak obtained at high flow. Compared to the mAb, the merged BiSA peak is much broader for all three columns indicating that factors other than mass transfer alone affect band broadening during elution for this more complex molecule.

Figure 5.3 shows the results obtained by collecting fractions of each of the three peaks obtained for BiSA at high flow rate (1 ml/min or 2.7 min residence time) on the PPG-S column and re-chromatographing them. In these experiments, 0.5 CV fractions near the maximum of each peak were collected as shown in Fig. 5.3a, diluted three-fold with load buffer, and then immediately re-injected into the same column and eluted with the same gradient and flow rate. As seen in Fig. 5.3b, the elution profile obtained from each re-injection is essentially indistinguishable from the original profile in Fig. 5.3a and the same regardless of which peak fraction is re-injected. This result suggests that the phenomena responsible for the three-peak elution behavior are reversible and occur within the timeframe of chromatographic elution.

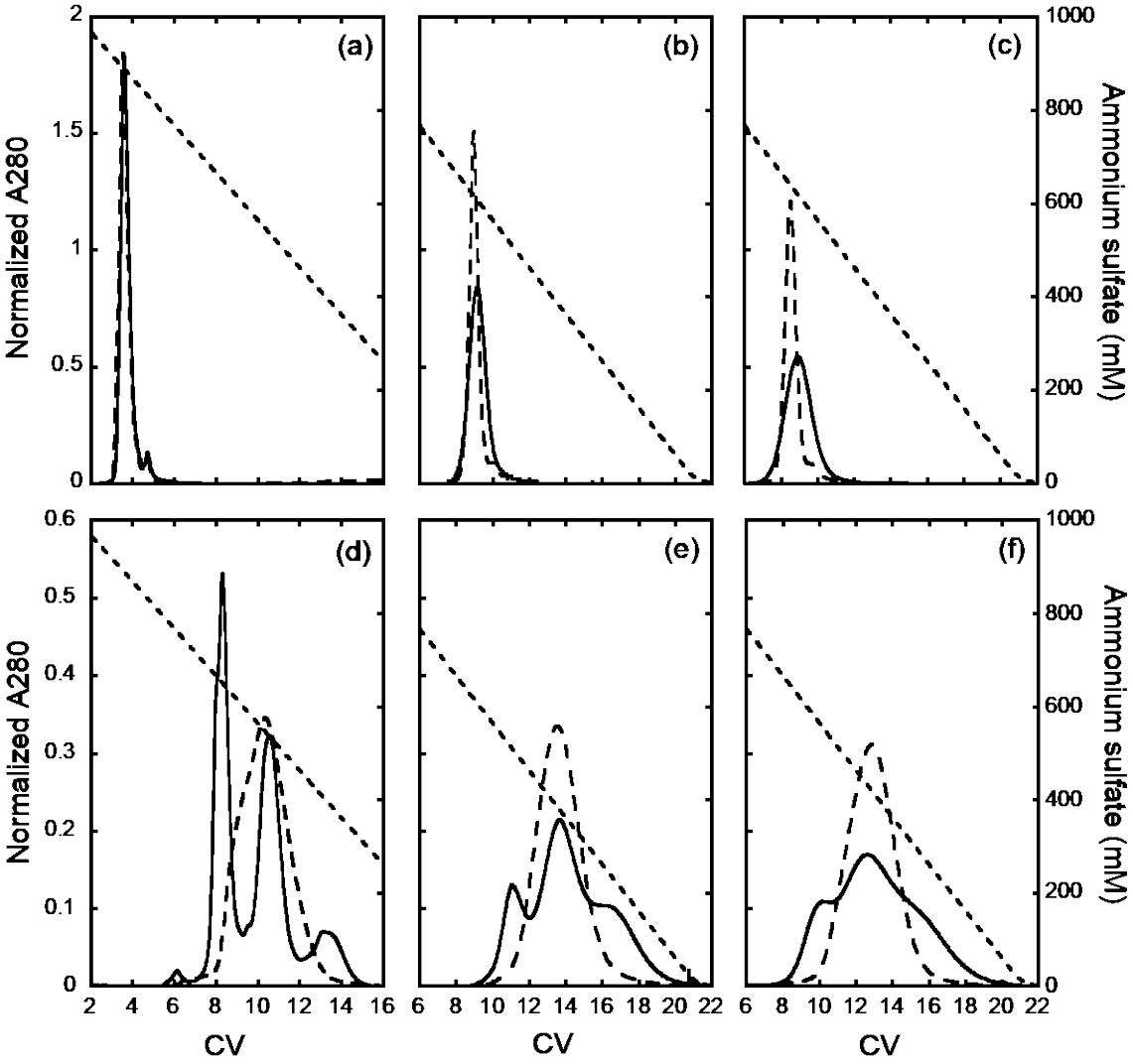

Figure 5.2. Elution behavior of the framework IgG in each of the BiSAb molecules (a), (b) and (c) and of BiSA (d), (e), and (f) on the Protein Pak Hi-Res HIC column (a) and (d), the 13.8 cm long PPG-S column (b) and (e), and the 14.6 cm long PPG-M column (c) and (f). Ammonium sulfate gradient from 1000 to 0 mM in 20 CV. Solid lines how the results at 1.0 ml/min and dashed lines show the results at 0.05 ml/min. High and low flow rates correspond to residence times of 0.55 and 11.1 for the Protein Pak Hi-Res HIC column, 2.7 and 54 min for the PPG-S column, and 2.9 and 57 min for the PPG-M column. The masses of protein injected for each panel are: 0.068±0.004, 0.45±0.01, 0.44±0.01, 0.093±0.002, 0.21±0.01, and 0.15±0.01 mg/ml for (a), (b), (c), (d), (e), and (f), respectively. The ammonium sulfate gradient shown by the dotted line is plotted after converting the conductivity trace to concentration using a calibration curve. The A280 absorbance is normalized to the amount of protein injected. Note the different CV-scales.

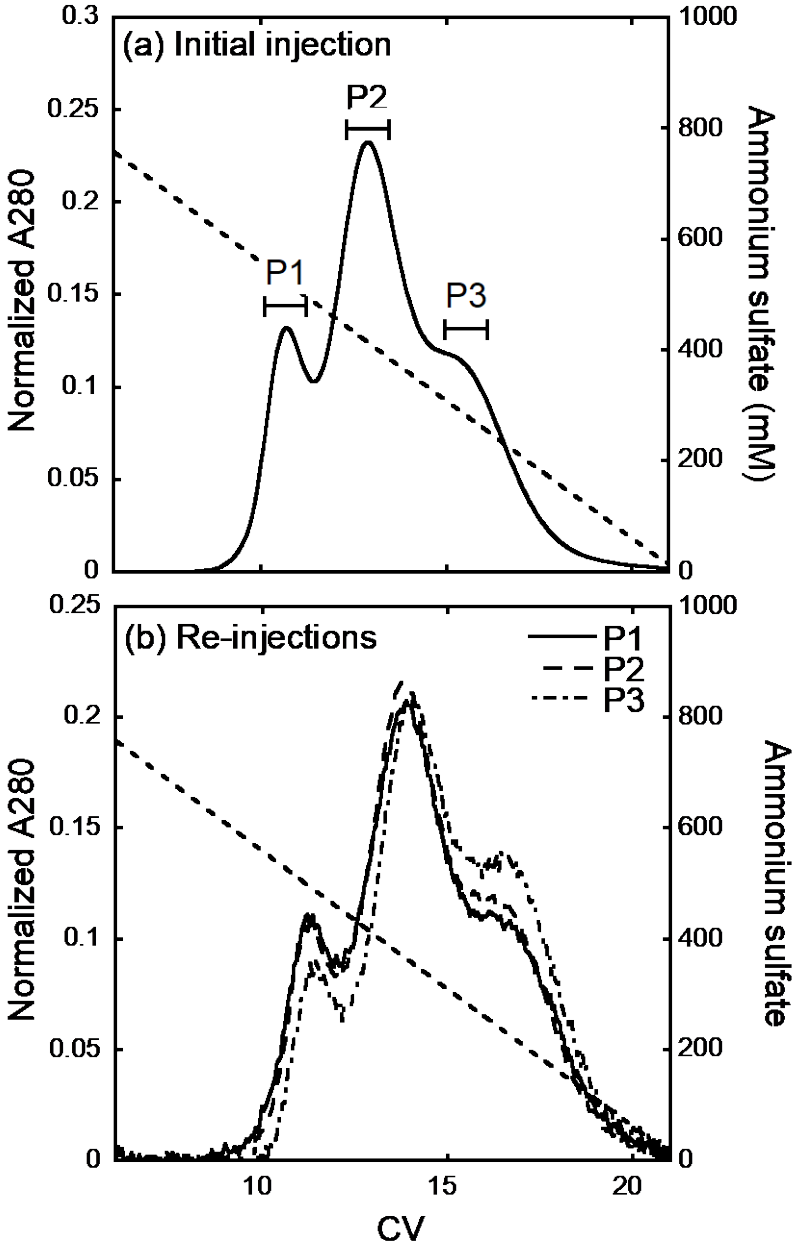

Figure 5.3. (a) Collection of fractions for the three peaks denoted P1, P2, and P3 in order of binding strength obtained for the elution of BiSA from the 13.8 cm long PPG-S column and (b) re-injection of each of the fractions in (a) after a three-fold dilution with load buffer into the same PPG-S column. All runs were with a 1000-0 mM ammonium sulfate gradient in 20 CV at a flow rate of 1.0 ml/min corresponding to a residence time of 2.7 min. Protein mass loads were 1.4 mg/ml for the initial injection and 0.027±0.013 mg/ml for the re-injections. The A280 absorbance is normalized to obtain the same peak area in order to account for slight differences in the amount of protein injected.

Figure 5.4 shows the elution profiles for each of the three BiSAb molecules for the PPG-S column at flow rates of 1.0, 0.5, 0.25, 0.1, and 0.05 ml/min corresponding to residence times of 2.7, 5.4, 10.8, 27, and 54 min, respectively, all with a 1000 to 0 mM ammonium sulfate gradient in 20 CVs. Although there are some differences in retention and peak breadth between the three different BiSAb molecules, in all three cases, the three partially overlapped peaks obtained at 1 ml/min, gradually merge into two peaks, then into a single skewed peak, and finally into a single nearly symmetrical peak as the flow rate is decreased from 1 to 0.05 ml/min. For all three molecules, the salt concentration at elution of each peak and, thus, retention of each in CV units remain essentially unchanged for each peak as the flow rate is reduced. Overall, this behavior is, of course, opposite to what is normally encountered in chromatographic separations where, for conditions where mass transfer is dominant, better resolution of multiple independent species is attained at lower flow rates. The fact that, in our case, resolution between peaks decreases as the flow rate is reduced indicates that the elution behavior is controlled by the on-column interconversion of multiple forms of the same molecule. The kinetic rates are evidently on the same order of magnitude as the rates of chromatographic separation. As such, at high flow rates there is insufficient time for interconversion to occur and the different molecular forms elute primarily as separate, independent species. As the flow rate is reduced, more time is available for interconversion leading to a merging of the peaks with reduced resolution between the different molecular forms. At the lowest flow rate, the on-column time during elution is long enough to attain near equilibrium conditions between the different forms, which then elute as a single merged peak.

As seen in Fig. 5.4, by comparing the three different BiSAbs, it is evident that the scFv attachment location affects the salt concentration at elution and, thus, the strength of interaction with the chromatographic surface. At 1 ml/min, the three peaks elute at 540, 380, and 220 mM ammonium

sulfate for BiSA (a), at 570, 450, and 330 mM ammonium sulfate for BiSB (b), and, at 510, 390, and 250 mM ammonium sulfate for BiSC (c). These results indicate that, among the three BiSAb molecules, BiSB, which has the scFv domains linked to the tip of the Fc region of the framework IgG (see Fig. 1.1), exhibits the weakest binding. Based on homology modeling, we have shown that while both the scFv domains and, to a lesser extent, the Fab domain of the framework IgG comprise surface-exposed area with high hydrophobicity (including surface-exposed tryptophan residues) the tip area of the Fc portion is highly charged and relatively non hydrophobic. It is plausible that if the scFv domains are primarily responsible for interaction with the HIC surface, their proximity to the more polar region of the Fc domain is responsible for weaker binding of BiSB compared to BiSA and BiSC. In addition to differences in retention, there also appear to be some difference in the relative magnitude of the three peaks observed at 1 ml/min. As seen in Fig. 5.4, the first eluting peak at 1 ml/min is significantly more pronounced for BiSB, which overall binds more weakly, compared to the peaks obtained for BiSA and BiSC, which overall bind more strongly. This result suggests that the binding strength of the BiSAb molecules influences the relative magnitude of the three peaks with stronger binding species leading to more pronounced generation of later eluting forms.

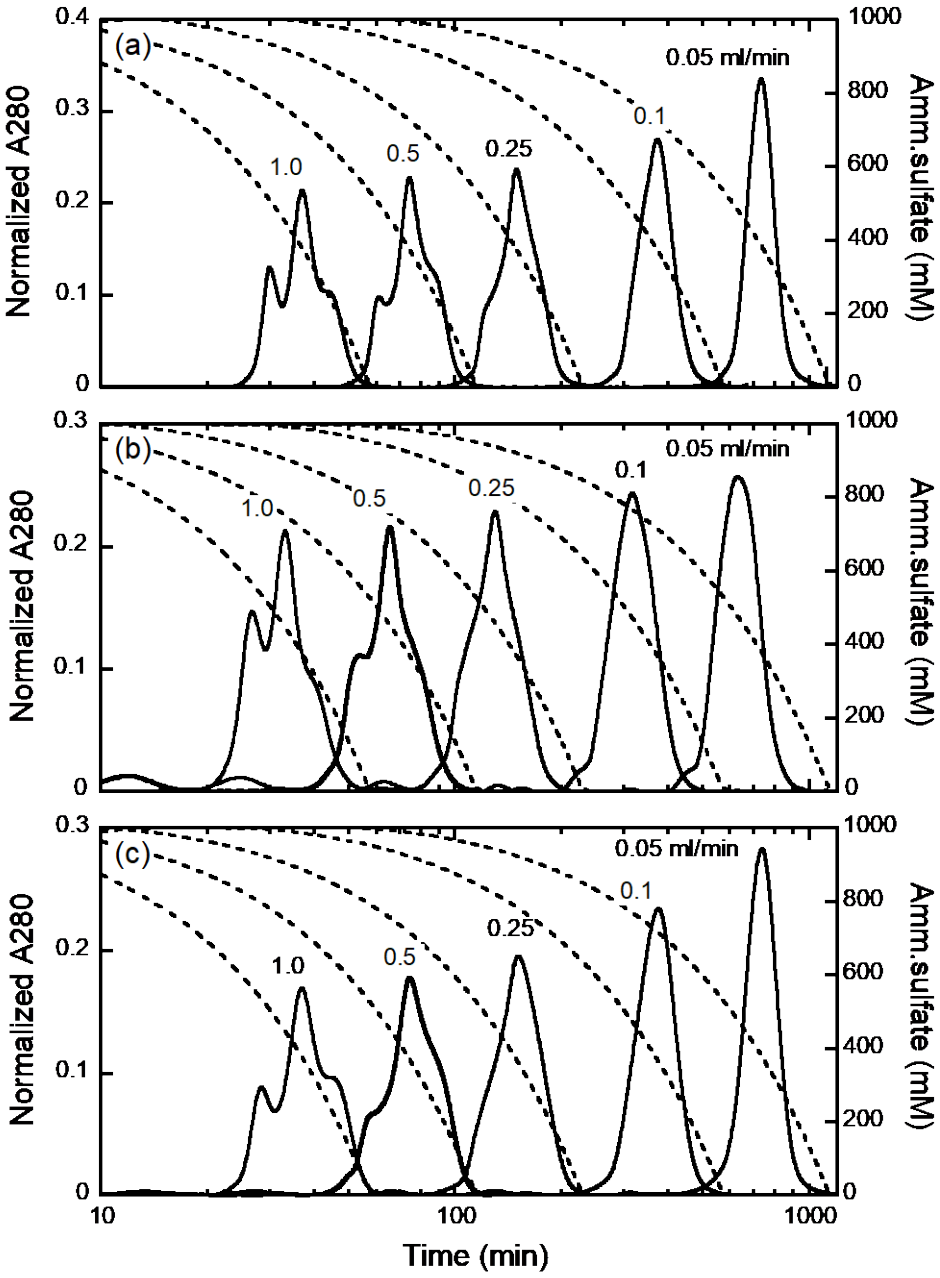

Figure 5.4. Linear gradient elution of (a) BiSA, (b) BiSB, and (c) BiSC for the 13.8 cm long PPG-S column with a 1000-0 mM ammonium sulfate gradient 20 CV at 1.0, 0.5, 0,25, 0.1, and 0.01 ml/min. The corresponding residence times are 2.7, 5.4, 10.8, 27, and 54 minutes. The mass of protein injected was 0.02±0.001 mg/ml in (a) 0.26±0.008 mg/ml in (b), and 0.25±0.01 in (c). The ammonium sulfate gradient shown by the dotted line is plotted after converting the conductivity trace to concentration using a calibration curve. The A280 absorbance is normalized to obtain the same peak area.

Figure 5.5 shows the effect of hold time prior to elution for BiSA on the 5 cm long PPG-S column. A short column and, thus, a short residence time was selected for these experiments in order to emphasize the effects of the length of time spent by the protein bound to the chromatographic surface. Because, for these experiments, the residence time during elution was just 0.98 min there was relatively little time for interconversion between molecular forms in solution phase once elution started. In all cases, the gradient was 1000 to 0 mM ammonium sulfate in 20 CVs. As seen in Fig. 5.5a for three particular cases, a longer hold time resulted in a marked reduction of the first eluted peak with a concomitant marked increase in the third eluting peak. The middle peak remained relatively constant for all three cases shown. Since the three peaks are significantly overlapped, their relative magnitude was quantified, following ref. [3], by fitting each chromatogram to three exponentially-modified Gaussian (EMG) curves and determining the relative peak areas. The results are shown in Fig. 5.5b for a range of hold times between 0 and 120 min. As seen in this figure, even if the gradient is started immediately after load (zero hold time), the first and second peaks have comparable areas. Thus, it appears that generation of multiple forms occurs essentially instantaneously upon contact with the chromatographic surface generating three peaks in the 40:40:20 ratio. Holding the protein in the bound state for longer periods of time reduces the first peak and increases the third eventually reaching an apparent equilibrium distribution for hold times longer than 60 min where the three peaks are eluted in a 10:45:45 ratio. This gradual shift toward the more strongly retained forms is consistent with a consecutive, kinetically limited interconversion mechanism where the more weakly bound forms are gradually converted into more strongly bound ones until equilibrium is achieved.

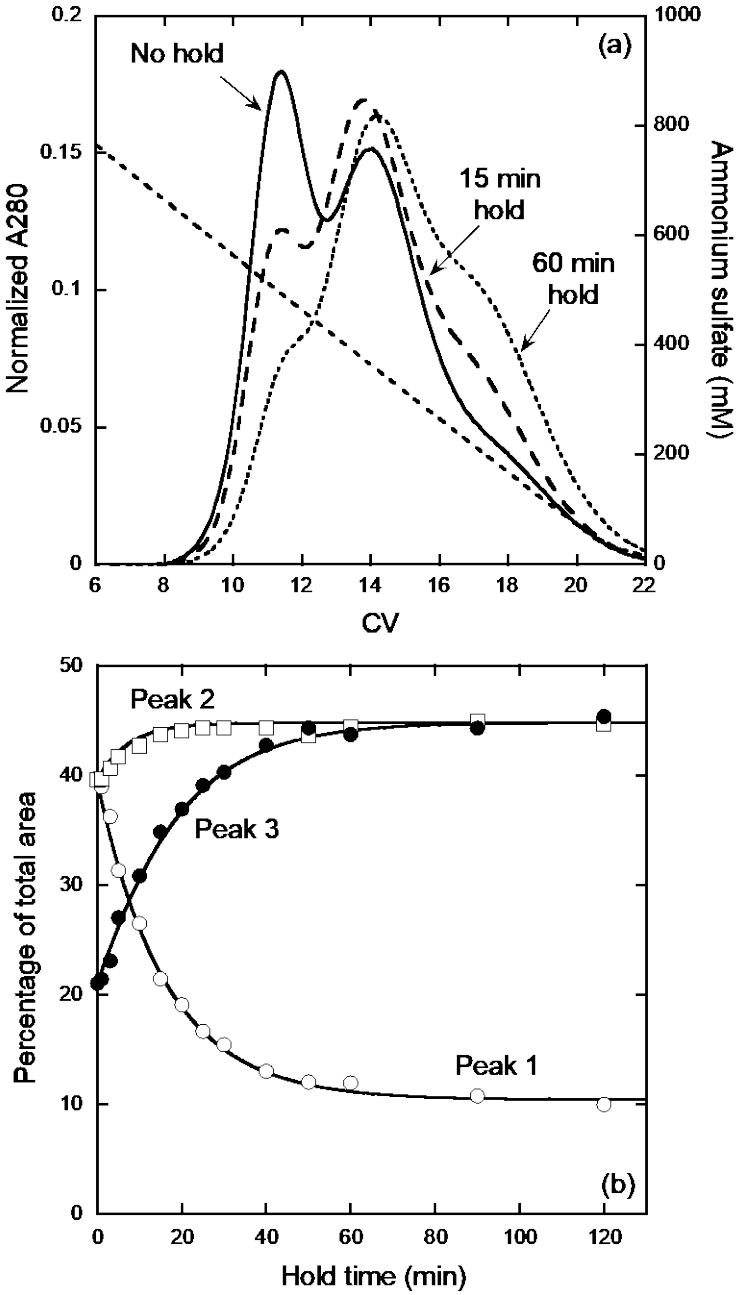

Figure 5.5. Effect of hold time prior to start of the gradient on the elution behavior of BiSA on the 5.0 cm long PPG-S column with a 1000-0 mM ammonium sulfate gradient at 1.0 ml/min. The corresponding residence time is 1 min. (a) Chromatograms obtained with 0, 15, and 60 min hold prior to start of the gradient. (b) Percentage of each peak area relative to the total area as a function of the hold time prior to start of the gradient. Solid lines are calculated from fits of eqs. 5.4-5.6. Protein mass injected was 0.31±0.01 mg/ml.

Figure 5.6 shows the effect of temperature on the elution profile of BiSA for the PPG-S column at a flow rate of 0.5 ml/min corresponding to a residence time of 5.4 min. The temperature was held at either 30 or 45 °C by placing the column in a thermostated compartment. For the 4 °C case, the column as well as the entire chromatographic workstation were placed in a cold room. These temperatures are well within the stability range of BiSA and no precipitation or cloudiness of any kind was seen in BiSA solutions held at these temperatures for prolonged periods of time. As shown in this figure, temperature has dramatic effects on the HIC elution behavior. Between 21 and 45 °C, the main effect of temperature is gradually altering the elution profile from three peaks to a single merged peak without a significant effect on retention. It is likely that increasing temperature speeds up the rate of interconversion of different molecular forms resulting in near equilibrium conditions even at the relatively short residence time of 5.4 min and, thus, resulting in single peak elution. On the other hand, as seen in Fig. 5.6, reducing the temperature to 4 °C substantially reduces retention also largely preventing formation of the third peak. It is well known that, in general, the protein binding strength on HIC columns decreases at lower temperatures since the adsorption process is typically considered to be entropy-driven [4][5][6]. We also expect that the rates of interconversion will be lower at this temperature. The net result is that, because of the weaker binding, both the first and the second peaks elute earlier compared to higher temperatures. At the same time, the weaker binding also hinders formation of the more retained form so that little if any of the protein is eluted in the third peak.

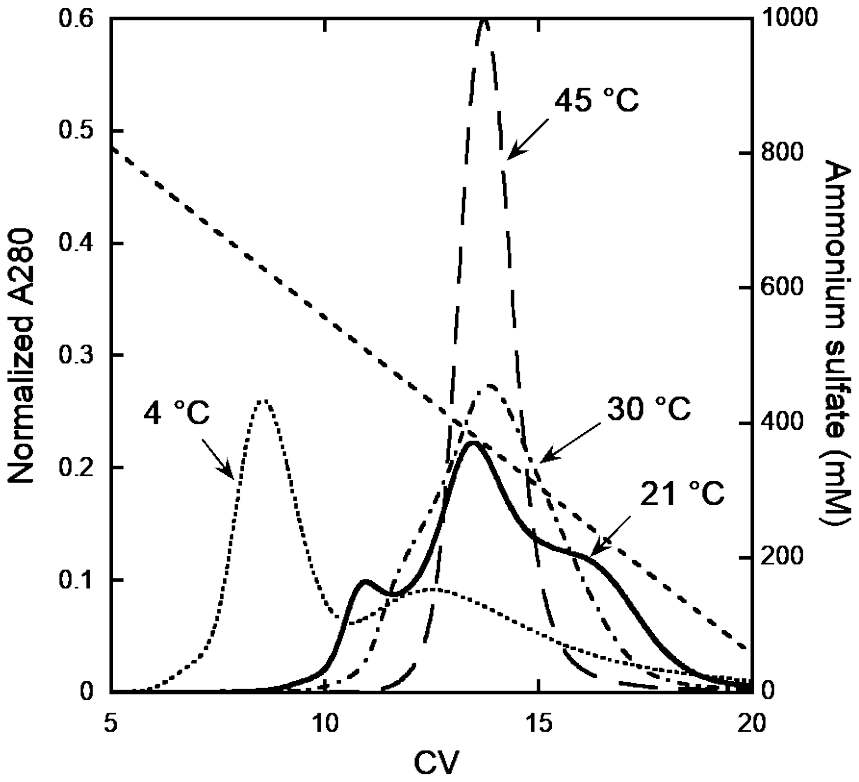

Figure 5.6. Effect of temperature on the elution behavior of BiSA for the 13.8 cm long PPG-S column with a 1000-0 mM ammonium sulfate gradient in 20 CV at a flow rate of 0.5 ml/min. The corresponding residence time is 5.4 min. The mass of protein injected was 0.0022±0.0003 mg/ml. The A280 absorbance is normalized to obtain the same peak area.

Figure 5.7a shows the tryptophan emission spectra at the apex of each peak, normalized by absorbance at 280 nm, collected with the in-line fluorescence monitor during elution of BiSA from the Protein Pak Hi-Res HIC column run at 0.8 ml/min corresponding to a residence time of 0.7 min. Linear gradient conditions are the same as in Fig. 5.2. The corresponding ratio of the maximum fluorescence intensities (F/F1) and spectral shifts at the fluorescence maximum (λ_{max} - $\lambda_{max,1}$) for the second and the third peak relative to the first are shown in Fig. 5.7b superimposed to the three-peak elution profile measured by UV at 280 nm. The data points are the average of three runs and the error bars correspond to the range of values. As seen from this figure, the normalized fluorescence intensity significantly increases from the first to the second and to the third eluted peaks and this increase is accompanied by a red-shift in emission maxima. Both increased tryptophan fluorescence and red spectral shifts are indicative of increased solvent exposure [7]. As shown by homology modeling in Figures 3.9-3.11, tryptophan residues are present both in the scFv domains as well as in the Fab region. The surface exposure of these residues is, however, likely dependent on the configuration of the scFv domains relative to the framework IgG. For example, one could expect greater solvent exposure when the scFv domains are outstretched away from the framework IgG but lower exposure when these domains are collapsed onto the framework IgG. In turn, it is plausible that configurations with two outstretched scFv domains will interact more favorably and, thus, be retained longer than configurations where the two scFv domains are collapsed on the framework IgG surface. Obviously, BiSAb configurations with one scFv domain outstretched and one collapsed on the framework IgG surface would be expected to have binding strength and autofluorescence properties intermediate between the two extreme cases. Because of the symmetry of our BiSAb molecules, we would expect three major peaks, corresponding to two collapsed, one collapsed and one outstretched, and two

outstretched scFv domains. Since the HIC surface is hydrophobic, it is plausible that interaction with the surface with the hydrophobic scFv domain will facilitate conformational change towards the outstretched configurations. During gradient elution, as binding becomes weaker, it is likely that the outstretched configurations are converted back to forms where the scFv domain are collapsed on the framework IgG, which are, likely, more stable in solution. Finally, because these configurations depend on changes in tertiary structure made possible by the flexible linker, rather than unfolding with loss secondary structure, we expect these configurations to be reversibly interconvertible on relatively short time scales.

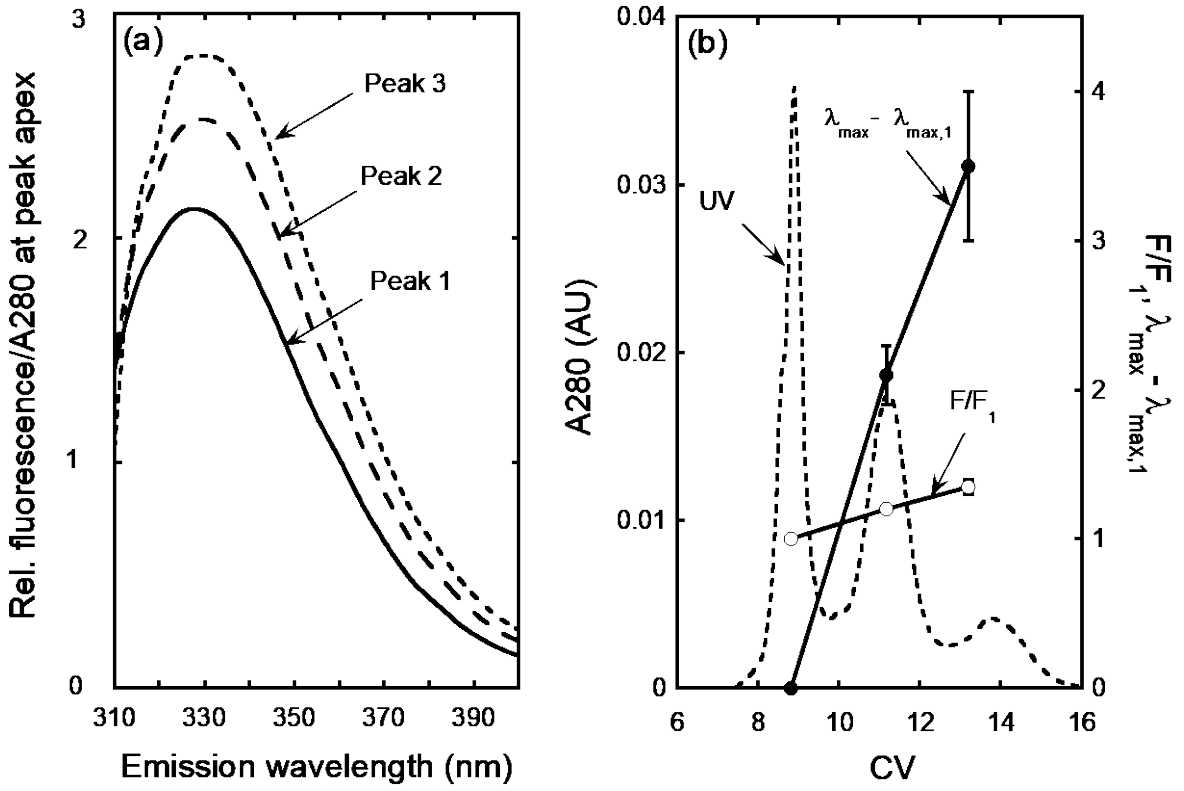

Figure 5.7. In-line auto-fluorescence measurements with excitation at 295 and emission monitored from 310 to 400 nm for BiSA on the Protein Pak Hi-Res HIC column with a 1000-0 mM ammonium sulfate gradient in 20 CV at a flow rate of 0.8 ml/min corresponding to a residence time of 0.7 min. (a) Emission spectra of each eluted peak at the peak maximum normalized by the corresponding UV280 absorbance. (b) UV280 chromatogram with overlaid normalized fluorescence intensity (F/F_1) and wavelength shift at maximum fluorescence ($\lambda_{max} - \lambda_{max,1}$) relative to peak 1. Data points in (b) are the averages of triplicate runs and error bars correspond to their range. The protein mass load was 0.034±0.01 mg/ml.

5.4 Modeling

Based on the similarities noted between CEX and HIC, a three-binding state phenomenological model, analogous to that developed for CEX in section 2.3.2, was developed to describe the BiSAb elution behavior observed for HIC columns. The main goal is to help confirm our hypothesis that the multiple peaks result from the existence of three different binding states of the same molecule. The model framework differs from the previous CEX model mainly with regards to the expression used to represent protein retention by using an isotherm relevant for HIC media. Analogous models have been proposed by Haimer et al. to describe multiple peak elution resulting from protein unfolding [8] and by McCue et al. [9] to describe irreversible unfolding of monomer and aggregate species of a recombinant fusion protein.

Physically, we hypothesize that the three binding states correspond to configurations of the scFv differing where none, one, or two of the scFv domains are outstretched away from the framework IgG being increasingly able to interact with the resin. We focus on the elution behavior of BiSA on PPG-S column at room temperature, which gave a reasonable separation of the eluted peaks while still preserving the characteristics of a resin for preparative applications. The model is limited to low protein loads assuming that the protein-resin interaction can be described by a linear isotherm dependent only on the ammonium sulfate concentration.

The four components of our model are the isotherm model to predict retention of each form, a model to describe the interconversion of the different forms on the chromatographic surface and in solution, a model to describe transport in the resin pores, and a column mass balance for each species. Since the model contains many parameters, in order to avoid over-fitting, where possible, we obtained each parameter for experimental conditions where we expected the parameter of interest to be a dominant factor.

In the model, we consider three molecular forms, 1, 2, and 3, corresponding to the first, second, and third eluted peaks, which interconvert into each according to the following scheme:

$$P_1 \rightleftharpoons P_2 \rightleftharpoons P_3$$

We assume that the same scheme applies to both the solution phase with first order rate constants k_1 and k_2 and equilibrium constants K_1 and K_2 for the first and second reaction, respectively, and to the chromatographic surface with corresponding first order rate constants $\bar{k}_1$ and $\bar{k}_2$ and equilibrium constants $\bar{K}_1$ and $\bar{K}_2$. The solvophobic theory [5][6] was chosen to represent the adsorption isotherm for each of these forms. At high salt and low protein loads, this theory reduces to the following exponential relationship between the Henry constant or distribution coefficient, $K_{a,i}$, describing partitioning between the solution and the chromatographic surface, and the ammonium sulfate concentration C_M:

$$K_{a,i} = A_i e^{\lambda_i C_M} \tag{5.1}$$

where A_i and λ_i are molecule-specific parameters. For each form, the adsorbed concentration, q_i, is related to the fluid phase concentration, C_i, by the equation:

$$q_i = K_{a,i} C_i \tag{5.2}$$

With a negative linear ammonium sulfate gradient, the following relationship is obtained between the normalized gradient slope, $\gamma' = (1-\varepsilon)\left(C_M^f - C_M^0\right)/CV_G$, and the ammonium sulfate concentration at elution, $C_{M,i}^R$ [10]:

$$C_{M,i}^{R} = -\frac{\ln\left(-\gamma' A_i \lambda_i\right)}{\lambda_i} \tag{5.3}$$

where C_M^0 and C_M^f are the initial and final ammonium sulfate concentrations, respectively, and CV_G is the duration of the gradient in CV units. According to eq. 5.3, a plot of $\ln\left(-\gamma'\right)$ vs. $C_{M,i}^{R}$ is linear with slope $-\lambda_i$ and intercept $\ln\left(A_i \lambda_i\right)$. Figure 5.8 shows the chromatograms at varying gradient slope conducted with 10, 15, 20, 25, and 40 CV gradients at 1.0 ml/min in the 13.8 cm column. Figure 5.9 shows the experimentally determined $C_{M,i}^{R}$values for each of the three peaks measured by fitting three exponentially modified Gaussian curves to each chromatograms. Since the residence time was short in these runs (2.7 min), there was minimal on-column interconversion during elution so that three distinct peaks were obtained with all five gradients. As seen in Fig. 5.9, the $\ln\left(-\gamma'\right)$ vs. $C_{M,i}^{R}$ plots are linear for all three forms in agreement with eq. 5.3. This agreement suggests that, for these conditions, although the relative size of each peak will depend on the rate of interconversion, the salt concentration at elution is determined only by the equilibrium relationship describing the interaction of each protein form with the resin. Table 5.1 summarizes the fitted values of A_i and λ_i. As seen from these values, while form 1 is bound more weakly at a given salt concentration, as shown by its smaller value of A, its retention is also more sensitive to salt concentration, as shown by its larger value of λ. As seen form Table 5.1, for form 3 binding is stronger, but less sensitive to the ammonium sulfate concentration. Form 2 has an intermediate behavior between that of form 1 and form 3 with regards to binding strength and sensitivity to ammonium sulfate concentration.

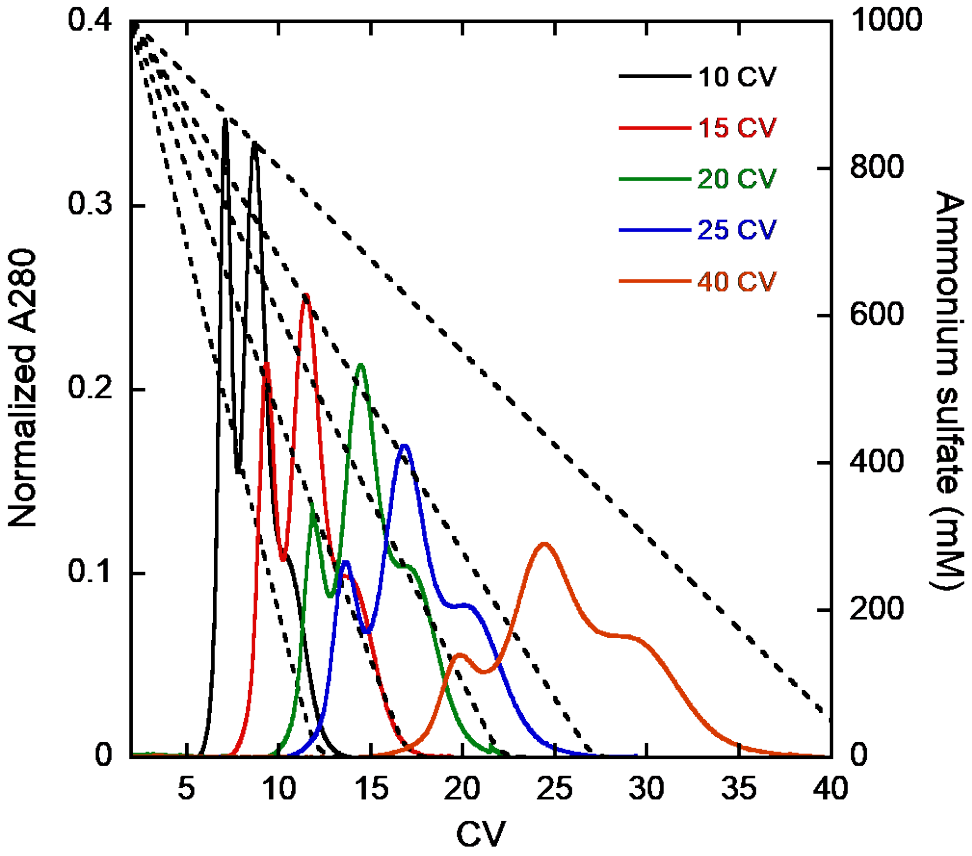

Figure 5.8. Effect of gradient slope on the elution of BiSA on the13.8 cm long PPG-S column with 1000-0 mM ammonium sulfate gradients in 10, 15, 20, 25, and 40 CV operated at a flow rate of 1.0 ml/min corresponding to a residence time of 2.7 minutes. The mass of protein injected was 0.20±0.007 mg/ml. Ammonium sulfate concentration shown on the right hand y-axis is plotted after conversion from the conductivity trace using a standard curve. The A280 absorbance is normalized to obtain the same peak area.

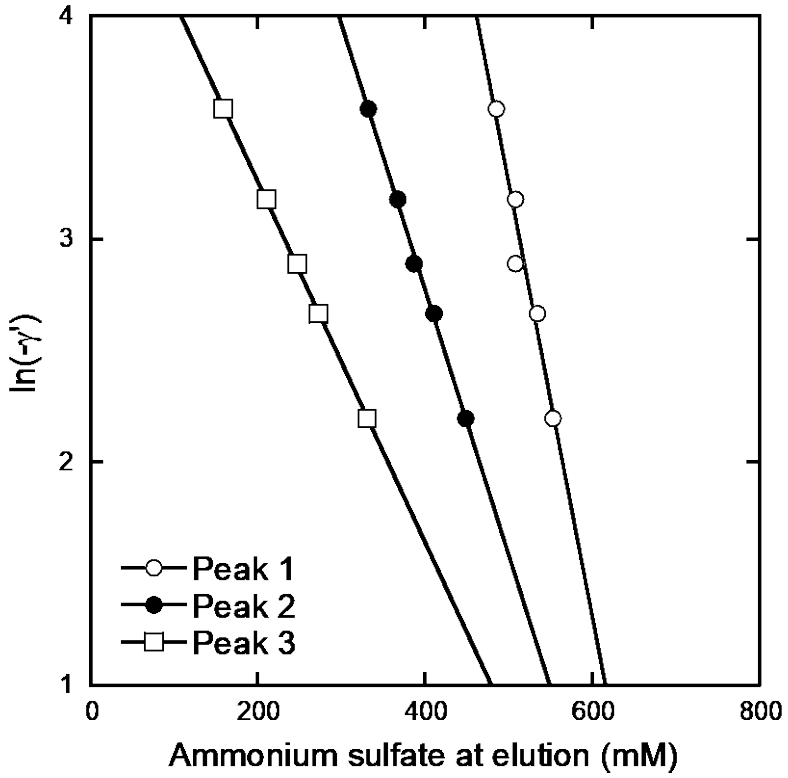

Figure 5.9. Plot of the natural logarithm of the normalized gradient slope, γ', in mM units vs. the ammonium sulfate concentration at elution, $C_{M,i}^{R}$, for each BiSA peak eluted from the 13.8 cm PPG-S column with 1000-0 mM ammonium sulfate gradients in 10, 15, 20, 25, and 40 CV at a flow rate of 1.0 ml/min. The corresponding residence time is 2.7 min. Solid lines are based on eq. 5.3. The regressed parameters A_i and λ_i are given in Table 5.1.

Table 5.1. Parameter values estimated for BiSA on the PPG-S columns.

Parameter	Peak 1	Peak 2	Peak 3
A	0.00012	0.045	0.94
λ (mM^{-1})	0.019	0.012	0.0081
k_1 (s^{-1})	0.0025		
k_2 (s^{-1})	0.0001		
$\bar{k}_1$ (s^{-1})	0.001		
$\bar{k}_2$ (s^{-1})	0.001		
K_1	1.0		
K_2	0.25		
$\bar{K}_1$	4.3		
$\bar{K}_2$	1.0		

The next component of the model is a description of the three-state reversible interconversion which is assumed to occur both in the adsorbed phase and in solution. As seen from the short-column, short-residence time experiments in Fig. 5.5, the distribution of the different molecular forms responsible for each peak varies with the hold time on the chromatographic surface. Neglecting interconversion during elution, we describe the interconversion on the chromatographic surface according to the following equations:

$$\frac{\partial q_1}{\partial t} = -\bar{k}_1\left(q_1 - \frac{q_2}{\bar{K}_1}\right) \tag{5.4}$$

$$\frac{\partial q_2}{\partial t} = \bar{k}_1\left(q_1 - \frac{q_2}{\bar{K}_1}\right) - \bar{k}_2\left(q_2 - \frac{q_3}{\bar{K}_2}\right) \tag{5.5}$$

$$\frac{\partial q_3}{\partial t} = \bar{k}_2\left(q_2 - \frac{q_3}{\bar{K}_2}\right) \tag{5.6}$$

Initial conditions for these equations are based on the initial distribution of the three peaks with zero hold time (see Fig. 5.5b). The four constants $\bar{k}_1$, $\bar{k}_2$, $\bar{K}_1$, and $\bar{K}_2$ were regressed to the data in Fig. 5.5b and are summarized in Table 5.1. Calculated lines are shown in Fig. 5.5b. As seen in this figure, the model equations provide a reasonable description of the peak distribution.

The next consideration is the description of interconversion in solution. One can, of course, write equations analogous to eqs. 5.4-6. However, more insight can be obtained by first examining the merged chromatographic peaks that are obtained for each of the BiSAb molecules at long residence times with a 20 CV gradient (see Fig. 5.10). These experiments were repeated for BiSA at 0.05 ml/min, corresponding to 54 min residence time, for gradient lengths of 10, 20, 40, and 80 CV. Figure 5.10 shows the chromatograms. Each of these gradients gave a single merged peak with

salt concentration at elution varying as a function of gradient slope. As shown in Appendix of ref. [11], assuming that local interconversion equilibrium is established, the relationship between the normalized gradient slope and the salt concentration at elution is given by the following integral expression:

$$-\gamma' = \int_{C_M^0}^{C_M^R} \frac{1 + K_1 + K_1 K_2}{K_{a,1} + K_{a,2} K_1 + K_{a,3} K_1 K_2} dC_M \tag{5.7}$$

where K_1 and K_2 are equilibrium constant for the conversion of form 1 into form 2 and of form 2 into form 3, respectively, in solution. Integrating this equation with the expressions of $K_{a,i}$ in eqs. 5.1 and 5.2 using the A_i and λ_i from Table 5.1 provides the line shown in Fig. 5.11. The values of K_1=1 and K_2=0.25 used for this calculation were found by fitting and appear to represent the behavior of the merged peak well. Obviously, the rate constants in solution cannot be determined from these data at near equilibrium conditions and are obtained, instead, by fitting the overall model prediction to the chromatographic data for conditions where multiple peaks are observed.

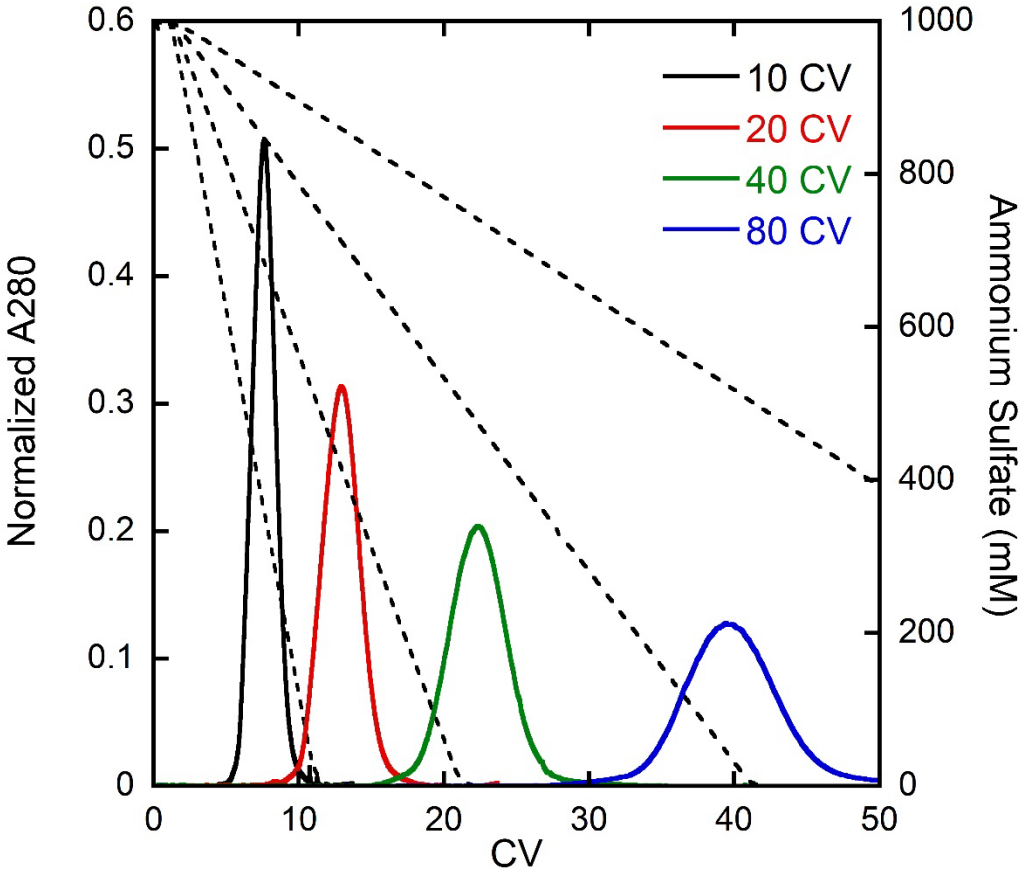

Figure 5.10. Effect of gradient slope on the elution of BiSA on the 13.8 cm long PPG-S column with 1000-0 mM ammonium sulfate gradients in 10, 20, 40, and 80 CV operated at a flow rate of 0.05 ml/min corresponding to a residence time of 54 minutes. The mass of protein injected was 0.30±0.02 mg/ml. Ammonium sulfate concentration shown on the right hand y-axis is plotted after conversion from the conductivity trace using a standard curve. The A280 absorbance is normalized to obtain the same peak area.

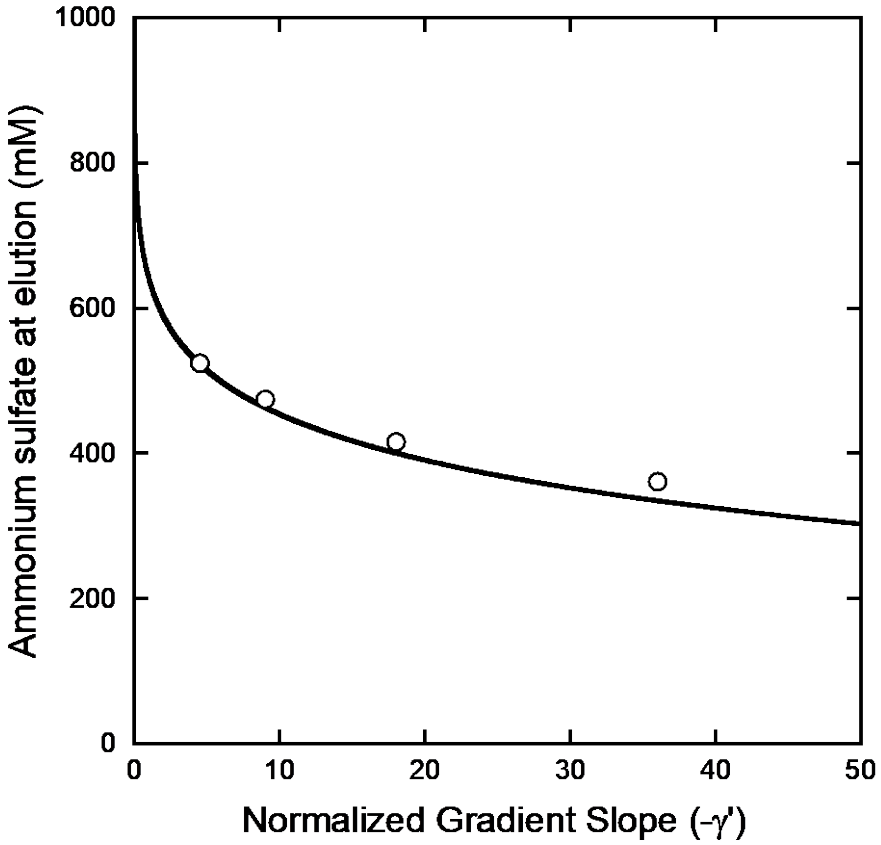

Figure 5.11. Ammonium sulfate concentration at elution of the merged BiSA peak eluted from the 13.8 cm long PPG-S column with 1000-0 mM ammonium sulfate gradients in 10, 20, 40, and 80 CV at a flow rate of 0.05 ml/min. The corresponding residence time is 54 min. The solid line is based eq. 7. The regressed values of the K_1 and K_2 parameters are given in Table 5.1.

Next, we consider the description of mass transfer between solution and adsorbed phase. As in the case of CEX, we assume that pore diffusion is the dominant transport mechanism and use the linear driving force (LDF) approximation as a description of mass transfer [12]:

$$\frac{\partial \hat{q}_i}{\partial t} = \frac{15 D_e}{r_p^2}\left(C_i - C_i^*\right) \tag{5.8}$$

where $\hat{q}_i = q_i + \varepsilon_p C_i$ is the concentration in the resin particles including both adsorbed molecules and those partitioned into the pore fluid, D_e is the effective pore diffusivity in the particle, r_p, is the particle radius, and C_i^* the solution concentration at equilibrium with $\hat{q}_i$. Ideally, D_e could be determined by measuring the protein HETP as a function of flow rate for conditions where there is no retention and, thus, no interconversion, as we did in Chapter 2 for BiSA with CEX resins. In the present case, however, unfortunately we could not find conditions where BiSA was not retained, as relatively strong binding occurred even in the absence of ammonium sulfate. This behavior is not unusual for hydrophobic proteins (e.g. see ref. [13]), but would complicate the analysis for BiSA since band broadening would be affected by interconversion. In order to circumvent this problem, we determine D_e from nonbinding HETP measurements using a relatively hydrophilic mAb available in our lab as a model protein. Since the pore size of the PPG-S is relatively large (75 nm according to the manufacturer [14]), we anticipate that the small difference in size between the mAb (~5.5 nm in hydrodynamic radius [15]) and BiSA (~6.2 nm in hydrodynamic radius) would not greatly affect diffusional hindrance. As seen in Fig. 5.12, the HETP determined form isocratic pulse injections of this mAb in 50 mM Na_3PO_4 at pH 7 without addition of ammonium sulfate increases linearly with flow rates indicating that band broadening for this mAb is mas-transfer controlled. The corresponding value of D_e, obtained from the linear slope of this relationship as described in ref. [10] was $D_e = 5.3 \times 10^{-8}$ cm^2/s.

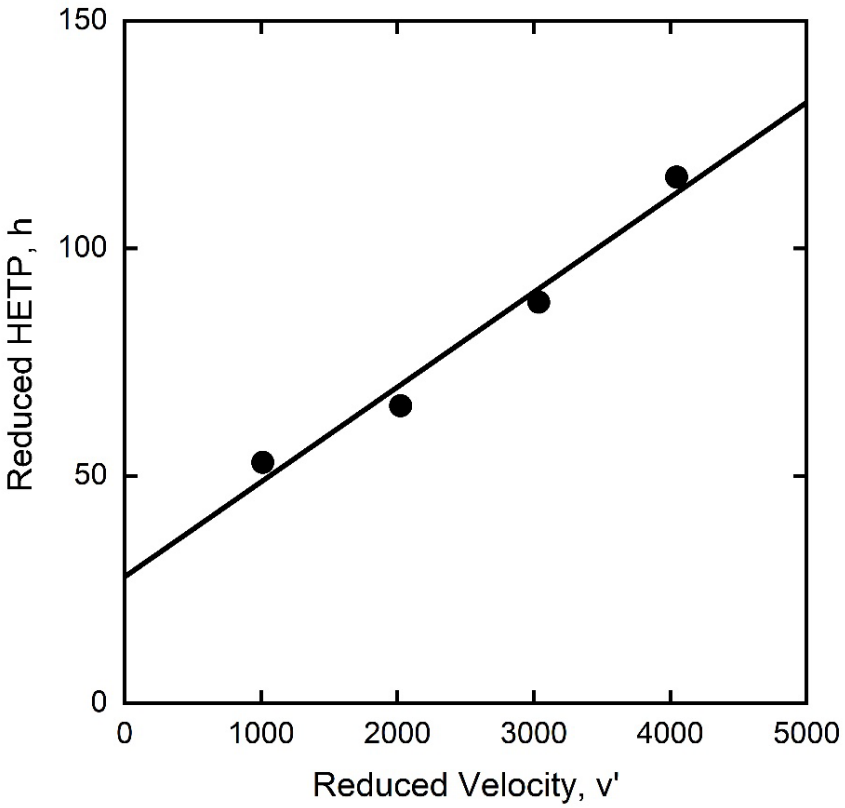

Figure 5.12. van Deemter plot of a mAb on the 13.8 cm long PPG-S column. Isocratic pulse injections performed at nonbinding conditions (50 mM Na_3PO_4, pH 7.0) were performed at varying reduced velocity. The reduced HETP is calculated using the moment method.

Finally, the D_e-value of BiSA was estimated by scaling the value determined for the mAb according to the ratio of hydrodynamic radii of the two molecules giving $D_e = 4.7\text{x}10^{-8}$ cm^2/s. As an approximation, the same value was assumed for all three forms hypothesized with collapsed or outstretched scFv domains.

The final component of the overall model are the material balances expressed by the following equations

$$\frac{\partial \hat{q}_1}{\partial t} = \frac{15 D_e}{r_p^2}\left(C_1 - C_1^*\right) - \bar{k}_1\left(q_1 - \frac{q_2}{\bar{K}_1}\right) \tag{5.9a}$$

$$\frac{\partial \hat{q}_2}{\partial t} = \frac{15 D_e}{r_p^2}\left(C_2 - C_2^*\right) + \bar{k}_1\left(q_1 - \frac{q_2}{\bar{K}_1}\right) - \bar{k}_2\left(q_2 - \frac{q_3}{\bar{K}_2}\right) \tag{5.9b}$$

$$\frac{\partial \hat{q}_3}{\partial t} = \frac{15 D_e}{r_p^2}\left(C_3 - C_3^*\right) + \bar{k}_2\left(q_2 - \frac{q_3}{\bar{K}_2}\right) \tag{5.9c}$$

$$\varepsilon\frac{\partial C_1}{\partial t} = -\varepsilon v\frac{\partial C_1}{\partial x} - (1-\varepsilon)\frac{15 D_e}{r_p^2}\left(C_1 - C_1^*\right) - \varepsilon k_1\left(C_1 - \frac{C_2}{K_1}\right) \tag{5.10a}$$

$$\varepsilon\frac{\partial C_2}{\partial t} = -\varepsilon v\frac{\partial C_2}{\partial x} - (1-\varepsilon)\frac{15 D_e}{r_p^2}\left(C_2 - C_2^*\right) + \varepsilon k_1\left(C_1 - \frac{C_2}{K_1}\right) - \varepsilon k_2\left(C_2 - \frac{C_3}{K_2}\right) \tag{5.10b}$$

$$\varepsilon\frac{\partial C_3}{\partial t} = -\varepsilon v\frac{\partial C_3}{\partial x} - (1-\varepsilon)\frac{15 D_e}{r_p^2}\left(C_3 - C_3^*\right) + \varepsilon k_2\left(C_2 - \frac{C_3}{K_2}\right) \tag{5.10c}$$

where x is the column axial coordinate. The model equations above reduce to the limiting cases used to determine most of the parameters. The remaining parameters describing the rates of inter-conversion in solution, k_1 and k_2, were determined by comparing the numerical solution of the full model equations (eqs. 5.9 and 5.10) with the experimental elution data. The numerical solution

was obtained discretizing eqs. 5.10a-10c by Euler backward finite differences and integrating the corresponding set of ordinary differential equations using MATLAB's multistep, variable order ODE solver, ode15s. Since backwards discretizations introduces numerical dispersion [16][17], the number of discretizations was set equal to the number of theoretical plates found experimentally from a salt pulse injection for each column, 350, 170, and 300 for the 13.8 cm long PPG-S column, the 5.0 cm long PPG-S column, and the 14.6 cm long PPG-M column, respectively. The ammonium sulfate gradient was simulated assuming ideal conditions due the its small size and, hence, high effective diffusivity expected to yield virtually the same results as rigorous calculations due to the slow mass transfer of large BiSAb proteins compared to salt [18].

Figure 5.13 compares model predictions using the parameters summarized in Table 5.1 and experimental data for BiSA gradient elution runs on the PPG-S columns under different conditions. Panels (a) and (b) compare short and long residence times (2.7 and 54 min) with no hold time for the 13. 8 cm PPG-S column. Panels (c) and (d) compare no hold and 60 min hold conditions with a 0.98 min residence time. In agreement with the data, for panels (a) and (b) the model predicts three distinct peaks at a residence time of 2.7 min and a single, nearly symmetrical peak at 54 min residence time. For panels (c) and (d) the model predicts trends in agreement with the experimental data with respect to the effect of hold time prior to start of the gradient. These data were obtained for the short PPG-S column (5.0 cm column length) and high flow rate (1 ml/min), leading to a very short residence time. Quantitatively, the agreement is only approximate, likely because of differences in packing quality for this short column. Nevertheless, the experimentally observed trend of an increased percentage of protein eluting in the third peak and a decreasing percentage of protein eluting in the first peak at increased hold times is predicted by the model.

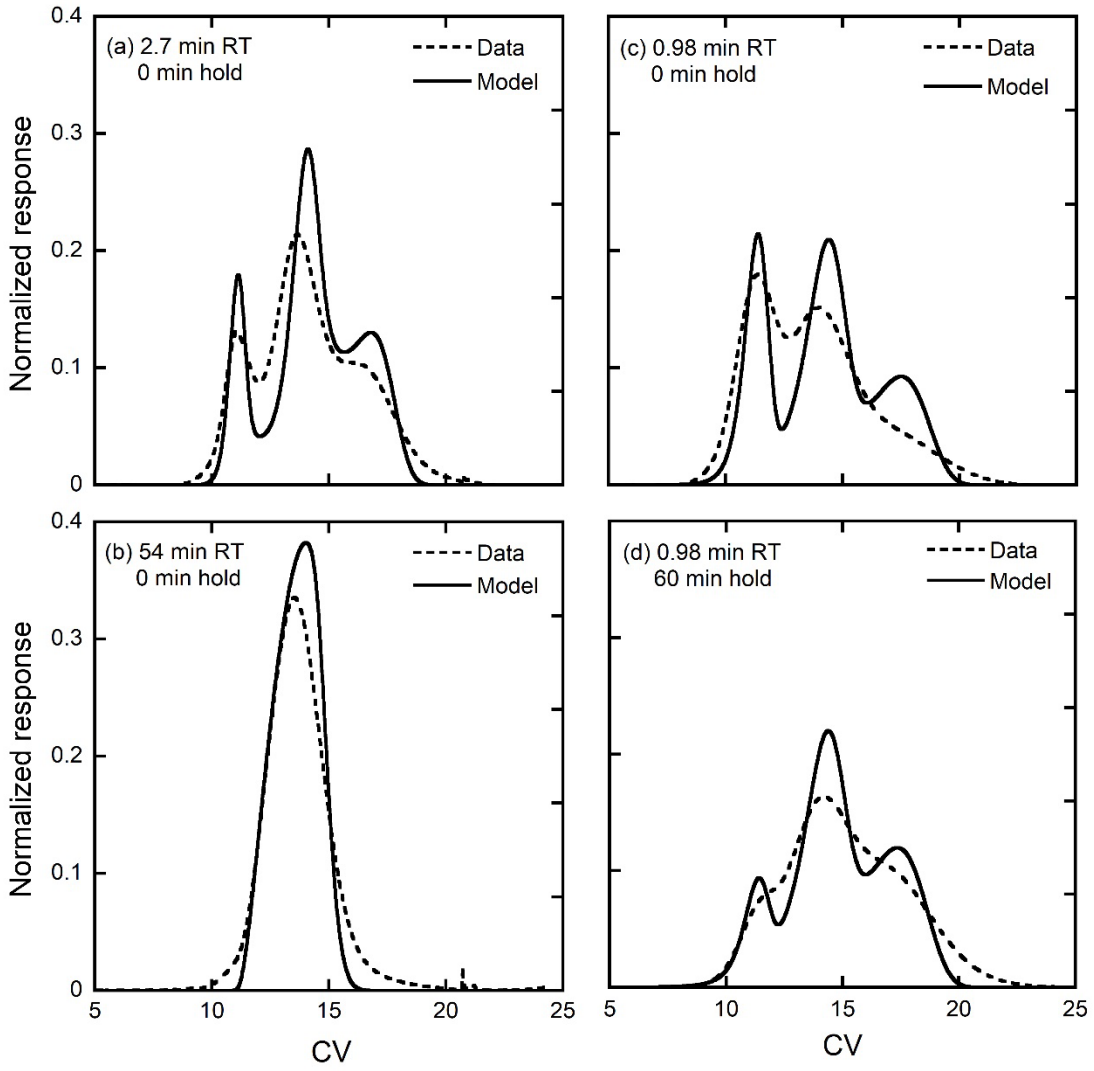

Figure 5.13. Comparison of predicted and experimental elution profiles for BiSA on different PPG-S columns with a 1000-0 mM ammonium sulfate gradient in 20 CV at different flow rates, column lengths, and hold times. Panel (a) and (b) are for the 13.8 cm PPG-S column and panels (c) and (d) are for the 5.0 cm PPG-S column. Model parameters are from Table 5.1. Experimental and predicted curves are normalized to the same peak area for comparison. For simplicity, the ammonium sulfate gradient is not shown but was in nearly perfect agreement with the model.

Figure 5.14 compares the PPG-M experimental results at short and long residence times (2.9 and 57 min) with curves predicted by the model using the same parameters determined for PPG-S except for the particle diameter that as adjusted from 33 to 73 μm. As seen in this figure, except for a slight difference in retention, which is expected because of the slightly lower apparent hydrophobicity of PPG-M compared to PPG-S, the experimental trends observed for the PPG-M column with respect to residence time are well predicted by the model. In comparison to the PPG-S profiles, at the short residence time of 2.9 min, the model predicts broader peaks compared to those predicted for the PPG-S column as a result to the greater effects of mass transfer due to the larger particle size of the PPG-M resin. This effect leads to lower resolution between the three peaks observed at the shorter residence times, also in agreement with the experimental data. As seen in Fig. 5.14b, the model predicts that increasing the residence time to 57 min by reducing the flow rate leads to the elution of a nearly symmetrical peak. For both cases in Fig. 5.14, shifting the predicted peaks to the left by about 1.8 CV units brings experimental and predicted peaks in close quantitative agreement. Despite this difference, which is expected because of the slightly different hydrophobicity of the two PPG resins, the fact that the model captures the experimental trends indicates that the underlying mechanisms leading to the complex elusion behaviors observed for BiSA are the same for both resins and occur at similar rates.

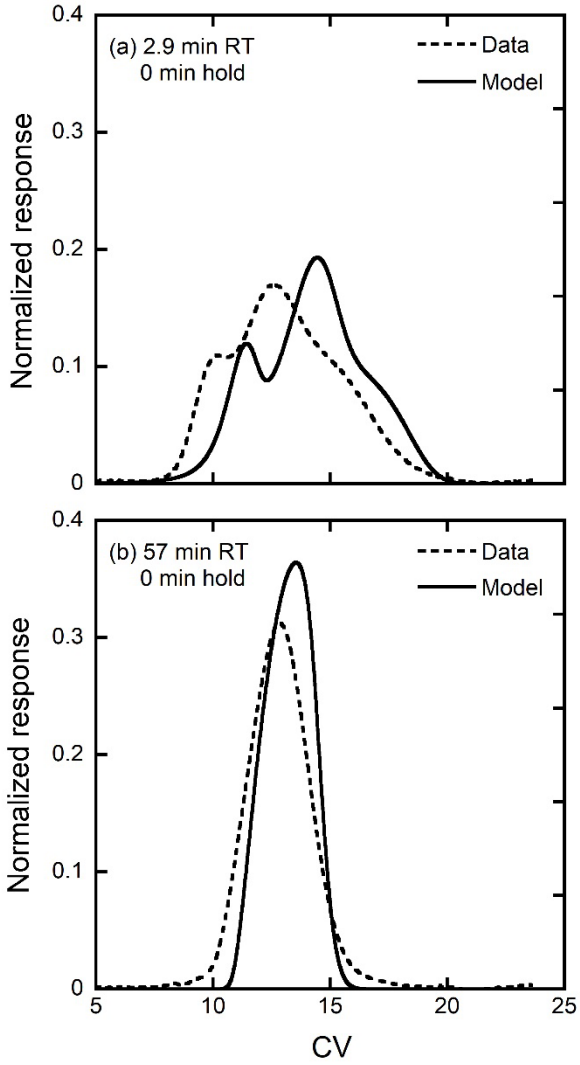

Figure 5.14. Comparison of predicted and experimental elution profiles for BiSA on the PPG-M column with a 1000-0 mM ammonium sulfate gradient in 20 CV at different flow rates. Model predictions are based on the parameters determined for PPG-S in Table 5.1 except for the particle diameter that was set at the experimental value of 73 μm and adjusted column length and corresponding number of discretizations. Note that the model overestimates retention in the column by about 1.8 CV which is due to the slightly lower hydrophobicity of the PPG-M resins compared to PPG-S. Experimental and predicted curves are normalized to the same peak area for comparison. For simplicity, the ammonium sulfate gradient is not shown but was in nearly perfect agreement with the model.

5.5 Comparison between HIC and CEX behavior

Comparing the HIC and CEX behaviors of the BiSAb molecules is instructive and reveals remarkable similarities. Despite the fact that the main protein-surface interaction mechanisms are completely different in the two cases and that protein elution is obtained with an increasing concentration of a chaotropic salt (NaCl) in CEX and with a decreasing concentration of a kosmotropic salt (ammonium sulfate) in HIC, essentially the same three-peak elution behavior is observed. In both instances, the elution behavior is dependent on the residence time, where short residence time elutes three peaks, and residence times on the order of 30 min or longer elute a single peak. Additionally, in both cases, the chromatographic surface is responsible for catalyzing the generation of more strongly retained forms that elute later in the gradient at short residence times. The relative amount of these stronger binding forms increases while bound until an apparent equilibrium state is reached at about 60 min after initial binding. Another remarkable similarity is the effect of temperature which appears to speed up interconversion rates. In both cases, operating at temperatures around 45–55 °C resulted in a single elution peak. Finally, in both cases, the root cause of the three peak elution behavior appears to be related to the scFv configuration relative to the framework IgG surface with outstretched configurations with the scFv domains extended away from the framework IgG being more strongly retained. Tryptophan fluorescence measurements for both HIC and CEX indicate step-wise increases in solvent exposure from the least to most retained peak. These similarities indicate that these behaviors are caused by the molecular properties of these molecules in a manner that is qualitatively independent of the binding mechanism. It is evident that the elution behavior is dependent on a balance of inter-domain interactions (between scFv domain and framework IgG) and domain-chromatographic surface interactions.

5.6 References

[1] L.K. Kimerer, T.M. Pabst, A.K. Hunter, G. Carta, Chromatographic behavior of bivalent bispecific antibodies on hydrophobic interaction chromatography columns, J. Chromatogr. A. 1617 (2020) 460836. doi:10.1016/j.chroma.2019.460836.

[2] G. Carta, A.R. Ubiera, T.M. Pabst, Protein Mass Transfer Kinetics in Ion Exchange Media : Measurements and Interpretations, Chem. Eng. Technol. Rev. 28 (2005) 1252–1264.

[3] Y. Kalambet, Y. Kozmin, K. Mikhailova, I. Nagaev, P. Tikhonov, Reconstruction of chromatographic peaks using the exponentially modified Gaussian function, J. Chemom. 25 (2011) 352–356.

[4] D. Haidecher, A. Vailaya, C. Horvath, Temperature effects in hydrophobic interaction chromatography, Proc. Natl. Acad. Sci. 93 (1996) 2290–2295.

[5] W.R. Melander, C. Horvath, Salt effect on hydrophobic interactions in precipitation and chromatography of proteins: an interpretation of the lyotropic series, Arch. Biochem. Biophys. 183 (1977) 200–215.

[6] W.R. Melander, D. Corradini, C. Horvath, Salt mediated retention of proteins in hydrophobic interaction chromatography, J. Chromatogr. 317 (1984) 67–85.

[7] M. Weichel, S. Bassarab, P. Garidel, Probing Thermal Stability of MAbs By Intrinsic Tryptophan Fluorescence, Bioprocess Int. (2008) 42–52.

[8] E. Haimer, A. Tscheliessnig, R. Hahn, A. Jungbauer, Hydrophobic interaction chromatography of proteins IV Kinetics of protein spreading, J. Chromatogr. A. 1139 (2007) 84–94.

[9] J.T. McCue, P. Engel, A. Ng, R. Macniven, J. Thommes, Modeling of protein monomer / aggregate purification and separation using hydrophobic interaction chromatography, Biopr. Biosyst. Eng. 31 (2008) 261–275.

[10] G. Carta, A. Jungbauer, Protein Chromatography, 2nd ed., Wiley-VCH, Weinheim, Germany, 2020.

[11] L.K. Kimerer, T.M. Pabst, A.K. Hunter, G. Carta, Chromatographic behavior of bivalent bispecific antibodies on cation exchange columns. I. Experimental observations and phenomenological model, J. Chromatogr. A. 1601 (2019) 121–132.

[12] M.D. LeVan, G. Carta, J.A. Ritter, K.S. Walton, Section 16 Adsorption and Ion Exchange, in: D.W. Green, M.Z. Southward (Eds.), Perry's Chem. Eng. Handb., 9th ed., McGraw Hill, 2018.

[13] A. Creasy, J. Lomino, G. Barker, A. Khetan, G. Carta, Gradient elution behavior of proteins in hydrophobic interaction chromatography with U-shaped retention factor curves, J. Chromatogr. A. 1547 (2018) 53–60.

[14] Principles of hydrophobic interaction chromatography, Tosoh Biosci. (n.d.). https://www.separations.eu.tosohbioscience.com/solutions/process-media-products/by-

mode/hic (accessed September 8, 2019).

[15] J.M. Reck, T.M. Pabst, A.K. Hunter, X. Wang, G. Carta, Adsorption equilibrium and kinetics of monomer-dimer monoclonal antibody mixtures on a cation exchange resin, J. Chromatogr. A. 1402 (2015) 46–59.

[16] Z. Ma, G. Guiochon, Application of orthogonal collocation on finite elements in the simulation of non-linear chromatography, Comput. Chem. Eng. 15 (1991) 415–426.

[17] M. Czok, G. Guiochon, The physical sense of simulation models of liquid chromatography: propogation through a grid or solution of the mass balance equation, Anal. Chem. 62 (1990) 189–200.

[18] A. Creasy, J. Lomino, G. Carta, Gradient elution behavior of proteins in hydrophobic interaction chromatography with a U-shaped retention factor curve under overloaded conditions, J. Chromatogr. A. 1578 (2018) 28–34.

6 Fragment Separation

6.1 Introduction

Shown in Fig. 2.2, two acidic impurities were resolved in the BiSB sample on cation exchange columns. These impurities were identified as fragments that were formed in the bioreactor during cell culture. The aim of this section is to 1) identify the structure of the fragments via mass spectrometry, 2) compare the linear gradient elution behavior of fragments with intact BiSAb proteins and quantify differences in binding strength to the resin surface, and 3) evaluate multicomponent high load behavior where there is competition for binding sites between protein species. High load equilibrium is measured using adsorption isotherms and kinetics are studied with confocal laser scanning microscopy. Although fairly small differences in binding strength are measured by gradient elution, high selectivity is observed for the intact protein over both fragments at high load. Nearly full displacement of the fragments by the intact protein is also observed using confocal microscopy. This work was published in the Journal of Chromatography A publications as ref. [1].

6.2 Materials and Methods

6.2.1 Materials

Based on analytical cation exchange chromatography, the raw sample contained approximately 74% of the intact species along with 12% and 14% of two early eluting fragments, identified as Fragment 1 and Fragment 2, respectively. The intact species and fragment proteins were isolated by cation exchange chromatography as described below. Analytical size exclusion chromatography (SEC) of the isolated fractions with an Acquity BEH 200 SEC column (Waters, Milford, MA, USA), performed using a Waters Acquity H-Class UPLC system at 0.3 ml/min with

a running buffer containing 100 mM Na_2PO_4 with 200 mM NaCl at pH 7, showed absence of aggregated species. The cation exchange resins used in this work are ProPac WCX-10 (Dionex Corporation, Sunnyvale, CA, USA) and Nuvia HR-S (BioRad Laboratories, Hercules, CA, USA).

6.2.2 Methods

The fragments and the intact species were isolated by collecting fractions of the eluate from linear gradient elution runs with the Nuvia HR-S column using an ÄKTA Pure 25 system (Cytiva, Marlborough, MA, USA). The gradient used was 0-125 mM NaCl over 20 CV in 10 mM Na_2PO_4 buffer at pH 7 with an 8 mg/ml load of the BiSB protein sample. The fractions collected were analyzed first by intact mass spectrometry. For this purpose, each fraction (2 µg) was first run on an Acquity BEH 300 C4 reversed phase column (Waters, Milford, MA, USA) using an Acquity I-Class UPLC system also from Waters at a flow rate of 0.15 ml/min, with in-line mass spectrometry using a Q Exactive HF-X mass spectrometer (ThermoFisher Scientific, Waltham, MA, USA) operated in positive polarity, full scan mode. The scan range of precursor ions was set at 600-5000 *m/z* with resolving power of 15,000. Intact masses of biomolecules were obtained from spectra deconvolution using Intact Mass software (Protein Metrics Inc., Cupertino, CA, USA).

The isolated proteins were further characterized at the domain level using a “middle-up” approach by coupling immunoglobulin degrading IdeS enzyme digestion with mass spectrometry. Towards this, each isolated sample was first enzymatically cleaved using the IdeS Fabricator enzyme from Genovis AB (Cambridge, MA, USA) by mixing the enzyme with the sample for 1 hr at 37 °C [22][23]. The Fabricator enzyme cleaves IgG1 specifically between glycines 243 and 244 generating a $(Fab)_2$ fragment and a mixture of Fc-scFv and $(Fc\text{-}scFv)_2$ domains. The latter results from strong non-covalent interactions between the Fc heavy chain domains. After enzymatic digestion, each cleaved sample was injected into a Waters Acquity BEH 300 C4 reversed phase

column and eluted with a 22-min linear gradient (mobile phase A: 0.1% formic acid in water; mobile phase B: 0.1% formic acid in acetonitrile) using the same UPLC system and in-line MS system described above. Measured masses were identified using the Intact Mass software along with an in-house developed fragment identifier software.

Chromatographic methods were performed as described in 2.2.2. The method for obtaining adsorption isotherms follows that of section 4.2. The confocal microscopy method described in section 4.2 was altered to multicomponent use for this section. The isolated species fragment 1, fragment 2, and intact protein were labeled with AlexaFluor 633, Rhodamine Green-X, and Rhodamine Red-X, respectively. All labels are amine reactive and were purchased from ThermoFisher Scientific (Waltham, MA, USA). In each case, the protein was concentrated to between 4 and 8 mg/ml with an Amicon Ultracel centrifugal filter (MilliporeSigma, MO, USA), buffer exchanged to 500 mM $NaHCO_3$ at pH 8.5, and mixed with the fluorescent dye in a ratio of 1:3 mole dye per mole of protein for 1 hr. The unreacted dye was then removed by SEC using EconoPac DG-10 gravity desalting columns (Bio-Rad Laboratories, Hercules, CA, USA). The resulting labeling ratios, measured with the NanoDrop 2000 UV-Vis spectrophotometer, were 0.29, 0.37, and 0.07 for the intact protein and for the two fragments, respectively. Different amounts of each labeled protein were mixed with the raw BiSB sample to obtain a labelling ratio of 1 labeled protein molecule to 160 unmodified protein molecules for each species. The ensuing kinetic experiment followed the same protocol mixing protein sample with a small amount of resin and imaging with a Zeiss LSM 510 microscope (Carl Zeiss MicroImaging, LLC, Thornwood, NY, USA) using excitation lasers at 561, 488, and 633 nm to visualize intact protein and the two fragments, respectively.

6.3 Results and Discussion

6.3.1 Fragment Identification

Figure 6.1 shows the whole protein mass spectra of the three isolated species along with their corresponding putative structures. As seen from this figure, the observed masses are in good agreement with the theoretical masses calculated based on the known sequence. Both fragments identified are consistent with a structure where one of the heavy chains was clipped which removed a linker and a scFv. The difference between the fragments is one residue: a C-terminal lysine. C-terminal lysine is a common source of heterogeneity in monoclonal antibodies which is caused by reduced carboxypeptidase activity in the cell culture supernatant [2][3].

Figure 6.2 shows the RP-HPLC of each isolated protein following digestion with the IdeS enzyme, which cleaves selectively below the hinge region of the framework IgG. The corresponding masses are also shown for each major peak along with the deduced structure. For the intact protein, the main peak corresponds to the $(Fab)_2$ fragment, to the $(Fc\text{-}scFv)_2$ fragment, and to the Fc-scFv fragment. As shown previously in Chapter 3, digesting with this enzyme does not completely dissociate the Fc heavy chains, so it is not surprising that residual $(Fc\text{-}scFv)_2$ is observed. For both fragment 1 and 2, the main peaks are the $(Fab)_2$ fragment, the Fc-scFv fragment, and the Fc fragment. For fragment 2, the mass of the Fc fragment is consistent with the presence of an additional C-terminal lysine. Figure 6.3 shows analytical UPLC-SEC of the isolated samples. SEC chromatograms show molecular sizes consistent with the masses of the intact protein and of the two fragments determined by MS. The fragments are smaller, and thus able to access larger pore space in the SEC resin media causing them to emerge from the column later than the intact protein. A leading shoulder for fragment 2 shows a small amount of intact protein is in the sample

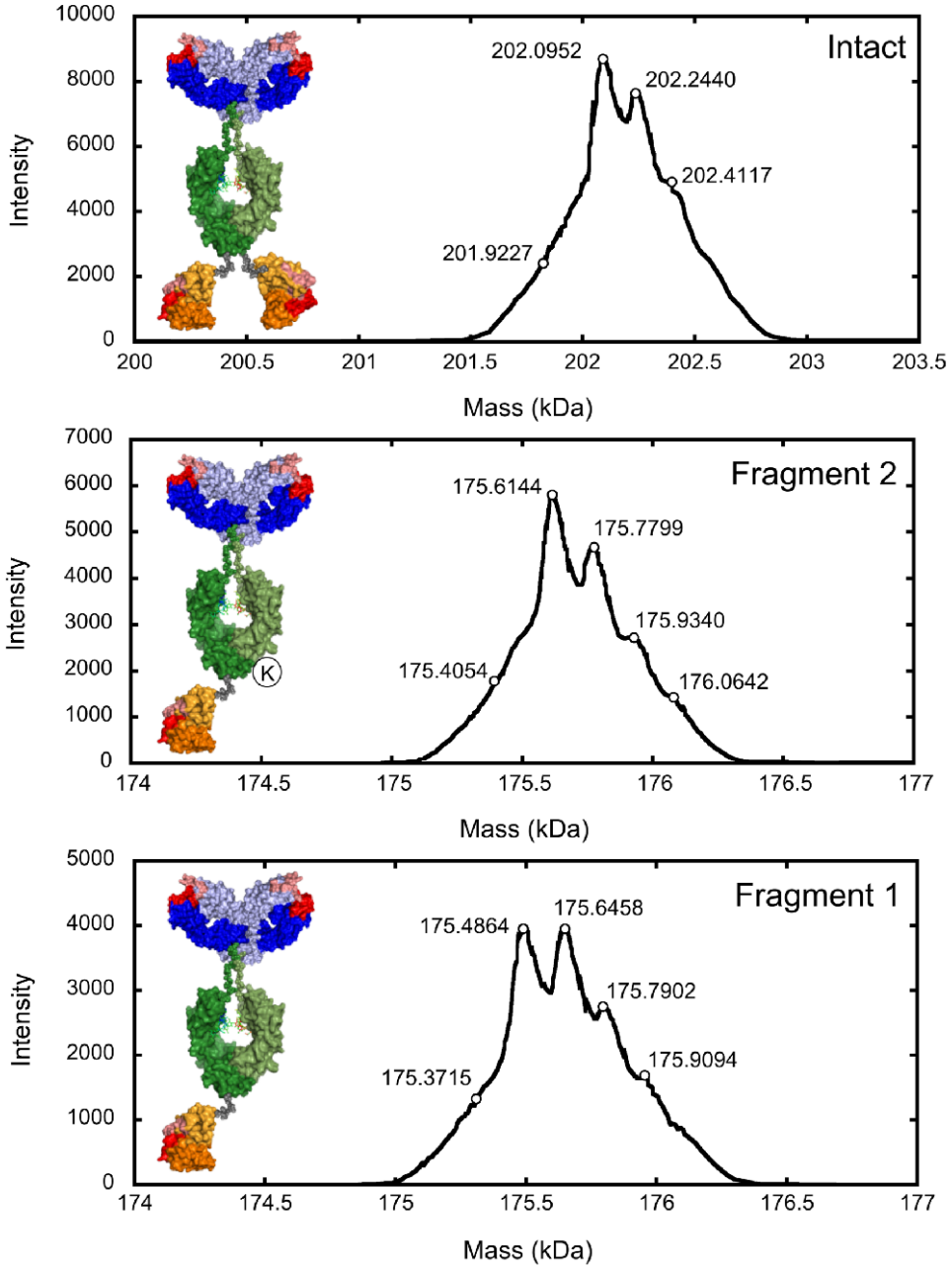

Figure 6.1. Structure and whole-protein MS spectra of the intact protein (top), fragment 2 (middle), and fragment 1 (bottom). The Fab domain is shown in blue, the CDR region in red, the Fc domain in green, and the scFv domains in orange. Theoretical masses are 202.095 kDa for the intact protein, 175.614 for fragment 2, and 175.486 for fragment 1. Different peaks within each panel correspond to the intact protein with different glycoforms (G0F/G0F, G0F/G1F, etc.).

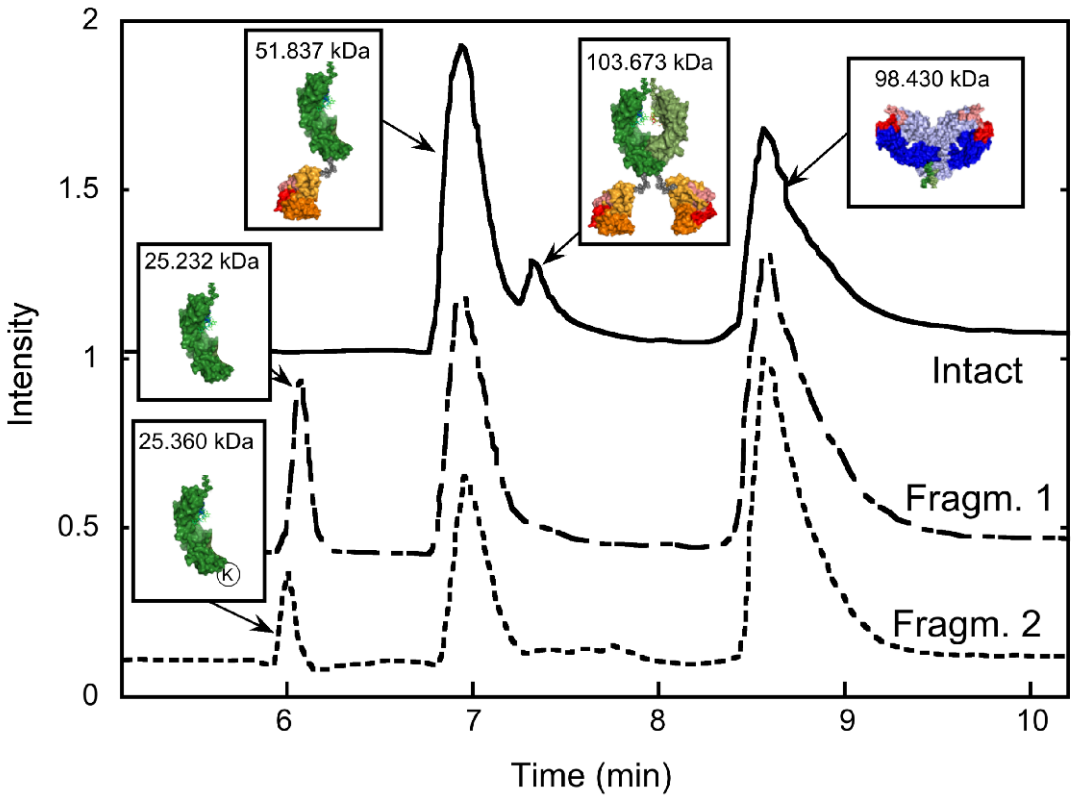

Figure 6.2. Overlaid reversed phase HPLC chromatograms for the intact protein, for fragment 1, and for fragment 2 preceded by digestion with IdeS, which cleaves below the hinge region. Insets show the masses obtained from non-reduced MS analysis of each major peak and the corresponding structures. The fragments identified are: $(Fab)_2$ (98.430 kDa), $(Fc\text{-}scFv)_2$ (103.673 kDa), Fc-scFv (51.837 kDa), Fc (25.232 kDa), and Fc-K (25.360 kDa).

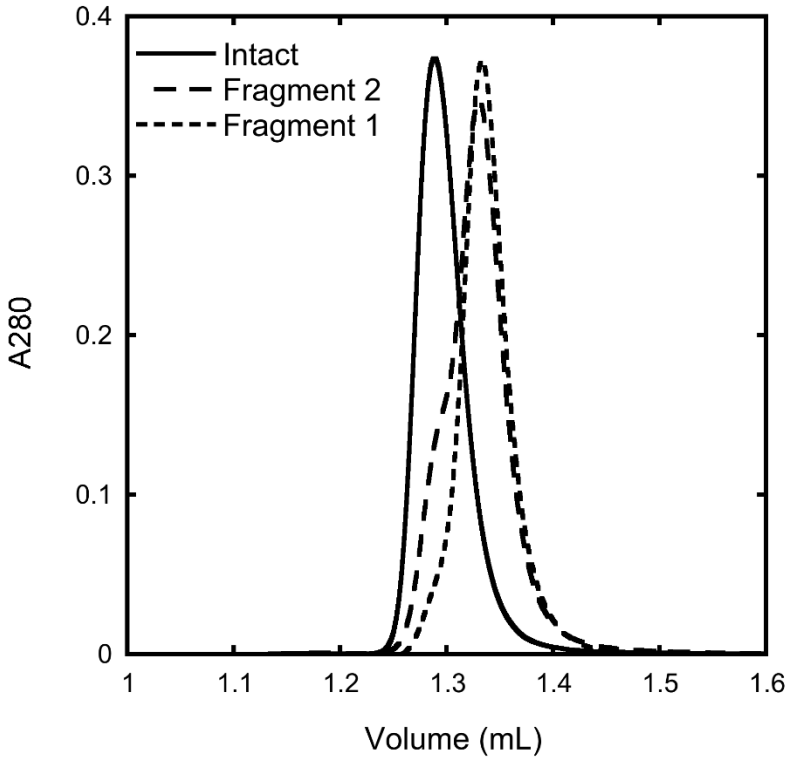

Figure 6.3. UPLC-SEC analysis of isolated fragment 1, fragment 2, and intact protein with an Acquity BEH 200 SEC column operated at 100 mM Na_2PO_4, 200 mM NaCl, pH 7 at 0.3 ml/min.

6.3.2 Chromatographic Behavior

Figure 6.4 shows the gradient elution behavior of the raw BiSAb sample and of the isolated protein species on the ProPac WCX-10 at 0.5 ml/min, which corresponds to a residence time of 2.5 min (panels a and b), and on the Nuvia column at 2.0 ml/min, which corresponds to a residence time of 1.5 min (panels c and d). The pellicular structure and ensuing higher-resolution capability of the ProPac column demonstrates important features of the eluted peaks. As seen in this figure, the raw sample comprises five major peaks. The first two peaks correspond to the isolated fragments 1 and 2, while the last three peaks correspond to the intact protein. Re-injection of the two early-eluting fractions obtained from the Nuvia column, each containing an isolated fragment, results in two major distinct peaks on the ProPac column (Fig. 6.4b). On the other hand, re-injection of the intact species fraction from the Nuvia column into the ProPac column results in three major peaks. A shoulder is also seen for some of the peaks. This shoulder peak occurs, at least in part, because the purity of the isolated fractions is not absolute. These more detailed features of the ProPac elution behavior are not visible with the Nuvia column as a result of its larger particle size, porous structure, and, thus, more limited resolution capability. Due to increased mass transfer effects leading to broader peaks for Nuvia HR-S, each set of multiple peaks on the ProPac column appears as a single, broader peak on the Nuvia column.

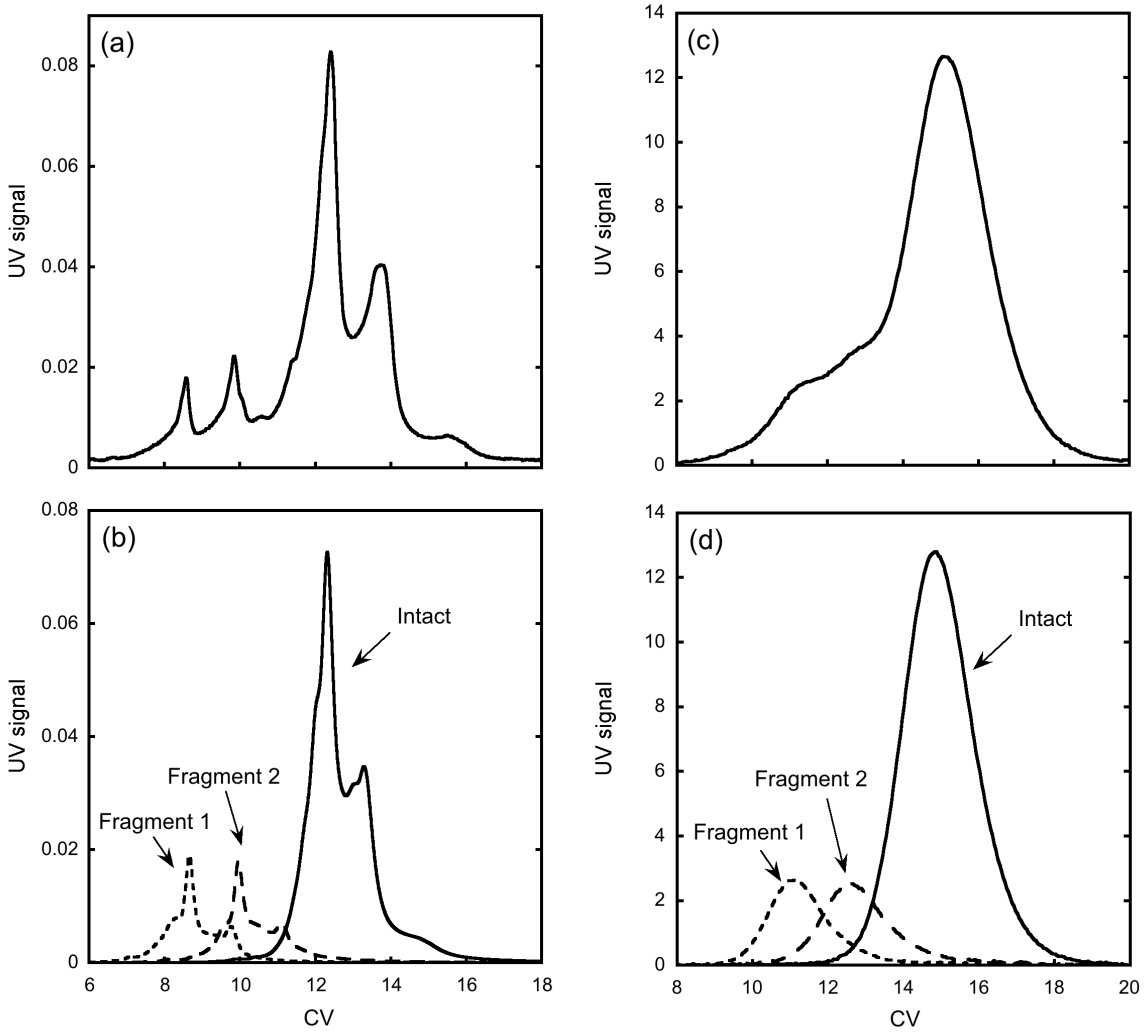

Figure 6.4. Gradient elution results for the raw BiSB sample (a and c) and for the isolated species (b and d) with 0-125 mM NaCl gradients in 20 CV. Panels (a) and (b) are for the ProPac column at 0.5 ml/min corresponding to a 2.5 min residence time. Panels (c) and (d) are for the Nuvia HR-S column at 2.0 ml/min corresponding to a 1.5 min residence time. Protein loads in (a) and (b) were 0.12, 0.05, 0.013, and 0.023 mg/ml for the raw sample, intact, fragment 2, and fragment 1, respectively. Protein loads in (c) and (d) were 0.12, 0.1, 0.02, and 0.02 mg/ml for the raw sample, intact, fragment 2, and fragment 1, respectively.

Figure 6.5 shows the effect of flow rate on the ProPac chromatography of the raw sample (a) and of each of the isolated species (b, c, and d). In all four cases, multiple peak elution is observed for each component at the higher flow rate of 0.5 ml/min. However, the peaks corresponding to each individual component merge into a single, somewhat tailing peak at the lower flow rate of 0.05 ml/min. When two scFv domains are present, as in the intact species, the molecule can exist in three extreme configurations – one with both scFv domains extended away from the framework IgG, one with one scFv extended away and the other collapsed onto the IgG framework, and one with both scFv domains collapsed on the IgG framework. As a result, three peaks are eluted, each containing a predominance of one species or the other when the residence time is short compared to the rate of interconversion between the three configurations. In contrast, if only one scFv domain is present, as in the case of the two fragments, only two extreme configurations are possible – one with the scFv extended away and the other with the scFv collapsed onto the framework IgG. The result is that, in this case, two peaks are eluted when the residence time is short compared to the rate of interconversion between the two configurations. At the lower flow rate, when the residence time is longer, the peaks merge and the resulting peak tends to elute as an equilibrium mixture of multiple configurations. In Chapter 3, we showed that a two-peak elution behavior is also observed for a fragment of a BiSAb molecule that contained a single scFv domain, obtained by enzymatic digestion, consistent with the results obtained here for the BiSB fragments. It should be noted that in our reasoning we have considered only the extreme molecular configurations that are possible. In reality, however, an essentially infinite number of intermediate configurations are likely possible leading to peaks that are more spread out that would be expected if only a finite number of configurations existed.

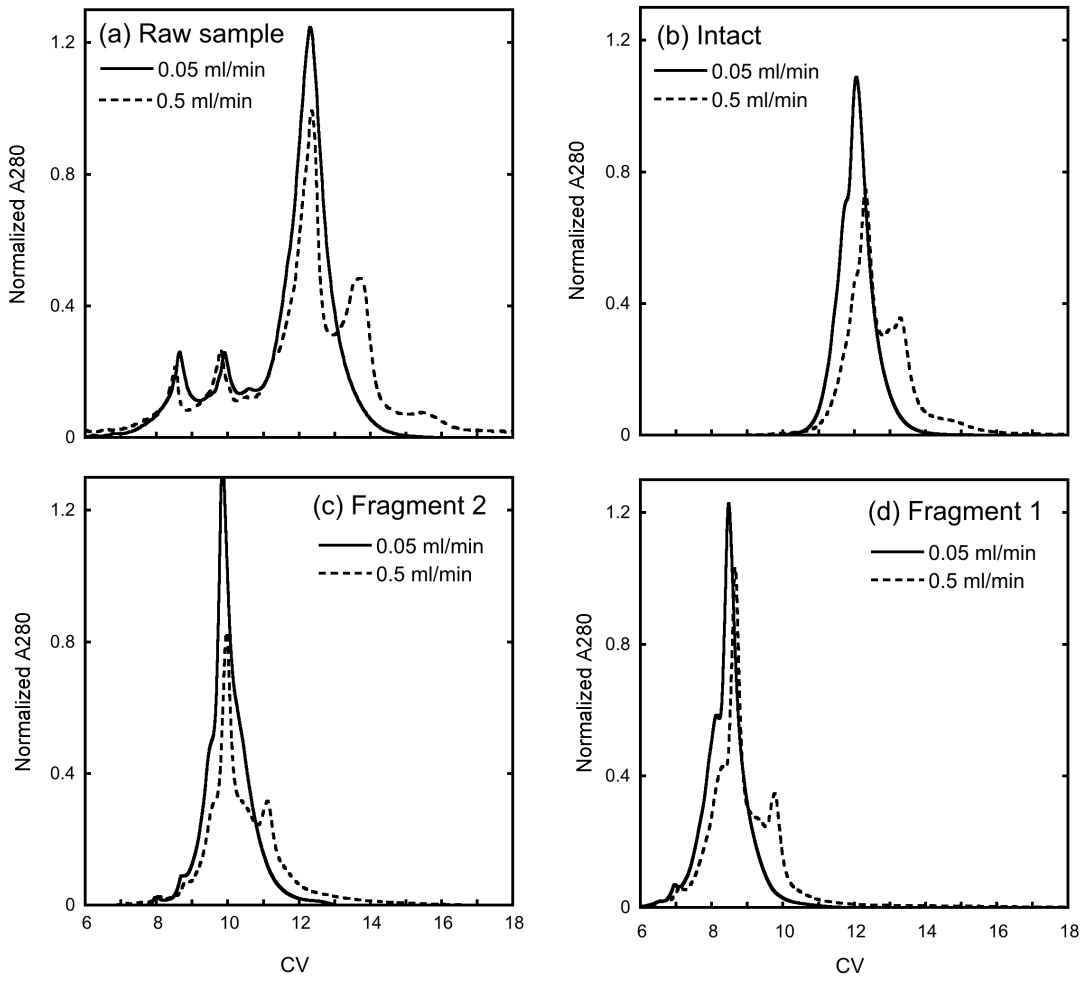

Figure 6.5. Effect of flow rate on the elution behavior of the raw sample and of each isolated component on the ProPac WCX-10 column with a 0-125 mM NaCl linear gradient over 20 CV. (a) raw sample, (b) intact protein, (c) fragment 2, (d) fragment 1. Residence times corresponding to flow rates of 0.05 and 0.5 ml/min are 25.0 and 2.5 min, respectively. Protein mass load were 0.22±0.1 mg/ml for (a), 0.12±0.07 for (b), 0.03±0.02 for (c), and 0.06±0.03 for (d). Absorbance values are normalized to the same total peak area.

Figure 6.6 shows the effect of temperature on the elution behavior of the isolated species on the ProPac column. As seen in this figure, the multiple peaks seen in each case at 21 °C tend to merge into a single peak with slightly lower retention than the average of the multiple 21 °C peaks when the temperature is increased to 40 °C. This behavior parallels that seen as a function of flow rate. In this case, a higher temperature appears to have the same effect as a lower flow rate (or longer residence time). A similar behavior was observed for intact BiSAb molecules in Chapter 2 for CEX and Chapter 5 for HIC and was attributed to the kinetics of the configurational interconversion becoming faster at higher temperature. As seen in this figure the same behavior and, likely, the same underlying molecular mechanism appears to determine the chromatographic behavior of the BiSB fragments.

The final effect explored for the ProPac column is that of the hold time during which the protein sits on the chromatographic surface in a low-salt buffer where the protein binding strength is high. Figure 6.7 compares the elution behavior of the isolated fractions with or without a 60 min hold prior to commencing the gradient. In all three cases, the fraction of total protein emerging in the late elution peaks is somewhat higher when a hold time is included compared to the case without a hold suggesting that interactions with the chromatographic surface tend to shift the molecular configuration toward that of the more retained species increasingly over time. In Chapter 3, we showed, through a number of independent measurements including in-line tryptophan fluorescence spectroscopy, that the more strongly retained peaks correspond to configurations with the scFv domains extended away from the framework IgG. By extrapolation, we surmise that this is also likely to be the case for the BiSB fragments studied in this work

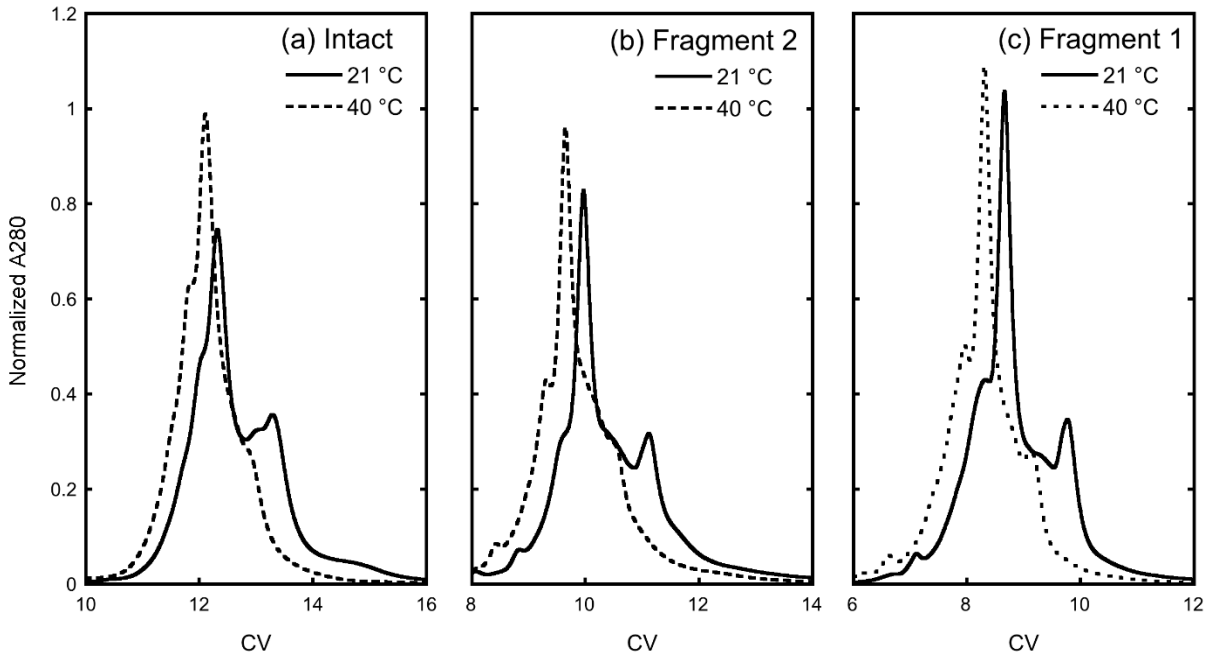

Figure 6.6. Effect of temperature on the elution behavior of the isolated components on the ProPac WCX-10 column with a 0-125 mM NaCl linear gradient over 20 CV at 0.5 ml/min corresponding to a 2.5 min residence time. (a) intact protein, (b) fragment 2, (c) fragment 1. Protein mass loads were 0.05±0.005 mg/ml for (a), 0.02±0.001 for (b), and 0.01±0.001 for (c). Absorbance values are normalized to the same total peak area. Note that the x-axis scales are different in each in panel.

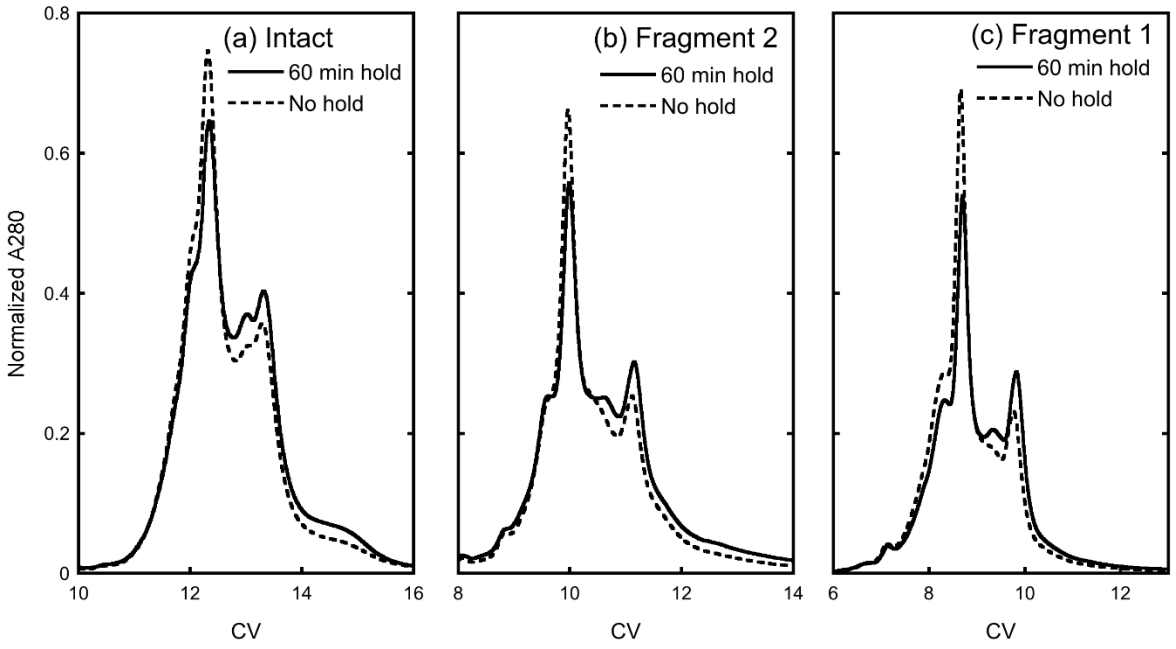

Figure 6.7. Effect of hold time on the elution behavior of the isolated components on the ProPac WCX-10 column with a 0-125 mM NaCl linear gradient over 20 CV at 0.5 ml/min corresponding to a 2.5 min residence time. (a) intact protein, (b) fragment 2, (c) fragment 1. Protein mass loads were 0.05±0.005 mg/ml for (a), 0.01±0.001 for (b), and 0.02±0.001 for (c). Absorbance values are normalized to the same total peak area. Note that the x-axis scales are different in each in panel.

The remaining chromatographic studies were performed with the Nuvia column. While resolution is lower compared to the ProPac column, which prevents observing many of the details of the multiple elution peak behaviors, Nuvia HR-S is suitable for preparative/process scale applications as a result of its larger surface area and, thus, greater binding capacity. Figure 6.8a shows the raw BiSB sample chromatograms obtained with 5, 10, 15, 20, and 40 CV gradients. As seen in this figure, resolution increases and elution occurs at lower Na^+ concentrations as the length of the gradient is increased. Disregarding the presence of multiple configurations, an average retention factor of the intact species and of the two fragments can be obtained by analyzing these chromatograms according to the method of Yamamoto [4][5][6][7]. Based on the stoichiometric displacement (SD) model [8] or, equivalently, on the steric mass action (SMA) law model [9], in the linear region of the isotherm, binding of each species is described by the following equation:

$$q_i = \frac{K_i \left(q_0\right)^{z_i}}{\left(C_{Na^+}\right)^{z_i}} C_i \tag{6.1}$$

where q_i and q_0 are the bound protein concentration and the resin charge density, respectively, C_i is the protein concentration in solution, C_{Na^+} is the Na^+ concentration, K_i is an equilibrium constant for the exchange of protein and Na^+, and z_i is the protein effective charge. Accordingly, the protein retention factor is:

$$k_i^{'} = \phi \left[\frac{K_i \left(q_o\right)^{z_i}}{\left(C_{Na^+}\right)^{z_i}} + \varepsilon_{p,i} \right] \tag{6.2}$$

where $\phi = \left(1-\varepsilon\right)/\varepsilon$ is the phase ratio and $\varepsilon_{p,i}$ is the intraparticle porosity accessible by the protein. Based on eq. 6.2, the following relationship is obtained between the normalized gradient slope, γ, and the Na^+ concentration at elution, $C_{Na^+}^R$ [10]:

$$\gamma' = \int_{C_{Na^+}^{f}}^{C_{Na^+}^{R}} \frac{1}{k_i' - k_{Na^+}'} dC_{Na^+} = \int_{C_{Na^+}^{f}}^{C_{Na^+}^{R}} \frac{1}{\phi\left[K_i \left(q_o\right)^{z_i} \left(C_{Na^+}\right)^{-z_i} + \varepsilon_{p,i} - \varepsilon_{p,Na^+}\right]} dC_{Na^+} \tag{6.3}$$

where $\gamma = \left(1-\varepsilon\right)\left(C_{Na^+}^{f} - C_{Na^+}^{0}\right)/CV_G$. In this expression, $C_{Na^+}^{f}$ and $C_{Na^+}^{0}$ are the final and initial Na^+ concentrations in the gradient, respectively, CV_G is the length of the gradient, and ε_{p,Na^+} is the intraparticle porosity accessible by Na^+. Since the Nuvia HR-S gradient elution peaks were only partially resolved, the values of $C_{Na^+}^{R}$ were determined by deconvoluting the experimental chromatograms shown in Fig. 6.8 by regressing a composite of three exponentially modified Gaussian (EMG) curves [11]. The Na+ concentration at elution for the two fragments and for the intact protein were then calculated based on the conductivity curve at the mean retention of each EMG curve. Figure 6.8b shows the γ-$C_{Na^+}^{R}$ data obtained by deconvoluting the elution profiles using three exponentially modified Gaussian (EMG) functions [11]. Lines calculated according to eq. 6.3 with the parameters z_i and K_i determined by non-linear regression and summarized in Table 6.1. Values of $\varepsilon_{p,i}$ = 0.51±0.01 for all three proteins species and ε_{p,Na^+} = 0.78±0.01, determined from pulse injections under non-binding conditions were used for these calculations. A Wolfram Mathematica 10 script using the function NonlinearModelFit was used for the computation.

Table 6.1. Stoichiometric displacement model parameters.

	Fragment 1	Fragment 2	Intact
z_i	7.65±0.20	8.22±0.33	9.32±0.13
K_i	0.0632±0.0058	0.132±0.015	0.366±0.010

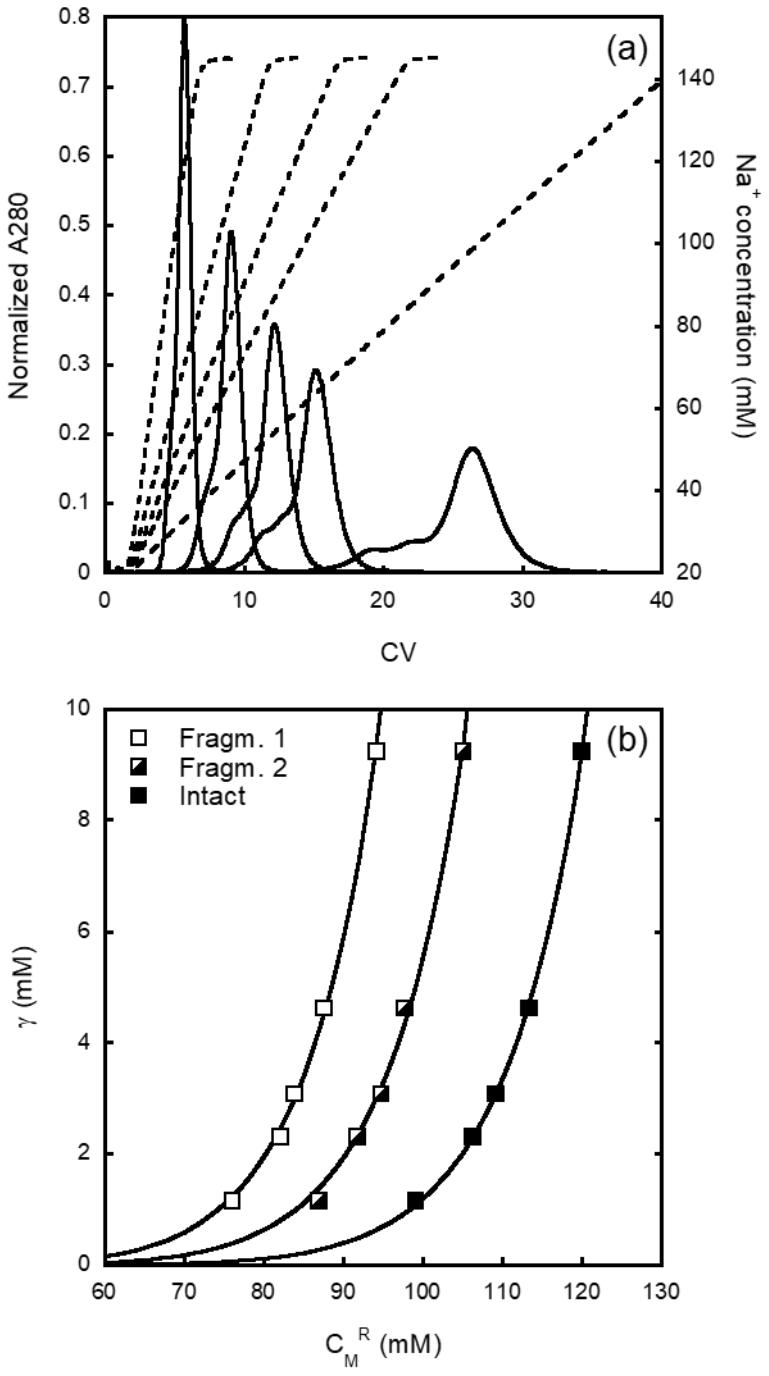

Figure 6.8. Effect of gradient length on the elution behavior of the raw sample on the Nuvia HR-S column with 0-125 mM NaCl linear gradients over 5, 10, 15, 20, and 40 CV at 2.0 ml/min corresponding to a 1.5 min residence time. (a) chromatograms, (b) normalized gradient slope vs. Na+ concentration at elution. Protein mass loads were 0.11±0.03 mg/ml. Absorbance values are normalized to the same total peak area. Lines in (b) are based on eq. 6.3 with parameters in Table 6.1.

Based on these results, it is evident that the z-values of the three components are relatively close to each other indicating that the number of resin ligands that each species interacts with is similar. We believe that this is because of the large size of these molecules, which restricts the number of resin ligands that they can interact with to a relatively small portion of the protein surface. On the other hand, the *K*-values are clearly statistically different for the different species indicating that affinity of interaction with between the protein molecules and the resin ligands, rather than differences in effective charge, tend to drive the separation. In Chapter 3, we have shown that surface charge maps of the scFv and Fc domains of the BiSAb structures used in this work. Both the scFv and the C-terminal region of the Fc domain were found to be highly positively charged at this pH. As a result, it is possible that removing a scFv domain does not affect the effective charge significantly. On the other hand, since the surface charge distribution is different for the scFv and for the Fc domain, it is possible that the specific affinity for binding is different for the different species and is what is responsible for the different affinity constants observed experimentally.

6.3.3 Adsorption Isotherms and Kinetics

Figure 6.9 shows the single component adsorption isotherms for the intact molecule and for the two fragments along with a limited number of data points for the three-component system obtained for Nuvia HR-S in 10 mM Na_2PO_4 at pH 7. As seen in Fig. 6.9a, the single-component maximum adsorption capacity is similar for all three species and is between 110 and 120 mg/ml, only slightly lower than the capacity of 137 mg/ml observed for a monoclonal antibody (IgG1) on this resin in the same buffer [12]. The binding affinity, however, indicated by the initial slope of the isotherm data, appears to be highest for the intact molecule and lowest for fragment 1, which is consistent with the retention behavior observed in the gradient elution experiments (Fig. 6.8). The data for

the three-component system (Fig. 6.9b) confirm that the selectivity favors greatly binding of the intact species. It is evident that while little binding of the fragments is seen at equilibrium, binding of the intact species is comparable in magnitude to that observed for the single component case.

The lines in Fig. 6.9a are based on SMA isotherm model, which is given by:

$$q_i = \frac{K_i\left[q_0 - \left(z_i + \sigma_i\right)q_i\right]^{z_i}}{\left(C_{Na^+}\right)^{z_i}} C_i \tag{6.4}$$

for a single protein and by

$$q_i = \frac{K_i\left[q_o - \sum_{j=1}^{M}\left(z_j + \sigma_j\right)q_j\right]^{z_i}}{\left(C_{Na^+}\right)^{z_i}} C_i \tag{6.5}$$

for mixture of *M* proteins [9]. In these equations, σ_i is the hindrance parameter or shielding factor. Its value was determined by fitting eq. 6.4 to the single component isotherm data using the values of z_i and K_i derived from the LGE data. The resulting values of σ_i were 130±2, 123±3, and 153±2 for fragment 1, fragment 2, and the intact species, respectively. These values are intermediate between those obtained by Reck et al. [12] for the adsorption of a monoclonal antibody and its dimer on this resin (σ_{monomer} = 111 and σ_{dimer} = 229). Table 6.2 compares the experimental three-component adsorption data with predictions based on eq. 6.5 using these parameters. As seen from this table, the agreement is only qualitative, which is not surprising consider the complexity of these molecules and the fact that they exist in multiple structural configurations. Nevertheless, the model shows that, in agreement with the experimental observations, binding of the intact species is vastly predominant at equilibrium with only a small amount of adsorption of the fragments.

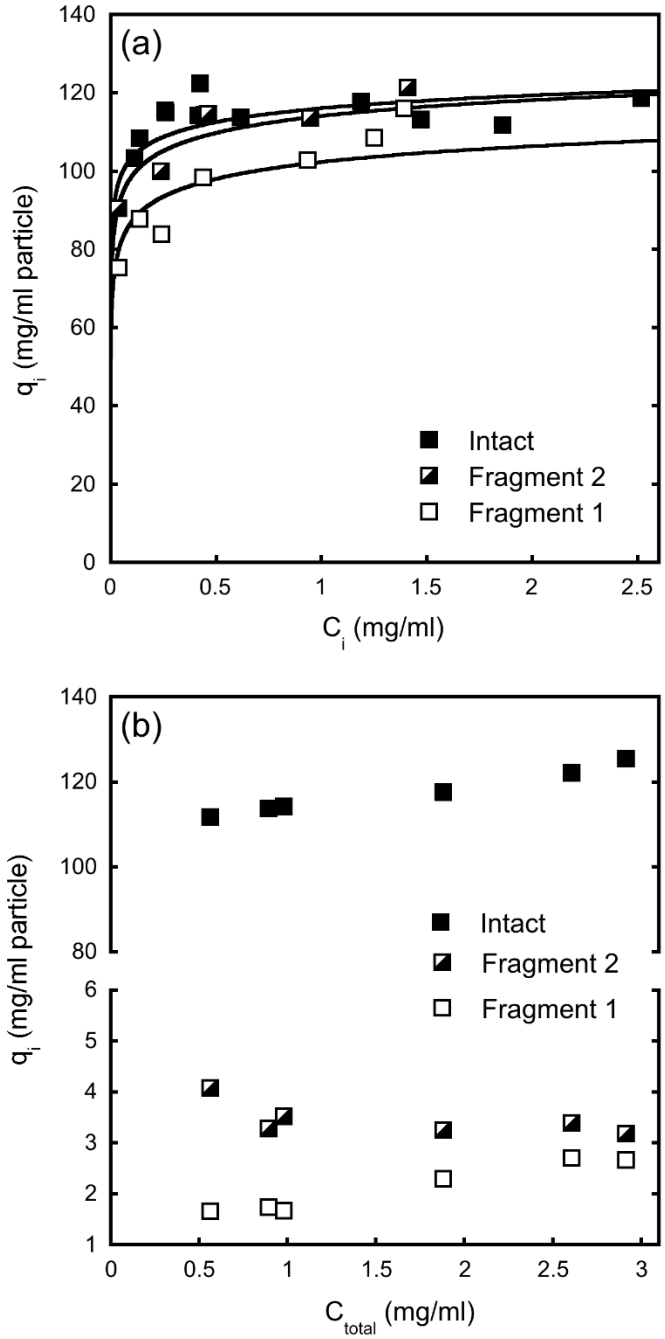

Figure 6.9. Adsorption isotherms for Nuvia HR-S in 10 mM Na_2PO_4 at pH 7.0 after 24 h equilibration. (a) one-component isotherms for the isolated species. (b) mixture adsorption isotherms plotted vs. the total residual protein concentration in solution. The individual values of q_i and C_i are given in Table 6.2. Lines in (a) are based on eq. 6.4.

Table 6.2. Comparison of experimental and predicted three-component competitive binding. Predicted values are based on eq. 6.5. Values reported in mg/ml.

Experimental						Predicted		
$C_{\text{Fragm.1}}$	$C_{\text{Fragm.2}}$	C_{Intact}	$q_{\text{Fragm.1}}$	$q_{\text{Fragm.2}}$	q_{Intact}	$q_{\text{Fragm.1}}$	$q_{\text{Fragm.2}}$	q_{Intact}
0.13	0.16	0.28	1.7	4.1	112	2.4	9.2	101
0.15	0.20	0.55	1.7	3.3	114	1.6	6.7	107
0.18	0.24	0.56	1.7	3.5	114	1.9	7.9	106
0.30	0.40	1.18	2.3	3.3	118	1.8	7.0	110
0.31	0.42	1.88	2.7	3.4	122	1.3	5.1	115
0.32	0.43	2.17	2.7	3.2	126	1.2	4.6	116

Figure 6.10 shows representative CLSM images of the patterns of bound protein within individual particles during transient adsorption of a three-component mixture containing 1.48 mg/ml of intact protein, 0.24 mg/ml of fragment 2, and 0.28 mg/ml of fragment 1 for the same conditions of Fig. 6.9. In Fig. 6.10, the top three rows show the individual fluorescent images representing the intact protein in red, fragment 2 in green, and fragment 1 in blue, respectively, while the bottom row shows a digital superposition of the three colors. As seen in this figure, adsorption of the three species is accompanied by the formation of a series of fronts where the intact protein appears to displace fragment 2, which, in turn, appears to displace fragment 1. Each of the two displaced components tends to accumulate toward the center of the particle but is eventually nearly completely desorbed. At 30 min, only a small amount of the fragments remains in the particle, which is consistent with the equilibrium behavior shown in Fig. 6.9b and in Table 6.2. This behavior is a result of the selective binding of the intact species relative to fragment 2 and of fragment 2 relative to fragment 1 coupled with a pore-diffusion limited mass transfer mechanism.

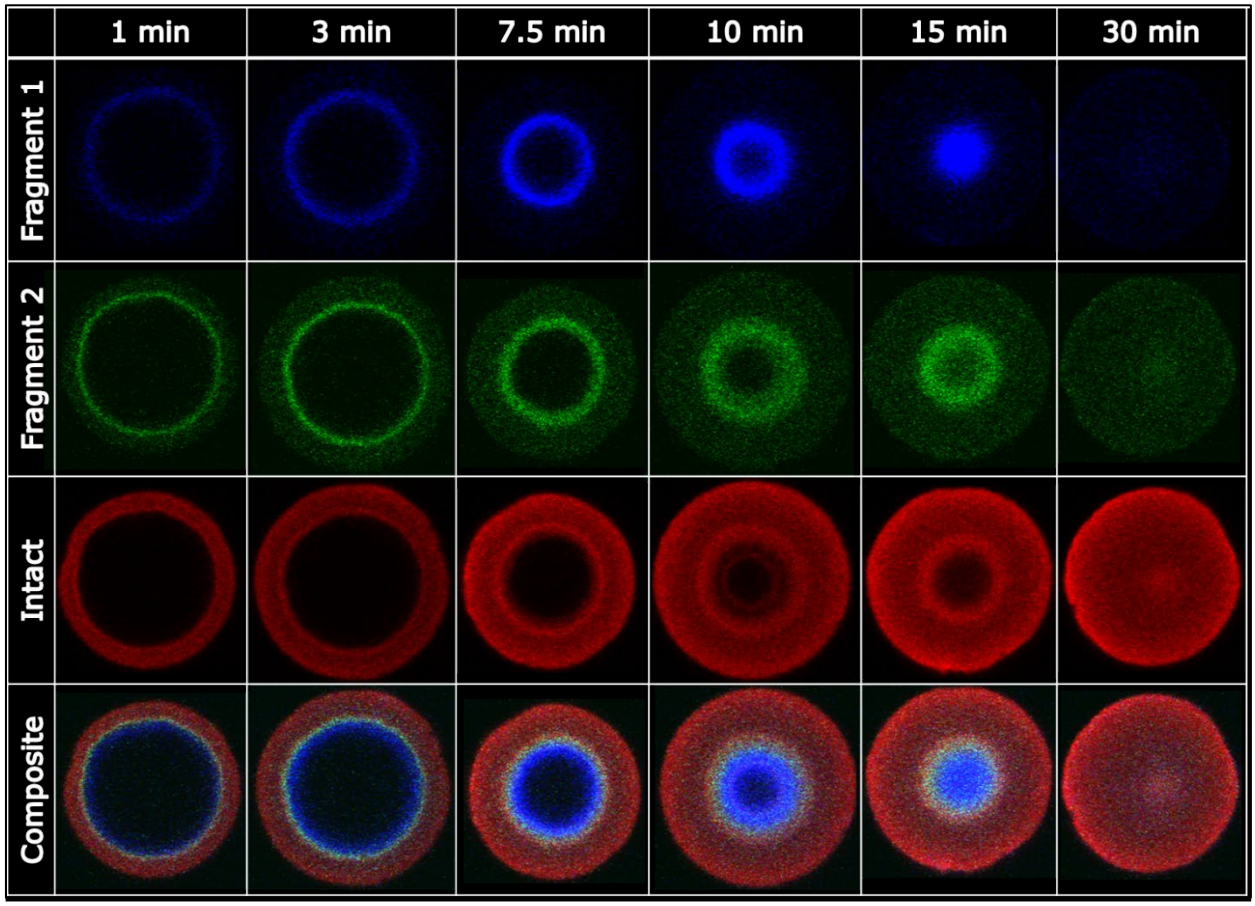

Figure 6.10. Representative CLSM images of patterns of protein binding during the adsorption of a mixture containing 1.48 mg/ml of the intact species, 0.24 mg/ml of fragment 2, and 0.28 mg/ml of fragment 1 on Nuvia HR-S in 10 mM Na_2PO_4 at pH 7. The top three rows show individual fluorescence channels corresponding to fragment 1, fragment 2, and the intact species as indicated. The bottom row shows a composite of the three channels. Actual particle diameters were, from left to right, 46.9, 51.9, 44.9, 51.6, 48.3, and 46.3 μm.

This result is akin to the results observed for this resin and other macroporous adsorbents for the adsorption of an antibody mixture containing deaminated variants [13] and for the adsorption of mixtures of antibody monomer and dimer [12]. An important difference between the results obtained in this work and those of these previous studies for the co-adsorption of deamidated variants and for the co-adsorption of monomer-dimer mixtures is that, in this case, the displacement fronts are much smoother. The phenomena was studied in Chapter 4 and found to be due to the different configurations in competition with one another and having different local capacities. Note that, in the case of the intact species (red), a more intense band (also in red) is observed at the leading edge of the displacement front between the intact species and fragment 2 (shown in green). This thin band is associated with the moderate purity of the isolated intact sample used for fluorescent labeling. Since this sample contained a small percentage of fragment 2 (confirmed by ProPac analysis), the additional red band is actually associated with this fragment.

A detailed analysis of the interplay of mass transfer and configurational interconversion of the intact species and of the associated fragments is beyond the scope of this work. Nevertheless, some useful information about the mass transfer mechanism and the rates at which transport occurs within the Nuvia HR-S particles can be obtained by modeling the system as if binding occurred without configurational interconversion. The model used for this approximate analysis is that developed by Martin et al.[14], which assumes that mass transfer occurs by pore diffusion with highly favorable adsorption isotherms. According to this model, for a three-component mixture of strongly, but competitively bound species, there will be three sharp fronts: the adsorption front of the most-weakly bound species (fragment 1, in our case), the fragment 2-fragment 1 displacement front, and the intact-fragment 2 displacement front. Assuming that each species completely

displaces the other (which is only approximate in our case), the radial position of these fronts is given as a function of time by the following equations:

$$2\rho_{\mathrm{I}}^3 - 3\rho_{\mathrm{I}}^2 + 1 = \frac{6D_{e,\mathrm{I}}C_{\mathrm{I}}}{q_{m,\mathrm{I}}r_p^2}t \tag{6.6}$$

$$2\rho_{\mathrm{F2}}^3 - 3\rho_{\mathrm{F2}}^2 + 1 = \left(1 + \frac{q_{m,\mathrm{I}}D_{e,\mathrm{F2}}C_{\mathrm{F2}}}{q_{m,\mathrm{F2}}D_{e,\mathrm{I}}C_{\mathrm{I}}}\right)\frac{6D_{e,\mathrm{I}}C_{\mathrm{I}}}{q_{m,\mathrm{I}}r_p^2}t \tag{6.7}$$

$$2\rho_{\mathrm{F1}}^3 - 3\rho_{\mathrm{F1}}^2 + 1 = \left(1 + \frac{q_{m,\mathrm{I}}D_{e,\mathrm{F1}}C_{\mathrm{F1}}}{q_{m,\mathrm{F1}}D_{e,\mathrm{I}}C_{\mathrm{I}}} + \frac{q_{m,\mathrm{I}}D_{e,\mathrm{F2}}C_{\mathrm{F}_2}}{q_{m,\mathrm{F2}}D_{e,\mathrm{I}}C_{\mathrm{I}}}\right)\frac{6D_{e,\mathrm{I}}C_{\mathrm{I}}}{q_{m,\mathrm{I}}r_p^2}t \tag{6.8}$$

where $\rho_i = r_{s,i}/r_p$ is the dimensionless radial position of each adsorption front, $q_{m,i}$, $D_{e,i}$, and C_i are, respectively, the binding capacity, the effective pore diffusivity, and the solution concentration of component i, and r_p is the radius of the particle. Subscripts I, $\mathrm{F2}$, and $\mathrm{F1}$ in these equations indicate the intact species, fragment 2, and fragment 1, respectively. In order to compare these equations to the experimental results, approximate positions of the adsorption fronts were determined graphically along with the radius of each individual particle. The results are shown in Fig. 6.11 with each value of ρ_i plotted as a function of t/r_p^2. Lines corresponding to eqs. 6.6-8 are also shown. These lines were calculated using the values predicted by eq. 6.4 for single-component adsorption capacities, $q_{m,i}$, and using effective diffusivities regressed to these experimental data.

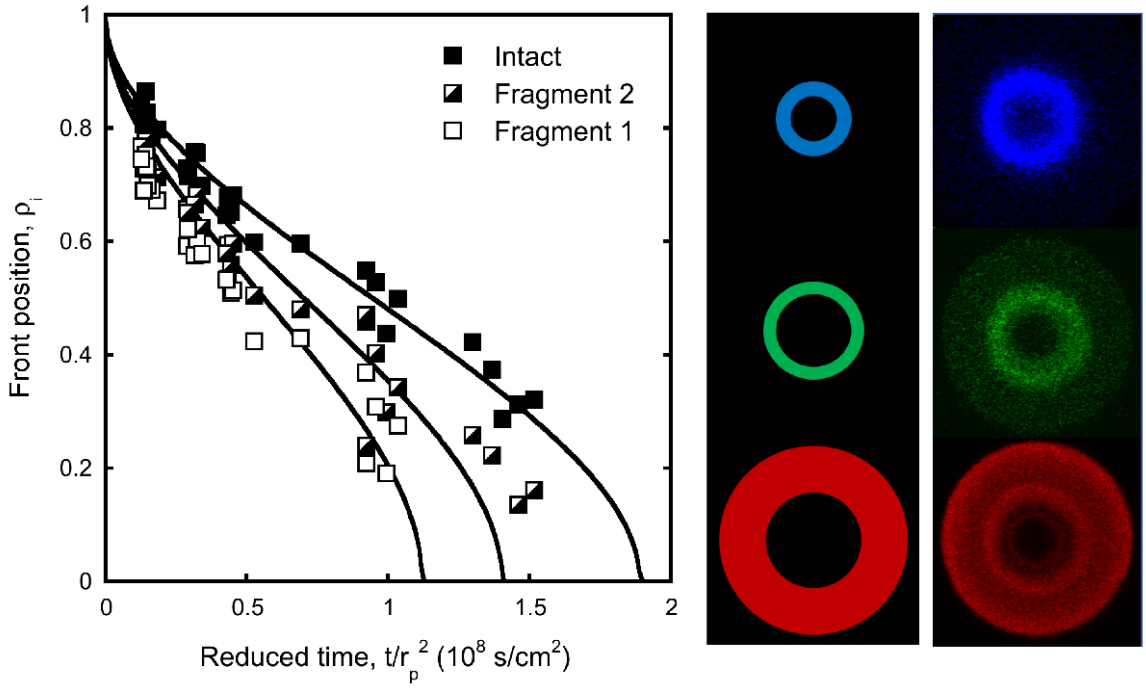

Figure 6.11. Dimensionless position of the adsorption fronts vs. reduced time for the adsorption of a mixture containing 1.48 mg/ml of the intact species, 0.24 mg/ml of fragment 2, and 0.28 mg/ml of fragment 1 on Nuvia HR-S in 10 mM Na_2PO_4 at pH 7. The lines correspond to the three-front model according to eqs. 6.6-6.8 with $q_{m,i}$ = 118, 105, and 95 mg/ml and $D_{e,i}$ = 7.02x10^{-8}, 12.9x10^{-8}, and 10.1x10^{-8} cm^2/s for the intact species, fragment 2 and fragment 1, respectively. The panels on the right-hand-side show the predicted adsorption fronts at t/r_p^2 = 0.92x10^8 s/cm^2 and the corresponding CLSM images at t = 615 s for a particle with r_p = 25.8 μm for fragment 1, fragment 2, and the intact species shown from top to bottom.

The corresponding values of $D_{e,i}$ were (7.02±0.14)x10^{-8} cm^2/s, (12.9±1.1)x10^{-8} cm^2/s, and (10.1±0.3)x10^{-8} cm^2/s for the intact species, for fragment 2, and for fragment 1, respectively. These values are comparable to those obtained for diffusion of an antibody monomer and dimer in the same resin for comparable conditions (8.0x10^{-8} and 4.1x10^{-8} cm^2/s, respectively) [12]. As seen in Fig. 6.11, while not exact, the model appears to capture the main trends observed experimentally. What is not captured, of course, is the actual relative smoothness of the adsorption fronts, which is attributed to the existence of multiple binding configurations for each species as shown in Chapter 4.

6.4 References

[1] L.K. Kimerer, B. Niu, W. Zhai, T.M. Pabst, A.K. Hunter, G. Carta, Chromatographic and Adsorptive Behavior of a Bivalent Bispecific Antibody and its Associated Fragments, J. Chromatogr. A. (2021).

[2] K.A. Johnson, K. Paisley-Flango, B.S. Tangarone, T.J. Porter, J.C. Rouse, Cation exchange – HPLC and mass spectrometry reveal C-terminal amidation of an IgG1 heavy chain, Anal. Biochem. 360 (2007) 75–83. doi:10.1016/j.ab.2006.10.012.

[3] L.W.J. Dick, D. Qiu, D. Mahon, M. Adamo, K. Cheng, C-Terminal Lysine Variants in Fully Human Monoclonal Antibodies : Investigation of Test Methods and Possible Causes, Biotechnol. Appl. Biochem. 100 (2008) 1132–1143. doi:10.1002/bit.21855.

[4] S. Yamamoto, K. Nakanishi, R. Matsuno, Ion-Exchange Chromatography of Proteins, Marcel-Dekker, New York, 1988.

[5] S. Yamamoto, K. Nakanishi, R. Matsuno, T. Kamikubo, Ion Exchange Chromatography of Proteins-Prediction of Elution Curves and Operating Conditions. I. Theoretical Considerations, Biotechnol. Bioeng. XXV (1983) 1465–1483.

[6] S. Yamamoto, K. Nakanishi, R. Matsuno, T. Kamikubo, Ion Exchange Chromatography of Proteins-Prediction of Elution Curves and Operating Conditions. II. Experimental Verification, Biotechnol. Bioeng. XXV (1983) 1373–1391.

[7] G. Carta, A.R. Ubiera, T.M. Pabst, Protein Mass Transfer Kinetics in Ion Exchange Media : Measurements and Interpretations, Chem. Eng. Technol. Rev. 28 (2005) 1252–1264.

[8] W. Kopaciewicz, M.A. Rounds, J. Fausnaugh, F.E. Regnier, Retention model for high-performance ion-exchange chromatography, J. Chromatogr. 266 (1983) 3–21.

[9] C.A. Brooks, S.M. Cramer, Steric mass-action ion exchange: Displacement profiles and

induced salt gradients, AIChE J. 38 (1992) 1969–1978. doi:10.1002/aic.690381212.

[10] G. Carta, A. Jungbauer, Protein Chromatography, 2nd ed., Wiley-VCH, Weinheim, Germany, 2020.

[11] Y. Kalambet, Y. Kozmin, K. Mikhailova, I. Nagaev, P. Tikhonov, Reconstruction of chromatographic peaks using the exponentially modified Gaussian function, J. Chemom. 25 (2011) 352–356.

[12] J.M. Reck, T.M. Pabst, A.K. Hunter, X. Wang, G. Carta, Adsorption equilibrium and kinetics of monomer-dimer monoclonal antibody mixtures on a cation exchange resin, J. Chromatogr. A. 1402 (2015) 46–59.

[13] Y. Tao, E.X.P. Almodovar, G. Carta, G. Ferreira, D. Robbins, Adsorption kinetics of deamidated antibody variants on macroporous and dextran-grafted cation exchangers. II. Adsorption Kinetics, J. Chromatogr. A. 1218 (2011) 8027–8035.

[14] C. Martin, G. Iberer, A. Ubiera, G. Carta, Two-component protein adsorption kinetics in porous ion exchange media, J. Chromatogr. A. 1079 (2005) 105–115. doi:10.1016/j.chroma.2005.03.007.

7 Conclusions and Recommendations

Bivalent bispecific antibodies were studied for their complex adsorptive and chromatographic behavior. Slow interconversion between major configurations caused multiple peak elution on both cation exchange and hydrophobic interaction chromatography columns. A wide range of biophysical techniques were utilized to determine the underlying mechanism including intramolecular crosslinking, autofluorescence, and enzyme proteolysis to determine domain contributions to binding. Phenomenological models were developed to predict column behavior during linear gradient elution and adsorption kinetics within macroporous particles at high load conditions. BiSAb fragments, which contain one less scFv, were found to have small differences in binding strength compared to the intact molecule. However, high selectivity and nearly full displacement was observed at high load conditions. More specific conclusions, as well as recommendations for future work, are presented below.

7.1 Chromatographic Behavior on Cation Exchange Columns

The goal of this work was to explore the complex elution behavior of BiSAbs where a pure protein feed eluted three reversible peaks on high resolution cation exchange columns. In-line dynamic light scattering measured all three peaks to be monomer-sized, showing that the underlying mechanism was not due to on-column aggregation. Residence time, temperature, and hold time were found to significantly alter elution profiles. When gradients were operated at short residence time, ~ 2 min, and room temperature, three peaks eluted with high resolution. When either the residence time was elongated to ~ 40 min or temperature was elevated to 55 °C, a single peak eluted. When the protein was held bound on the resin prior to elution, the third, strongest binding peak increased in relative size. The observed phenomena is due to the relative time scales of

transitions between three major binding forms and column time. When transitions are slow relative to column time, at short residence time and room temperature, the different binding states elute as separate peaks. When transitions between binding states are fast relative to column time, at elongated residence time or increased temperature, the binding states are in equilibrium with one another and move down the column with average retention and elute as a single peak. The biophysical nature of the three binding states is studied in Chapter 3 with conclusions discussed in section 7.2.

A phenomenological column model was developed including three interconvertible binding states and was able to capture the trends observed experimentally. Column models of this type contain a large number of parameters to describe interconversion, binding, and mass transfer. To increase robustness of the model, parameters were fit to experiments where they were most impacful. For example, adsorbed phase kinetic rate and equilibrium parameters were fit to hold time data, which were measured with very short columns to minimize back exchange in solution. Isotherm parameters governing binding strength of each of three states were measured at short residence time to minimize effects of interconversion. Solution phase equilibrium constants were fit to equilibrium analysis to deconvolute the relative amounts of the three species at the long residence time of 185 min.

Recommendations for future work would be to utilize the column model to optimize productivity for a separation of the intact monomer species from product related variants such as fragments or aggregates. Obviously, finding chromatography resins or mobile phase conditions where the multiple peak elution does not occur is a first priority in method development as the multiple peaks cause very broad elution pools. However, if multiple peak elution is unavoidable, depending on the nature of the contaminant, the key parameters observed can be taken advantage of to increase

productivity. One hypothetical example is the separation of a fragment that elutes prior to the first peak of the intact BiSAb molecule. Adding a hold step would cause interconversion of the intact molecule toward stronger binding forms which may increase resolution from the weaker binding fragment. Another effect that could be utilized is that of temperature. Kinetic rate parameters could be fit at varying temperatures for temperature predictability to increase the sharpness of the peaks by increasing both interconversion rates between binding states and mass transfer rates. Multiple peak elution behavior greatly complicates process development, however using the developed model would allow parameters to be varied *in silico,* decreasing the development time and amount of protein required for experimentation.

7.2 Biophysical Basis

The biophysical nature of the three reversible binding states was studied using homology modeling, intramolecular crosslinking, enzyme proteolysis to determine domain contributions, and autofluorescence. Results indicate that the observed complex elution behavior is directly caused by the flexible linker allowing extreme scFv configurations. The scFvs can either be in a collapsed configuration, where they interact with the framework mAb, or the scFvs can be outstretched, and have greater freedom to bind to the resin with greater strength. Enzyme proteolysis of different BiSAb formats produced fragments with and without linked scFvs. Based on the chromatographic response of these fragments, the scFvs were determined to contribute the largest share of binding strength, as well as the number of linked domains was found to directly determine the number of reversible peaks. Fragments with two scFvs showed reversible three peak elution, fragments with one linked scFv showed reversible two peak elution, and fragments without linked scFvs eluted as a single peak. When residence time was elongated, all cases of multiple peaks merged to a single eluted peak reflecting the intact BiSAb behavior. Intramolecularly crosslinking BiSA, which

"freezes" the molecule in its conformation, removed the multiple peak elution behavior. Homology modeling supported our domain response observations as large patches of positive charge were observed on the scFv domains which bind strongly to the cation exchange surface. Homology modeling also identified multiple solvent exposed tryptophan residues in the scFv and the Fab domains. Different configurations of the scFv attached to the N-terminus of the framework mAb, as in BiSA, would cause differences in the microenvironment of these tryptophans. Indeed, we measured differences in autofluorescence between the peaks, with the stronger binding peaks having greater solvent accessibility of these tryptophans compared to the weaker binding peaks.

Homology modeling in these studies was used in a qualitative manner to match surface properties with experimental chromatographic binding strength data and locate surface exposed tryptophan residues that could have differences in solvent exposure between different molecular configurations. Future computational work can further probe the inter-domain interactions using protein docking simulation servers such as ClusPro [1][2][3][4] or HawkDock [5][6][7]. These servers calculate favorable protein docking orientations by assuming an implicit solvent and minimizing free energy. To simulate domain-domain interactions, major domains such as the Fab and scFv can be input with restrictive statements requiring the termini of each domain to be less than the distance of the flexible linker [8]. Analyzing the most favorable docked structures for interacting amino acid residues between domains informs how favorable the interaction is and the nature of interaction, whether it is based on electrostatic charged pairs or hydrophobic interactions. Screening these docking models could also assist in rationally mutating single amino acids to weaken or strengthen the domain-domain interaction.

7.3 Interconversion Effects on Mass Transfer

The adsorption kinetics of BiSAbs in a macroporous cation exchanger is affected by the configurational flexibility of these molecules leading to multiple binding forms that interconvert at finite rates. The interplay of transport, adsorption, and interconversion between different molecular forms led to complex patterns of bound protein within the particle. While the adsorption kinetics of a simple mAb is very well described by the classical shrinking core model, a complex model accounting for these combined effects is needed to describe the experimental trends observed with BiSAbs. Since transport is limited by pore diffusion and the interconversion follows first order kinetics, the transient adsorption behavior is linearly related to the protein concentration in solution. Thus, the results observed at different protein concentrations are the same when compared at times that scale in inverse proportion to the protein solution concentration. The buffer salt concentration and pH affect the BiSAb adsorption kinetics by altering the relative strength of binding of the different molecular configurations. At either lower salt concentrations or lower pH, binding becomes stronger for all of the different binding forms leading to patterns of total bound protein within the particles that conform again to the classical shrinking core behavior. Temperature also affects the BiSAb binding kinetics in unique ways. For a simple mAb, the only significant effect of temperature is on the diffusivity and, thus, on the adsorption rate. For BiSAb molecules, temperature affects not only the diffusivity but also, to a greater extent, the interconversion rates between different binding forms leading to faster equilibration. The model developed in this work is consistent with these experimental observations and provides the means to understand how the distribution of the different binding forms affects the overall adsorption kinetics.

The primary method used in this chapter, confocal microscopy, allows visualization of the intraparticle adsorption profiles using a small amount of protein. Mechanistic models, that can be used to speed up process development, require an understanding of the mass transfer mechanism. Without further study, the complex profiles of BiSAbs appeared to follow a solid diffusion or parallel pore diffusion transport mechanism [9][10]. However, the rate at which the protein front penetrated the particle was directly related to protein concentration in the bulk, showing that the correct mechanism is pore diffusion. Varying critical parameters, such as protein concentration, ensures an accurate interpretation of the mass transfer mechanism.

7.4 Chromatographic Behavior on Hydrophobic Interaction Columns

BiSAb linear gradient elution behavior was evaluated on a range of HIC columns varying by resin functional ligand, particle structure, and particle size. HIC complex elution behavior fully matched that observed for CEX despite the mobile phase composition and protein-surface interaction mechanisms being completely different. BiSAbs eluted three reversible peaks, regardless of resin characteristics, at room temperature and short residence times. Elongating the residence time or increasing temperature caused a merger of the peaks and elution of a single peak. Increasing hold time caused an enrichment of the strongest binding peaks. A phenomenological column model was developed in the same manner as the CEX model. The developed column model successfully captured the behavior and assisted with comparisons between CEX and HIC. Interestingly, the interconversion kinetic rates were found to be very similar across modalities. One example is reflected in the hold time experiments shown in Figs. 2.9 and 5.5. An apparent equilibrium between the forms is reached after hold times of about 60 min for HIC and about 40 min for CEX. One major difference between modalities was the solution phase equilibrium constants. The favorability of the weakest binding form in solution was much greater for CEX compared to HIC.

This effect may be due to the higher salt content in the mobile phase of HIC, which could shield the electrostatic contribution to the domain-domain interaction. Because the favorability of the domain-domain interactions was weakened, but this form was still favored overall in solution, the interaction between scFv and framework IgG is likely a combination of both electrostatic and hydrophobic interactions.

We found great utility in studying the experimental resin PPG-S, which is similar to a commercial resin, Toyopearl PPG-M, but had a smaller particle size. The reduced particle size decreased mass transfer resistance and allowed greater resolution to more accurately quantify the relative size of each peak, even at short residence times. The added resolution increased confidence in measurements of peak area after set hold times necessary to measure the kinetic rates and equilibrium constants. Because the PPG-S and PPG-M resins consisted of the same structure and functional ligand, the model for PPG-S was able to be applied to PPG-M by only changing the particle size. Our recommendation is to utilize resins with matching properties and smaller particle size when studying complex elution behavior to gain as much resolution as possible.

7.5 Fragment Separation

The chromatographic and adsorptive behavior of BiSB and two associated fragments were studied on two cation exchange resins – ProPac WCX-10, which is pellicular and suitable for analytical use, and Nuvia HR-S, which is macroporous and suitable for preparative and process scale uses. Both fragments were identified by mass spectrometry as missing one of the two scFv domains and its flexible linker, but one of them also contains an additional C-terminal lysine. On both of the cation exchangers considered in this work, the intact species containing two scFv domains is retained more strongly compared to the clipped fragment containing a single scFv domain. Retention of the clipped variant with an additional C-terminal lysine is intermediate between the

intact and the single-scFv species. Interestingly, the addition of a single charged amino acid, a C-terminal lysine, provided a significant difference in binding strength and caused the variant to be resolved for both resins. For the ProPac WCX-10 column, multiple peak elution behaviors are observed, as a result of the linker flexibility. This results in two peak elution for the fragments, which contain a single linked scFv, and three peak elution for the intact molecule, which contains two linked scFvs. This behavior is affected by residence time, temperature, and hold time in the same manner as that observed for the intact molecules. The behavior of the fragments containing the full framework IgG and a single scFv reflect the results obtained in our prior work in Chapter 3 for fragments generated through enzyme proteolysis containing either the Fc or Fab domain and a single linked scFv. These findings further our understanding that the flexibly linked scFv domain is responsible for the multiple peak behavior.

As a result of the band broadening associated with the structure and larger particle size of the resin, the multiple peak elution behavior is obfuscated for the Nuvia HR-S column. Nevertheless, the effects of multiple binding configurations are still evident at the particle scale. For this resin, the patterns of protein binding observed by CLSM show that competitive adsorption of the three species occurs within the resin beads with kinetics controlled by macropore diffusion. The selectivity strongly favors binding of the intact species over the fragments following the trends observed for the gradient elution experiments. However, the binding patterns are much smoother than the sharp fronts expected for a pore-diffusion based displacement process. It appears likely that the multiple binding configurations that exist for each species is responsible for the patterns observed, as shown in Chapter 4. An approximate model for the adsorption kinetics that neglects the multiple binding configurations and assumes that binding occurs through a series of full displacement fronts, shows that the intraparticle effective diffusivities in this resin are relatively

large considering the large molecular mass of the intact species and fragments and are comparable to the effective diffusivities reported previously for ordinary monoclonal antibodies in this resin. The high selectivity observed by CLSM, ability of the intact species to displace the fragments, and the relatively fast kinetics suggest that separation at high loadings will be effective for the separation of these fragments from the desired intact product. Future work could focus on altering parameters for this multicomponent case which were found to affect the smoothness of profiles in Chapter 4 such as temperature, salt concentration in the mobile phase, and pH. If selectivity between protein species persists at stronger binding conditions, altering the mobile phase may sharpen the displacement fronts between protein species. The effect of temperature would also be of interest to determine how the displacement profiles are affected by altering the rates of mass transfer and interconversion kinetics.

7.6 References

[1] I.T. Desta, K.A. Porter, B. Xia, D. Kozakov, S. Vajda, Performance and its Limits in Rigid Body Protien-Protein Docking, Structure. 28 (2020) 1071–1081.

[2] S. Vajda, C. Yueh, D. Beglov, T. Bohnuud, S.E. Mottarella, B. Xia, D.A. Hall, D. Kozakov, New additions to the ClusPro server motivated by CAPRI, Proteins Stucture, Funct. Bioinforma. 85 (2017) 435–444.

[3] D. Kozakov, D.R. Hall, B. Xia, K.A. Porter, D. Padhorny, C. Yueh, D. Beglov, S. Vajda, The ClusPro web server for portien-protein docking, Nat. Protoc. 12 (2017) 255–278.

[4] D. Kozakov, D. Beglov, T. Bohnuud, S. Mottarella, B. Xia, D.R. Hall, S. Vajda, How good is automated protein docking?, Proteins Stucture, Funct. Bioinforma. 81 (2013) 2159–2166.

[5] M. Zacharias, Protein-protein docking with a reduced protein model accounting for side-chain flexibility, Protein Sci. 12 (2003) 1271–1282.

[6] T. Feng, F. Chen, Y. Kang, H.Y. Sun, H. Lui, D. Li, F. Zhu, T.J. Hou, HawkRank: a new scoring function for protein-protein docking based on weighted energy terms, J. Chemom. 9 (2017) 1–15.

[7] T.J. Hou, X.B. Qiao, W. Zhang, X.J. Xu, Empirical Aqueous Solvation Models Based on Accessible Surface Areas with Implicit Electrostatics, J. Phys. Chem. B. 106 (2002) 11295–11304.

[8] B. Xia, S. Vajda, D. Kozakov, Accounting for pairwise distance restraints in FFT-based protein-protein docking, Bioinformatics. 32 (2016) 3342–3344.

[9] A.M. Lenhoff, Multiscale Modeling of Protein Uptake Patterns in Chromatographic Particles, Langmuir. 24 (2008) 5991–5995.

[10] B.D. Bowes, A.M. Lenhoff, Protein adsorption and transport in dextran-modified ion-exchange media. III. Effects of resin charge density and dextran content on adsorption and intraparticle uptake, J. Chromatogr. A. 1218 (2011) 7180–7188. doi:10.1016/j.chroma.2011.08.039.Protein.